INVESTIGATION OF LAYERED DOUBLE HYDROXIDES AND COMPOSITE MATERIALS WITH EMPHASIS ON OPTICAL PROPERTIES AND ENVIRONMENTAL ASPECTS

Thesis Submitted to the Delhi Technological University for the Award of the Degree of

DOCTOR OF PHILOSOPHY
IN
CHEMISTRY

by

BHAMINI
(2K18/PHDAC/501)

Under the supervision of
Dr. POONAM SINGH
(DTU)
and Co-supervision of
Dr. VINOD KUMAR
(JNU)

DEPARTMENT OF APPLIED CHEMISTRY
DELHI TECHNOLOGICAL UNIVERSITY
DELHI-110042 (INDIA)

2024

© DELHI TECHNOLOGICAL UNIVERSITY-2024

All rights reserved

DEPARTMENT OF APPLIED CHEMISTRY
DELHI TECHNOLOGICAL UNIVERSITY
Delhi-110042 (INDIA)

DECLARATION

This is to certify that the work presented in this thesis entitled **"Investigation of layered double hydroxides and composite materials with emphasis on optical properties and environmental aspects"** is original and has been carried out by me for the degree of **Doctorate of Philosophy** under the supervision of Dr. Poonam Singh, Assistant Professor, Department of Applied Chemistry, DTU and co-supervision of Dr. Vinod Kumar, Assistant Professor, Special Centre for Nanoscience, JNU. This thesis is a contribution of my original research work. Wherever research contributions of others are involved, every effort has been made to clearly indicate the same. To the best of my knowledge, this research work has not been submitted in apart or full for the award of any degree or diploma of Delhi Technological University or any other University/Institution.

Date:

BHAMINI
Research Scholar
2K18/PHDAC/501

DEPARTMENT OF APPLIED CHEMISTRY
DELHI TECHNOLOGICAL UNIVERSITY
Delhi-110042 (INDIA)

CERTIFICATE

This is to certify that the PhD thesis entitled **"Investigation of layered double hydroxides and composite materials with emphasis on optical properties and environmental aspects"** submitted to Delhi Technological University, Delhi-110042, in the fulfilment of the requirement for the award of the degree of Doctor of Philosophy by the candidate Ms. Bhamini (2K18/PDHAC/501) under the supervision of Dr. Poonam Singh, Assistant Professor, Department of Applied Chemistry, DTU and co-supervision of Dr. Vinod Kumar, Assistant Professor, Special Centre for Nanoscience, JNU. It is further certified that the work embodied in this thesis has neither partially nor fully submitted to any other university or institution for the award of any degree or diploma.

Dr. Poonam Singh
(Supervisor)
Department of Applied Chemistry
Delhi Technological University

Dr. Vinod Kumar
(Co-supervisor)
Special Centre for Nanoscience
Jawaharlal Nehru University

Prof. Anil Kumar
Head of Department
Applied Chemistry, DTU

Dedicated to my beloved family

ACKNOWLEDGEMENTS

First and foremost, I wish to express my heartfelt gratitude and sincere thanks to my PhD supervisors **Dr. Poonam Singh**, Assistant Professor DTU and **Dr. Vinod Kumar,** Assistant Professor JNU for their invaluable guidance and advice throughout my research. I am extremely grateful to both of them for their constructive criticism, encouragement, unending support, and motivation. There are no words to express my gratitude for their tireless efforts and enthusiasm during the completion of my research.

I owe my heartfelt gratitude to **Prof. Prateek Sharma**, Honourable Vice-Chancellor, Delhi Technological University and **Prof. Anil Kumar,** Head, Department of Applied Chemistry, DTU for providing the necessary facilities to carry out this research work. I wish to express my sincere thanks to the whole faculty members of Department of Applied Chemistry, DTU for their help and support during this research work.

Furthermore, I appreciate the valuable suggestions provided by my SRC and DRC members in a timely manner. I am also obliged to all the technical and non-technical staff of Department of Applied Chemistry, DTU for their obligatory help whenever needed.

My deepest thanks to my seniors, friends and fellow researchers of DTU especially **Dr. Khushbu**, **Ms. Jigyasa**, and **Ms. Pooja** who were there to inspire, motivate, and encourage me in all ups and downs during my Ph.D.

No words are adequate enough to express my heartfelt admiration for my family. I dedicate this research study to my parents (**Dr. H. P. Pandey** and **Mrs. Manju Pandey)** and my siblings (**Ms. Chitra** and **Mr. Yugal)**. This research would not have been possible without their immense support and blessings. My mother had been my constant support, and it is the prayers of my siblings which showed me the way out.

Above all I thank Lord for his guidance and strength and helping me through hard times.

(Bhamini)

ABSTRACT

The thesis mainly focuses on the low-temperature synthesis of layered double hydroxides (LDH) and their composite materials, with emphasis on optical properties and environmental aspects. Different spectroscopic techniques, i.e., PXRD, FTIR, TGA, SEM/EDX, XPS, and BET were adopted for the detailed characterization of synthesized materials. The potential application of synthesized Zn/Cu LDH for the selective and efficient removal of anionic azo dyes (CR, EBT, and MO) from synthetic and real wastewater samples was carried out and a statistical tool was employed for optimizing the process parameters involved during adsorption to get maximum efficiency. In addition, the Layered double oxide (LDO) obtained upon calcination of LDH acts as an efficient adsorbent and demonstrated high removal efficiency of 128.20 mg/g for cationic dye (Malachite green was selected as model dye). Furthermore, a smartphone-based detection technique was employed for the determination of dye concentration and the results obtained were found to be in accordance with the data obtained using UV-vis spectrophotometric analysis. Additionally, the present work summarizes the synthesis of EG-modified Zn/Cu hydroxy double salt and its adsorption behavior towards the sequestration of Congo red dye. The regeneration experiments performed revealed that the adsorbent can be efficiently reused for up to 5 regeneration cycles. Furthermore, the composites of PMMA and Polystyrene (PS) with Zn/Cu LDH were also synthesized. The PMMA/LDH composite was used as an adsorbent for the removal of food dye (brilliant black BN) and the isotherm as well as kinetics of the adsorption process were studied using different equilibrium and kinetic models. However, PS/LDH composite films showed enhanced thermal, morphological, and optical properties upon the incorporation of LDH into the polymeric matrix. The structure regaining capability, i.e., memory effect and anion

exchange properties of Zn/Cu LDH were also studied where PANI was incorporated into the interlayer region of synthesized LDH. The PXRD, FTIR, TGA, and SEM/EDX results confirmed that the lattice demonstrated structure regaining capability as well as incorporation of PANI in interlayer region.

OVERVIEW OF THESIS

The whole thesis is divided into eight chapters. ***Chapter 1*** summarizes the background and relevant literature survey including various synthesis routes adopted for the preparation of layered double hydroxides (LDHs) and their applications in water treatment and as polymer additives.

Chapter 2 deals with the synthesis of novel zinc and copper based LDHs (Zn/Cu LDH) containing acetate as interlayer anion. The layered arrangement of synthesized material was confirmed by PXRD, SEM, and TEM analysis. The central composite design-response surface methodology (CCD-RSM) based approach was adopted to optimize the process parameters for the sequestration of anionic dye (Congo red) using the synthesized anionic clay. The study shows that the material can be successfully employed for environmental remediation applications in real wastewater systems.

Chapter 3 of the thesis deals with the synthesis and environmental applications of layered double oxides (LDO) obtained upon calcination of parent LDH. The formation of lattice was confirmed using PXRD, FTIR, and SEM/EDX analytical techniques and pore size was determined using BET analysis. The application of synthesized LDO in the uptake of malachite green (MG) dye has been studied. Furthermore, smartphone-based colorimetry which incorporates RGB parameters, proved to be an efficient, accurate, and quantitative technique for estimating dye removal compared to UV-Vis spectroscopy. In ***Chapter 4*** the facile and one-pot synthesis of ethylene glycol-modified Zn/Cu hydroxy double salt and its application in removal of anionic azo dyes has been studied.

In ***Chapter 5***, synthesis and environmental application of polymethyl methacrylate/LDH composite for removal of brilliant black dye has been discussed. A comprehensive understanding of the effect of Zn/Cu LDH incorporation into the polymer matrix on physico-chemical and sorption properties of the composites has also been studied. In ***Chapter 6*** the preparation of

polystyrene/LDH composite films was carried out and the effects of LDH loading on morphological, thermal, and optical properties of polystyrene has been examined.

Chapter 7 deals with the study of anion exchange and memory effect properties of Zn/Cu LDH. The regeneration ability of Zn/Cu LDH was perceived from PXRD patterns and FTIR spectrum. Moreover, the incorporation of PANI in LDH was confirmed using various spectroscopic techniques. The conclusions and the future scope of the work have been presented in ***Chapter 8*** of the thesis.

CONTENTS

DECLARATION iii

CERTIFICATE iv

ACKNOWLEDGEMENTS vi

ABSTRACT viii

OVERVIEW OF THESIS x

LIST OF FIGURES xvii

LIST OF TABLES xxi

LIST OF ABBREVIATIONS xxiii

Chapter 1 INTRODUCTION AND LITERATURE REVIEW 1

1.1 Introduction 1

1.1.1 Layered materials 1

1.1.2 Anionic layered solids 2

1.2 Structural aspects of LDHs 6

1.3 Conventional methods for synthesis of LDHs 7

1.3.1 Co-precipitation method 7

1.3.2 Urea hydrolysis route 9

1.3.3 Anion exchange method 9

1.3.4 Hydrothermal/Solvothermal synthesis 10

1.3.5 Reconstruction method 11

1.4 Applications of LDHs 11

1.4.1 Water treatment application 12

1.4.2 Polymer additives 15

1.4.3 Other applications of LDHs 19

1.5 Significant findings and Research gap 20

1.6 Research objectives 21

1.7 References 22

Chapter 2 SYNTHESIS AND CHARACTERIZATION OF NOVEL Zn/Cu LAYERED DOUBLE HYDROXIDE: OPTIMIZATION OF PROCESS PARAMETERS USING CCD-RSM APPROACH FOR ANIONIC DYE SEQUESTRATION **41**

2.1 Introduction 41

2.2 Materials and methods 43

2.2.1 Materials 43

2.2.2 Instrumentation 44

2.2.3 Zn/Cu LDH synthesis 44

2.2.4 Batch experiments 45

2.2.5 Design of experiment using RSM 46

2.3 Results and Discussion 47

2.3.1 Structural and morphological properties 47

2.3.2 Adsorption studies 52

2.3.3 Different adsorbents for CR uptake 67

2.3.4 Sequestration of CR dye in real water samples 68

2.3.5 Reusability of Zn/Cu LDH 69

2.3.6 Adsorption mechanism 70

2.4 Conclusion 72

2.5 References 41

Chapter 3 SYNTHESIS AND CHARACTERIZATION OF Zn/Cu LAYERED DOUBLE OXIDE: SMARTPHONE-BASED AND SPECTROPHOTOMETRIC DETECTION OF ULTRASOUND ASSISTED UPTAKE OF MALACHITE GREEN **81**

3.1 Introduction 81

3.2 Experimental Details 83

3.2.1 Chemicals and reagents 83

3.2.2 Synthesis of Zn/Cu LDH and Zn/Cu LDO 84

3.2.3 Instrumentation 84

3.2.4 Ultrasound-assisted adsorption studies 84

3.3 Results and Discussion 85

3.3.1 Structural and morphological properties of LDO 85

3.3.2 Adsorptive removal of Malachite green dye 89

3.3.3 Assessment of ultrasound-assisted method for MG dye uptake 97

3.3.4 Smartphone-assisted determination of percentage dye uptake 99

3.4 Conclusion 101

3.5 References 81

Chapter 4 SYNTHESIS AND CHARACTERIZATION OF ETHYLENE GLYCOL MODIFIED Zn/Cu HYDROXY DOUBLE SALT: MORPHOLOGICAL, THERMAL AND ADSORPTION STUDY **107**

4.1 Introduction 107

4.2 Experimental Section 110

4.2.1 Chemicals 110

4.2.2 Preparation of EG modified Zn-Cu HDS 110

4.2.3 Instrumentation 111

4.2.4 Details of adsorption experiments 111

4.3 Results and Discussion 112

4.3.1 Structure, morphology, and thermal stability 112

4.3.2 Adsorption study 119

4.4 Conclusion 136

4.5 References 107

Chapter 5 SYNTHESIS AND CHARACTERIZATION OF PMMA/Zn-Cu LDH COMPOSITES: MORPHOLOGICAL, THERMAL AND ADSORPTION PROPERTIES

5.1 Introduction 143

5.2 Experimental Section 146

5.2.1 Materials and method 146

5.2.2 Preparation of Poly(methyl methacrylate) (PMMA) 146

5.2.3 Preparation of PMMA/LDH composites 146

5.2.4 Ultrasound-assisted adsorption experiment 147

5.3 Results and Discussion 149

5.3.1 Structural and morphological properties 149

5.3.2 Thermal stability 151

5.3.3 Adsorption behavior 155

5.4 Conclusions 163

5.5 References 163

Chapter 6 SYNTHESIS AND CHARACTERIZATION OF POLYSTYRENE AND Zn/Cu LDH COMPOSITE FILMS: MORPHOLOGICAL, THERMAL, AND OPTICAL PROPERTIES **167**

6.1 Introduction 167

6.2 Experimental Section 169

6.2.1 Preparation of Zn/Cu LDH and PS/LDH composite film 169

6.2.2 Instrumentation 170

6.3 Results and Discussion 171

6.3.1 Structural and morphological properties 171

6.3.2 Thermal properties 175

6.3.3 Optical properties 176

6.4 Conclusion 177

6.5 References 177

Chapter 7 STRUCTURAL MEMORY EFFECT PROPERTY AND ANION EXCHANGE ABILITY OF Zn/Cu LAYERED DOUBLE HYDROXIDE **181**

7.1 Introduction 181

7.2 Experimental Section 183

7.2.1 Decomposition and regeneration of layered structure 184

7.2.2 PANI modified Zn/Cu LDH synthesis 184

7.2.2 Instrumentation 184

7.3 Results and discussion 185

7.3.1 Memory effect property of synthesized material 185

7.3.2 PANI-modified Zn/Cu LDH 187

7.4 Conclusion 196

7.5 References 196

Chapter 8 CONCLUSION AND FUTURE PROSPECTS **203**

8.1 Conclusion 203

8.2 Future prospects 204

LIST OF PUBLICATIONS AND CONFERENCES **205**

LIST OF FIGURES

Figure 1.1 Classification of layered materials. 2

Figure 1.2 Structure of Layered Double Hydroxides. 3

Figure 1.3 Conventional methods of synthesis of LDHs. 8

Figure 1.4 Various applications of LDHs. 12

Figure 1.5 Classification of pollutants and their harmful effects on biotic-abiotic components. 13

Figure 2.1 PXRD pattern of LDHs formed with different compositions of Zn and Cu (a) 4.5:0.5 mmoles, (b) 4.9:1.0 mmoles, (c) 4.9:1.25 mmoles, and (d) 3.74:1.2 mmoles 48

Figure 2.2 (a) PXRD pattern (b) FTIR spectrum (c) TG profile and (d) adsorption-desorption isotherm with pore size distribution of Zn/Cu LDH. 49

Figure 2.3 (a) SEM micrograph (b) EDX analysis (c-d) TEM image and (e) SAED pattern of Zn/Cu LDH. 51

Figure 2.4 (a) Plot of percentage removal of and (b) visual representation of different anionic dyes after adsorption using Zn/Cu LDH. 53

Figure 2.5 Desirability plot for different variables and their combined effect. 58

Figure 2.6 Counter plots for interaction between (a) pH and dye concentration, (b) pH and adsorbent amount, and (c) dye concentration and dose of adsorbent. 59

Figure 2.7 Linear plots for (a) Langmuir (b) Freundlich and (c) Temkin isotherms. 61

Figure 2.8 The linear plots of (a) PFO (b) PSO and (c) Elovich models. 64

Figure 2.9 (a) Van't Hoff plot for ln K vs 1/T and (b) plot of effect of temperature on adsorption capacity. 66

Figure 2.10 Plot of (a) percentage removal of CR dye in different water samples and (b) reusability of adsorbent up to 4 cycles. 70

Figure 2.11 Comparative plots of adsorbent before and after sorption (a) FTIR and (b) PXRD. 71

Figure 3.1 (a) PXRD pattern, (b) FTIR spectra of LDH and LDO, (c) SEM image, (d) average particle size distribution histogram, and (e) EDX plot of Zn/Cu LDO. 87

Figure 3.2 (a) N_2 adsorption-desorption isotherm and (b) pore size distribution plot of Zn/Cu LDO. 88

Figure 3.3 (a) Wavelength vs absorbance and (b) contact time vs percent dye removal plots. 89

Figure 3.4 Plot of (a) concentration variation of MG dye vs adsorption capacity, (b) % removal vs pH of dye solution, (c) pHpzc vs ΔpH, and (d) effect of adsorbent dosage of MG dye sequestration. 90

Figure 3.5 Plots of (a) PFO, (b) PSO, and (c) Elovich models. 93

Figure 3.6 Plots of (a) Langmuir, (b) Freundlich, and (c) Temkin isotherms. 96

Figure 3.7 Plots of (a) Dye uptake efficiency of Zn/Cu LDO up to 4 cycles and (b) assessment of adsorption methods for MG dye uptake. 98

Figure 3.8 (a) Setup for smartphone-based determination of RGB and calibration plot for MG dye concentration based on (b) RGBparameter and (c) UV-vis spectrophotometry. 101

Figure 4.1 Structure of Congo red dye. 110

Figure 4.2 PXRD pattern of EG modified Zn/Cu HDS. 112

Figure 4.3 FTIR analysis of EG modified Zn/Cu HDS. 113

Figure 4.4 (a) SEM image, (b) EDX spectrum and (c−f) corresponding elemental mapping of O, C, Zn, and Cu respectively of EG intercalated Zn/Cu HDS. 115

Figure 4.5 Thermogravimetric trace of EG modified Zn/Cu HDS. 116

Figure 4.6 (a) Survey XPS spectrum of EG modified Zn/Cu HDS. (b), (c), (d), and (e) show the XPS spectrum of C *1s*, O *1s*, Zn *2p*, and Cu *2p*, respectively. 117

Figure 4.7 (a) N_2 Adsorption-desorption isotherm and (b) Plot of BJH pore size distribution of EG-modified Zn/Cu HDS. 118

Figure 4.8 Plots of (a) % removal of different dyes and (b) selective removal of CR dye. 120

Figure 4.9 Plots of (a) absorbance vs wavelength, (b) effect of contact time and (c) effect of adsorbent dosage on percentage dye removal. 121

Figure 4.10 (a) pH effect on percentage dye removal and (b) plot of pH_{PZC}. 123

Figure 4.11 Influence of (a) concentration variation on adsorption capacity and (b) interfering anions on dye adsorption. 125

Figure 4.12 (a) Langmuir, (b) Freundlich, and (c) Temkin isotherm plots for removal of CR dye using EG-Zn/Cu HDS. 128

Figure 4.13 Linear plots of (a) Pseudo first order, (b) pseudo-second-order, and (c) Intra-particle diffusion kinetic models. 130

Figure 4.14 Plausible mechanism of adsorption of CR dye onto EG-Zn/Cu HDS. 132

Figure 4.15 (a) Van't Hoff plot for ln K vs 1/T and (b) effect of temperature on adsorption capacity. 134

Figure 4.16 Reusability of EG-Zn/Cu HDS for Congo red removal. 135

Figure 5.1 Schematic representation for synthesis of (a) pure PMMA and (b) PMMA/LDH composites. 147

Figure 5.2 (a) PXRD pattern, (b) FTIR spectra, and (c)-(e) SEM/EDX analysis of pure PMMA, PML10, and PML20. 150

Figure 5.3 (a) TGA thermogram and (b) Derivative of TGA plot. 153

Figure 5.4 (a) Representation of S1, S2, and S3 for IPDT determination and (b) linear dependence of LDH content on thermal stability of PMMA composites. 154

Figure 5.5 Influence of (a) pH, (b) dye concentration, (c) time, and (d) adsorbent dosage on removal efficiency of BB dye. 157

Figure 5.6 Comparison of removal efficiencies of PMMA, PML10, and PML20. 158

Figure 5.7 Linear plots of (a) Langmuir and (b) Freundlich isotherm for BB dye uptake. 159

Figure 5.8 Plots of (a) PFO and (b) PSO kinetic models. 161

Figure 6.1 Preparation of Polystyrene/LDH composite files with 0%, 5%, and 10% loading of LDH. 170

Figure 6.2 PXRD patterns of PS, PSL05 (5% LDH), PSL10 (10% LDH), and Zn/Cu LDH. 172

Figure 6.3 FTIR spectra of PS, PSL05 (5% LDH), PSL10 (10% LDH), and Zn/Cu LDH. 173

Figure 6.4 SEM micrographs and EDX analysis of (a) PS, (b) PSL05, and (b) PSL10. 174

Figure 6.5 TGA plots of PS, PSL10 (10% LDH), and Zn/Cu LDH. 175

Figure 6.6 Photoluminescence emission spectra of (a) Zn/Cu LDH and (b) pure PS and PS/LDH composite films with 5% and 10% loading of Zn/Cu LDH. 176

Figure 7.1 Illustration of structural memory effect of LDH. 182

Figure 7.2 Structures of different forms of polyaniline. 183

Figure 7.3 Comparative plots of (a) PXRD patterns and (b) FTIR spectra of pristine and regenerated Zn/Cu LDH. 187

Figure 7.4 PXRD pattern of (a) Zn-Cu LDH having acetate as interlayer anion and (b) PANI intercalated Zn-Cu LDH. 188

LIST OF TABLES

Table 1.1 Examples of anionic layered materials. 5

Table 1.2 Influence of interlayer anion on *d*-spacing values of Mg/Al LDHs. 7

Table 1.3 Water treatment application of LDHs. 14

Table 1.4 Application of LDHs as polymer additives. 16

Table 2.1 Structure and formula of azo dyes employed in the study. 43

Table 2.2 Independent variables and ranges in CCD method. 46

Table 2.3 Central composite design statistics with observed and predicted % removal responses. 53

Table 2.4 Table 2.4 ANOVA for Reduced Quadratic model. 55

Table 2.5 Optimized conditions for dye uptake obtained by desirability function. 57

Table 2.6 Equilibrium constants for CR dye removal. 62

Table 2.7 Kinetic parametric values for CR dye uptake. 64

Table 2.8 Thermodynamic parametric values for CR uptake. 67

Table 2.9 Different sorbents reported for uptake of CR dye. 67

Table 3.1 Structure and formula of MG dye. 83

Table 3.2 Surface properties of synthesized adsorbent. 88

Table 3.3 Kinetic parameters for MG dye sequestration. 93

Table 3.4 Equilibrium parameters for MG dye removal. 96

Table 3.5 Different sorbents reported in literature for MG dye uptake. 98

Table 3.6 Color parameters of known concentration of malachite green dye. 100

Table 4.1 Analyses of adsorption efficiencies of some sorbents for removal of CR dye. 109

Table 4.2 Langmuir, Freundlich, and Temkin isotherm constants for the adsorption of CR dye onto EG modified HDS from aqueous solution. 128

Table 4.3 Kinetic parameters for CR dye adsorption onto EG modified Zn/Cu HDS. 130

Table 4.4 Thermodynamic parametric values for CR dye uptake. 133

Table 5.1 TGA data of PMMA and its composites. 154

Table 5.2 Equilibrium constants for CR dye removal. 159

Table 5.3 Kinetic parametric values for BB dye uptake. 161

Table 5.4 Comparison of maximum adsorption capacity of adsorbents reported in literature for BB dye sequestration. 162

Table 7.1 Functional group analysis of pristine and modified LDH using FTIR. 189

Table 7.2 TGA data for Zn/Cu LDH and PANI-modified LDH. 192

LIST OF ABBREVIATIONS

HDS	Hydroxy Double Salts
LRH	Layered Rare-earth Hydroxides
LDH	Layered Double Hydroxides
RSM	Response Surface Methodology
CCD	Central Composite Design
LDO	Layered Double Oxide
MMO	Mixed Metal Oxide
EG	Ethylene Glycol
PMMA	Poly(methyl methacrylate)
PANI	Polyaniline
PS	Polystyrene
SEM	Scanning Electron Microscopy
FTIR	Fourier Transform Infrared
TGA	Thermogravimetric Analysis
TEM	Transmission Electron Microscopy
XPS	X-ray Photoelectron Spectroscopy
EDX	Energy Dispersive X-ray Spectroscopy
PXRD	Powder X-Ray Diffraction
TG Profile	Thermogravimetric Profile
ANOVA	Analysis of Variance
CR	Congo red
EBT	Eriochrome Black T
MO	Methyl orange

MG	Malachite green
BB	Brilliant black
PFO	Pseudo first order
PSO	Pseudo second order
LI	Langmuir isotherm
FI	Freundlich isotherm
IPDT	Integral procedure decomposition temperature
NC	Nanocomposites

Chapter 1 INTRODUCTION AND LITERATURE REVIEW

1.1 Introduction

1.1.1 Layered materials

Layered solids represent a class of inorganic materials having a two-dimensional stacked structure held together by weak forces of attraction including electrostatic, van der Waals forces, or hydrogen bonding [1]. These layered materials have been attracting a great deal of attention from researchers due to their anisotropy in bonding and wide-ranging applications in fields of catalysis, biology and medicine, energy storage, fillers in polymer nanocomposite materials, and environmental protection [2–6]. The layered structure and variable chemical composition of these materials allow them to be modified and tuned in a variety of ways [7]. A variety of solids for instance, clays, transition metal chalcogenides, layered double hydroxides (LDHs), graphene, graphite, phosphonate, etc. belong to the class of layered materials. Depending upon the presence of fixed charges in the planar macromolecule, layered solids can be classified into neutral, anionic, and cationic solids as depicted in Figure 1.1.

Graphite is a neutral layered solid with a two-dimensional array of hexagonally packed carbon atoms stacking together to form three-dimensional structures. On the other hand, cationic layered solids like smectite clays consist of negatively charged layers having cations – mostly alkali metal ions, in the interlamellar region [8]. Anionic layered solids consist of positively charged layers having exchangeable anions in the interlayer region to maintain charge neutrality [1].

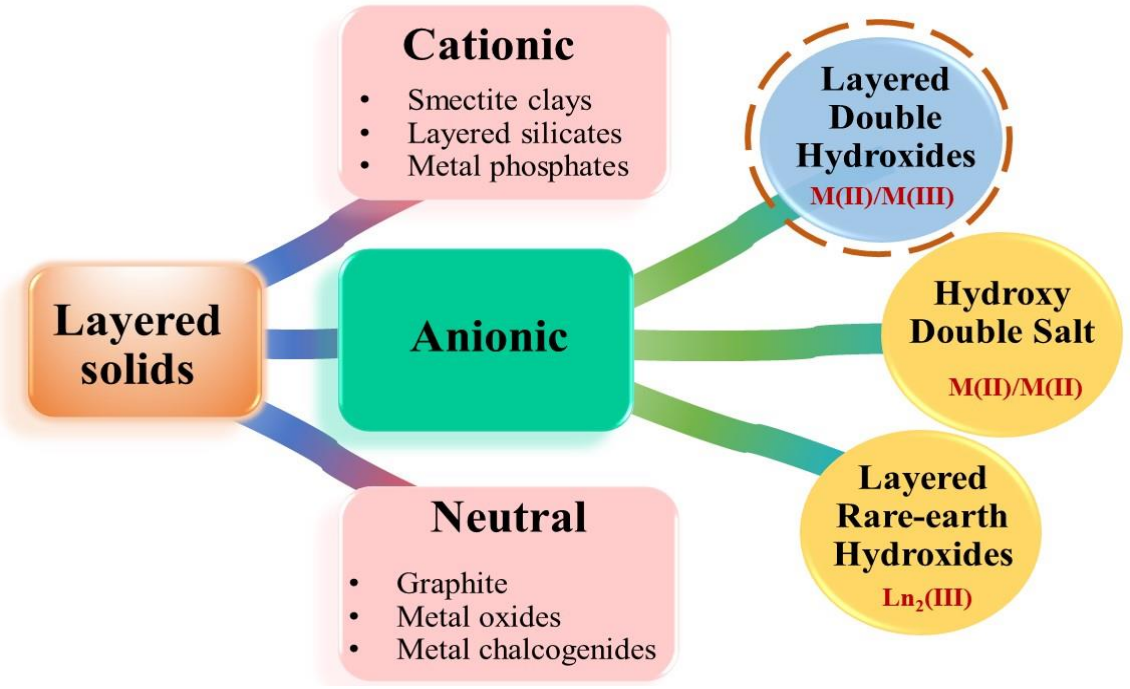

Figure 1.1 Classification of layered materials.

The maximum of layered materials occurring in the mineral form are cationic and neutral. However, layered materials having anion exchange properties are very limited. Although, they can be synthesized using various synthetic methodologies and the selection of method depends on the purpose for which the LDH needs to be used [9]. Recently the studies of these layered materials have attracted immense attention of scientific community owing to the anisotropy in bonding which results in properties such as ion exchange, intercalation, ability to swell in solvents, and formation of monolayer colloidal dispersions.

1.1.2 Anionic layered solids

Anionic layered materials possess properties opposite to that of cationic materials. These materials are composed of layers of positively charged sheets intercalated with anions and water molecules. Anionic layered solids can further be classified (Figure 1.1) as hydroxy

double salts (HDSs), layered double hydroxides (LDHs), and layered rare earth hydroxides (LRHs). Some of the examples of anionic layered materials are presented in Table 1.1

1.1.2.1 Layered double hydroxides (LDHs)

LDHs belong to one such class of layered materials and are also called anionic clays or hydrotalcite-like compounds [10]. Several forms of these materials exist in nature in forms of minerals and can also be prepared readily in the laboratory. LDHs have gained much attention due to their rich intercalation chemistry, anion exchange properties, and superior thermal stability [11]. The general composition of LDHs is given by $[M(II)_{1-x}\ M(III)_x\ (OH)_2]^{x+}(A^{n-})_{x/n}\ .mH_2O$, where M(II) and M(III) are divalent (Zn, Cu, Co, Ni or Ca) and trivalent metal ions (Cr, Mn, Al or Fe) respectively and A^{n-} is an interlamellar anion having valency n; and x, defined as $[M^{III}]/([M^{III}]+[M^{II}])$ (Figure 1.2), is generally between 0.25 and 0.33 [12]. Despite most studies reporting M^{2+}/M^{3+} cations in the layers, some groups have also reported the combination of the M^{2+}/M^{4+} (substitution of Zr^{4+} in brucite layer) as well as M^{+}/M^{3+} (the known example is $Li_2[Al_2(OH)_6]_2CO_3{\cdot}nH_2O$) cations in the layer [13,14].

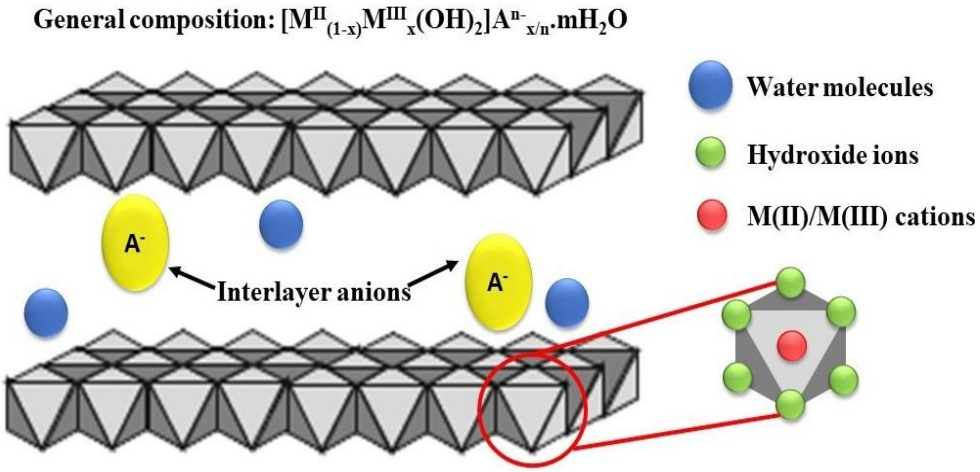

Figure 1.2 Structure of Layered Double Hydroxides.

It is possible to construct LDHs using a variety of M(II) and M(III) cations, atomic ratios, and interlayer anion configurations. These compositional variations do not fundamentally change the material's structure [15]. LDH-based materials have the potential to be useful in a variety of fields such as water treatment, biomedical applications, catalysts for organic transformations, biosensors, polymer fillers, and flame retardants [16–22].

1.1.2.2 Layered Hydroxy double salts (HDSs)

HDSs represent a promising class of layered compounds that are similar to LDHs consisting of two types of divalent metal cations (M^{2+}). Approximately one quarter of the octahedral sites in HDSs are vacant, and M^{2+} cations are arranged in tetrahedral coordination just above and below the empty octahedral sites, causing an extra positive charge on the layers, which is compensated by A^{m-} anions in the interlayer region. HDSs is typically represented as $M^{a}_{1-y}M^{b}_{y}(OH)_{2-x}(A^{m-})_{x/m}.nH_2O$ where M^a and M^b are bivalent metal ions and A^{m-} is interlayer anion [23].

1.1.2.3 Layered rare earth hydroxides (LRHs)

They are a special class of solids having hydroxide layers of rare earth metal cation. The general composition of LRHs is $Ln_2(OH)_{6-m}(A^{x-})_{m/x}\cdot nH_2O$ where Ln represents trivalent rare-earth cation and A^{x-} denotes interlayer exchangeable anion; $1.0 \leq m \leq 2.0$). The positive charge on layers in LRHs is mainly caused by trivalent rare earth cations which is neutralized by interlayer anions: halides, nitrates as well as large organic anions such as dodecyl sulfate (DS^-), 2,6-anthraquinonedisulfonate ($AQDS^{2-}$), etc [24]. Examples of LRHs are $[Eu_8(OH)_{20}(H_2O)_{4.4}]Cl_4$, $Yb_2(OH)_5NO_3\cdot H_2O$ and $Yb_4(OH)_{10}[C_{14}H_6O_2(SO_3)_2]\cdot 4H_2O$ (YB-AQDS) [24]. The properties of rare earth elements

are coupled with intercalation chemistry and host-guest interactions to make them novel multifunctional materials.

Table 1.1 Examples of anionic layered materials.

Anionic layered materials	**Interlayer anion**	**Synthesis method**	**Application**	**References**
Mg/Al LDH	Molybdate (MoO_4^{2-})	Co-precipitation	Catalyst for the synthesis of Schiff base	[25]
Ni/Fe LDH	Molybdate (MoO_4^{2-})	Hydrothermal	Electrocatalytic oxidation of water	[26]
Co/Bi LDH	Nitrate (NO_3^-)	Co-precipitation	Removal of Pb (II) ions	[27]
Zn/Al LDH	Carbonate (CO_3^{2-})	Co-precipitation	Anticancer, antimicrobial, and environmental applications	[28]
Ni/Zn HDS	Acetate (CH_3COO^-)	Hydrothermal	Pd (II) catalyst support	[29]
Cu/M HDS (M = Zn, Ca, La & Pb)	Nitrate (NO_3^-)	Hydrothermal	Methyl orange degradation	[30]
Ni/Zn HDS	Acetate (CH_3COO^-)	Hydrothermal	Catalyzed 1,4-addition of enones and boronic acid	[31]

$RE_2(OH)_5NO_3{\cdot}nH_2O$ LRHs (RE = Sm, Gd, Er, and Y)	Nitrate (NO_3^-)	Ion-exchange	Phosphate uptake from water	[32]
$Y_2(OH)_5Cl{\cdot}1.5H_2O$	Chloride (Cl^-)	Hydrothermal	Sequestration of selenium	[33]
LEuH (Layered europium hydroxide)	Nitrate (NO_3^-)	Hydrothermal	Naproxen drug delivery	[34]

1.2 Structural aspects of LDHs

LDH possesses a structure very similar to that of mineral brucite [$Mg(OH)_2$], derived from CdI_2 consisting of $Mg(OH)_6$ octahedra held together by hydrogen bonds. LDH can be constructed by substituting a fraction of M^{2+} cations in the brucite-type octahedral layer with M^{3+} cations, creating a positive charge on the layers. The positive charge is balanced by charge-compensating anions whose identity affects the interlayer spacing [35]. The magnesium ions are octahedrally coordinated with hydroxy ions forming infinite layers of octahedral units. A three-dimensional structure is formed by stacking these layers on top of each other. Electrostatic interaction and hydrogen bonding are responsible for bonding between octahedral layers and interlayers. The cations in the hydroxide layers, anions, and water molecules present in the interlamellar region influence the crystal parameters of LDH. The distance between two adjacent layers defines the gallery height of the LDH [36]. The basal spacings of Mg/Al based-LDHs exhibiting different interlayer anions are presented in Table 1.2. From the data, a clear correlation can be found in between gallery

height of the LDH and the presence of different anions. As the size of charge compensating anion increases the basal spacing increases which gives information regarding the orientation of anionic species present in the interlayer region.

Table 1.2 Influence of interlayer anion on *d*-spacing values of Mg/Al LDHs.

Interlayer anion of Mg/Al LDH	***d*-spacing (Å)**	**References**
Carbonate (CO_3^{2-})	7.6	[37]
Nitrate (NO_3^-)	7.9	[38]
Sulphate (SO_4^{2-})	7.94	[39]
Molybdate (MoO_4^{2-})	8.9	[25]
Dodecylsulfate [$CH_3(CH_2)_{11}SO_4^-$]	26.8	[37]
Tartrate ($C_4H_4O_6^{2-}$)	29.0	[40]

1.3 Conventional methods for synthesis of LDHs

It is possible to synthesize LDHs on a laboratory and industrial scale, as they are simple and inexpensive materials. A variety of methods can be used to synthesize LDHs with desired physical and chemical properties for a wide range of applications [41]. A schematic representation of most commonly adopted methods for synthesizing LDHs are illustrated in Figure 1.3.

1.3.1 Co-precipitation method

LDHs are primarily synthesized by Co-precipitation or one-pot synthesis method. In this, M(II) and M(III) metal salts are used as precursors and numerous anions can be intercalated in between the hydroxyl layers. The synthesis should take place under supersaturation conditions for the simultaneous precipitation of divalent and trivalent metal salts. The pH plays a very crucial role in this preparative method as it affects the structural properties of

the LDHs formed. Most often alkaline solutions of NaOH, KOH, and NH_4OH are used and solution pH is kept in the range of 8-10 for the precipitation [42]. At the initial stage, metal hydroxides are formed which after further addition of base leads to precipitation and formation of LDHs. Since Co-precipitation method is pH dependent it can be divided into three main types: (i) precipitation at low supersaturation, (ii) precipitation at high supersaturation, and (iii) precipitation at constant pH.

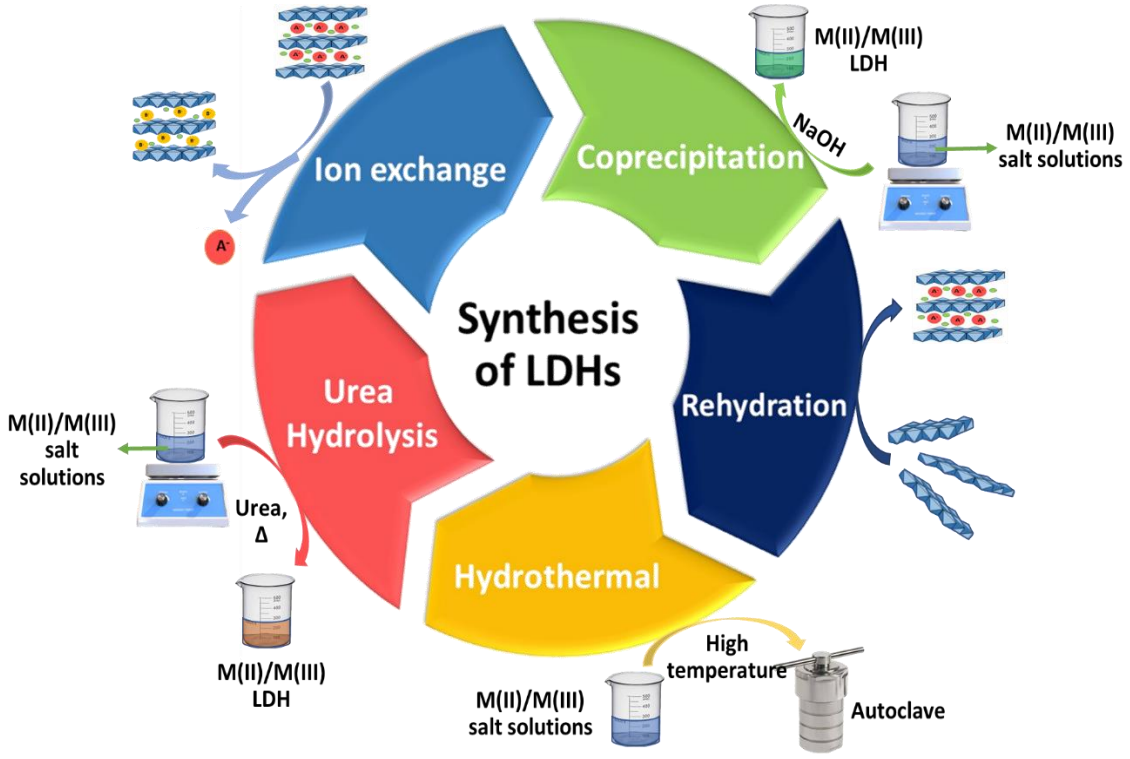

Figure 1.3 Conventional methods of synthesis of LDHs.

In the first type, desired amount of di and trivalent metal ion salts are added to the solution containing anions to be intercalated with the simultaneous addition of base to maintain the pH [43]. The second type includes the gradual addition of metal salt solutions to the alkaline solution containing desired anion for the intercalation [44]. The precipitation at low supersaturation gives rise to LDH exhibiting greater crystallinity in contrast to

precipitation at high supersaturation. The most widely used type of coprecipitation is precipitation at a constant pH. In this method, the metal cation solutions are added to the solution containing anions and to keep the pH constant the alkaline solution is added continuously. The final step is same for all the methods that is the product is filtered and washed with deionized water (DI) repeatedly and dried at moderate temperature.

1.3.2 Urea hydrolysis route

It is also a type of precipitation method. Urea possesses some unique properties which make it ideal for precipitation of metal hydroxides i.e., is highly water soluble and acts as a weak Bronsted base which exhibits controllable hydrolysis rate. In this method, urea is added to the solution of M(II) and M(III) ions and is refluxed for several hours to get the precipitate, which is then filtered and washed with DI water. The process of urea hydrolysis proceeds in two steps, first is the formation of ammonium cyanate (NH_4CNO) which is also the rate-determining step and the second step is the subsequent rapid hydrolysis of the cyanate to ammonium carbonate. The hydrolysis of ammonium ions to give ammonia and carbonate to give hydrogen carbonate results in a pH of about 9, depending on the reaction temperature [45]. The ammonium carbonate formed causes the precipitation leading to formation of LDH having carbonate as an interlayer anion. LDHs obtained by this method have homogenous sizes, platelet-like particles, and hexagonal shapes.

1.3.3 Anion exchange method

Anion-exchange can also be used to intercalate a variety of different types of anions. The method involves the addition of LDH synthesized via co-precipitation having Cl^-, NO_3^- or CO_3^{2-} as interlayer anions to the desired solution containing excess anions to be exchanged. It is mostly used when co-precipitation cannot be employed, such as in cases where the

metal salts are unstable in the alkaline solution or there is a strong possibility of interaction between guest anions and metal ions [46]. This method is rendered useless when carbonate ions are present in the lattice since they bind quite effectively to the metal hydroxide layers and hence, de-intercalation becomes difficult due to which the reaction is performed under inert atmosphere. The interlayer anions of LDHs which can be exchanged with other anions in the medium with the affinity is as follows:

$$NO_3^- < Br^- < Cl^- < F^- < OH^- < SO_4^{2-} < CO_3^{2-}$$

Due to the relative ease with which the nitrate anions can be displaced from the interlayers of LDHs, these are the best precursors for anion-exchange synthesis. For an anion exchange to be carried out the anions to be intercalated must be stable at the exchange pH as well as the layers must be stable if the divalent:trivalent metal ratio is to be retained [47].

1.3.4 Hydrothermal/Solvothermal synthesis

Hydrothermal or solvothermal methods of synthesis are also employed for the preparation of LDH. For instance, the method is termed as hydrothermal when water is used as a solvent and conversely it is called solvothermal when organic solvent is used. In reaction when reactants are subjected to temperatures above the boiling point of water, they are called hydrothermal treatments. During high-temperature processes, the dielectric constant of water decreases, as does its viscosity, and the dissociation constant increases, resulting in an increase in electrostatic interactions, which accelerates the ripening of crystals. A solution containing a base is stirred vigorously at room temperature while two solutions containing M(II) and M(III) metal salts are added dropwise. Then, the suspension is transferred to a Teflon-lined autoclave and treated at high temperature and pressure [48]. It is used in cases where co-precipitation or ion exchange preparative methods are not

applicable. It generally results in high crystallinity in the products, and also reduces the number of byproducts produced.

1.3.5 Reconstruction method

It is also known as rehydration method which uses the unique structural 'memory effect' property of LDHs [14]. The LDHs are first calcined at high temperatures nearly 350-500 °C to remove interlayer H_2O, anions, and -OH groups resulting in the formation of layered double oxides (LDO) or mixed metal oxides (MMO). These LDOs formed can be reformed to the LDHs by dissolving calcined LDH in an aqueous solution of preferred anion [49]. The anions included need not be the same as those originally present. Therefore, LDHs having desired organic or inorganic species can be easily synthesized using this preparative method. However, it results in the formation of products with poor crystallinity and partial intercalation as compared to other methods. In addition to preventing the inclusion of competing inorganic counter anions into the LDH, the advantage of this method is that it also prevents the incorporation of carbonate from atmospheric CO_2 into the LDH.

1.4 Applications of LDHs

LDHs are promising materials for many practical applications, including catalysis, adsorption, pharmaceuticals, photochemistry, and electrochemistry (Figure 1.4). They are highly versatile, easily tailored, and low in cost, enabling them to be used to produce materials that meet a variety of requirements [50]. LDH materials exhibit excellent expanding properties due to their relatively weak interlayer bonding. In light of this, over the past few years, layered inorganic solids have gained increasing interest as host materials for creating hybrid inorganic-organic host-guest structures with desirable physico-

chemical properties [51]. A new platform of functional materials with novel properties can be created by forming pillared layered structures through suitable intercalation processes.

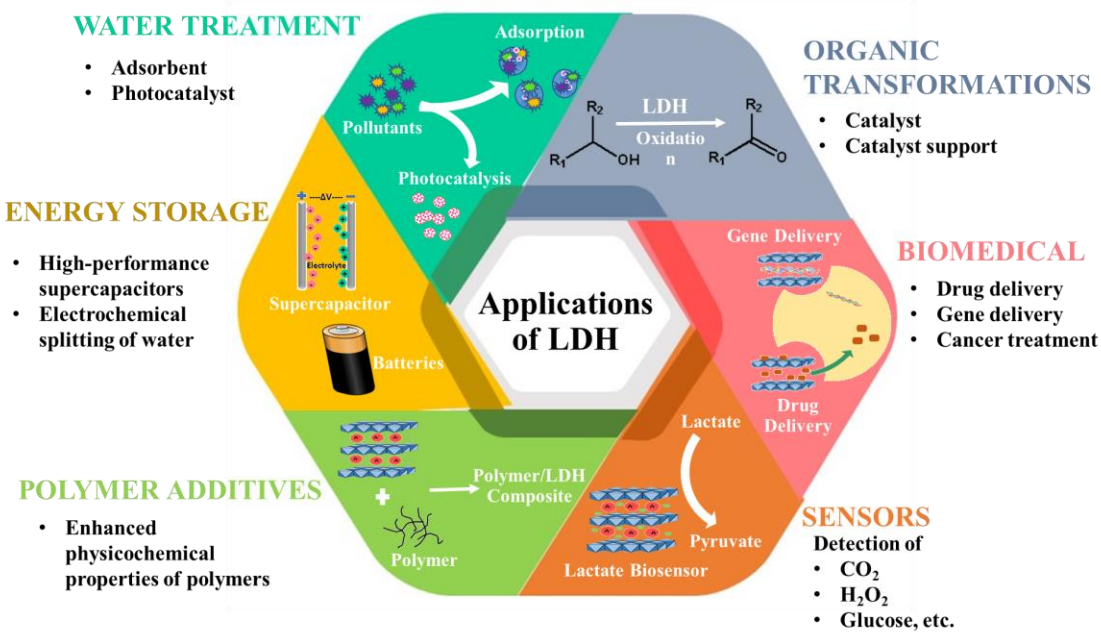

Figure 1.4 Various applications of LDHs.

1.4.1 Water treatment application

The availability of clean and potable water is a basic requirement for a healthy lifestyle but the scarcity of clean water is a global problem that poses an immense threat to this basic human right. Water contamination has emerged as a dire issue, making it a prominent concern in the 21st century [52]. Recent decades have seen rapid industrial expansion, coupled with unregulated population growth, resulting in a degradation of water quality, through release of toxic effluents i.e., heavy metals, dyes, surfactants, pesticides, and fertilizers into the water resources [53–56]. As a consequence of the widespread use of dyes in various industries, including plastics, cosmetics, textiles, rubber, and food, toxic effluents are released into the water without prior treatment, thereby adversely affecting

the environment, human health, and aquatic life [57]. In addition to organic dyes, the discharge of heavy metal ions (arsenic, mercury, lead, cadmium, chromium, etc.) into water bodies from chemical industries are equally accountable for the pollution of water resources.

Aquatic ecosystems are severely threatened by the cyclic structure of dyes, their high toxicity, chemical stability, and low degradation rate. Azo dyes contain aromatic amine structures that resist environmental degradation, making them carcinogenic. Owing to their long shelf-life, these dyes pose a threat to fauna and flora in the long run [58,59]. The graphical representation of toxic effluents and their impact on biotic-abiotic components is given in Figure 1.5. Consequently, it is imperative to find an effective way to clean up aquatic environments.

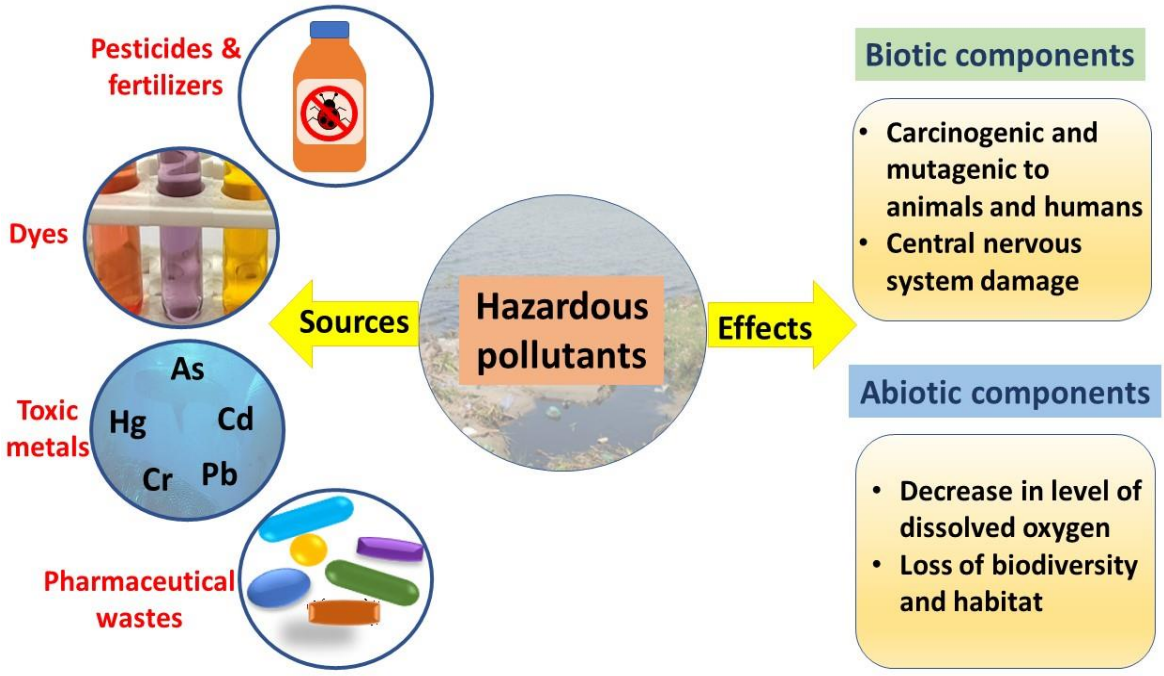

Figure 1.5 Classification of pollutants and their harmful effects on biotic-abiotic components.

Traditionally, several methodologies like coagulation, precipitation, adsorption, photocatalysis, ion exchange, reverse osmosis, microbial degradation, etc. have been employed to remove toxic pollutants from aquatic environments [60,61]. However, among all the conventional techniques, adsorption has appeared as the highly efficient, economical, and most favorable technology for water remediation [62–64]. The adsorption process is based on the contaminant transfer from solution to the surface of the adsorbent material [65]. Various adsorbents (activated carbon, zeolite, silica gel, graphite oxide, etc.) have been explored for the elimination of toxic pollutants [66–71]. Despite that, most of the materials have several shortcomings like high operational cost, the problem of residual metal sludge disposal, etc. [72]. As a consequence, there is an imperative need to synthesize low-cost adsorbents for providing safe and clean drinking water [73,74]. The development of layered materials can open a new vista for solving the problem of the ever-increasing population's inability to access safe drinking water. As a result of their exceptional physicochemical properties, LDH-based materials have received critical attention within the past few years for their use as a viable alternative to traditional adsorbents [75–77]. Table 1.3 summarizes the efficiency of various LDH materials employed for the sequestration of toxic dyes, metal cations, and toxic anions from the wastewater.

Table 1.3 Water treatment application of LDHs.

Adsorbents	**Pollutants**	**pH**	**Adsorption capacity q_{emax} (mg/g)**	**Removal efficiency (%)**	**References**
Mg/Al LDH	Congo red	~7	111.11	-	[78]
Ca/Al LDH	Cu(II)	-	381.9	-	[79]
	Cd(II)		1035.4		

Co/Al LDH	Methylene blue	3	54.01	75	[80]
	Reactive orange 16	9	53.04	97	
SDS-Mg/Al LDH	17β-estradiol	7	67.69	94	[81]
Calcined Mg/Fe LDH	Acid brown 14	4	370	~100	[82]
EDTA-Zn/Al LDH	Cu(II)	5.5	1117	-	[83]
	Cd(II)		375		
	Pb(II)		871		
Mg/Al LDH	Pb(II)	5.7	66.16	88	[84]
Li/Al LDH	Arsenate	4	-	67	[85]
Zn/Al LDH	Arsenate	7.4	40.37	97.1	[86]
Calcined Mg/Al LDH	Pesticide (Dicamba)	~3	-	80	[87]
Mg/Al LDH	Chromium	6	125.97	-	[88]
Ca/Al(MoS_4) LDH	Ciprofloxacin	6	707.2	80	[89]
	Ofloxacin		476.7	68	
Zn/Al MMO	Salicylic acid	-	28.4	94.59	[90]

1.4.2 Polymer additives

Composite materials are constituted of physically/chemically discrete phases (matrix and dispersed phase), having properties of bulk phase considerably different from that of the pure components. Due to their unique physicochemical properties, polymer matrix

composites are considered among the most interesting composite materials. They have a wide array of uses in engineering, medicine, and wastewater treatment [91,92]. Since polymeric materials are inexpensive, lightweight, have low specific gravities, are easily processable, and can withstand chemical exposure, they are extensively used in industry. Polymers have many advantages, but their low strength and modulus, low operating temperatures, and susceptibility to environmental degradation complicate their use in practical applications compared to metals and ceramics [93]. Consequently, the introduction of metal and ceramic as reinforcement materials can result in a unique combination of magnetic, electronic, optical, or catalytic properties [94]. Furthermore, the addition of inorganic fillers such as LDHs results in the formation of composites possessing remarkably superior properties, i.e., high modulus, high strength, chemical resistance, higher electrical conductivity, and flame retardancy [95,96]. LDHs also provides the ability to adsorb toxic pollutants efficiently, due to their high selectivity, large surface area, and numerous adsorption sites [97]. Due to their remarkable physicochemical properties, polymer/LDH composites have gained critical attention in recent years, and are seen as an alternative to traditional adsorbent materials [75–77]. Table 1.4 summarizes the applications of LDH as polymer additives reported in literature.

Table 1.4 Application of LDHs as polymer additives.

LDH	Polymer	Potential application	Highlights	References
Mg/Al LDH	Polystyrene (PS)	Chloride entrapment	Composite exhibited high chloride uptake capacity (505.05 mg/g)	[98]

Surface-modified Ca/Fe LDH	Polyaniline (PANI)	Lead ions removal	LDH loading increases maximum adsorption capacity (PANI: 47 mg/g, NC5%: 56 mg/g and NC10%: 110 mg/g)	[99]
Zn/Cr LDH	Polysulfone	Fluoride removal	Wet composite material showed 91% fluoride uptake capacity	[100]
Mg/Al LDH	Polymethyl methacrylate (PMMA)	Packaging material	Significant decrease in oxygen permeability (PMMA = 6 L/cm^2/min and PMMA/LDH = 3 L/cm^2/min)	[101]
Cu/Al LDH	Polyethyleneimine (PE)/Tannic acid	Methylene blue dye removal	Novel polymer/LDH composite exhibited exceptionally high adsorption capacity of 1428.57 mg/g	[102]
Ni/Al LDH	Graphene/polypyrrole (GPPY)	Pseudo-capacitor	Composite exhibits excellent capacitive performance (845 F/g)	[103]

Mg/Al LDH	Polypropylene (PP)	Lithium-sulfur batteries	Incorporation of LDH blocked polysulfide crossover	[104]
Zn/Al-NO_3	Polypyrrole (PPY)	Ni-Zn Secondary batteries	PPY improved electrochemical performance of Ni-Zn batteries (Impedance values: Ni-Zn LDH = 0.0289 ohm g) and PPY/Ni-Zn LDH = 0.3206 ohm g)	[105]
Mg/Al-NO_3	Chitosan	Removal of oil particles	Composite showed high removal efficiency of 78% as compared to that of pure LDH (30%)	[106]
Mg/Al-Cl	Poly(ε-caprolactone) (PCL)	Biomedical application	Composite enhanced cell adhesion and proliferation	[107]

NC5% and NC10% = Nanocomposites with 5 and 10% LDH loading

In a study done by Suresh *et al.*, Polystyrene (PS) nanocomposites (NC) incorporating Co/Al LDH exhibit improved mechanical, structural, and thermal properties when compared with pure PS [108]. Barik *et al.* found that Polymethyl methacrylate (PMMA) reinforced with Mg/Al LDH could be used as an efficient packaging material because of

its improved heat stability and reduced oxygen permeability with the addition of LDH [101].

1.4.3 Other applications of LDHs

Considering LDH's high surface area, high charge density, uniform distribution of cations, and ability to intercalate catalytic anions, it acts as an excellent catalytic material. For instance, a wide range of reactions can be catalyzed by LDH, including organic transformations, photoreductions, and decomposition reactions. In brucite layers, the combination of abundant basic sites and even distribution of cations makes LDH sheets the ideal catalyst for catalysis and in addition, the cations present may also act as active sites for catalysis. Additionally, LDH results in formation of MMOs on calcination which also exhibit high catalytic properties [19]. A hybrid structure formed from LDH and other suitable materials can further enhance the catalytic activity of the materials.

Layered double hydroxides can act as a promising flame retardant owing to their ability to retard flame growth in three possible ways: (i) due to endothermic decomposition LDHs act as heat sink, (ii) a thin insulating film of MMOs is formed on the surface upon decomposition of LDH, and (iii) the flammable gases are dispersed on release of bound carbon dioxide and water molecules. LDH is preferred over commercial flame retardants because it requires only very low concentrations, is non-toxic, and is highly efficient [109]. When appropriate anions such as phosphate, borate, etc. are intercalated into the inter-gallery region of LDH, the flame retardancy can be further enhanced.

1.5 Significant findings and Research gap

LDHs with varying cationic compositions have been manufactured using a variety of synthesis routes over the years, including co-precipitation, hydrothermal, urea hydrolysis, anion exchange, and reconstruction methods. However, each of these methods has its own set of disadvantages. The co-precipitation and urea hydrolysis methods require the usage of strong alkaline conditions. In addition, LDHs with high charge density cannot be prepared via urea hydrolysis whereas since LDHs have a very high affinity for carbonate ions the atmospheric carbon dioxide may interfere with the co-precipitation process. On the contrary, the hydrothermal and rehydration methods require high-temperature conditions and have high production costs, and also result in products that are poorly crystallized and will have partial intercalation. Comparatively to other methods, ion-exchange also suffers the disadvantage of carbonate intercalation and since CO_2 cannot be deintercalated easily, nitrogen atmosphere is used to avoid absorption of atmospheric carbon dioxide during synthesis. Conventional methods of chemical synthesis of LDHs are hindered by the use of extreme reaction conditions and toxic precursors. Therefore, an attempt has been made to fabricate novel LDH solids via acid hydrolysis method without use of strong acids and bases, under ambient conditions. To the best of our knowledge, very limited literature is available on the synthesis and intercalation study of selected combinations of M(II) and M(III) metal ions (M^{2+} = Zn, M^{3+} = Cu) and also their potential applications in water remediation is not fully explored.

Activated carbon (AC) is the most widely used adsorbents for the uptake of dyes from wastewater owing to its remarkable properties including high removal efficiency, ease of application, and large surface area. Despite these advantages, AC has limited practical

applications due to its regeneration or disposal difficulties, sludge production problems, and economic feasibility concerns. Therefore, numerous studies on dye adsorption by non-conventional adsorbents have been reported during the last decades, including algae, fungi, industrial waste, agricultural wastes, metal oxides, composites, clays, and polymers. However, the adsorbents derived from different origins, either organic or inorganic, exhibit inefficient sorption capabilities for removing dyes compared with commercially used activated carbon. In light of all these limitations, as well as operational hurdles, it has been observed that effective adsorbents are required that have characteristics including low cost, high surface area, and easy synthesis and regeneration ability. Furthermore, the physicochemical properties of LDHs and Polymer/LDH composites, suggest they are an ideal candidate for use as a sorbent in efficient and selective sequestration of toxic dyes from wastewater.

1.6 Research objectives

I. The optimal synthesis conditions for obtaining solids of technological importance were explored.

II. Various combinations of LDH containing Zn (divalent metal ion) and Cu (trivalent metal ion) were synthesized using methodologies such as acid hydrolysis, and ion exchange.

III. Regeneration experiments were carried out to see the structure regaining capability of synthesized LDH after calcination.

IV. Intercalation of simple/complex organic and inorganic anions within the LDH lattices was performed using the ion exchange method.

V. Polymer incorporation into the LDH galleries was achieved via in situ polymerization of a high molecular weight macromolecule.

VI. The synthesized organic-inorganic hybrid layered materials were thoroughly characterized using a variety of techniques. The formation of layered structure was confirmed using PXRD patterns, SEM, EDX, and TEM techniques. The presence of interlayer anion was verified using FTIR. The composition of these samples was ascertained from the results of combustion, and XPS analysis. Thermal analysis methods were also employed to comprehend the stability of synthesized materials.

VII. Optimization of phase composition was followed by a detailed study and analysis of adsorption and optical behavior of synthesized inorganic-organic hybrid materials.

1.7 References

[1] Miyamoto N, Yamamoto S. Functional Layered Compounds for Nanoarchitectonics. Elsevier Inc.; 2017. https://doi.org/10.1016/B978-0-323-37829-1.00007-9.

[2] Manohara G V., Vishnu Kamath P, Milius W. Reversible hydration and aqueous exfoliation of the acetate-intercalated layered double hydroxide of Ni and Al: Observation of an ordered interstratified phase. J Solid State Chem 2012;196:356–61. https://doi.org/10.1016/j.jssc.2012.06.017.

[3] Centi G, Perathoner S. Catalysis by layered materials: A review. Microporous Mesoporous Mater 2008;107:3–15. https://doi.org/10.1016/j.micromeso.2007.03.011.

[4] Kumar P, Abuhimd H, Wahyudi W, Li M, Ming J, Li L-J. Review—Two-Dimensional Layered Materials for Energy Storage Applications. ECS J Solid State Sci Technol 2016;5:Q3021–5. https://doi.org/10.1149/2.0051611jss.

[5] Gamboa G, Mazumder S, Hnatchuk N, Catalan JA, Cortes D, Chen Ik, et al. 3D-printed and injection molded polymer matrix composites with 2D layered materials. J Vac Sci Technol A 2020;38:042201. https://doi.org/10.1116/6.0000121.

[6] Perreault F, Faria, Andreia Fonseca de Elimelech M. Environmental applications of graphene-based nanomaterials. Chem Soc Rev 2015;44:5861–96. https://doi.org/https://doi.org/10.1039/C5CS00021A.

[7] Kuthati Y, Kankala RK, Lee CH. Layered double hydroxide nanoparticles for biomedical applications: Current status and recent prospects. Appl Clay Sci 2015;112–113:100–16. https://doi.org/10.1016/j.clay.2015.04.018.

[8] Selvam T, Inayat A, Schwieger W. Reactivity and applications of layered silicates and layered double hydroxides. Dalt Trans 2014;43:10365–87. https://doi.org/10.1039/c4dt00573b.

[9] Rojas R. Layered double hydroxides applications as sorbents for environmental remediation. Nova Science Publishers, Inc.; 2012.

[10] Rajamathi JT, Britto S, Rajamathi M. Synthesis and anion exchange reactions of a layered copper-zinc hydroxy double salt, $Cu_{1.6}Zn_{0.4}(OH)_3(OAc)\cdot H_2O$. J Chem Sci 2005;117:629–33. https://doi.org/10.1007/BF02708291.

[11] Singh P, Nagarajan R. Synthesis and characterization of hydrotalcite type structure containing Zn^{2+} and La^{3+}-ions. Mater Lett 2015;159:58–60. https://doi.org/10.1016/j.matlet.2015.06.071.

[12] Zubair M, Daud M, McKay G, Shehzad F, Al-Harthi MA. Recent progress in layered double hydroxides (LDH)-containing hybrids as adsorbents for water remediation. Appl Clay Sci 2017;143:279–92. https://doi.org/10.1016/j.clay.2017.04.002.

[13] Yan H, Wei M, Jing M, Li F, Evans DG, Duan X. Theoretical study on the structural properties and relative stability of M(II)-Al layered double hydroxides based on a cluster model. J Phys Chem A 2009;113:6133–41. https://doi.org/10.1021/jp810129h.

[14] Wong F, Buchheit RG. Utilizing the structural memory effect of layered double hydroxides for sensing water uptake in organic coatings. Prog Org Coatings 2004;51:91–102. https://doi.org/10.1016/j.porgcoat.2004.07.001.

[15] Evans DG, Duan X. Preparation of layered double hydroxides and their applications as additives in polymers, as precursors to magnetic materials and in biology and medicine. Chem Commun 2006:485–96. https://doi.org/10.1039/b510313b.

[16] Yang Z, Wang F, Zhang C, Zeng G, Tan X, Yu Z, et al. Utilization of LDH-based materials as potential adsorbents and photocatalysts for the decontamination of dyes wastewater: A review. RSC Adv 2016;6:79415–36. https://doi.org/10.1039/c6ra12727d.

[17] Wang Z, Fang P, Kumar P, Wang W, Liu B, Li J. Controlled growth of LDH films with enhanced photocatalytic activity in a mixed wastewater treatment. Nanomaterials 2019;9:807. https://doi.org/10.3390/nano9060807.

[18] Sharma R, Bhawna, Kumar S, Singh P, Gupta A, Kumar V. Layered Double Hydroxide Nanomaterials: Biomedical Applications, Current Status and Challenges. Nano Life 2021;11:2130008. https://doi.org/10.1142/s1793984421300089.

[19] Xu M, Wei M. Layered Double Hydroxide-Based Catalysts: Recent Advances in Preparation, Structure, and Applications. Adv Funct Mater 2018;28:1–20. https://doi.org/10.1002/adfm.201802943.

[20] Mousty C, Kaftan O, Prevot V, Forano C. Alkaline phosphatase biosensors based on layered double hydroxides matrices: Role of LDH composition. Sensors Actuators, B Chem 2008;133:442–8. https://doi.org/10.1016/j.snb.2008.03.001.

[21] Illaik A, Vuillermoz C, Commereuc S, Taviot-Guého C, Verney V, Leroux F. Reactive and functionalized LDH fillers for polymer. J Phys Chem Solids 2008;69:1362–6. https://doi.org/10.1016/j.jpcs.2007.10.019.

[22] Gao Y, Wu J, Wang Q, Wilkie CA, O'Hare D. Flame retardant polymer/layered double hydroxide nanocomposites. J Mater Chem A 2014;2:10996–1016. https://doi.org/10.1039/c4ta01030b.

[23] Morioka H, Tagaya H, Karasu M, Kadokawa J, Chiba K. Preparation of hydroxy double salts exchanged by organic compounds. J Mater Res 1998;13:848–51. https://doi.org/10.1557/JMR.1998.0112

[24] Zhu Q, Wang X, Li JG. Recent progress in layered rare-earth hydroxide (LRH) and its application in luminescence. J Adv Ceram 2017;6:177–86. https://doi.org/10.1007/s40145-017-0238-0.

[25] Klemkaite-Ramanauske K, Žilinskas A, Taraškevičius R, Khinsky A, Kareiva A. Preparation of Mg/Al layered double hydroxide (LDH) with structurally embedded molybdate ions and application as a catalyst for the synthesis of 2-adamantylidene(phenyl)amine Schiff base. Polyhedron 2014;68:340–5. https://doi.org/10.1016/j.poly.2013.11.009.

[26] Han N, Zhao F, Li Y. Ultrathin nickel-iron layered double hydroxide nanosheets intercalated with molybdate anions for electrocatalytic water oxidation. J Mater Chem A 2015;3:16348–53. https://doi.org/10.1039/c5ta03394b.

[27] Jaiswal A, Chattopadhyaya MC. Synthesis and characterization of novel Co/Bi-layered double hydroxides and their adsorption performance for lead in aqueous solution. Arab J Chem 2017;10:S2457–63. https://doi.org/10.1016/j.arabjc.2013.09.010.

[28] Dutta S, Jana TK, Halder SK, Maiti R, Dutta A. $Zn_2Al\text{-}CO_3$ Layered Double Hydroxide : Adsorption , Cytotoxicity and Antibacterial Performances. ChemistrySelect 2020;5:6162–71. https://doi.org/10.1002/slct.202001264.

[29] Hara T, Ishikawa M, Sawada J, Ichikuni N, Shimazu S. Creation of highly stable monomeric Pd(II) species in an anion-exchangeable hydroxy double salt interlayer: Application to aerobic alcohol oxidation under an air atmosphere. Green Chem

2009;11:2034–40. https://doi.org/10.1039/b918350g.

[30] Weeramonkhonlert V, Srikhaow A, Meejoo S. Formation of copper hydroxy double salts derived from metal oxides and their catalytic activity in degradation of methyl orange. Ceram Int 2019;45:993–1000. https://doi.org/10.1016/j.ceramint.2018.09.278.

[31] Hara T, Fujita N, Ichikuni N, Wilson K, Lee AF, Shimazu S. E ffi cient 1 , 4-Addition of Enones and Boronic Acids Catalyzed by a Ni − Zn Hydroxyl Double Salt-Intercalated Anionic Rhodium (III) Complex. ACS Catal 2014;4:4–10. https://doi.org/dx.doi.org/10.1021/cs501267h.

[32] Jeon HG, Kim H, Jung H, Byeon SH. Phosphate uptake behavior of layered rare earth hydroxides l-RE(OH)$_3$ (RE = Sm, Gd, Er, and Y) from water. Solid State Sci 2018;81:1–7. https://doi.org/10.1016/j.solidstatesciences.2018.04.008.

[33] Zhu L, Zhang L, Li J, Zhang D, Chen L, Sheng D, et al. Selenium Sequestration in a Cationic Layered Rare Earth Hydroxide: A Combined Batch Experiments and EXAFS Investigation. Environ Sci Technol 2017;51:8606–15. https://doi.org/10.1021/acs.est.7b02006.

[34] Gu Q, Chen W, Duan F, Ju R. Fabrication of nano-drug delivery system based layered rare-earth hydroxides integrating drug-loading and fluorescence properties. Dalt Trans 2016;45:2137–12143. https://doi.org/https://doi.org/10.1039/C6DT01875K.

[35] Bouali AC, Serdechnova M, Blawert C, Tedim J, Ferreira MGS, Zheludkevich ML.

Layered double hydroxides (LDHs) as functional materials for the corrosion protection of aluminum alloys: A review. Appl Mater Today 2020;21:100857. https://doi.org/10.1016/j.apmt.2020.100857.

[36] Arrabito G, Bonasera A, Prestopino G, Orsini A, Mattoccia A, Martinelli E, et al. Layered double hydroxides: A toolbox for chemistry and biology. Crystals 2019;9:361. https://doi.org/10.3390/cryst9070361.

[37] Costa FR, Leuteritz A, Wagenknecht U, Jehnichen D, Häußler L, Heinrich G. Intercalation of Mg-Al layered double hydroxide by anionic surfactants: Preparation and characterization. Appl Clay Sci 2008;38:153–64. https://doi.org/10.1016/j.clay.2007.03.006.

[38] Mustapha Bouhent M, Derriche Z, Denoyel R, Prevot V, Forano C. Thermodynamical and structural insights of orange II adsorption by Mg_RAlNO_3 layered double hydroxides. J Solid State Chem 2011;184:1016–24. https://doi.org/10.1016/j.jssc.2011.03.018.

[39] Fahami A, Beall GW. Mechanosynthesis and characterization of Hydrotalcite like Mg-Al-SO_4-LDH. Mater Lett 2016;165:192–5. https://doi.org/10.1016/j.matlet.2015.11.132.

[40] Shi H, He J. Orientated intercalation of tartrate as chiral ligand to impact asymmetric catalysis. J Catal 2011;279:155–62. https://doi.org/10.1016/j.jcat.2011.01.012.

[41] Chubar N, Gilmour R, Gerda V, Mičušík M, Omastova M, Heister K, et al. Layered double hydroxides as the next generation inorganic anion exchangers: Synthetic

methods versus applicability. Adv Colloid Interface Sci 2017;245:62–80. https://doi.org/10.1016/j.cis.2017.04.013.

[42] Crepaldi EL, Pavan PC, Valim JB. Comparative Study of the Coprecipitation Methods for the Preparation of Layered Double Hydroxides. J Braz Chem Soc 2000;11:64–70. https://doi.org/10.1590/S0103-50532000000100012.

[43] Tonelli D, Gualandi I, Musella E, Scavetta E. Synthesis and characterization of layered double hydroxides as materials for electrocatalytic applications. Nanomaterials 2021;11:1–20. https://doi.org/10.3390/nano11030725.

[44] Wijitwongwan R, Intasa-Ard S, Ogawa M. Preparation of layered double hydroxides toward precisely designed hierarchical organization. ChemEngineering 2019;3:1–22. https://doi.org/10.3390/chemengineering3030068.

[45] Inayat A, Klumpp M, Schwieger W. The urea method for the direct synthesis of ZnAl layered double hydroxides with nitrate as the interlayer anion. Appl Clay Sci 2011;51:452–9. https://doi.org/https://doi.org/10.1016/j.clay.2011.01.008.

[46] Colombo K, Maruyama SA, Yamamoto CI, Wypych F. Intercalation of molybdate ions into Ni/Zn layered double hydroxide salts: Synthesis, characterization, and preliminary catalytic activity in methyl transesterification of soybean oil. J Braz Chem Soc 2017;28:1315–22. https://doi.org/10.21577/0103-5053.20160298.

[47] Khan AI, O'Hare D. Intercalation chemistry of layered double hydroxides: Recent developments and applications. J Mater Chem 2002;12:3191–8. https://doi.org/10.1039/b204076j.

[48] Farghali MA, Selim AM, Khater HF, Bagato N, Alharbi W, Alharbi KH, et al. Optimized adsorption and effective disposal of Congo red dye from wastewater: Hydrothermal fabrication of MgAl-LDH nanohydrotalcite-like materials. Arab J Chem 2022;15:104171. https://doi.org/10.1016/j.arabjc.2022.104171.

[49] Zhang H, Chen H, Azat S, Mansurov ZA, Liu X, Wang J, et al. Super adsorption capability of rhombic dodecahedral Ca-Al layered double oxides for Congo red removal. J Alloys Compd 2018;768:572–81. https://doi.org/10.1016/j.jallcom.2018.07.241.

[50] Li F, Duan X. Applications of layered double hydroxides. vol. 119. Springer-Verlag Berlin Heidelberg; 2005. https://doi.org/10.1007/430_007.

[51] Taviot-Guého C, Prévot V, Forano C, Renaudin G, Mousty C, Leroux F. Tailoring Hybrid Layered Double Hydroxides for the Development of Innovative Applications. Adv Funct Mater 2018;28:1–33. https://doi.org/10.1002/adfm.201703868.

[52] Rojas S, Horcajada P. Metal-Organic Frameworks for the Removal of Emerging Organic Contaminants in Water. Chem Rev 2020;120:8378–415. https://doi.org/10.1021/acs.chemrev.9b00797.

[53] Galiano F, Figoli A, Deowan SA, Johnson D, Altinkaya SA, Veltri L, et al. A step forward to a more efficient wastewater treatment by membrane surface modification via polymerizable bicontinuous microemulsion. J Memb Sci 2015;482:103–14. https://doi.org/10.1016/j.memsci.2015.02.019.

[54] Sun DT, Peng L, Reeder WS, Moosavi SM, Tiana D, Britt DK, et al. Rapid, Selective Heavy Metal Removal from Water by a Metal-Organic Framework/Polydopamine Composite. ACS Cent Sci 2018;4:349–56. https://doi.org/10.1021/acscentsci.7b00605.

[55] Liu L, Gao ZY, Su XP, Chen X, Jiang L, Yao JM. Adsorption removal of dyes from single and binary solutions using a cellulose-based bioadsorbent. ACS Sustain Chem Eng 2015;3:432–42. https://doi.org/10.1021/sc500848m.

[56] Kim KH, Kabir E, Jahan SA. Exposure to pesticides and the associated human health effects. Sci Total Environ 2017;575:525–35. https://doi.org/10.1016/j.scitotenv.2016.09.009.

[57] Kadirvelu K, Kavipriya M, Karthika C, Radhika M, Vennilamani N, Pattabhi S. Utilization of various agricultural wastes for activated carbon preparation and application for the removal of dyes and metal ions from aqueous solutions. Bioresour Technol 2003;87:129–32. https://doi.org/10.1016/S0960-8524(02)00201-8.

[58] Harja M, Buema G, Bucur D. Recent advances in removal of Congo Red dye by adsorption using an industrial waste. Sci Rep 2022;12:1–18. https://doi.org/10.1038/s41598-022-10093-3.

[59] Yaseen DA, Scholz M. Textile dye wastewater characteristics and constituents of synthetic effluents: a critical review. Int J Environ Sci Technol 2019;16:1193–226. https://doi.org/10.1007/s13762-018-2130-z.

[60] Wang J, Chen C. Biosorbents for heavy metals removal and their future. Biotechnol Adv 2009;27:195–226. https://doi.org/10.1016/j.biotechadv.2008.11.002.

[61] Shannon MA, Bohn PW, Elimelech M, Georgiadis JG, Marĩas BJ, Mayes AM. Science and technology for water purification in the coming decades. Nature 2008;452:301–10. https://doi.org/10.1038/nature06599.

[62] Rajkumar D, Kim JG. Oxidation of various reactive dyes with in situ electro-generated active chlorine for textile dyeing industry wastewater treatment. J Hazard Mater 2006;136:203–12. https://doi.org/10.1016/j.jhazmat.2005.11.096.

[63] Chong MN, Jin B, Chow CWK, Saint C. Recent developments in photocatalytic water treatment technology: A review. Water Res 2010;44:2997–3027. https://doi.org/10.1016/j.watres.2010.02.039.

[64] Ali I. New Generation Adsorbents for Water Treatment. Chem Rev 2012;112:5073–91. https://doi.org/10.1021/cr300133d.

[65] Ullberg M, Lavonen E, Köhler SJ, Golovko O, Wiberg K. Pilot-scale removal of organic micropollutants and natural organic matter from drinking water using ozonation followed by granular activated carbon. Environ Sci Water Res Technol 2021;7:535–48. https://doi.org/10.1039/d0ew00933d.

[66] Nagarajan R, Kumar V, Ahmad S. Anion doped binary oxides, SnO 2 , TiO 2 and ZnO: Fabrication procedures, fascinating properties and future prospects. Indian J Chem - Sect A Inorganic, Phys Theor Anal Chem 2012;51:145–54. https://doi.org/10.1002/chin.201214211.

[67] Kumar V, Bhawna, Yadav SK, Gupta A, Dwivedi B, Kumar A, et al. Facile Synthesis of Ce–Doped SnO 2 Nanoparticles: A Promising Photocatalyst for Hydrogen Evolution and Dyes Degradation. ChemistrySelect 2019;4:3722–9. https://doi.org/10.1002/slct.201900032.

[68] Lee KM, Lai CW, Ngai KS, Juan JC. Recent developments of zinc oxide based photocatalyst in water treatment technology: A review. Water Res 2016;88:428–48. https://doi.org/10.1016/j.watres.2015.09.045.

[69] Rao S, Lade HS, Kadam TA, Ramana T V., Krishnamacharyulu SKG, Deshmukh S, et al. Removal of chromium from tannery industry effluents with (Activated Carbon and Fly Ash) adsorbents. J Environ Sci Eng 2007;49:255–8. https://doi.org/http://dx.doi.org/10.1186/s13104-021-05855-7.

[70] Shaw R, Sharma R, Tiwari S, Tiwari SK. Surface Engineered Zeolite: An Active Interface for Rapid Adsorption and Degradation of Toxic Contaminants in Water. ACS Appl Mater Interfaces 2016;8:12520–7. https://doi.org/10.1021/acsami.6b01754.

[71] Zou JP, Liu HL, Luo J, Xing QJ, Du HM, Jiang XH, et al. Three-Dimensional Reduced Graphene Oxide Coupled with Mn_3O_4 for Highly Efficient Removal of Sb(III) and Sb(V) from Water. ACS Appl Mater Interfaces 2016;8:18140–9. https://doi.org/10.1021/acsami.6b05895.

[72] Crini G. Non-conventional low-cost adsorbents for dye removal: A review. Bioresour Technol 2006;97:1061–85.

https://doi.org/10.1016/j.biortech.2005.05.001.

[73] Dubey SP, Gopal K, Bersillon JL. Utility of adsorbents in the purification of drinking water: A review of characterization, efficiency and safety evaluation of various adsorbents. J Environ Biol 2009;30:327–32.

[74] Kamal T, Ul-Islam M, Khan SB, Asiri AM. Adsorption and photocatalyst assisted dye removal and bactericidal performance of ZnO/chitosan coating layer. Int J Biol Macromol 2015;81:584–90. https://doi.org/10.1016/j.ijbiomac.2015.08.060.

[75] Camargo PHC, Satyanarayana KG, Wypych F. Nanocomposites: Synthesis, structure, properties and new application opportunities. Mater Res 2009;12:1–39. https://doi.org/10.1590/S1516-14392009000100002.

[76] Shifrina ZB, Matveeva VG, Bronstein LM. Role of Polymer Structures in Catalysis by Transition Metal and Metal Oxide Nanoparticle Composites. Chem Rev 2020;120:1350–96. https://doi.org/10.1021/acs.chemrev.9b00137.

[77] Huo L, Zeng X, Su S, Bai L, Wang Y. Enhanced removal of As (V) from aqueous solution using modified hydrous ferric oxide nanoparticles. Sci Rep 2017;7:1–12. https://doi.org/10.1038/srep40765.

[78] Lafi R, Charradi K, Amine M, Ben A, Amara H, Hafiane A. Adsorption study of Congo red dye from aqueous solution to Mg – Al – layered double hydroxide. Adv Powder Technol 2015;27:232–7. https://doi.org/10.1016/j.apt.2015.12.004.

[79] Zhang S, Chen Y, Li J, Li Y, Song W, Li X, et al. Highly efficient removal of

aqueous Cu(II) and Cd(II) by hydrothermal synthesized CaAl-layered double hydroxide. Colloids Surfaces A Physicochem Eng Asp 2022;641:128584. https://doi.org/10.1016/j.colsurfa.2022.128584.

[80] Kheradmand A, Negarestani M, Kazemi S, Shayesteh H, Javanshir S, Ghiasinejad H. Adsorption behavior of rhamnolipid modified magnetic Co/Al layered double hydroxide for the removal of cationic and anionic dyes. Sci Rep 2022;12:1–17. https://doi.org/10.1038/s41598-022-19056-0.

[81] Kong Y, Huang Y, Meng C, Zhang Z. Sodium dodecylsulfate-layered double hydroxide and its use in the adsorption of 17β-estradiol in wastewater. RSC Adv 2018;8:31440–54. https://doi.org/10.1039/c8ra05726e.

[82] Guo Y, Zhu Z, Qiu Y, Zhao J. Enhanced adsorption of acid brown 14 dye on calcined Mg/Fe layered double hydroxide with memory effect. Chem Eng J 2013;219:69–77. https://doi.org/10.1016/j.cej.2012.12.084.

[83] Pérez MR, Pavlovic I, Barriga C, Cornejo J, Hermosín MC, Ulibarri MA. Uptake of Cu^{2+}, Cd^{2+} and Pb^{2+} on Zn-Al layered double hydroxide intercalated with edta. Appl Clay Sci 2006;32:245–51. https://doi.org/10.1016/j.clay.2006.01.008.

[84] Zhao D, Sheng G, Hu J, Chen C, Wang X. The adsorption of Pb(II) on Mg_2Al layered double hydroxide. Chem Eng J 2011;171:167–74. https://doi.org/10.1016/j.cej.2011.03.082.

[85] Liu YT, Wang MK, Chen TY, Chiang PN, Huang PM, Lee JF. Arsenale sorption on lithium/aluminum layered double hydroxide intercalated by chloride and on

gibbsite: Sorption isotherms, envelopes, and spectroscopic studies. Environ Sci Technol 2006;40:7784–9. https://doi.org/10.1021/es061530j.

[86] Meng Z, Lv F, Li X, Zhang Q, Chu PK, Komarneni S, et al. Simultaneous arsenate and alkali removal from alkaline wastewater by in-situ formation of Zn-Al layered double hydroxide. Microporous Mesoporous Mater 2016;227:137–43. https://doi.org/10.1016/j.micromeso.2016.02.046.

[87] You Y, Zhao H, Vance GF. Adsorption of dicamba (3,6-dichloro-2-methoxy benzoic acid) in aqueous solution by calcined-layered double hydroxide. Appl Clay Sci 2002;21:217–26. https://doi.org/10.1016/S0169-1317(01)00102-8.

[88] Zhang B, Luan L, Gao R, Li F, Li Y, Wu T. Rapid and effective removal of Cr(VI) from aqueous solution using exfoliated LDH nanosheets. Colloids Surfaces A Physicochem Eng Asp 2017;520:399–408. https://doi.org/10.1016/j.colsurfa.2017.01.074.

[89] Gupta K, Huo JB, Yang JCE, Fu ML, Yuan B, Chen Z. $(MoS_4)^{2-}$ intercalated CAMoS4·LDH material for the efficient and facile sequestration of antibiotics from aqueous solution. Chem Eng J 2019;355:637–49. https://doi.org/10.1016/j.cej.2018.08.200.

[90] Elhalil A, Farnane M, Machrouhi A, Mahjoubi FZ, Elmoubarki R, Tounsadi H, et al. Effects of molar ratio and calcination temperature on the adsorption performance of Zn/Al layered double hydroxide nanoparticles in the removal of pharmaceutical pollutants. J Sci Adv Mater Devices 2018;3:188–95.

https://doi.org/10.1016/j.jsamd.2018.03.005.

[91] Avella M, Errico ME, Martelli S, Martuscelli E. Preparation methodologies of polymer matrix nanocomposites. Appl Organomet Chem 2001;15:435–9. https://doi.org/10.1002/aoc.168.

[92] Spearing SM, Beaumont PWR, Case SW, Reifsnider KL, Bogy DB, Barenblatt GI, et al. Nanoparticle Polymer Composites : Where Two Small Worlds Meet. Science 2006;314:1107–11. https://doi.org/10.1126/science.1130557.

[93] Yuan B, Zhao S, Hu P, Cui J, Niu QJ. Asymmetric polyamide nanofilms with highly ordered nanovoids for water purification. Nat Commun 2020;11:1–12. https://doi.org/10.1038/s41467-020-19809-3.

[94] Cadek M, Coleman JN, Ryan KP, Nicolosi V, Bister G, Fonseca A, et al. Reinforcement of Polymers with Carbon Nanotubes : The Role of Nanotube Surface Area. Nano Lett 2004;4:353–6. https://doi.org/https://doi.org/10.1021/nl035009o.

[95] Ma P, Liu M, Zhang H, Wang S, Wang R, Wang K, et al. Enhanced Electrical Conductivity of Nanocomposites Containing Hybrid Fillers of Carbon Nanotubes and Carbon Black. Appl Mater Interfaces 2009;1:1090–6. https://doi.org/10.1021/am9000503.

[96] Naskar AK, Keum JK, Boeman RG. Polymer matrix nanocomposites for automotive structural components. Nat Nanotechnol 2016;11:1026–30. https://doi.org/10.1038/nnano.2016.262.

[97] Tanahashi M. Development of fabrication methods of filler/polymer nanocomposites: With focus on simple melt-compounding-based approach without surface modification of nanofillers. Materials (Basel) 2010;3:1593–619. https://doi.org/10.3390/ma3031593.

[98] Suresh K, Pugazhenthi G, Uppaluri R. Properties of polystyrene (PS)/Co-Al LDH nanocomposites prepared by melt intercalation. Mater Today Proc 2019;9:333–50. https://doi.org/10.1016/j.matpr.2019.02.163.

[99] Barik S, Badamali SK, Behera L, Kumar P. Mg – Al LDH reinforced PMMA nanocomposites : a potential material for packaging industry. Compos Interfaces 2018;6440:1–12. https://doi.org/10.1080/09276440.2018.1439628.

[100] Kartsonakis IA, Karaxi EK, Charitidis CA. Evaluation of polymer composites based on core/shell polystyrene/Mg-Al-NO_3 layered double hydroxides for chloride entrapment. Plast Rubber Compos 2016;45:50–7. https://doi.org/10.1080/14658011.2015.1133116.

[101] Dinari M, Neamati S. Surface modified layered double hydroxide/polyaniline nanocomposites: Synthesis, characterization and Pb^{2+} removal. Colloids Surfaces A Physicochem Eng Asp 2020;589:124438. https://doi.org/10.1016/j.colsurfa.2020.124438.

[102] Koilraj P, Kannan S. Aqueous fluoride removal using ZnCr layered double hydroxides and their polymeric composites: Batch and column studies. Chem Eng J 2013;234:406–15. https://doi.org/10.1016/j.cej.2013.08.101.

[103] Ghanbari N, Ghafuri H. Design and preparation the novel polymeric layered double hydroxide nanocomposite (LDH/Polymer) as an efficient and recyclable adsorbent for the removal of methylene blue dye from water. Environ Technol Innov 2022;26:102377. https://doi.org/10.1016/j.eti.2022.102377.

[104] Li X, Zhang Y, Xing W, Li L, Xue Q, Yan Z. Sandwich-like graphene / polypyrrole / layered double hydroxide nanowires for high-performance supercapacitors. J Power Sources 2016;331:67–75. https://doi.org/10.1016/j.jpowsour.2016.09.034.

[105] Zhou Y, Hu G, Zhang W, Li Q, Zhao Z, Zhao Y, et al. Cationic two-dimensional sheets for an ultralight electrostatic polysulfide trap toward high-performance lithium-sulfur batteries. Energy Storage Mater 2017;9:39–46. https://doi.org/10.1016/j.ensm.2017.06.005.

[106] Yan J, Yang Z. Based on the performance of hydrotalcite as anode material for a Zn-Ni secondary cell, a modification: PPY coated Zn-Al-LDH was adopted. RSC Adv 2016;6:85117–24. https://doi.org/10.1039/c6ra14012b.

[107] Elanchezhiyan SS, Meenakshi S. Synthesis and characterization of chitosan/Mg-Al layered double hydroxide composite for the removal of oil particles from oil-in-water emulsion. Int J Biol Macromol 2017;104:1586–95. https://doi.org/10.1016/j.ijbiomac.2017.01.095.

[108] Shafiei SS, Shavandi M, Ahangari G, Shokrolahi F. Electrospun layered double hydroxide/poly (ε-caprolactone) nanocomposite scaffolds for adipogenic differentiation of adipose-derived mesenchymal stem cells. Appl Clay Sci

2016;127–128:52–63. https://doi.org/10.1016/j.clay.2016.04.004.

[109] Matusinovic Z, Wilkie CA. Fire retardancy and morphology of layered double hydroxide nanocomposites: A review. J Mater Chem 2012;22:18701–4. https://doi.org/10.1039/c2jm33179a.

Chapter 2 SYNTHESIS AND CHARACTERIZATION OF NOVEL Zn/Cu LAYERED DOUBLE HYDROXIDE: OPTIMIZATION OF PROCESS PARAMETERS USING CCD-RSM APPROACH FOR ANIONIC DYE SEQUESTRATION

2.1 Introduction

Layered double hydroxides (LDH) as discussed in previous chapter are synthetic inorganic lamellar materials (also called anionic clays) with structure similar to that of hydrotalcite are used extensively in multidisciplinary fields like, environmental remediation, energy storage, biomedical applications, polymer nanocomposites, and flame-retardant additives [1–4].

The contamination of water resources by toxic pollutants affects abiotic as well as biotic components of the ecosystem and is one of the most critical environmental concerns in recent years. Dyes are complex and toxic organic compounds that are released into water streams from various industries including food, textile, pharmaceuticals, petrochemicals, etc. [5]. The cyclic structure of dyes, along with their high toxicity and chemical stability, and low degradation rate make these substances a serious threat to aquatic ecosystems. Due to the presence of aromatic amine structure in azo dye they are resistant to environmental degradation and are considered carcinogenic in nature [6,7]. It is therefore essential to find an effective method to remove these pollutants from aquatic environments.

Till today a variety of methodologies have been opted to eradicate these toxic organic compounds from water streams, including membrane filtration, chemical oxidation,

ozonation, biosorption, and photodegradation [8]. However, all the reported methodologies either lead to the generation of secondary pollutants or are time-consuming. But among all the processes, adsorption process involving use of adsorbents that are cheap and readily available makes the adsorption method one of the most efficient, easiest, and economical approaches for removing toxic pollutants [9]. Since the efficiency of adsorption is regulated by the quality and cost-effectiveness of the sorbent, a variety of adsorbents has been studied in recent decades, including activated carbon, layered double hydroxides (LDH), graphene oxide (GO), clay, metal oxides (such as zinc oxide, titanium dioxide, etc.), polymer nanocomposites, and zeolite [10–14]. LDHs have received consistent recognition as highly effective adsorbents due to various advantages, including economic feasibility, high anion exchangeability, high adsorption capacity, and regeneration ability [15]. With the high chemical and thermal stability, extensive presence of hydroxyl groups, and ability to intercalate multiple molecules, LDHs are an important tool for removing contaminants from water. An investigation by Kheradmand *et al.* (2022) examined the sequestration of methylene blue and reactive orange 16 dyes by rhamnolipid-modified Co/Al LDH. Accordingly, both acidic and basic dyes can be effectively removed using Co/Al LDH (Kheradmand *et al.* 2022). Recently, Zhang *et al.* (2022) prepared Ca/Al LDH hydrothermally and studied its performance for the uptake of Cu (II) and Cd (II) ions [16]. RSM (response surface methodology) is an efficient method utilized to optimize processes whose outcome is dependent on more than two variables. Set of experimental designs and models are constructed using these statistical techniques. RSM experiment uses an experimental design and interaction analysis to estimate quadratic effects and interactions between the process parameters [17]. In RSM, six steps are involved in simulating and

optimizing physicochemical processes: (1) and (2) involve selection of desired response and strategy, (3) running the experiments, (4) analyzing experimental data and fitting a model, (5) validation of the fitted model and (6) optimization of the process parameters [18]. In addition to being an effective and reliable statistical tool, it saves time and money by enabling reliable and accurate experiment design and analysis.

In the present study acid hydrolysis route was adopted for the synthesis of novel adsorbent containing zinc and copper as divalent and trivalent metal ions, respectively. The study evaluated the adsorption efficiency of synthesized lattice to remove azo dyes from synthetic and natural water samples. The uptake of series of anionic dyes, i.e., Congo red (CR), Methyl orange (MO), and Eriochrome black T (EBT) was performed out of which maximum efficiency was calculated for CR dye. Therefore, the adsorption experiments and statistical studies were performed for the same. Central composite design (CCD) was utilized to determine optimal operating conditions for CR dye uptake from the solution employing response surface methodology (RSM). An analysis of batch experimental data was conducted to determine the isotherm and kinetics for the removal of CR dye.

2.2 Materials and methods

2.2.1 Materials

Copper acetate monohydrate, zinc acetate dihydrate and H_2O_2 (30 %) solution were purchased from Merck Germany, whereas CR, MO, and EBT were obtained from CDH. Table 2.1 gives information about the structure, formulas, and λ_{max} of dyes employed.

Table 2.1 Structure and formula of azo dyes employed in the study.

Azo dye	Structure	λ_{max} (nm)	Molecular formula

CR	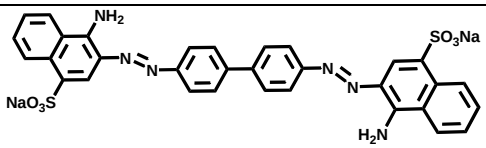	498	$C_{32}H_{22}N_6Na_2O_6S_2$
MO	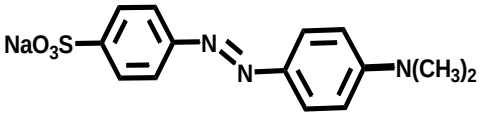	464	$C_{14}H_{14}N_3NaO_3S$
EBT	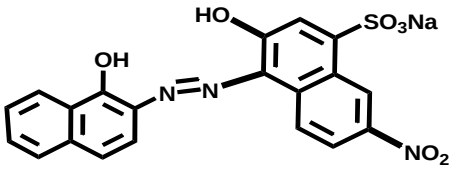	531	$C_{20}H_{12}N_3O_7SNa$

2.2.2 Instrumentation

A Bruker D8 diffractometer was used to record the PXRD pattern in the range of 2θ = 5-70° having step size and a scanning rate of 0.02° and 1.0 second/step, respectively, using Cu Kα radiation of 1.54 Å wavelength. FTIR analysis was performed using PerkinElmer FTIR (version 10.5.3) by preparing KBr disks. Thermal analysis was done with PerkinElmer thermogram at 10 °C min^{-1} heating rate under N_2 atmosphere Zeta potential was determined using Pananalytical Zetasizer (Version. 7.13). Surface area and other related properties were determined using Brunauer-Emmett-Teller (BET) by a Quanta chrome Nova-1000 instrument by N_2 adsorption-desorption isotherm. Tecnai G2 20 S-Twin TEM and ZEISS Gemini FE-SEM were used to study surface morphology of material.

2.2.3 Zn/Cu LDH synthesis

Zn/Cu layered double hydroxide was synthesized using an acid hydrolysis route having various composition of zinc and copper metal ions. An aqueous solution of copper acetate

(0.5 mmol in 10 mL distilled water) was transferred to solution of zinc acetate (4.5 mmol in 10 mL distilled water), followed by the addition of 5 mL of oxidant (30% hydrogen peroxide solution) and 30 mL miliQ water. The mixture was then ultrasonicated for 30 minutes followed by 24 hours stirring and later the obtained products were dried in oven at 60℃. Similar other trials were also carried out for the synthesis having varying compositions of Zinc:Copper metal ions, i.e., 4.9:1 mmoles, 4.9:1.25 mmoles, and 3.74:1.2 mmoles.

2.2.4 Batch experiments

Batch sorption experiments were performed with 20 mg/L concentration of anionic dyes (20 mL) and 0.01 g of sorbent where 0.1 N NaOH and HCl were used to maintain the pH. Small aliquots of solutions were drawn after fixed intervals, then centrifuged and later analyzed using UV-Vis spectrophotometer. The removal efficiency was determined from equation (2.1) whereas equations (2.2) and (2.3) were utilized to determine sorption capacity.

$$\% \text{ Removal} = \frac{\text{Co-Ce}}{\text{Co}} \times 100 \quad (2.1)$$

$$q_e = \frac{C_o\text{-}C_e}{W} \times V \quad (2.2)$$

$$q_t = \frac{C_o\text{-}C_t}{W} \times V \quad (2.3)$$

Where C_0, C_e, and C_t are defined as concentration of dyes (mg/L) at initial stage, at equilibrium, and at time t, respectively. Dye solution volume and amount of adsorbent are denoted by V (in mL) and W (in mg).

2.2.5 Design of experiment using RSM

The CCD tool of RSM allows for parallel execution of large numbers of experiments and is highly efficient for studying four factors at once [19]. The influence of four different process parameters on the CR dye uptake was assessed using RSM. pH, concentration, adsorbent dosage, and contact time designated as A-D respectively, are chosen as independent variables for the sportive removal of CR dye. Table 2.2 shows pH (A) ranging from 4 to 7, concentration (B) ranging from 20 to 50 mg/L, dosage (C) ranging from 0.005 to 0.01 g, and contact time ranging from 4 to 8 minutes. Eq. 2.4 was used in the model to evaluate the number of experiments to be conducted:

$$N = 2^k + 2k + n \quad (2.4)$$

Where, k and n are number of factors and replicates of center point, respectively.

Table 2.2 Independent variables and ranges in CCD method.

Factor	Name	Low Level	High Level	-α	+α
A	pH	4	7	2.5	8.5
B	Concentration of dye	20	50	5	65
C	Adsorbent dosage	0.005	0.01	0.0025	0.0125
D	Contact time	4	8	2	10

The design of the experiments and processing of the obtained data was performed using the Design-expert13 (Stat.Ease.Inc. trial version) software. According to eq. 2.4, the CCD-RSM approach suggested 30 experiments. Some preliminary experiments were performed

for the selected ranges of the variables. The significance and appropriateness of the regression model was confirmed using values of ANOVA and determination coefficient (R^2).

2.3 Results and Discussion

2.3.1 Structural and morphological properties

The PXRD patterns of pure phase LDHs exhibit a strong and intense peak at a lower 2θ value followed by low intensity peaks at higher 2θ values, i.e., characteristic of anionic clays. Figure 2.1 shows PXRD patterns of LDHs synthesized with varying ratios of zinc and copper acetate precursors. Notably in LDH sample with 4.5:0.5 mmoles zinc-to-copper composition, a single, sharp, and intense reflection corresponding to the (002) plane was observed around 12° (2θ value), suggesting a well-defined LDH phase.

However, in LDH samples with 4.9:1.0 mmoles, 4.9:1.25 mmoles, and 3.74:1.2 mmoles composition, an additional peak appeared alongside the sharp (002) reflection. This additional peak was indicative of impurity phases, demonstrating that an increased concentration of copper ions introduced impurities into the LDH structure. The presence of impurities was consistent with the hypothesis that excessive copper incorporation might disrupt the LDH crystal structure, resulting in the formation of impure phase.

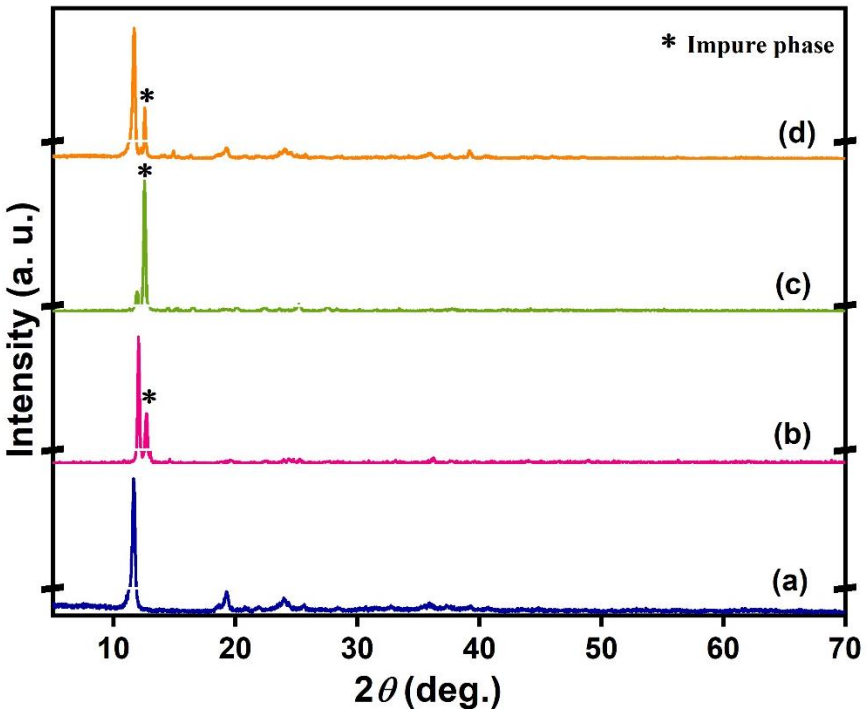

Figure 2.1 PXRD pattern of LDHs formed with different compositions of Zn and Cu (a) 4.5:0.5 mmoles, (b) 4.9:1.0 mmoles, (c) 4.9:1.25 mmoles, and (d) 3.74:1.2 mmoles.

The PXRD pattern of Zn/Cu LDH (4.5:0.5 mmoles) with d-spacing and hkl values is presented in Figure 2.2a. The intense reflections with d-spacing values of 7.47, 4.55, 3.72, 2.72, 2.50, and 2.28 Å can be assigned (002), (003), (004), (101), (006), and (103) hkl planes, respectively. In addition, these prominent reflections could be indexed in hexagonal symmetry with a = 3.19 and c = 14.9 Å. The presence of a characteristic peak of anionic clays around 11.9° (2θ) with a d-spacing value of 7.47 Å confirmed the formation of a layered arrangement. Moreover, brucite layer thickness (4.8 Å) and acetate molecule length (3.6 Å) suggest monolayer arrangement of acetate ions in the interlamellar region of synthesized LDH [20]. Therefore, Zn/Cu lattice having 4.5:0.5 mmoles composition was further characterized using series of techniques to establish the presence of anions,

morphology, surface area, etc. and was then utilized as a sorbent for sequestration of anionic azo dyes.

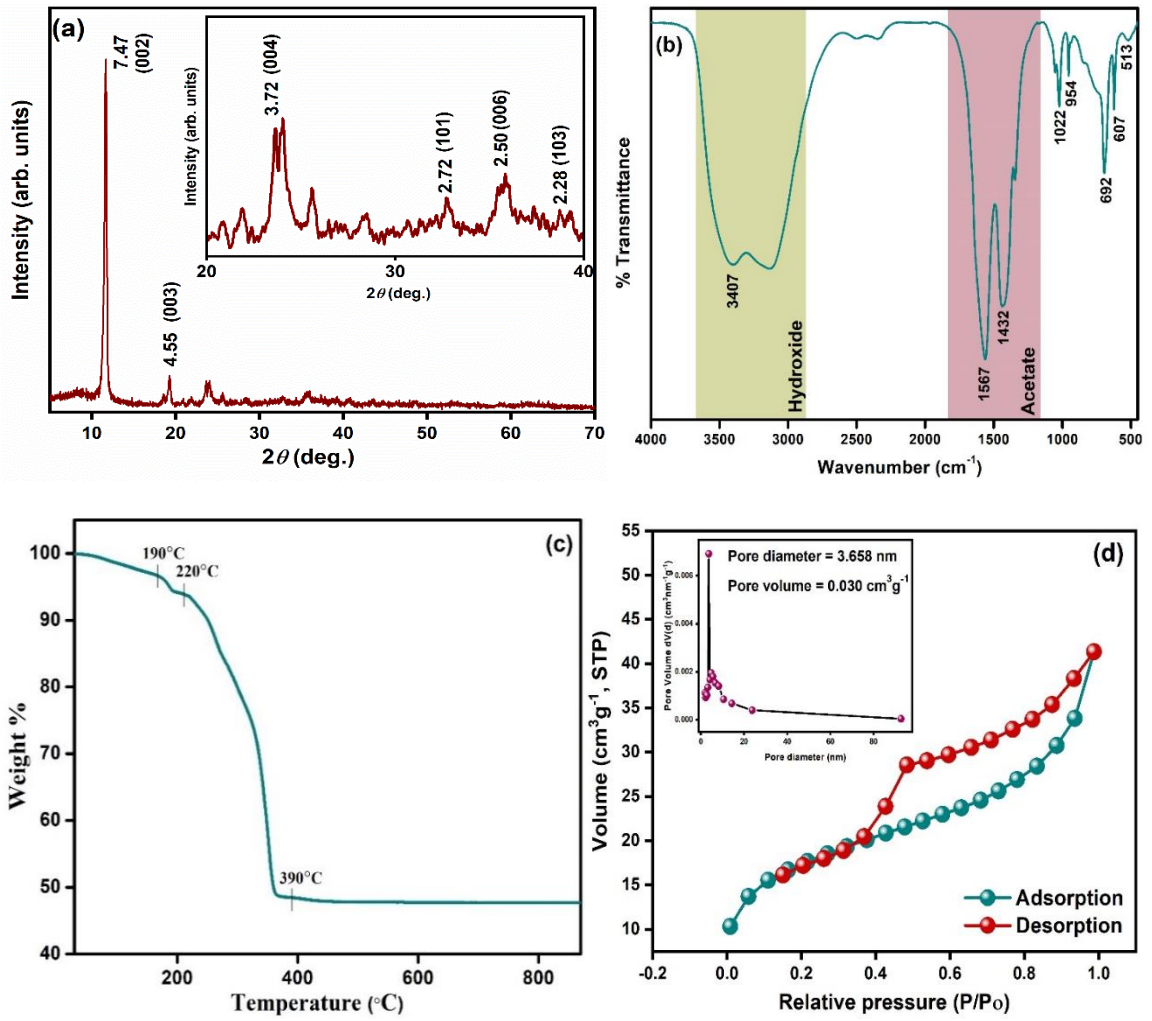

Figure 2.2 (a) PXRD pattern (b) FTIR spectrum (c) TG profile and (d) adsorption-desorption isotherm with pore size distribution of Zn/Cu LDH.

As can be viewed from Figure 2.2b, the FTIR spectrum confirms the existence of acetate as an interlamellar anion in Zn/Cu LDH. A broad absorption band at 3407 cm^{-1} is accompanied by hydroxyl groups in brucite-like sheets and interlayer H_2O molecules. As a result of the substantial hydrogen bond formation in these materials, the band accredited to the hydroxyl groups is fairly broad. The bands at 1567, 1432, 1022, 954, 692, and 607

cm^{-1} corroborate the presence of acetate as interlayer anion [21]. Further, at 1567 and 1432 cm^{-1} strong absorption bands were obtained due to the stretching of $-COO^-$ groups antisymmetrically and symmetrically, respectively. The band centered at 1022, 692, and 607 cm^{-1} were ascribed to the $-CH_3$ group rocking vibration, O-C-O bending, and rocking vibration of CO_2^- group, respectively [22]. Moreover, the band at 513 cm^{-1} evidenced the presence of metal-oxygen linkage (Zn/Cu-O) in the lattice.

The thermal stability of Zn/Cu LDH was assessed by performing thermal degradation under N_2 atmosphere (Figure 2.2c). It can be observed that a continuous loss of weight of 52.28 % occurred until 430℃, after which it remained constant. The decomposition of LDH mainly take place in three steps: (1) removal of surface adsorbed and interlayer H_2O molecules, (2) dehydroxylation of lattice, and (3) decomposition of acetate anions [23].

Surface area and porosity of Zn/Cu LDH were measured to an in-depth comprehension of the factors influencing the adsorptive properties of Zn/Cu LDH as adsorbent. The N_2 adsorption/desorption isotherm (type-IV isotherm) recorded at 77K is given Figure 2.2d with a hysteresis loop implying the material's mesoporous nature [11]. The specific surface area of synthesized material obtained from the BET method was 61.841 m^2g^{-1}. Based on the BJH (Barrett–Joyner–Halenda) method of pore size distribution, pore diameter and pore volume were estimated as 3.658 nm and 0.030 cm^3g^{-1}, respectively. The inset of Figure 2.2d displays pore size distribution of the Zn/Cu LDH.

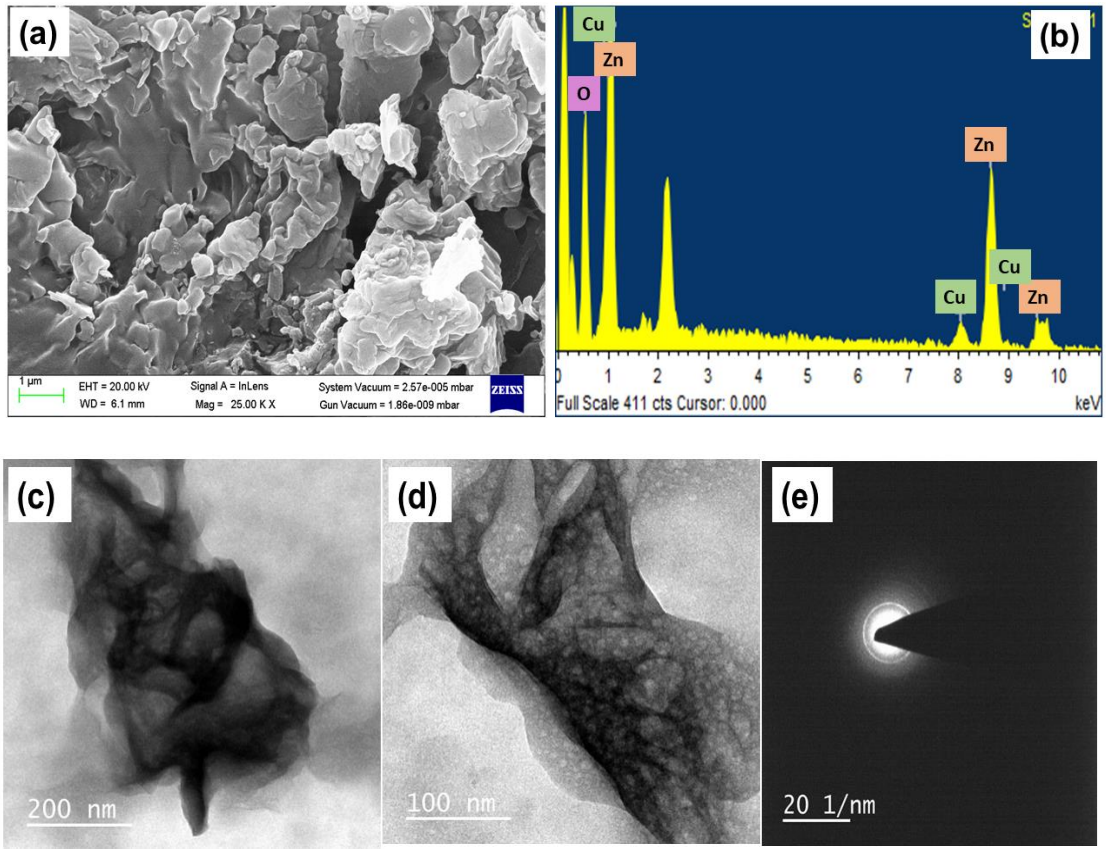

Figure 2.3 (a) SEM micrograph (b) EDX analysis (c-d) TEM image and (e) SAED pattern of Zn/Cu LDH.

The morphology of the sorbent material was examined by SEM/EDX and TEM analysis and are presented in Figure 2.3. The SEM micrograph (Figure 2.3a) revealed that the synthesized lattice exhibits plate-like morphology which is typical of inorganic layered materials [24]. The EDX analysis (Figure 2.3b) confirmed the uniform distribution of zinc and copper metal ions in the lattice.

The formation of pure phase material with the plate-like morphology can be also be confirmed from TEM images shown in Figure 2.3c-e. A clear diffraction ring pattern can

be viewed in the SAED pattern (Figure 2.3e) of the synthesized lattice which signifies the presence of a layered arrangement [25].

2.3.2 Adsorption studies

2.3.2.1 Adsorption of various azo dyes

The sorption capacity of the Zn/Cu LDH was examined mainly for the sequestration of three anionic dyes, i.e., CR, EBT, and MO. The initial adsorption experiments were carried out by providing similar experimental conditions, i.e., adsorbent dose: 0.01 g, adsorbate concentration: 20 mg/L, and contact time: 4 min.

The data for the percentage removal of azo dyes before and after sorption is given in Figure 2.4a-b. The adsorption efficiency follows the trend CR (99 %) > EBT (98 %) > MO (57 %) within 4 minutes of contact time. From the above experiment, it was deduced that the Zn/Cu LDH can be utilized as an efficient sorbent for anionic dye sequestration, especially CR.

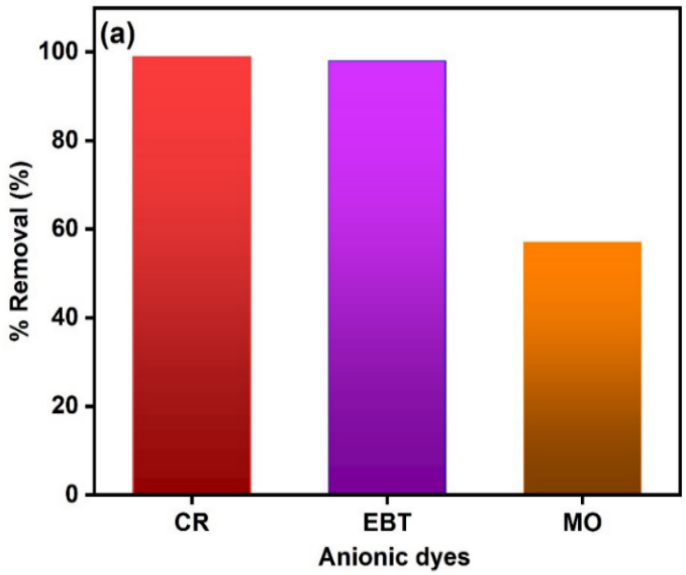

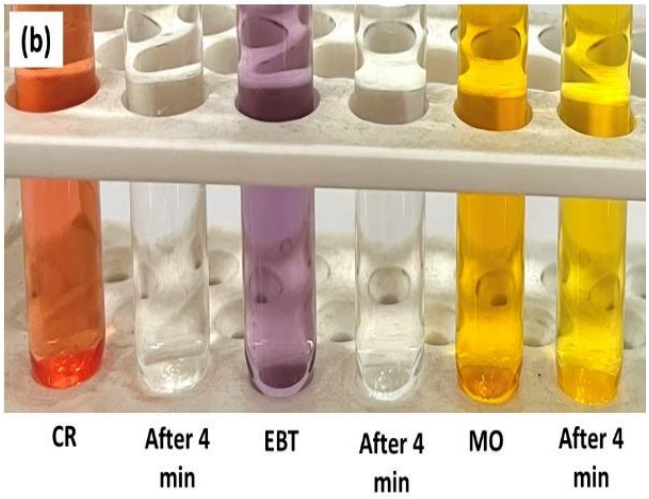

Figure 2.4 (a) Plot of percentage removal of and (b) visual representation of different anionic dyes after adsorption using Zn/Cu LDH.

2.3.2.2 Central composite design

The impact of parameters on CR dye uptake was examined using the CCD model of RSM. For environmental processes the most commonly used design approach is CCD. The CCD matrix with the experimental and predicted data for the response is presented in Table 2.3. The results were fitted to a modified quadratic model by employing ANOVA which is expressed by Eq. 2.5 where R is the percentage removal of CR dye [18].

$$R = X_0 + X_1A + X_2B + X_3C + X_4BC + X_5A^2 + X_6C^2 \quad (2.5)$$

Table 2.3 Central composite design statistics with observed and predicted % removal responses.

Run	Variables				% Removal	
	A: pH	B: Concentration of dye (mg/L)	C: Adsorbent dosage (g)	D: Contact time (min)	Observed	Predicted
1	5.5	35	0.0075	10	97.7	96.32
2	5.5	35	0.0125	6	98.56	99.64
3	7	20	0.005	8	99.91	97.67

4 (C)	5.5	35	0.0075	6	97.93	96.32
5	5.5	35	0.0075	2	97.21	96.32
6 (C)	5.5	35	0.0075	6	97.25	96.32
7 (C)	5.5	35	0.0075	6	97.55	96.32
8	7	20	0.01	8	99.12	101.52
9	4	50	0.01	8	98.86	94.62
10	5.5	5	0.0075	6	98.2	112.86
11	4	50	0.005	4	50.4	47.66
12	5.5	35	0.0025	6	46.98	48.84
13	7	50	0.01	8	99.29	106.53
14	2.5	35	0.0075	6	48.01	62.67
15	4	20	0.01	4	95.17	89.6
16	7	50	0.005	8	58.41	59.58
17	7	50	0.005	4	54.95	59.58
18	4	50	0.005	8	47.02	47.66
19	4	50	0.01	4	99.76	94.62
20	5.5	65	0.0075	6	79.2	79.78
21	**7**	**50**	**0.01**	**4**	**99.91**	**106.53**
22	8.5	35	0.0075	6	98.21	86.49
23	7	20	0.01	4	99.14	101.52
24 (C)	5.5	35	0.0075	6	97.72	96.32
25	4	20	0.01	8	98.41	89.6
26 (C)	5.5	35	0.0075	6	97.39	96.32
27	4	20	0.005	4	84.96	85.76
28	4	20	0.005	8	92.98	85.76
29	7	20	0.005	4	99.39	97.67

30 (C)	5.5	35		0.0075	6	97.18	96.32

(C) = Center points

Using the data obtained from RSM experiments a modified quadratic model was developed after the omission of nonsignificant terms as given in the following equation (in terms of designated factors):

$$R = 96.53 + 5.96A - 8.27B + 12.7C + 10.78BC - 5.51A^2 - 5.6C^2 \quad (2.6)$$

The outcomes of ANOVA (given in Table 2.4) were used to assess the predicted modified quadratic model. The relevance of the fitted model was correlated with the coefficient of determination (R^2) value and was further examined by the F-test (Fisher test). The high F-value for the model, i.e., 39.91 suggested that the model is considerable and there is only a 0.01% possibility that noise results in this high F-value. Statistically significant results obtained from the present study, shows that the developed quadratic model can predict % dye removal with a low p-value (<0.05). In the current study only those terms which have a p-value < 0.05 are included in the model other terms are considered insignificant. The high value of coefficient of determination ($R^2 = 0.9124$) suggested that the calculated and predicted response data were in good agreement.

Table 2.4 Table 2.4 ANOVA for Reduced Quadratic model.

Source	**Sum of squares**	**df**	**Mean square**	**F-value**	**p-value**	
Model	9803.22	6	1633.86	39.91	< 0.0001	significant
A-pH	851.41	1	851.41	20.8	0.0001	
B-Concentration of dye	1641.18	1	1641.18	40.09	< 0.0001	

C-Adsorbent dosage	3871.21	1	3871.21	94.56	< 0.0001
BC	1858.27	1	1858.27	45.39	< 0.0001
A^2	864.97	1	864.97	21.13	0.0001
C^2	891.83	1	891.83	21.78	0.0001
Residual	941.63	23	40.94		
Lack of Fit	941.63	18	52.31		
Pure Error	0	5	0		
Cor Total	10744.85	29			
Standard deviation		6.38			
Mean		87.56			
C.V.%		7.3			
R^2		0.9124			
Adjusted R^2		0.8895			
Predicted R^2		0.7347			
Adequate Precision		21.145			

C.V.% = Coefficient of variation, df = Degree of freedom

Table 2.4 also presents the fit statistic data for the model. The difference among Predicted R^2 (0.7347) and Adjusted R^2 (0.8895) was < 0.2, i.e., the values obtained were in good agreement. The obtained value of Adeq Precision is 21.145 indicating an adequate signal. Thus, confirming that the model can be utilized to direct the design space.

2.3.2.3 Optimization of adsorption parameters using the desirability function

The ideal conditions for the dye uptake were obtained by the desirability calculation employing design-expert software (trial version), with 0.963 value of desirability. In this method, factors that contribute to positive outcomes are maximized, while factors that

cause negative outcomes are minimized. The target function is set as high as possible to get the maximum percentage removal. Based on the predicted model, the optimum parameters for maximum dye uptake were found to be at pH 7 having dye concentration 50 mg/L and 0.01 g of adsorbent within 4 minutes contact time (Table 2.5). The percentage removal of CR dye predicted by the model was computed to be 100 % which was in correlation with experimentally observed value (99.91 %). Based on these results, the CCD model was proven to be effective in studying and optimizing the colour removal process.

Table 2.5 Optimized conditions for dye uptake obtained by desirability function.

Coded Variables				**Predicted %R**	**Experimental %R**
A: 7	B: 50 ppm	C: 0.01 g	D: 4 min	100	99.91

2.3.2.4 Effect of operating parameters on dye uptake

RSM was employed to analyze the impact of independent variables on the CR dye uptake using Zn/Cu LDH adsorbent. In the present study, the plot obtained by desirability calculations (Figure 2.5) illustrates that the % removal of CR dye was independent of contact time as it shows zero value for desirability. It also depicts that the response was equally influenced by pH and concentration of dye whereas the impact of adsorbent dosage was slightly less than the other two factors.

Based on these observations the interactions between these three variables with respect to CR dye uptake was studied using 3-D response surface plots illustrated in Figure 2.6. It was evident from these plots that the curvature indicates the extent to which variables are interacting. In Figure 2.6a the interactive influence of pH and dye concentration at constant

adsorbent dosage (0.01 g) is depicted. Results demonstrated that pH greatly affects percentage removal of CR dye as removal increases with increasing pH.

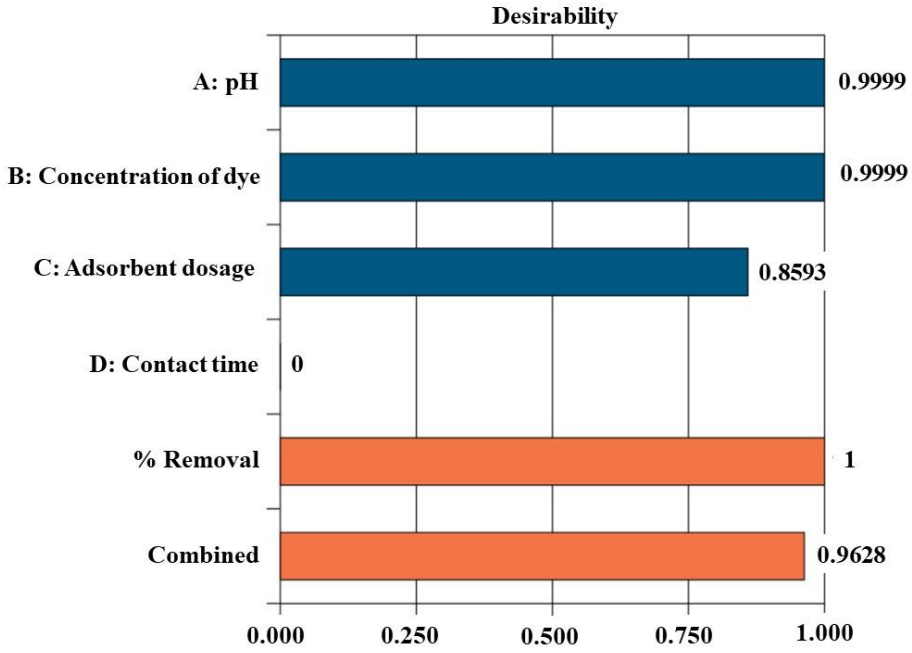

Figure 2.5 Desirability plot for different variables and their combined effect.

The adsorbent amount is one of the key factors that directly influences uptake of dye, Figure 2.6b illustrates the 3D response surface plot of % removal dependent on pH and dose of sorbent. It clearly states that with increasing adsorbent amounts, the % removal increases as a larger surface area and increased active sites become accessible for sorption.

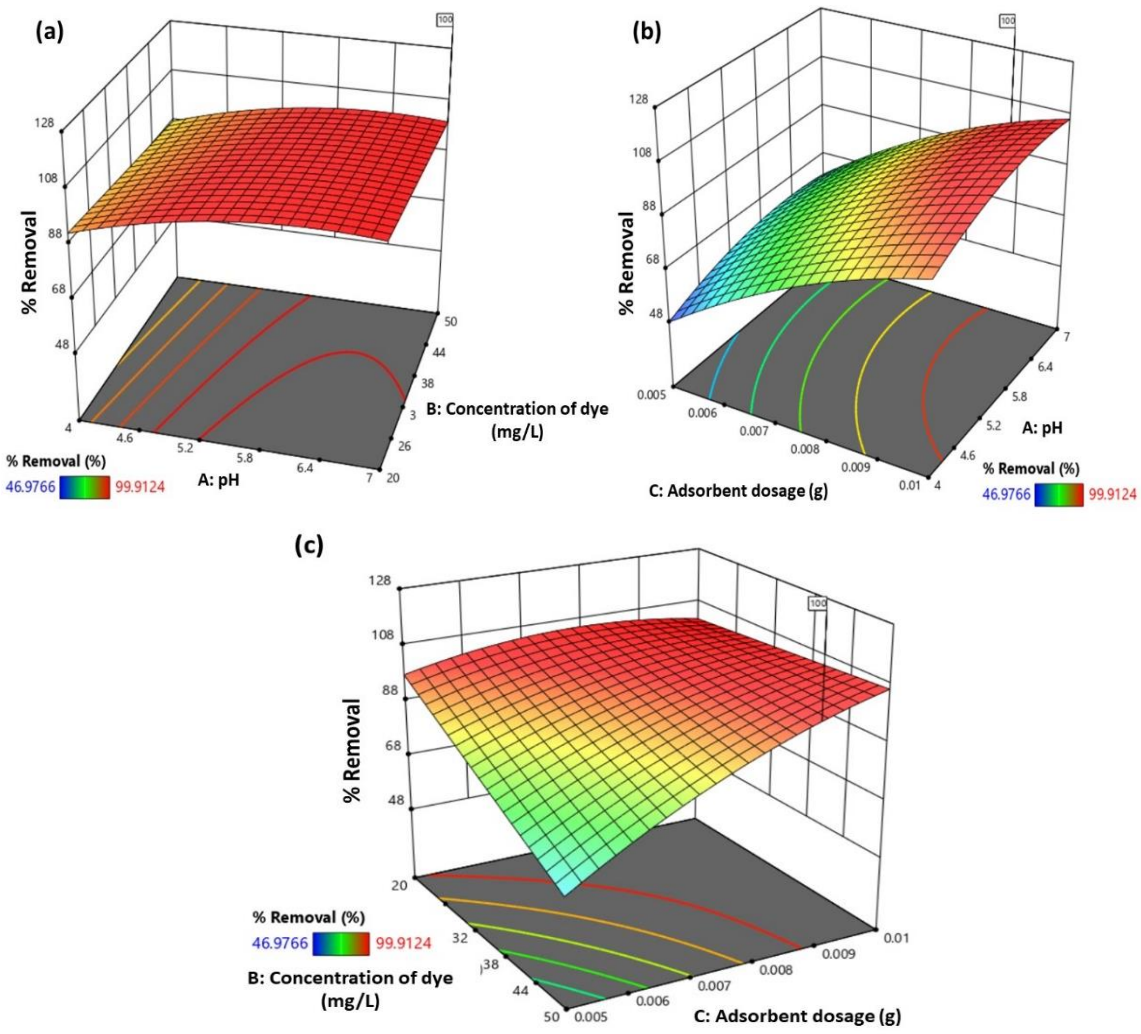

Figure 2.6 Counter plots for interaction between (a) pH and dye concentration, (b) pH and adsorbent amount, and (c) dye concentration and adsorbent amount.

In addition, the interaction between adsorbent dosage and dye concentration is depicted in Figure 2.6c which clearly indicates that % removal maximizes at higher adsorbent dosage and lower initial concentration of dye. A decrease in dye concentration results in a lower ratio between the concentration of solute and active adsorbent sites, which accelerates dye adsorption, resulting in an increase in dye uptake. Whereas, at increased dye concentration the saturation of adsorption sites of adsorbent results in a decrease in adsorption.

2.3.2.5 Adsorption equilibrium isotherm

For understanding adsorption mechanisms, isotherm studies are helpful since they provide information about the adsorption capacity and how the adsorbate molecules interact with the adsorbent, i.e., physically or chemically. The adsorption was performed at different concentrations of CR dye (keeping other parameters constant) to investigate the sorption mechanism. The obtained data were analysed using three isotherm models: Langmuir, Freundlich, and Temkin. According to the Langmuir isotherm (LI) (Eq. 2.7) adsorbents are assumed to bind at specific homogeneous sites, and adsorbed ions are assumed to adhere to the homogeneous surface of adsorbents in monolayer. There occur no interactions between molecules of adsorbent. Freundlich isotherm (FI) (Eq. 2.8) states that adsorption occurs on non-homogeneous adsorbent sites (multilayer adsorption) with non-uniform energy distribution to the active sites [26]. An adsorption isotherm for a two-phase system is represented by the Temkin isotherm (TI) by considering some aspects of indirect adsorbate-adsorbent interactions. The linear expression of the model is given in Eq. 2.9.

$$\frac{C_e}{q_e} = \frac{1}{q_{max} K_L} + \frac{C_e}{q_{max}} \tag{2.7}$$

$$\ln q_e = \ln K_F + \frac{1}{n} \ln C_e \tag{2.8}$$

$$q_e = B \ln A_T + B \ln C_e \tag{2.9}$$

Where q_e and q_{max} (mg/g) are equilibrium and maximum adsorption capacity, respectively and C_e is final dye concentration (mg/L). Langmuir and Freundlich equilibrium constants are denoted by K_L (L/mg) and K_F (mg/g) respectively, constant n is Freundlich adsorption intensity and the value of n>1 indicates favorable condition for adsorption. Constant B is associated with heat of adsorption (J/mol) and A_T (L/g) is binding constant of Temkin isotherm.

The favourability of the adsorption can be predicted by the LI by using a separation factor R_L (a constant without dimensions) and can be expressed as follows:

$$R_L = \frac{1}{1+k_L C_0} \tag{2.10}$$

where the process can be called irreversible, favorable, linear, and unfavorable when R = 0, 0 < R_L < 1, R = 1, and R > 1, respectively.

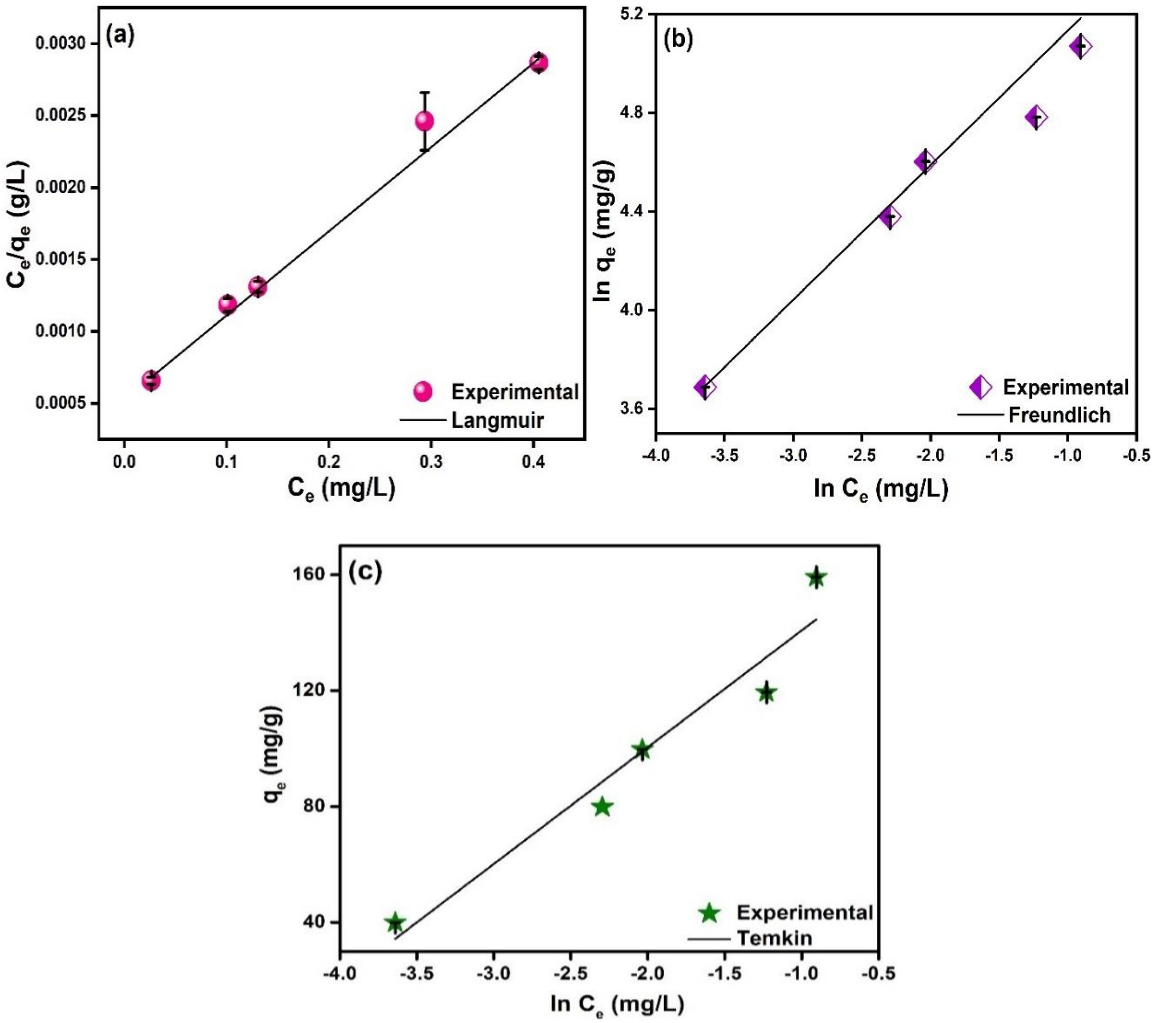

Figure 2.7 Linear plots for (a) Langmuir (b) Freundlich and (c) Temkin isotherms.

Based on the linear fit of experimental data, isotherm parameters and R^2 values are presented in Table 2.6 and plots are presented in Figure 2.7. LI model showed the maximum value of determination coefficient (R^2) among all the isotherms studied,

denoting that the adsorbent molecules are adsorbed homogeneously on the surface of Zn/Cu LDH in a monolayer arrangement. In addition, the value of maximum adsorption capacity was calculated to be 167.22 mg/g. Additionally, R_L values evaluated in this study range from 0 to 1, suggesting a favorable process for dye adsorption over Zn/Cu LDH.

Table 2.6 Equilibrium constants for CR dye removal.

Equilibrium isotherms	**Plot**	**Slope and intercept**	**Parameters**	
Langmuir	C_e/q_e vs	Slope = $1/q_{max}$	q_{max} (mg/g)	167.22
$\frac{C_e}{q_e} = \frac{1}{q_{max}K_L} + \frac{C_e}{q_{max}}$	C_e	Intercept =	K_L (L/mg)	11.96
		$1/(K_L q_{max})$	R^2	0.9965
Freundlich	ln q_e vs	Slope = 1/n	K_F (mg/g)	292.54
$\ln q_e = \ln K_F + \frac{1}{n}\ln C_e$	ln C_e	Intercept = ln K_F	$(L/mg)^{1/n}$	0.55
			1/n	0.9913
			R^2	
Temkin	q_e vs ln	Slope = B	B (J/mol)	40.29
$q_e = B \ln A_T + B \ln C_e$	C_e	Intercept = B ln	A_T (L/g)	89.38
		A_T	R^2	0.9208

2.3.2.6 Adsorption kinetics

Kinetic studies were performed using Zn/Cu LDH (dose = 0.01 g at solution pH 7.0) with 50 ppm initial CR concentration. Following adsorption, samples were taken at fixed intervals and analysed for CR dye concentration. The experimental data was fitted in linear

equations of three different kinetic models. The reversible equilibrium between adsorbent and adsorbate phases is expressed by the first model, i.e., pseudo-first-order (PFO) model (Eq. 2.11). The pseudo-second-order kinetics (PSO) (Eq. 2.12) presumes that the chemical adsorption is the rate limiting step of adsorption process. As a result of assumption of exponential growth of adsorption sites, the Elovich model (Eq. 2.13) indicates multilayer sorption [27].

$$\ln(q_e - q_t) = \ln q_e - K_1 t \tag{2.11}$$

$$\frac{t}{q_t} = \frac{1}{K_2 q_e^{\,2}} + \frac{t}{q_e} \tag{2.12}$$

$$q_t = \beta(\ln \alpha\beta) + \beta \ln t \tag{2.13}$$

Where q_e and q_t (mg/g) are denoted as adsorption capacity at equilibrium and time t respectively. The PFO and PSO rate constants are denoted by K_1 (min^{-1}) and K_2 (g mg^{-1} min^{-1}), respectively. β (mg/g min) is desorption constant and α (mg/g min) is the adsorption rate at initial stage.

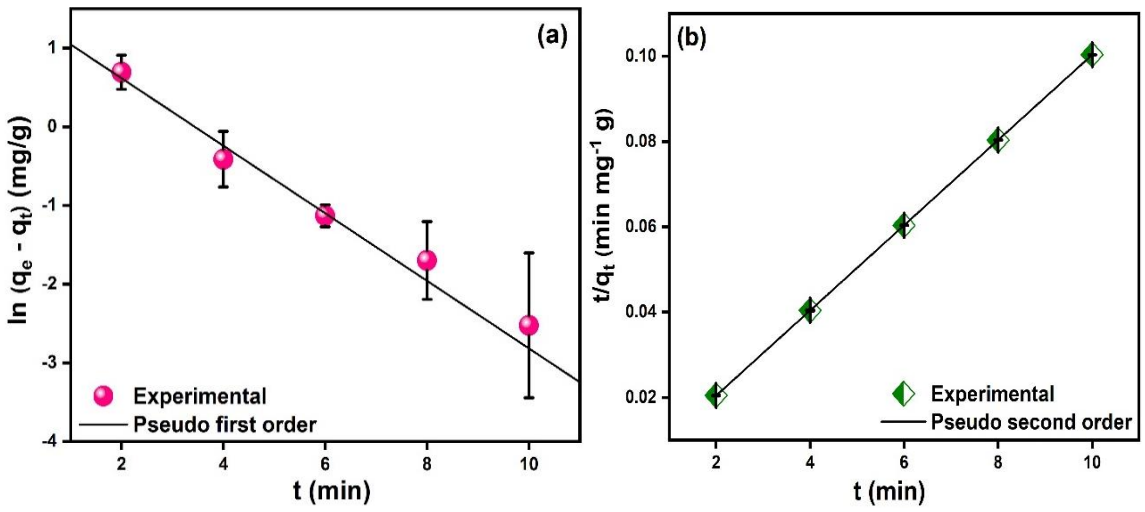

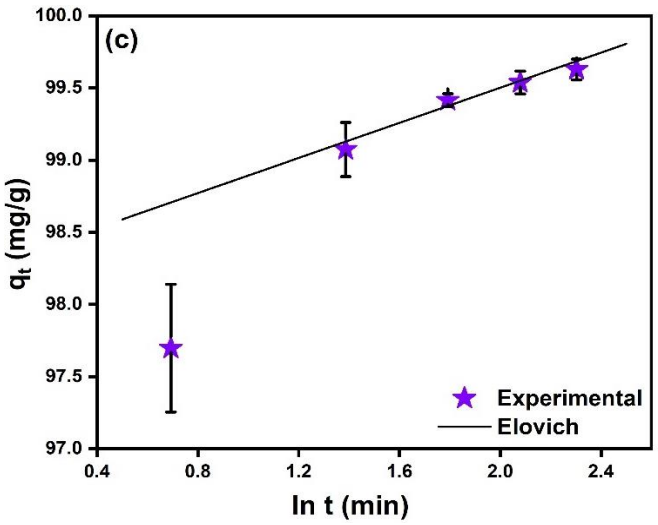

Figure 2.8 The linear plots of (a) PFO (b) PSO and (c) Elovich models.

Table 2.7 Kinetic parametric values for CR dye uptake.

Kinetic models	**Plot**	**Slope and intercept**	**Parameters**	
Pseudo-first order	ln (q_e-q_t)	Slope = -K_1	K_1 (min^{-1})	0.43
$\ln(q_e - q_t) = \ln q_e - K_1 t$	vs t	Intercept = ln q_e	q_e (mg/g)	4.37
			R^2	0.9826
Pseudo-second order	t/q_t vs t	Slope = $1/q_e$	K_2 (g mg^{-1}	0.24
$\frac{t}{q_t} = \frac{1}{K_2 q_e^{\,2}} + \frac{t}{q_e}$		Intercept = $1/(K_2 q_e^2)$	min^{-1})	101.01
			q_e (mg/g)	1.0
			R^2	
Elovich model	q_t vs ln t	Slope = β	α (mg g^{-1}	2.42
$q_t = \beta(\ln \alpha\beta) + \beta \ln t$		Intercept = β (ln αβ)	min^{-1})	0.61
			β (g mg^{-1})	0.6756
			R^2	
Experimental value	-	-	q_{exp} (mg/g)	99.72

The linear plots of models employed are illustrated in Figure 2.8 and the linear regressions and kinetic parameters of the models are summarized in Table 2.7. It is apparent from the

data obtained that the PSO model has the maximum determination coefficient value (almost equal to 1) and also the calculated value of adsorption capacity (101.01 mg/g) is in accordance with the experimentally obtained value (99.72 mg/g). Whereas a significant deviation in q_e and q_{exp} can be observed for PFO model. Thus, confirming the appropriateness of PSO model to fit the kinetic data and inferring that the CR dye adsorption onto Zn/Cu LDH is chemisorption process.

2.3.2.7 Thermodynamic studies

The synthesized lattice was used as an adsorbent to study CR adsorption at 303.15, 313.25, and 323.15 K temperatures. The thermodynamic parameters, i.e., enthalpy, entropy, and free energy were estimated from the following equations:

$$\ln K = -\frac{\Delta H^0}{RT} + \frac{\Delta S^0}{R} \quad (2.14)$$

$$K = \frac{q_e}{C_e} \quad (2.15)$$

$$\Delta G^0 = \Delta H^o - T\Delta S^0 \quad (2.16)$$

Where, K, R, C_e, T, and q_e, are the equilibrium constant, gas constant (8.314 J K^{-1} mol^{-1}), concentration of dye at equilibrium, temperature (K), and adsorption capacity (mg/g), respectively. ΔS°, ΔH°, and ΔG° are change in entropy (J/mol/K), enthalpy (kJ/mol), and Gibbs free energy (kJ/mol) respectively (the values are given in Table 2.8).

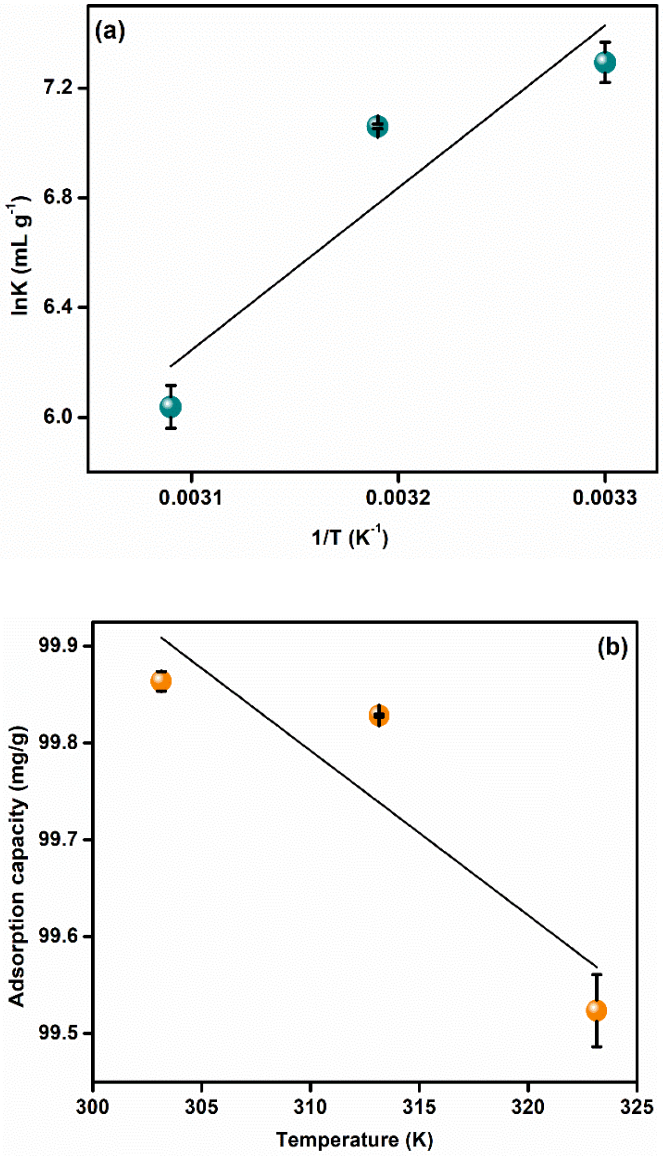

Figure 2.9 (a) Van't Hoff plot for ln K vs 1/T and (b) plot of effect of temperature on adsorption capacity.

Van't Hoff plot was used to calculate the value of enthalpy and entropy, whereas ΔG° was calculated using Eq. 2.16. According to the results, with increasing solution temperature, the adsorption capacity decreases owing to the weakening of adsorbent-adsorbate adsorptive forces [28]. It can also be stated that with an increase in temperature the equilibrium shifts in the backward direction resulting in the release of adsorbed ions at

higher temperatures (Figure 2.9). As a result of a negative enthalpy change, the adsorption is exothermic in nature. In addition, the entropy change was also negative thus, attributing to a decrease in the degree of randomness of adsorbed species. The negative value of free energy indicated that sorption process is feasible and spontaneous.

Table 2.8 Thermodynamic parametric values for CR uptake.

Temperature (K)	qe (mg/g)	ΔS° (J/mol/K)	ΔH° (KJ/mol)	ΔG° (KJ/mol)
303.15	99.87	-100.50	-49.16	-18.70
313.15	99.83			-17.69
323.15	99.52			-16.68

2.3.3 Different adsorbents for CR uptake

The study also compared the optimized conditions and removal efficiency of some of the newly reported sorbents for the removal of CR with Zn/Cu LDH (Table 2.9). The results showed the absorbent used in the present study was highly effective at removing CR dye in a very short timeframe, compared to other adsorbents reported. In addition to its excellent porous structure, it contains positively charged metal hydroxide sheets, which contributes to its high adsorption capacity toward anionic CR dye.

Table 2.9 Different sorbents reported for uptake of CR dye.

Adsorbent	Removal percentage (%)	Adsorption capacity (mg/g)	Contact time (min)	pH	References
MWCNTs	92	352.11	60	11	[29]

*p*TSA-Pani@GO-CNT	-	26.8	300	5	[30]
Chitosan hydrogel beads impregnated with CNT	-	450.4	360	5	[31]
ILNO-NH_2	97	43.10	30	4	[32]
Zeolite/algae composite (ZPG)	78.89	11.26	480	7	[33]
Fly ash	-	22.12	180	Natural pH of dye	[6]
Cashew net shell	98.52	5.184	120	2	[34]
Cu-Ca-Al-LDH/gellan gum nanocomposite	-	100	60	5	[35]
Acetate intercalated Zn/Cu LDH	**>99**	**167.22**	**4**	**7**	**Present work**

2.3.4 Sequestration of CR dye in real water samples

For the purpose of evaluating the real-time applicability of the synthesized material, the adsorption behavior was studied for CR dye sequestration from tap water, groundwater,

and textile water. The results obtained from real water sample analysis were then compared with that of distilled water (Figure 2.10a). The textile wastewater (obtained from Bawana Industrial Area New Delhi, India) used for analysis was first filtered to remove solid aggregates. Since native samples contained small traces of CR dye, they were spiked with a certain concentration of analyte. The trend for percentage removal of CR dye follows the order: Distilled water (98 %) > Tap water (94 %) > Groundwater (88 %) > Textile water (85 %). Thus, the synthesized layered material may be employed for environmental remediation applications in real wastewater as well as these observations support the current work more effectively than those reported in the literature.

2.3.5 Reusability of Zn/Cu LDH

A recyclability study of the adsorbent was also carried out to ensure the relevance of the system for real-time applications. For regeneration purposes, the adsorbent was collected and washed with water:ethanol mixture after adsorption, later dried in an oven to check its reusability. The removal efficiency of CR dye was estimated to be more than 85% in first three cycles and it decreased up to 70 % in the fourth cycle (Figure 2.10b). Hence, Zn/Cu LDH was able to adsorb effectively and could be reused multiple times.

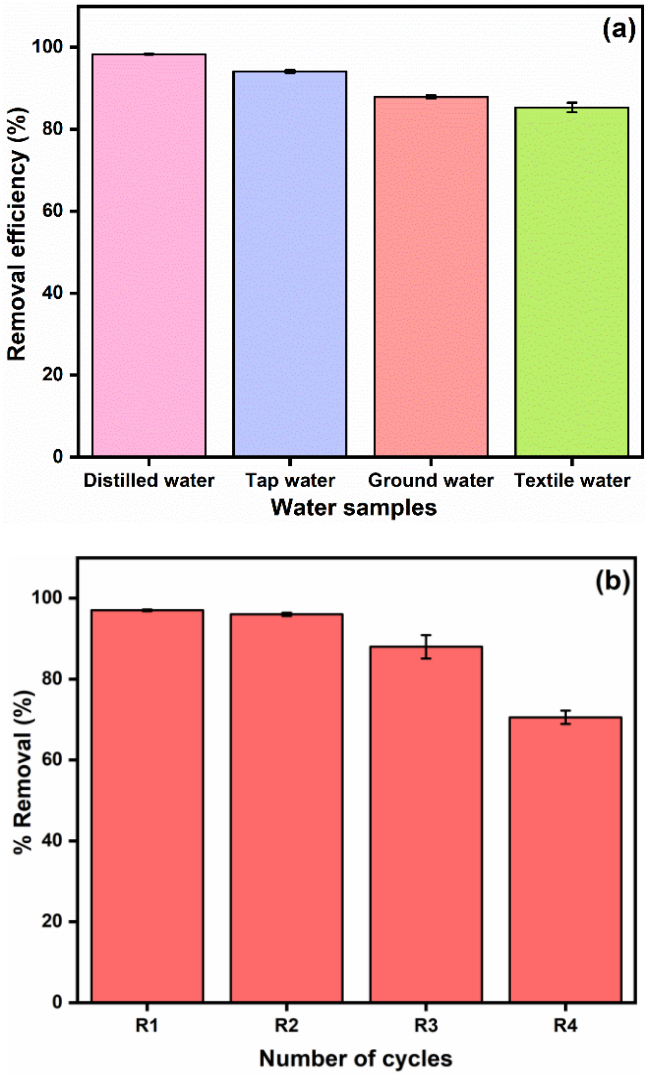

Figure 2.10 Plot of (a) percentage removal of CR dye in different water samples and (b) reusability of adsorbent up to 4 cycles.

2.3.6 Adsorption mechanism

The adsorption of toxic organic pollutants by LDHs mainly follows interlayer anion exchange, electrostatic interaction, and surface complexation [36]. The mechanistic aspects of anionic dye adsorption onto the synthesized sorbent can be elucidated from the results of zeta potential, FTIR, and PXRD analysis.

One of the significant factors affecting the adsorbent-pollutant interaction is the surface charge of the sorbent which can be determined using zeta potential [37]. The Zn/Cu LDH possesses a net positive surface charge of 30.1 mV and 10.5 mV before and after the CR dye uptake, respectively. The net positive charge of the material was found to decrease with the adsorption of anionic dye molecules. These results indicated that there occurred an electrostatic attractive interaction among positively charged layered material and anionic dye molecules. Thus, the material can act as a potential sorbent for anionic dyes.

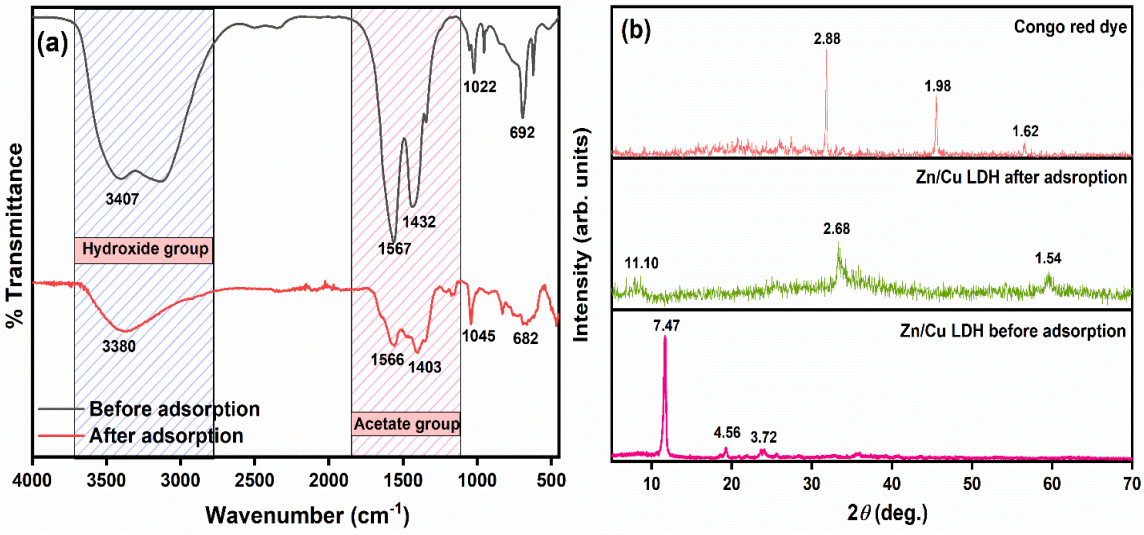

Figure 2.11 Comparative plots of adsorbent before and after sorption (a) FTIR and (b) PXRD.

An analysis of the FTIR spectra (Figure 2.11a) of the adsorbent before and after sorption depicted a notable decrease in the intensity of prominent bands along with the shifting of bands to a lower wavenumber value suggesting the occurrence of chemical interactions between CR dye and the adsorbent. The shift in hydroxide bands towards lower wavenumber, i.e., from 3407 to 3380 cm^{-1} can be ascribed to the H-bonding between -OH groups of Zn/Cu LDH and nitrogen/oxygen-containing groups of dye. Furthermore, the

decrease in intensity of the strong absorption band of acetate ions was observed which may be due to the exchange of interlayer acetate ions with that of the dye molecules [38].

The PXRD of synthesized adsorbent was recorded before and after adsorption of CR dye to examine the textural changes in the lattice after dye adsorption. The PXRD results obtained for the same are shown in Figure 2.11b with corresponding *d*-spacing values. The sample after the adsorption of CR dye shows a significant change in the PXRD pattern in which the sharp and intense reflection at 2θ value, i.e., 11.98° shifted to a lower 2θ value of 7.99° that maybe due to the strong chemical interactions existing in between dye molecules and the adsorbent as evident from the FTIR results [39,40]. In addition, no characteristic peaks of pure LDH and CR dye were observed in the PXRD pattern. Therefore, CR dye adsorption is governed by electrostatic interaction and anion exchange mechanisms, based on the above inferences.

2.4 Conclusion

In the present work, a facile and efficient method has been adopted for the fabrication of novel Zn/Cu LDH which overcomes the limitations posed by conventionally used methods including usage of extreme reaction conditions and toxic precursors which serve as a hindrance in the economical synthesis of LDHs. The study summarizes a comprehensive study of experimental and statistical results for the uptake of organic dyes in synthetic and real wastewater. RSM-CCD methodology was employed to predict the optimum parameters and conditions for removing CR dye. The outcomes of ANOVA established that modified quadratic model was considerable for removal of CR dye. Under the optimum conditions, i.e., 50 mg/L dye concentration, pH 7, and 0.01 g adsorbent dosage

within 4 minutes, the dye removal efficiency was maximum (99.91 %). Batch experiments have shown that CR adsorption onto Zn/Cu LDH followed Langmuir isotherm with 167.22 mg/g of maximum adsorption capacity and fitted well with PSO kinetic model. The reusability study suggested that adsorbent's efficiency was not significantly affected even after 3 cycles of adsorption and >85 % of CR was removed when tested on environmental water samples (tap water and groundwater). In conclusion, Zn/Cu LDH demonstrated efficiency and practicability in removing CR under optimized process conditions by CCD/RSM model.

2.5 References

[1] Wang Z, Fang P, Kumar P, Wang W, Liu B, Li J. Controlled growth of LDH films with enhanced photocatalytic activity in a mixed wastewater treatment. Nanomaterials 2019;9:807. https://doi.org/10.3390/nano9060807.

[2] Liu L, Hu X, Zeng HY, Yi MY, Shen SG, Xu S, et al. Preparation of NiCoFe-hydroxide/polyaniline composite for enhanced-performance supercapacitors. J Mater Sci Technol 2019;35:1691–9. https://doi.org/10.1016/j.jmst.2019.04.003.

[3] Kuthati Y, Kankala RK, Lee CH. Layered double hydroxide nanoparticles for biomedical applications: Current status and recent prospects. Appl Clay Sci 2015;112–113:100–16. https://doi.org/10.1016/j.clay.2015.04.018.

[4] Sharma R, Bhawna, Kumar S, Singh P, Gupta A, Kumar V. Layered Double Hydroxide Nanomaterials: Biomedical Applications, Current Status and Challenges. Nano Life 2021;11:2130008. https://doi.org/10.1142/s1793984421300089.

[5] Shfieizadeh S, Bayati B, Silva-Martínez S, Mansouri M, Aghaeinejad-Meybodi A.

Experimental and modeling study of dye removal by photocatalysis with chitin-stabilized TiO2/ZnO nanocomposite. Int J Environ Sci Technol 2022;19:7321–36. https://doi.org/10.1007/s13762-021-03638-y.

[6] Harja M, Buema G, Bucur D. Recent advances in removal of Congo Red dye by adsorption using an industrial waste. Sci Rep 2022;12:1–18. https://doi.org/10.1038/s41598-022-10093-3.

[7] Yaseen DA, Scholz M. Textile dye wastewater characteristics and constituents of synthetic effluents: a critical review. Int J Environ Sci Technol 2019;16:1193–226. https://doi.org/10.1007/s13762-018-2130-z.

[8] Mahmoodi NM. Synthesis of magnetic carbon nanotube and photocatalytic dye degradation ability. Environ Monit Assess 2014;186:5595–604. https://doi.org/10.1007/s10661-014-3805-7.

[9] Pandey B, Singh P, Kumar V. Photocatalytic-sorption processes for the removal of pollutants from wastewater using polymer metal oxide nanocomposites and associated environmental risks. Environ Nanotechnology, Monit Manag 2021;16:100596. https://doi.org/10.1016/j.enmm.2021.100596.

[10] Mahmoodi NM, Arami M, Limaee NY, Gharanjig K, Nourmohammadian F. Nanophotocatalysis using immobilized titanium dioxide nanoparticle. Degradation and mineralization of water containing organic pollutant: Case study of Butachlor. Mater Res Bull 2007;42:797–806. https://doi.org/10.1016/j.materresbull.2006.08.031.

[11] Deb A, Kanmani M, Debnath A, Bhowmik KL, Saha B. Ultrasonic assisted

enhanced adsorption of methyl orange dye onto polyaniline impregnated zinc oxide nanoparticles: Kinetic, isotherm and optimization of process parameters. Ultrason Sonochem 2019;54:290–301. https://doi.org/10.1016/j.ultsonch.2019.01.028.

[12] Pandey N, Shukla SK, Singh NB. Water purification by polymer nanocomposites: an overview. Nanocomposites 2017;3:47–66. https://doi.org/10.1080/20550324.2017.1329983.

[13] Crini G. Non-conventional low-cost adsorbents for dye removal: A review. Bioresour Technol 2006;97:1061–85. https://doi.org/10.1016/j.biortech.2005.05.001.

[14] Mahmoodi NM, Hayati B, Arami M, Mazaheri F. Single and binary system dye removal from colored textile wastewater by a dendrimer as a polymeric nanoarchitecture: Equilibrium and kinetics. J Chem Eng Data 2010;55:4660–8. https://doi.org/10.1021/je100248m.

[15] Yang Z, Wang F, Zhang C, Zeng G, Tan X, Yu Z, et al. Utilization of LDH-based materials as potential adsorbents and photocatalysts for the decontamination of dyes wastewater: A review. RSC Adv 2016;6:79415–36. https://doi.org/10.1039/c6ra12727d.

[16] Zhang S, Chen Y, Li J, Li Y, Song W, Li X, et al. Highly efficient removal of aqueous Cu(II) and Cd(II) by hydrothermal synthesized CaAl-layered double hydroxide. Colloids Surfaces A Physicochem Eng Asp 2022;641:128584. https://doi.org/10.1016/j.colsurfa.2022.128584.

[17] Karimifard S, Reza M, Moghaddam A. Application of response surface

methodology in physicochemical removal of dyes from wastewater : A critical review. Sci Total Environ 2018;640–641:772–97. https://doi.org/10.1016/j.scitotenv.2018.05.355.

[18] Gadekar MR, Ahammed MM. Modelling dye removal by adsorption onto water treatment residuals using combined response surface methodology-arti fi cial neural network approach. J Environ Manage 2019;231:241–8. https://doi.org/10.1016/j.jenvman.2018.10.017.

[19] Rao R, Tanzi M, Tavakkoli M, Sahu JN. Optimization and modeling of methyl orange adsorption onto polyaniline nano-adsorbent through response surface methodology and di ff erential evolution embedded neural network. J Environ Manage 2018;223:517–29. https://doi.org/10.1016/j.jenvman.2018.06.027.

[20] Wang C, Zhang X, Xu Z, Sun X, Ma Y. Ethylene Glycol-Intercalated Cobalt Nickel Layered Double Hydroxide Nanosheet Assemblies with Ultrahigh Specific Capacitance : Structural Design and Green Synthesis for Advanced Electrochemical Storage Ethylene Hydroxide Nanosheet Cobalt Nickel with Layer. Appl Mater Interfaces 2015;7:19601–10. https://doi.org/10.1021/acsami.5b03176.

[21] Manohara G V., Vishnu Kamath P, Milius W. Reversible hydration and aqueous exfoliation of the acetate-intercalated layered double hydroxide of Ni and Al: Observation of an ordered interstratified phase. J Solid State Chem 2012;196:356–61. https://doi.org/10.1016/j.jssc.2012.06.017.

[22] Meenakshi P, Sitharaman U, Rajamani N. Facile synthesis and characterization of acetate intercalated Co-La layered double hydroxide. J Rare Earths 2017;35:474–9.

https://doi.org/10.1016/S1002-0721(17)60936-0.

[23] Abrantes Leal D, Wypych F, Bruno Marino CE. Zinc-Layered Hydroxide Salt Intercalated with Molybdate Anions as a New Smart Nanocontainer for Active Corrosion Protection of Carbon Steel. ACS Appl Mater Interfaces 2020;12:19823–33. https://doi.org/10.1021/acsami.0c02378.

[24] Rathee G, Awasthi A, Sood D, Tomar R, Tomar V, Chandra R. A new biocompatible ternary Layered Double Hydroxide Adsorbent for ultrafast removal of anionic organic dyes. Sci Rep 2019;9:1–14. https://doi.org/10.1038/s41598-019-52849-4.

[25] Singh P, Nagarajan R. Synthesis and characterization of hydrotalcite type structure containing Zn^{2+} and La^{3+}-ions. Mater Lett 2015;159:58–60. https://doi.org/10.1016/j.matlet.2015.06.071.

[26] Kaur Y, Jasrotia T, Kumar R, Ram G, Chaudhary S. Adsorptive removal of eriochrome black T (EBT) dye by using surface active low cost zinc oxide nanoparticles : A comparative overview. Chemosphere 2021;278:130366. https://doi.org/10.1016/j.chemosphere.2021.130366.

[27] Ni ZM, Xia SJ, Wang LG, Xing FF, Pan GX. Treatment of methyl orange by calcined layered double hydroxides in aqueous solution: Adsorption property and kinetic studies. J Colloid Interface Sci 2007;316:284–91. https://doi.org/10.1016/j.jcis.2007.07.045.

[28] Sheela T, Nayaka YA, Viswanatha R, Basavanna S, Venkatesha TG. Kinetics and thermodynamics studies on the adsorption of Zn(II), Cd(II) and Hg(II) from aqueous

solution using zinc oxide nanoparticles. Powder Technol 2012;217:163–70. https://doi.org/10.1016/j.powtec.2011.10.023.

[29] Zare K, Sadegh H, Shahryari-ghoshekandi R, Maazinejad B, Ali V. Enhanced removal of toxic Congo red dye using multi walled carbon nanotubes : Kinetic , equilibrium studies and its comparison with other adsorbents Enhanced removal of toxic Congo red dye using multi walled carbon nanotubes : Kinetic , equilibrium studie. J Mol Liq 2018;212:266–71. https://doi.org/10.1016/j.molliq.2015.09.027.

[30] Ansari MO, Kumar R, Ansari SA, Ansari SP, Barakat MA, Alshahrie A, et al. Anion selective pTSA doped polyaniline@graphene oxide-multiwalled carbon nanotube composite for Cr(VI) and Congo red adsorption. J Colloid Interface Sci 2017;496:407–15. https://doi.org/10.1016/j.jcis.2017.02.034.

[31] Chatterjee S, Lee MW, Woo SH. Adsorption of congo red by chitosan hydrogel beads impregnated with carbon nanotubes. Bioresour Technol 2010;101:1800–6. https://doi.org/10.1016/j.biortech.2009.10.051.

[32] Shojaeipoor F, Elhamifar D, Masoumi B, Elhamifar D, Barazesh B. Ionic liquid based nanoporous organosilica supported propylamine as highly efficient adsorbent for removal of congo red from aqueous solution. Arab J Chem 2019;12:4171–81. https://doi.org/10.1016/j.arabjc.2016.05.001.

[33] Dryaz AR, Shaban M, Almohamadi H, Abu KA, Ola A, Hamd A, et al. Design, characterization, and adsorption properties of Padina gymnospora / zeolite nanocomposite for Congo red dye removal from wastewater. Sci Rep 2021;11:21058. https://doi.org/10.1038/s41598-021-00025-y.

[34] Kumar PS, Ramalingam S, Senthamarai C, Niranjanaa M, Vijayalakshmi P, Sivanesan S. Adsorption of dye from aqueous solution by cashew nut shell : Studies on equilibrium isotherm , kinetics and thermodynamics of interactions. Desalination 2010;261:52–60. https://doi.org/10.1016/j.desal.2010.05.032.

[35] Shabani S, Dinari M. Itaconic acid-modified layered double hydroxidegellan gum nanocomposites for Congo red adsorption. Sci Rep 2022;12:4356. https://doi.org/https://doi.org/10.1038/s41598-022-08414-7.

[36] Li J, Yu H, Zhang X, Zhu R, Yan L. Crosslinking acrylamide with EDTA-intercalated layered double hydroxide for enhanced recovery of Cr(VI) and Congo red: Adsorptive and mechanistic study. Front Environ Sci Eng 2020;14:1–13. https://doi.org/10.1007/s11783-020-1229-x.

[37] Mahmoodi NM, Taghizadeh A, Taghizadeh M, Azimi M. Surface modified montmorillonite with cationic surfactants: Preparation, characterization, and dye adsorption from aqueous solution. J Environ Chem Eng 2019;7:103243. https://doi.org/10.1016/j.jece.2019.103243.

[38] Ling F, Fang L, Lu Y, Gao J, Wu F, Zhou M, et al. A novel CoFe layered double hydroxides adsorbent: High adsorption amount for methyl orange dye and fast removal of Cr(VI). Microporous Mesoporous Mater 2016;234:230–8. https://doi.org/10.1016/j.micromeso.2016.07.015.

[39] Sirajudheen P, Meenakshi S. Encapsulation of Zn–Fe layered double hydroxide on activated carbon and its litheness in tuning anionic and rhoda dyes through adsorption mechanism. Asia-Pacific J Chem Eng 2020;15:1–13.

https://doi.org/10.1002/apj.2479.

[40] Sharma P, Saikia BK, Das MR. Removal of methyl green dye molecule from aqueous system using reduced graphene oxide as an efficient adsorbent: Kinetics, isotherm and thermodynamic parameters. Colloids Surfaces A Physicochem Eng Asp 2014;457:125–33. https://doi.org/10.1016/j.colsurfa.2014.05.054.

Chapter 3 SYNTHESIS AND CHARACTERIZATION OF Zn/Cu LAYERED DOUBLE OXIDE: SMARTPHONE-BASED AND SPECTROPHOTOMETRIC DETECTION OF ULTRASOUND ASSISTED UPTAKE OF MALACHITE GREEN

3.1 Introduction

Natural water resources are indispensable to humans, plants, and animals; therefore, contaminating water with chemicals and other toxic species is a significant issue that must be addressed immediately [1]. Different industries discharge toxic dyes into water that are highly carcinogenic, mutagenic, and teratogenic, posing serious health and ecological risks [2]. Most commonly utilized cationic dye in textile, lather, and paper industries is Malachite green (MG) dye. Although despite having various applications several groups have reported the toxicity of MG dye. It is extremely toxic to aquatic organisms due to its strong chelating tendency towards metal ions. Therefore, MG dye effluent must be removed or treated from aquatic stream to reduce its toxic impact on the ecosystem [3].

Till today dye effluents have been treated using a variety of wastewater treatment techniques, including coagulation, sorption, ion exchange, membrane filtration, catalysis, and photodegradation. Among all adsorption emerged out as one of the most widely applied techniques due to its high potential, cost-effectiveness, ease of operation, and eco-friendliness [4]. For carrying out water purification several sorbent materials have been used, such as activated charcoal, bio-adsorbents, silicates, polymeric adsorbents, etc [5–8]. These adsorbents, however, have limited application owing to their high cost, low adsorption efficiency, and complexity in regeneration.

The study of two-dimensional layered materials such as LDHs has recently gained increased attention as sorbent material because of its variable pore size, high surface area, tunable properties, and ability to exchange anion. The treatment of LDH at optimum temperature results in the topotactic transformation to mixed metal oxide (MMO) or layered double oxide (LDO) that can acts as efficient sorbent, catalyst, etc. [9,10].

The adsorption efficiency of LDH or LDO can be enhanced further by using sonication technique. Sonication is a method of agitating particles in a sample by applying sound energy. The process is called ultrasonication when ultrasonic frequencies are used. The phenomenon of acoustic cavitation is the driving force of the ultrasonication process where the formation and collapse of microbubbles formed near the ultrasound source intensify the mass transfer and breaks the adsorbent-adsorbate affinities [11]. Thus, the combined effect of the ultrasound-assisted adsorption process may result in shorter reaction time and improved efficiency [12].

Smartphones can be used for the colorimetric detection of organic/inorganic effluents depending upon the color received from the analyte solution. The advent of smartphones with high-resolution cameras and large storage capacities allows users to capture clear and detailed pictures. Analytical chemistry practices aim to take advantage of this IT boom to improve data collection, handling, and processing as well as make it easier and quicker without requiring sophisticated instruments and specialized knowledge [13]. An inexpensive, field-portable, and user-friendly platform based on RGB color modelling is offered in this approach for performing analytical tests, and its ease of use allows for effortless quantification of dye uptake, which has opened up new horizons for data analysis [14]. In a recent study by Bahrami *et al.* (2022) Fe-Cr LDH was employed

for mercury ions uptake and smartphone-based colorimetric method was used for the detection [15].

In the present study Zn/Cu based LDH was calcined to obtain Zn/Cu LDO for the sorptive uptake of MG dye. LDO was characterized using PXRD, FTIR, XPS, SEM/EDX, and BET techniques. The impact of various factors such as pH, time of ultrasonication, concentration of dye, and adsorption under different conditions have been studied. To propose a system that is applicable under all conditions, adsorption isotherms and kinetic models were examined. In addition, a smartphone-based detection ('Colorpicker application') of MG dye after adsorption has also been employed as an alternate method for colorimetric detection of residual concentration of MG dye.

3.2 Experimental Details

3.2.1 Chemicals and reagents

The MG dye was purchased from CDH. Accurate quantity of MG dye was dissolved in 500 mL of deionized (DI) water to prepare the stock solution of dye (100 mg L^{-1}). The details of azo dye employed in the study are given in Table 3.1.

Table 3.1 Structure and formula of MG dye.

Azo dye	Structure	λ_{max} (nm)	Molecular formula	Molecular weight
Malachite green	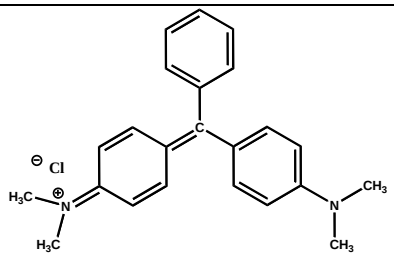	617	$C_{32}H_{22}N_6Na_2O_6S_2$	364.911 g/mol

3.2.2 Synthesis of Zn/Cu LDH and Zn/Cu LDO

Firstly Zn/Cu LDH was prepared by hydrolysis method [16]. Metal salt solutions were prepared with 0.9877 g of $Zn(CH_3COO)_2.2H_2O$ and 0.0998 g of $Cu(CH_3COO).H_2O$ in DI water. Then hydrogen peroxide solution (5 mL H_2O_2 + 30 mL DI water) was added to the metal salt solutions. The mixture was then ultrasonicated for 30 minutes and later stirred for 24 hours following drying of the product at 60℃. The prepared Zn/Cu LDH was then further calcined at 350℃ for six hours in a muffle furnace to obtain the Zn/Cu LDO.

3.2.3 Instrumentation

A Bruker D8 advance diffractometer operating at Cu K radiations at a step size of 0.02° was used in the $2\theta =$ 5-70° range to record PXRD patterns. PerkinElmer spectrometer was used to analyze the sample (version 10.5.3). N_2 adsorption-desorption isotherm was measured using a Quantachrome USA, Novatouch LX^4 to determine the Brunauer-Emmett-Teller (BET) surface area at 77 K. A Zeiss GeminiSEM was used for FE-SEM with EDX analysis of Zn/Cu LDO. XPS measurements were recorded with Al Kα photoelectron excitation using a PHI 5000 VersaProbe III.

3.2.4 Ultrasound-assisted adsorption studies

The experiments were performed in batch mode in an ultrasonic bath where a fixed amount of Zn/Cu LDO was added to different initial concentrations of MG dye (in 50 mL) solution for 30 minutes. Following adsorption and centrifugation for 10 minutes the remaining concentration of MG dye was determined using UV-visible spectrophotometer, Cary Series

(Cary 300). The λ_{max} of MG was chosen at 617 nm and the removal efficiency and adsorption capacities were estimated using following equations:

$$\text{Removal efficiency } (\%) = \frac{Co\text{-}Ce}{Co} \times 100\ \% \quad (3.1)$$

$$q_e = \frac{C_o\text{-}C_e}{W} \times V \quad (3.2)$$

$$q_t = \frac{C_o\text{-}C_t}{W} \times V \quad (3.3)$$

Where C_o, C_e and C_t are dye concentrations at initial, equilibrium, and final stage, respectively. q_e and q_t are the adsorption capacities and equilibrium and time t, respectively. V and w are volume of solution and amount of the adsorbent, respectively.

3.3 Results and Discussion

3.3.1 Structural and morphological properties of LDO

The PXRD patterns of both Zn/Cu LDH and Zn/Cu LDO are shown in Figure 3.1a. The formation of LDH was established by the presence of a sharp intense peak at 2θ value of 11.96°, ascribed to (002) reflection, indicating acetate intercalation in interlayer region. However, upon calcination at 350°C, the (002) reflection of LDH disappeared in the PXRD pattern of LDO as a result of the dehydroxylation/decomposition of interlayer acetate ions. From the PXRD pattern of Zn/Cu LDO was found to be similar to that of pure zinc oxide. The characteristic peaks of Zn/Cu LDO were observed at 31.99°, 34.64°, and 36.43° with a slight shift to lower angles from that of pure ZnO.

The FTIR spectra of Zn/Cu LDH and LDO (Figure 3.1b) demonstrated the disappearance of characteristic peaks of interlayer acetate ion on calcination. The spectra of LDH and LDO exhibit a broad band at 3418 and 3382 cm^{-1} corresponding to the presence of -OH

groups. The peaks in the range of 600-400 cm^{-1} can be assigned to the metal oxygen (M-O and M-O-H) linkages present in the lattices. In addition, the disappearance of a broad band around 3000 cm^{-1} due to the hydrogen bonding in LDH also corresponds to the removal of acetate ions confirming formation of LDO.

To determine the morphology and composition of LDO, SEM/EDX analysis was performed (Figure 3.1c-e). On calcination the plate-like structure of parent LDH transformed into smaller particles. The average particle size was also calculated from SEM image and was found to be 58 nm. The EDX analysis demonstrated the uniform or homogeneous distribution of zinc, copper, and oxygen elements.

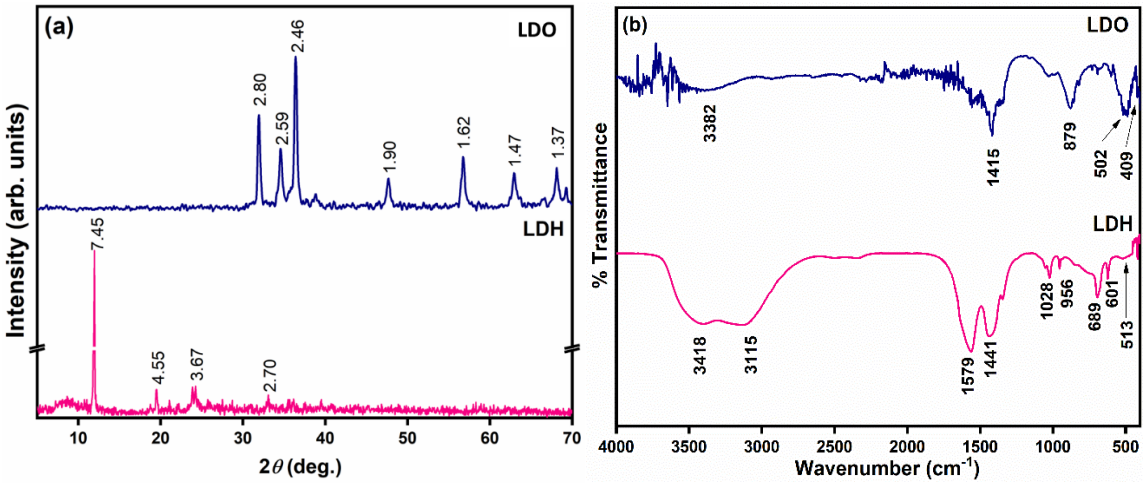

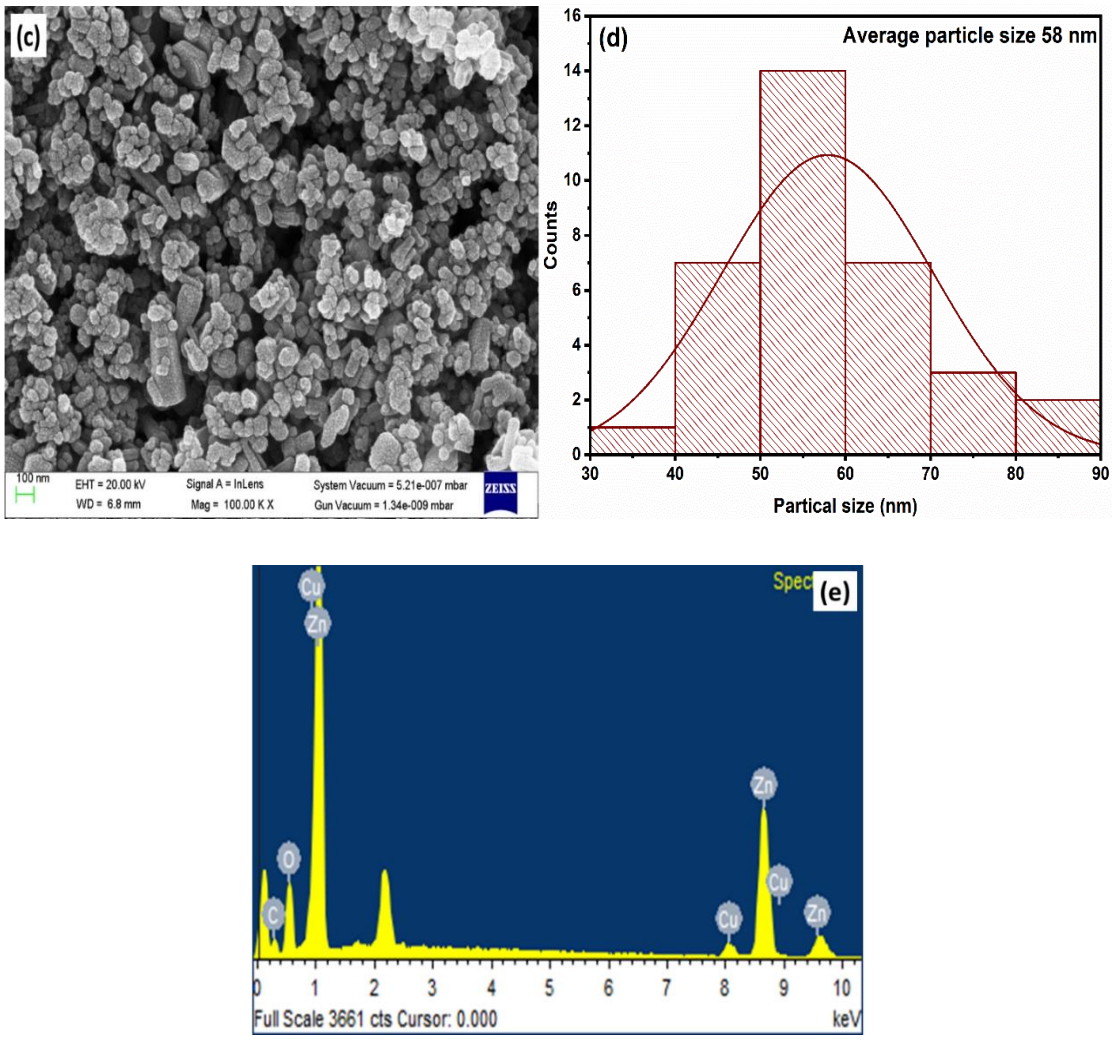

Figure 3.1 (a) PXRD pattern, (b) FTIR spectra of LDH and LDO, (c) SEM image, (d) average particle size distribution histogram, and (e) EDX plot of Zn/Cu LDO.

The BET surface area analysis was utilized to assess the size and pore volume of the adsorbent, as well as its specific surface area. The data for surface properties of prepared LDO in comparison with parent LDH are given in Table 3.2 [17]. In accordance with the IUPAC classification system, the nitrogen adsorption-desorption isotherm falls under type IV category with H_4 hysteresis loop (Figure 3.2a), which indicates microporous nature of material. Pore volumes of Zn/Cu LDO (0.122 cm^3/g) are greater than that of pristine LDH (0.030 cm^3/g), suggesting the collapse of layered arrangement after calcination (Figure

3.2b). Moreover, the removal of acetate ions and H_2O molecules from the interlamellar region resulted in an increased surface of LDO in comparison with LDH. It can also be summarized that the presence of interlayer anion in LDH resulted in smaller pore volume and larger diameter, respectively than that of Zn/Cu LDO [18].

Table 3.2 Surface properties of synthesized adsorbent.

Adsorbent	BET surface area (m^2/g)	Pore diameter (nm)	Pore volume (cm^3/g)
Zn/Cu LDH	61.841	3.658	0.030
Zn/Cu LDO	84.217	1.171	0.122

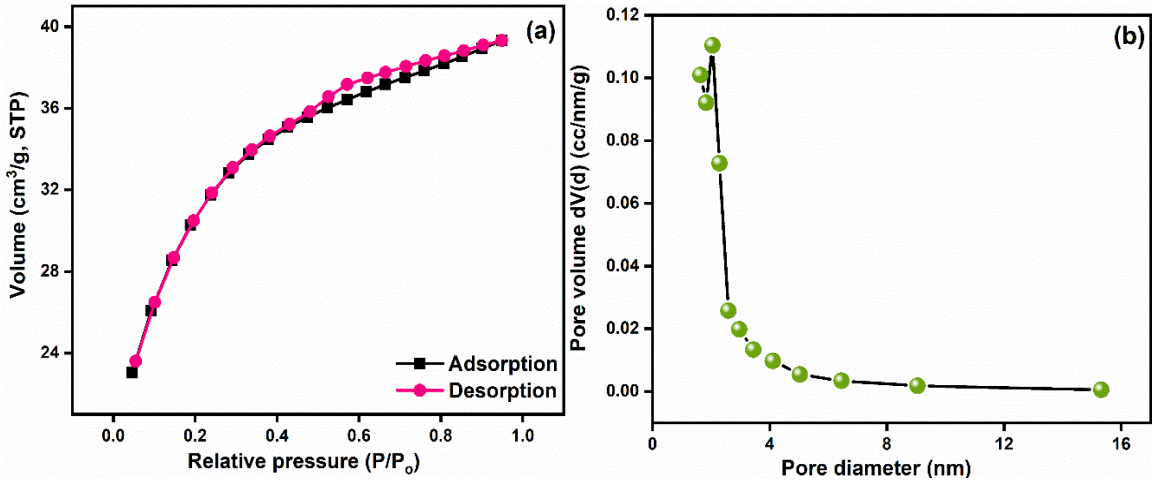

Figure 3.2 (a) N_2 adsorption-desorption isotherm and (b) pore size distribution plot of Zn/Cu LDO.

3.3.2 Adsorptive removal of Malachite green dye

3.3.2.1 Effect of contact time

Figure 3.3a-b represent the impact of sonication time on the removal efficiency of synthesized sorbent at 30 mg/L concentration of MG dye and 0.2 g/L of adsorbent dosage. A significant and sharp increase in the removal efficiency can be observed in the initial 5 minutes of ultrasonic irradiation, i.e., reaching >85% after which equilibrium was achieved gradually. Consequently, of the adsorbent's large surface area and active sites, it exhibits a high initial adsorption rate. In addition, a large amount of mass is transferred from the adsorbate to the adsorbent during sonication which contributes to the high MG adsorption.

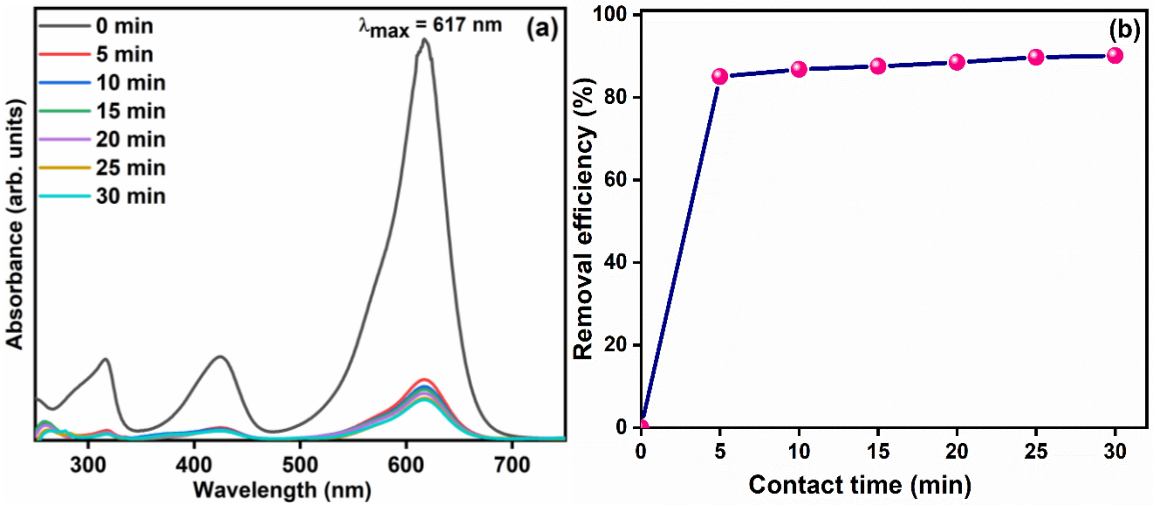

Figure 3.3 (a) Wavelength vs absorbance and (b) contact time vs percent dye removal plots.

3.3.2.2 Effect of concentration of MG

Experiments were performed with different initial MG concentrations in order to assess the influence of the dye concentration on the removal efficiency of the Zn/Cu LDO (Figure 3.4a). A fixed amount of adsorbent was added to different initial concentrations of MG dye

(5-30 mg/L) solutions and ultrasonically treated for 30 minutes. According to the findings of the study, a higher initial dye concentration resulted in increased adsorption of MG dye at equilibrium. When concentrations are high, molecular collisions are more likely to occur with adsorbent surfaces, leading to greater transfer of masses from solution to solid. In response to increasing collisions, molecules are removed from the solution phase at a faster rate.

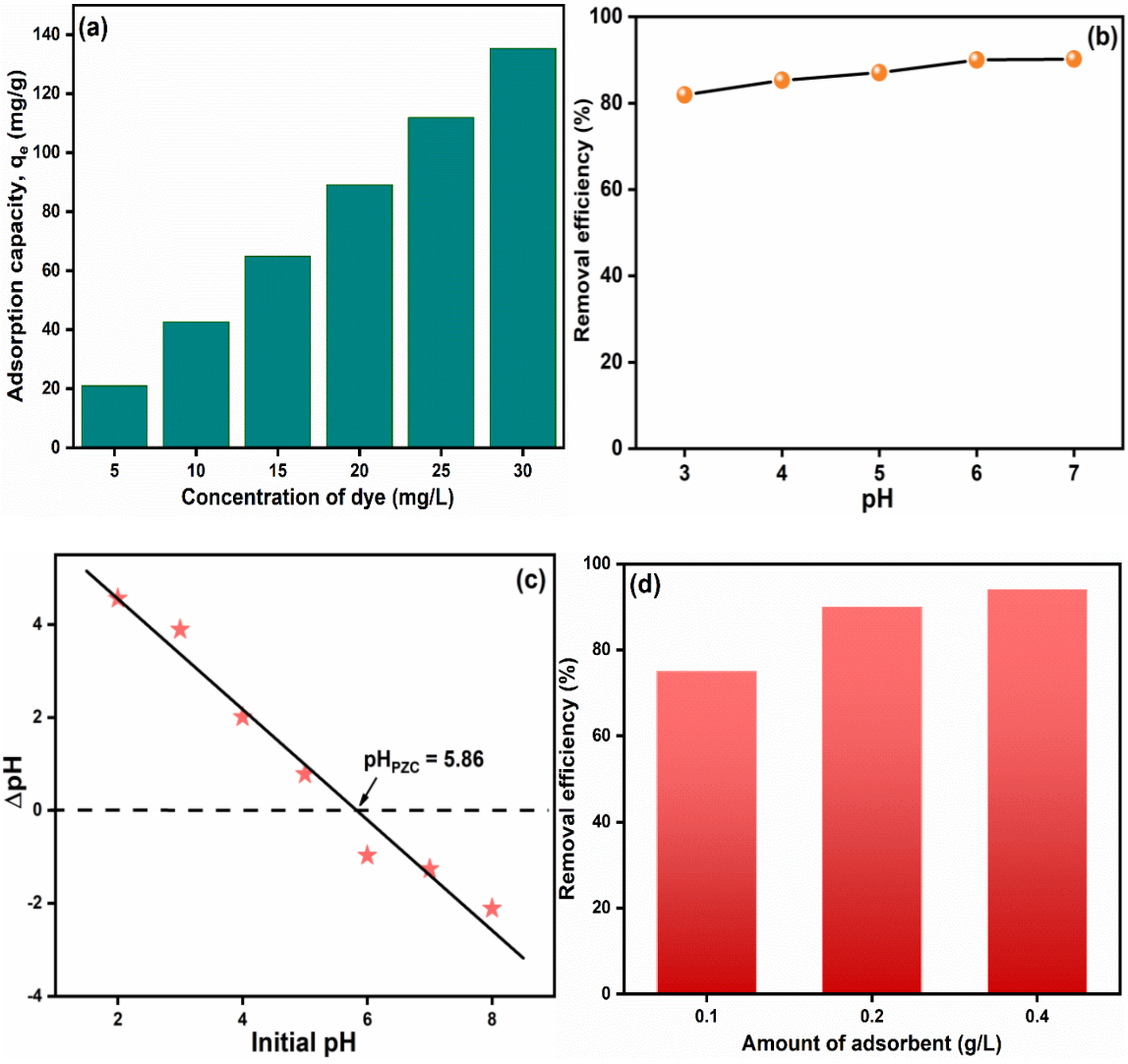

Figure 3.4 Plot of (a) concentration variation of MG dye vs adsorption capacity, (b) % removal vs pH of dye solution, (c) pHpzc vs ΔpH, and (d) effect of adsorbent dosage of MG dye sequestration.

3.3.2.3 Effect of pH and pH_{PZC} determination

The sorption of effluents from the aqueous phase is strongly affected by pH of solution because it influences surface charge of adsorbent. It is noteworthy that the detection of MG dye is difficult above pH 8 due to the interaction of hydroxy ions and cationic dye molecules leading to the precipitation of MG, which discolors the dye solution [19]. In addition, MG dye is unstable and decolorizes at high pH therefore, the impact of pH on dye uptake was investigated in 3 to 7 pH range. At low pH conditions there exists higher concentration of H^+ ions which may compete with the positively charged dye molecules for the sorbent adsorption sites. Figure 3.4b depicts that dye removal efficiency increases with increase in pH values which may be ascribed to the negative surface charge of the adsorbent at high pH conditions which interact with the positive dye molecules.

The pH_{pzc} was found to be 5.86 implying that the surface of adsorbent is positive and negative below and above 5.86 pH value, respectively (Figure 3.4c). As a result, above pH 5.86 there occurs an electrostatic interaction between dye molecules (positively charged) and adsorbent surface (negatively charged). Additionally, LDO has the advantage of being able to carry out adsorption process at a pH range that is compatible with drinking water.

3.3.2.4 Effect of adsorbent dosage

Removal of contaminants from aqueous solutions is greatly influenced by the amount of the adsorbent. The MG removal efficiency increased from 74 to 90% as the dosage rate increased from 0.1 to 0.4 g L^{-1} (Figure 3.4d). Increased dosage results in a greater number of active sites for adsorption, contributing to a higher removal efficiency.

3.3.2.5 Adsorption kinetics

The adsorption kinetic study was conducted to understand possible mechanisms and predict adsorption rates. Pseudo-first-order (PFO), pseudo-second-order (PSO), and elovich models were employed to simulate the experimental kinetic factors of the adsorbent.

The general expression of the linearized form of PFO is as follows:

$$\ln(q_e - q_t) = \ln q_e - K_1 t \quad (3.4)$$

Where q_e (mg g^{-1}) and q_t (mg g^{-1}) are adsorption capacities at equilibrium and at time t, respectively and K_1 (min^{-1}) is the PFO rate constant [20].

Unlike other adsorption models, the PSO model predicts the adsorption behavior over the entire absorption range since it is based on the assumption that adsorption capacity depends on the available active sites [21]. The linearized form of PSO is expressed as:

$$\frac{t}{q_t} = \frac{1}{K_2 q_e^2} + \frac{t}{q_e} \quad (3.5)$$

Where K_2 (g mg^{-1} min^{-1}) is the second order rate constant which can be estimated from the linear plot of t/q_t vs t.

A second order kinetic equation based on adsorption capacity has been successfully described using the Elovich equation in linear form (Eq. 3.6), provided the solid surfaces are energetically heterogeneous. However, the equation does not propose a specific mechanism for the adsorbate–adsorbent interaction [22]. In general, it is widely agreed that the following semi-empirical equation can accurately describe the chemisorption process:

$$q_t = \beta (\ln \alpha\beta) + \beta \ln t \quad (3.6)$$

Where α (mg g^{-1} min^{-1}) is the adsorption rate at initial stage and β (g mg^{-1}) is desorption constant.

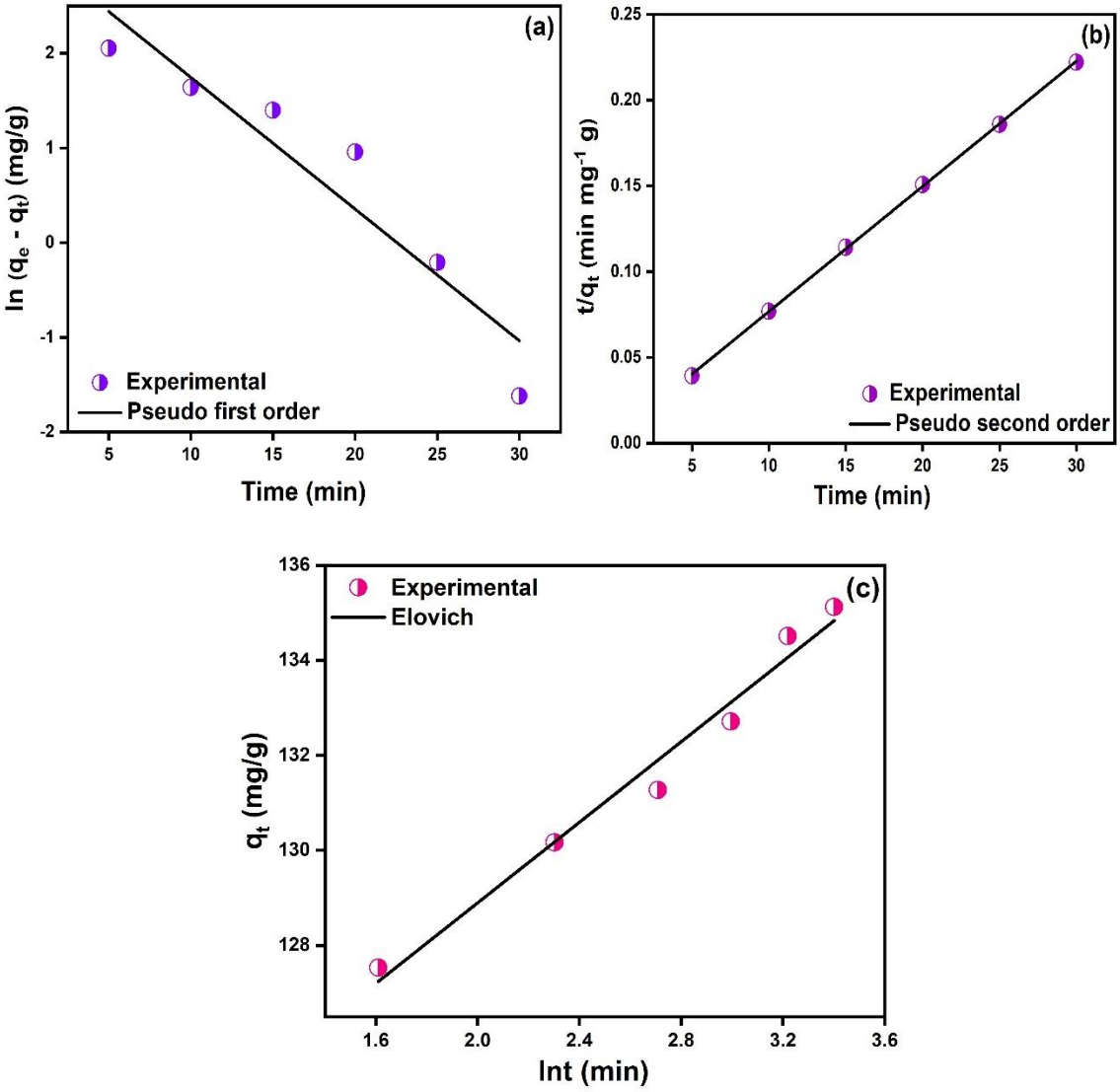

Figure 3.5 Plots of (a) PFO, (b) PSO, and (c) Elovich models.

Table 3.3 Kinetic parameters for MG dye sequestration.

Pseudo-first-order			**Pseudo-second-order**			**Elovich**		
K_1(min^{-1})	q_e (mg g^{-1})	R^2	K_2 (g mg^{-1} min^{-1})	q_e (mg g^{-1})	R^2	β (mgg^{-1}min^{-1})	α (gmg^{-1})	R^2
0.14	23.07	0.8938	0.015	136.99	0.9998	0.24	9.32	0.9771

Based on the models the kinetic parameters and correlation coefficients were calculated and are given in Table 3.3 and the plots are shown in Figure 3.5. The value of adsorption capacity calculated from the PSO kinetic model (q_e calculated) was found to be 136.99 mg/g which was in close agreement with the value obtained from UV-vis measurements (q_e experimental = 135.32 mg/g). Based on R^2 and q_e values, PSO model better explains the kinetics of adsorption, suggesting chemisorption is involved.

3.3.2.6 Adsorption isotherm

Adsorption isotherms were analyzed to determine the maximum adsorption capacity of adsorbent and to understand the nature of adsorption LI, FI, and TI were employed. First, LI was used to fit the ultrasound-assisted MG adsorption data. In the Langmuir model, adsorbent molecules are assumed to have no interaction with one another adsorption occurs in homogenous sites on the adsorbent. Furthermore, a finite amount of adsorbate can be absorbed by the adsorbent (at equilibrium) and all adsorption sites have the same energetic properties [23]. The linear form of LI is given below:

$$\frac{1}{q_e} = \frac{1}{q_m K_L C_e} + \frac{1}{q_m} \tag{3.7}$$

Where q_e (mg g^{-1}) and C_e (mg L^{-1}) are adsorption capacity and concentration of adsorbate at equilibrium. The maximum adsorption capacity is denoted by q_m (mg g^{-1}), and K_L (L mg^{-1}) is termed as Langmuir constant.

R_L is a dimensionless separation parameter that explains the main characteristics of the LI that is favorability of adsorption and is given by formula: $R_L = 1/(1 + K_L C_0)$. When the value of R_L lies in the range of 0 to 1 the process is favorable, and is unfavorable, linear, and irreversible when the value of R_L is more than 1, equal to 1 and equal to 0, respectively.

In FI, the adsorption is non-ideal and reversible and deals with multilayer adsorption on heterogeneous surfaces having distinct adsorption energies and affinities [24].

$$\ln q_e = \ln K_F + \frac{1}{n} \ln C_e \quad (3.8)$$

The Freundlich constants K_F and 1/n refer to the adsorbent's adsorption capacity and the favorability of isotherm, respectively, as follows:

$0 < 1/n < 1$ favorable

$1/n = 0$ irreversible

$1/n > 1$ unfavorable

In the Temkin isotherm model, all molecules in a layer are subjected to a linear decrease in heat of adsorption with coverage as a result of interactions between adsorbent and adsorbate molecules, and their binding energies are uniformly distributed [25].

$$q_e = B \ln K_T + B \ln C_e \quad (3.9)$$

Here K_T and B are Temkin constants termed as equilibrium binding constant (L mg^{-1}) and heat of adsorption (J mol^{-1}), respectively.

The plots for MG adsorption isotherm are given in Figure 3.6 and Table 3.4 summarizes the values of constants and correlation coefficients (R^2) obtained from different models. The Langmuir equation fitted the experimental data well, thus suggesting monolayer adsorption. It also appears that MG adsorption onto Zn/Cu LDO is a favorable process as the calculated value of R_L lies between 0 and 1, i.e., 0.1591.

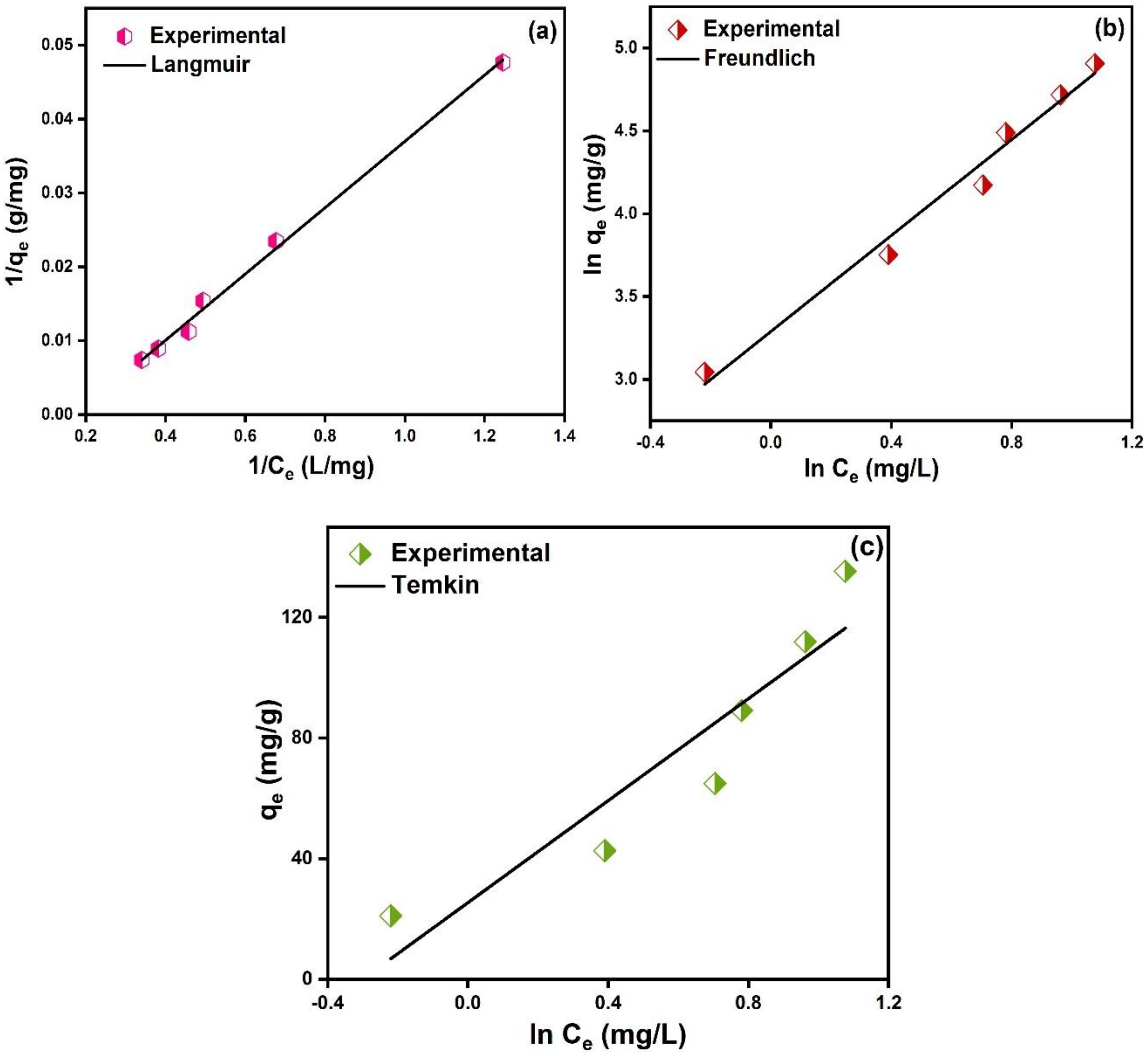

Figure 3.6 Plots of (a) Langmuir, (b) Freundlich, and (c) Temkin isotherms.

Table 3.4 Equilibrium parameters for MG dye removal.

Langmuir			**Freundlich**			**Temkin**		
K_L	q_m	R^2	K_F (g mg^{-1}	1/n	R^2	K_T (L mg^{-1})	B	R^2
(min^{-1})	(mg/g)	0.9960	min^{-1})	1.45	0.9814		84.57	0.8654
0.18	128.20		26.80			1.35		

3.3.2.7 Regeneration study

The regeneration study was performed at optimum conditions and obtained results are given in Figure 3.7a. The desorption of dye from the surface of adsorbent was carried out using 0.1M NaOH solution. As the regeneration cycle progressed, the removal efficiency decreased from 90% to 73%. The decrease in removal efficiency can be accredited to the adsorbent-adsorbate strong interactions, which results in decrease in number of active sites for adsorption after every cycle.

3.3.3 Assessment of ultrasound-assisted method for MG dye uptake

The adsorption efficiency of Zn/Cu LDO using ultrasound-assisted adsorption was compared with traditional adsorption methods such as magnetic stirring and incubator shaking (with contact time: 30 min, adsorbent dose: 10 mg, MG initial concentration: 30 mg/L). Figure 3.7b shows the percentage removal of MG with different adsorption methods. The % removal of MG in 30 minutes of reaction time followed the order: Ultrasonication (90 %) > Magnetic stirring (74 %) > Incubator shaker (64 %). Consequently, ultrasonication and sorption have synergistically reduced reaction time while enhancing dye removal efficiency as a result. Ultrasonic treatment of an adsorbent-adsorbate system enhances the surface porosity, thereby causing dye molecules to be distributed evenly inside the porous holes of the sorbent, which accelerates the mass transfer and sorption process and reduces the equilibrium time considerably.

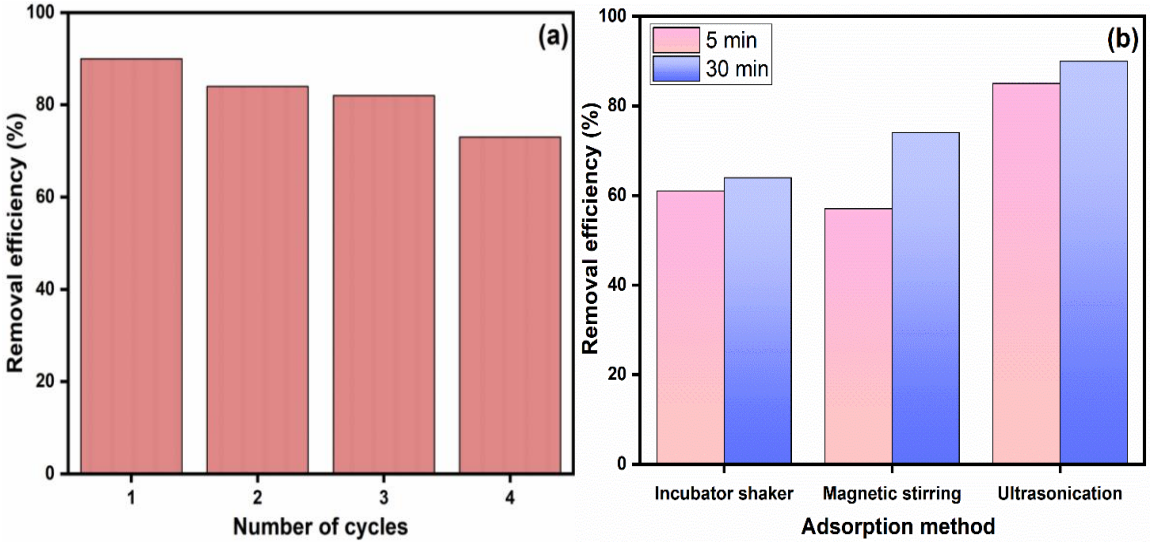

Figure 3.7 Plots of (a) Dye uptake efficiency of Zn/Cu LDO up to 4 cycles and (b) assessment of adsorption methods for MG dye uptake.

The adsorption capability of synthesized lattice was also compared with previously reported sorbents (Table 3.5). According to the proposed method, Zn/Cu LDO showed superior removal performance compared to other reported adsorbents in terms of adsorption capacity and contact time. As a consequence, the synthesized adsorbent can be used as potential material for the uptake of MG dye.

Table 3.5 Different sorbents reported in literature for MG dye uptake.

Adsorbent	**Removal percentage (%)**	**Adsorption capacity (mg/g)**	**Contact time (min)**	**pH**	**References**
Fe_3O_4@PANI	98	240	240	7	[26]
Acid treated coffee husk	96	264.81	120	6.8	[27]

GumT-cl-HEMA-TiO_2 hydrogel	99.3	103.09	110	7	[19]
Zeolitic imidazole framework-8 (ZIF-8)	95	224.14	90	7	[28]
Cu-MOFs/Fe_3O_4	90	113.67	70	-	[29]
Coal-assisted soil	> 95	89.97	60	6	[30]
Zn/Cu LDO	>90	128.20	30	7	Present work

3.3.4 Smartphone-assisted determination of percentage dye uptake

An approach based on smartphone colorimetry was utilized for the analysis of dye removal by using a simple and portable setup. The use of a smartphone to estimate dye adsorption rates using RGB (red, green, blue) color intensity is a rapid and efficient way to assess dye removal on-site [14]. Smartphones have an inbuilt camera and are capable of processing images, they eliminate the need for specialized instruments, and since they are readily available and simple to use, they do not require professional training. The setup uses two smartphones where one smartphone's screen is used to detect RGB values, while the other is used to generate white light, mounted on a fixed base separated by a fixed distance (Figure 3.8a). In the current study, MG dye color intensity was analyzed using Colorpicker app (Smartphone: iPhone 13 possessing 12 MP dual camera). Owing to non-linear relationship between RGB values and solution concentrations, a logarithmic scale was chosen and a calibration curve has been constructed for MG dye concentrations using $RGB_{parameter}$ which can be computed using the following equations:

$$RGB_{reference/sample} = \frac{(R+G+B)}{3} \quad (3.10)$$

$$RGB_{parameter} = Log\frac{(RGB_{reference})}{(RGB_{sample})} \quad (3.11)$$

Table 3.6 Color parameters of known concentration of malachite green dye.

Concentration (mg/L)		**R**	**G**	**B**	**$RGB_{parameter}$**
0		255	255	255	0.0
2		184	227	237	0.07
4		130	216	239	0.12
6		85	205	239	0.16
8		37	187	236	0.22
10		1	171	238	0.27

It is evident from the table that the RGB parameter increases as MG concentration increases, which is analogous to the absorption of light by the solution. The RGB parameters for known concentration of MG dye are given in Table 3.6 and the calibration curves obtained from smartphone app and UV-vis spectrophotometer are illustrated in Figure 3.8b-c, respectively. It is possible to determine the unknown dye concentration through calibration of the $RGB_{parameter}$ with the dye concentration. The good agreement between the % R and regression coefficient values obtained from smartphone (% R = 87 %, R^2 = 0.9977) and UV−vis spectrophotometry (% R = 90 %, R^2 = 0.99) demonstrates the validity of the smartphone-based colorimetry process for dye adsorption.

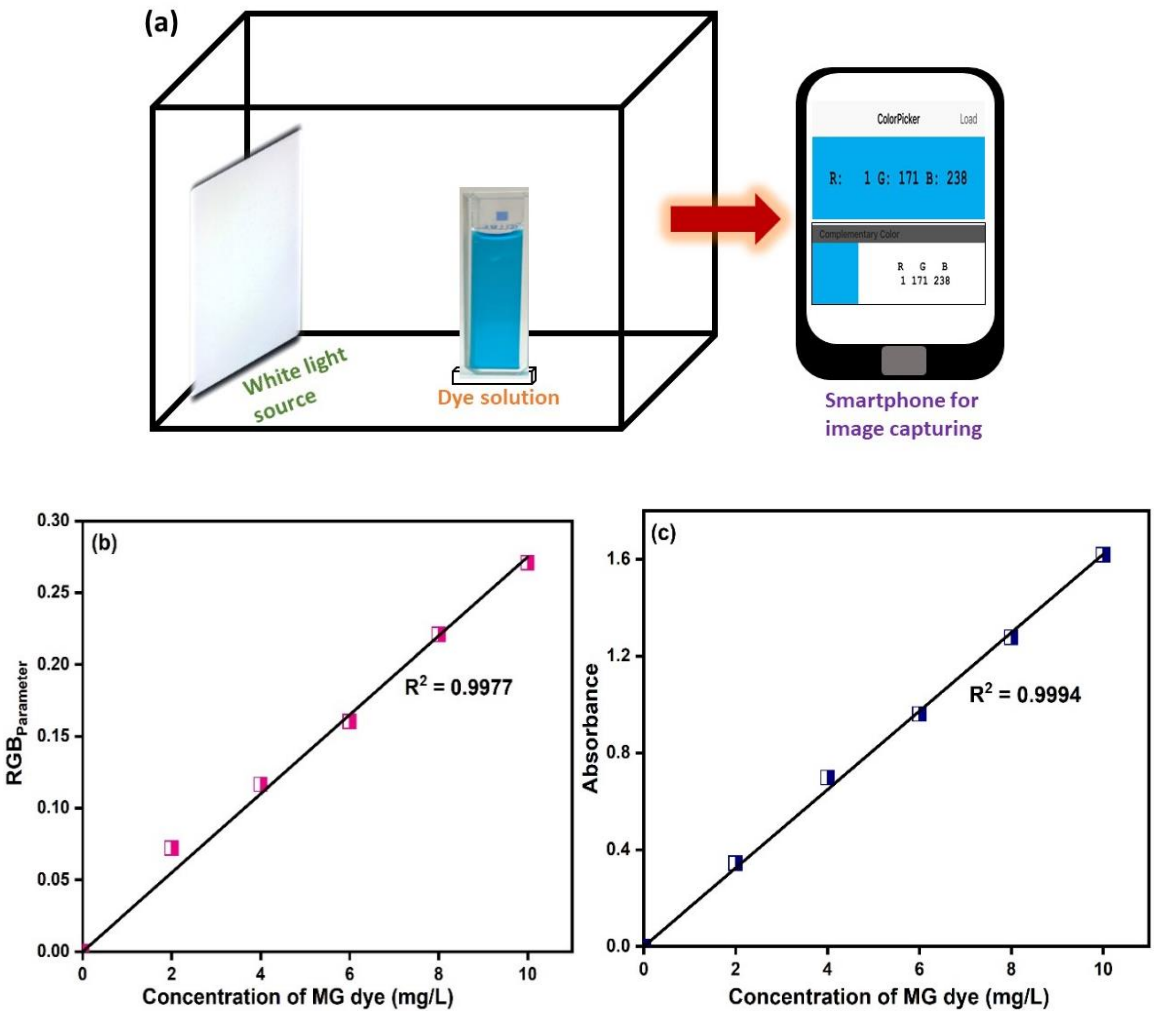

Figure 3.8 (a) Setup for smartphone-based determination of RGB and calibration plot for MG dye concentration based on (b) RGBparameter and (c) UV-vis spectrophotometry.

3.4 Conclusion

In conclusion, Zn/Cu LDO obtained from calcination of Zn/Cu LDH was utilized as a potential sorbent for the uptake of MG dye under the presence of ultrasonic waves at optimum conditions (dye: 30 mg/L, adsorbent dosage: 0.2 g/L, pH: 7, sonication time: 30 min). Zn/Cu LDO demonstrated a good fit to LI and PSO kinetic models for MG dye and exhibited a maximum monolayer adsorption capacity of 128.20 mg/g. Additionally, smartphone-assisted colorimetry based on RGB parameters proved to be a rapid, cost-

effective, precise, and quantitative method for estimation of percentage removal of dye (87%) in comparison to the data obtained using conventional method of detection, i.e., UV-vis spectroscopy (90%).

3.5 References

[1] Rathi BS, Kumar PS, Vo DN. Critical review on hazardous pollutants in water environment : Occurrence , monitoring , fate , removal technologies and risk assessment. Sci Total Environ 2021;797:149134. https://doi.org/10.1016/j.scitotenv.2021.149134.

[2] Sarkar S, Ponce NT, Banerjee A, Bandopadhyay R, Rajendran S, Lichtfouse E. Green polymeric nanomaterials for the photocatalytic degradation of dyes: a review. Environ Chem Lett 2020;18:1569–80. https://doi.org/10.1007/s10311-020-01021-w.

[3] Sundaram EJS, Dharmalingam P. Synthesis and characterization of PMMA polymer/clay nanocomposites for removal of dyes. Asian J Chem 2019;31:2589–95. https://doi.org/10.14233/ajchem.2019.22131.

[4] Pandey B, Singh P, Kumar V. Photocatalytic-sorption processes for the removal of pollutants from wastewater using polymer metal oxide nanocomposites and associated environmental risks. Environ Nanotechnology, Monit Manag 2021;16:100596. https://doi.org/10.1016/j.enmm.2021.100596.

[5] Foo KY, Hameed BH. An overview of dye removal via activated carbon adsorption process. Desalin Water Treat 2010;19:255–74. https://doi.org/10.5004/dwt.2010.1214.

[6] Liu L, Gao ZY, Su XP, Chen X, Jiang L, Yao JM. Adsorption removal of dyes from

single and binary solutions using a cellulose-based bioadsorbent. ACS Sustain Chem Eng 2015;3:432–42. https://doi.org/10.1021/sc500848m.

[7] Gier S, Johns WD. Heavy metal-adsorption on micas and clay minerals studied by X-ray photoelectron spectroscopy. Appl Clay Sci 2000;16:289–99. https://doi.org/https://doi.org/10.1016/S0169-1317(00)00004-1.

[8] Baiju V, Devadathan D, Sajeevkumar G, Raveendran R. PANI Based Metal Oxide Nanocomposite – A Novel Material for Water Purification. Adv Nanosci Nanotechnol 2020;4:37–40. https://doi.org/10.33140/ann.04.02.03.

[9] Mubarak M, Islam MS, Yoon DY, Lee JH, Park HJ, Bae JS, et al. Flower-like Mg/Fe-layered double oxide nanospheres with ultrahigh adsorption efficiency for anionic organic dyes. Colloids Surfaces A Physicochem Eng Asp 2021;618:126446. https://doi.org/10.1016/j.colsurfa.2021.126446.

[10] Yuan X, Niu J, Lv Y, Jing Q, Li L. Ultrahigh-capacity and fast-rate removal of graphene oxide by calcined MgAl layered double hydroxide. Appl Clay Sci 2018;156:61–8. https://doi.org/10.1016/j.clay.2018.01.018.

[11] Deb A, Kanmani M, Debnath A, Bhowmik KL, Saha B. Ultrasonic assisted enhanced adsorption of methyl orange dye onto polyaniline impregnated zinc oxide nanoparticles: Kinetic, isotherm and optimization of process parameters. Ultrason Sonochem 2019;54:290–301. https://doi.org/10.1016/j.ultsonch.2019.01.028.

[12] Mary Ealias A, Saravanakumar MP. A critical review on ultrasonic-assisted dye adsorption: Mass transfer, half-life and half-capacity concentration approach with future industrial perspectives. Crit Rev Environ Sci Technol 2019;49:1959–2015. https://doi.org/10.1080/10643389.2019.1601488.

[13] Laddha H, Yadav P, Agarwal M, Gupta R. Quick and hassle-free smartphone's RGB-based color to photocatalytic degradation rate assessment of malachite green dye in water by fluorescent Zr–N–S co-doped carbon dots. Environ Sci Pollut Res 2022;29:56684–95. https://doi.org/10.1007/s11356-022-19808-5.

[14] Koohkan R, Kaykhaii M, Sasani M, Paull B. Fabrication of a Smartphone-Based Spectrophotometer and Its Application in Monitoring Concentrations of Organic Dyes. ACS Omega 2020;5:31450–5. https://doi.org/10.1021/acsomega.0c05123.

[15] Bahrami H, Mejmarian M, Jafari H, Rasekh F. Synthesis of new Fe/Cr LDH for removal of Hg^{2+} ion from aqueous solutions and adsorption study using smartphone-based colorimetry. Environ Nanotechnology, Monit Manag 2022;18:100702. https://doi.org/10.1016/J.ENMM.2022.100702.

[16] Pandey B, Singh P, Kumar V. Facile synthesis of Zn/Cu and PANI modified layered double hydroxides with insights into structural memory effect property. Bull Mater Sci 2022;45:169. https://doi.org/10.1007/s12034-022-02754-w.

[17] Pandey B, Singh P. Statistical Optimization of Process Parameters for Ultrafast Uptake of Anionic Azo Dyes by Efficient Sorbent: Zn/Cu Layered Double Hydroxide. Appl Organomet Chem 2023;37:1–18. https://doi.org/10.1002/aoc.7072.

[18] Intachai S, Tongchoo P, Sumanatrakul P, Pankam P, Khaorapapong N. Efficient and practical adsorption of mixed anionic dyes in aqueous solution by magnetic NiFe-layered double oxide. Korean J Chem Eng 2022;39:2675–84. https://doi.org/10.1007/s11814-022-1099-y.

[19] Sharma B, Thakur S, Mamba G, Prateek, Gupta RK, Gupta VK, et al. Titania

modified gum tragacanth based hydrogel nanocomposite for water remediation. J Environ Chem Eng 2021;9:104608. https://doi.org/10.1016/j.jece.2020.104608.

[20] Ho YS. Citation review of Lagergren kinetic rate equation on adsorption reactions. Scientometrics 2004;59:171–7. https://doi.org/10.1023/B:SCIE.0000013305.99473.cf.

[21] Y.S. Ho GM. Pseudo-second order model for sorption processes Y.S. Process Biochem 1999;34:451–65. https://doi.org/https://doi.org/10.1016/S0032-9592(98)00112-5.

[22] Austin Taylor H, Thon N. Kinetics of Chemisorption. J Am Chem Soc 1952;74:4169–73. https://doi.org/10.1021/ja01136a063.

[23] Langmuir I. The constitution and fundamental properties of solids and liquids. Part II.-Liquids. J Franklin Inst 1917;184:721. https://doi.org/10.1016/s0016-0032(17)90088-2.

[24] Freundlich HMF. Over the adsorption in solution. J Phys Chem 1906;57:385–470.

[25] Olalekan AP, Olatunya A, Ekiti A, Dada AO. Langmuir , Freundlich , Temkin and Dubinin – Radushkevich Isotherms Studies of Equilibrium Sorption of Zn^{2+} Unto Phosphoric Acid Modified Rice Husk. J Appl Chem 2012;3:38–45. https://doi.org/10.9790/5736-0313845.

[26] Mahto TK, Chowdhuri AR, Sahu SK. Polyaniline-functionalized magnetic nanoparticles for the removal of toxic dye from wastewater. J Appl Polym Sci 2014;131:1–9. https://doi.org/10.1002/app.40840.

[27] Krishna Murthy TP, Gowrishankar BS, Chandra Prabha MN, Kruthi M, Hari Krishna R. Studies on batch adsorptive removal of malachite green from synthetic

wastewater using acid treated coffee husk: Equilibrium, kinetics and thermodynamic studies. Microchem J 2019;146:192–201. https://doi.org/10.1016/j.microc.2018.12.067.

[28] Khoshnamvand N, Jafari A, Kamarehie B, Mohammadi A, Faraji M. Removal of Malachite Green Dye from Aqueous Solutions Using Zeolitic Imidazole Framework-8. Environ Process 2019;6:757–72. https://doi.org/10.1007/s40710-019-00384-9.

[29] Shi Z, Xu C, Guan H, Li L, Fan L, Wang Y, et al. Magnetic metal organic frameworks (MOFs) composite for removal of lead and malachite green in wastewater. Colloids Surfaces A Physicochem Eng Asp 2018;539:382–90. https://doi.org/10.1016/j.colsurfa.2017.12.043.

[30] Sundararaman TR, Saravanan A, Kumar PS, Mabel MM, Hemavathy R V., Karishma S, et al. Adsorptive Removal of Malachite Green Dye onto Coal-Associated Soil and Conditions Optimization. Adsorpt Sci Technol 2021;2021:1–11. https://doi.org/10.1155/2021/5545683.

Chapter 4 SYNTHESIS AND CHARACTERIZATION OF ETHYLENE GLYCOL MODIFIED Zn/Cu HYDROXY DOUBLE SALT: MORPHOLOGICAL, THERMAL AND ADSORPTION STUDY

4.1 Introduction

In recent years, two-dimensional (2D) materials have attracted immense attention owing to their exceptional physiochemical and optical properties giving rise to potential applications in the field of catalysis, photonics, electronics, drug delivery, energy storage, etc [1–4]. Hydroxy double salts (HDS) are considered as a promising class of layered compounds, consisting of two types of divalent metal cations (M^{II}). The general composition of HDSs is $M^{a}_{1-y}M^{b}_{y}(OH)_{2-x}(A^{m-})_{x/m}.nH_2O$ where M^a and M^b are divalent metal ions and A^{m-} is interlamellar anion [5]. In HDS, one-quarter of octahedral sites are empty, and M^{II} cations are tetrahedrally coordinated just above and below the empty sites, as a consequence, a surplus of positive charge is produced, which is neutralized by charge compensating ions (A^{m-}) in the interlamellar region. Subsequently high surface area, high porosity, and anionic exchange capacity of HDS, result in efficient sorption of various anionic species [6]. The compositional diversity and intercalation chemistry enable these HDSs to be employed in a broad range of applications including wastewater remediation, drug delivery, catalysis, etc. Kaassis and group (2016) performed the intercalation of various bioactive anions in the Co/Zn and Ni/Zn HDSs and investigated their performance in drug delivery application [7]. Li *et al.* (2018) prepared another layered material for glucose detection using nanoflowers of Cu hydroxy double salt (HDS) [8]. Lu

et al. (2016) presented the formation of gold nanoclusters that supported Zn HDS for the sensing of silver ions [9].

Contamination of water resources with heavy metals and organic pollutants has aggravated environmental problems in the past few decades. Dyes are one of these pollutants, which are discharged into water resources from many sources, including textile, paper, leather, cosmetics, plastic, paint, food, and petrochemical industries [10]. The problems relating to dye effluent treatments arise from their differing synthetic origins and aromatic compositions. They are indeed not biodegradable either. Congo red is an anionic diazo dye composed of benzidine-based compounds that can cause allergic reactions and can be metabolized into Benzidine, a carcinogenic compound [11]. Traditional wastewater treatment processes cannot completely eliminate contaminants, so advanced technologies are needed to eliminate them from aqueous environments. In addition to enhanced oxidation technologies, constructed wetlands, adsorption, and filtration strategies are employed [12,13]. Adsorption is the most frequently used environmental remediation technique which is an economical, effective, flexible, and environmentally friendly technique and enables the development of a low-energy separation process with low-cost operational procedures and without toxic by-products [14].

In the past, HDS has been shown to remove several contaminants from the water via adsorptive removal [15]. Copper-containing hydroxy double salts (Cu-M HDSs where M = Zn, Ca, La & Pb) have been synthesized by Weeramonkhonlert *et al.* (2019) and its catalytic application for the degradation of carcinogenic methyl orange dye was investigated [16]. The synthesis of various organic species modified HDS reported in the literature led us to consider these materials as sorbent for organic pollutants and particularly

the anionic species. Table 4.1 outlines some of the sorbents identified in the literature for eliminating the CR dye based on their maximum adsorption capacities.

Table 4.1 Analyses of adsorption efficiencies of some sorbents for removal of CR dye.

Adsorbents	**Adsorption capacity, q_m (mg/g)**	**Percentage removal (%)**	**pH**	**References**
Mg-Al-LDH	111.11	93.4	9	[17]
Dialdehyde microfibrillated cellulose/chitosan film	152.5	99.9	-	[18]
Shrimp shell powder	288.20	96	<10.6	[11]
Kenaf-based activated carbon	14.749	95	6	[19]
Carboxymethyl chitosan/phytic acid hydrogel	8.49	89.7	7	[20]
Xanthan gum-g-Polyacrylamide/SiO_2 nanocomposite	209.205	96.37	4	[21]

To best of our knowledge, no previous work has reported the synthesis of EG modified Zn/Cu HDS via a one-pot synthesis route. Detailed characterization of layered material has been studied using various techniques involving PXRD, FTIR, TGA, SEM/EDX, and XPS. In the present work, the efficiency of EG modified HDS in uptake of CR dye has been

investigated. Studies were carried out to study contact time effect on CR removal. Also, mathematical models were employed to analyze experimental data to evaluate adsorption kinetics and equilibrium.

4.2 Experimental Section

4.2.1 Chemicals

All chemicals including Zinc acetate dihydrate [$Zn(CH_3CO_2)_2.2H_2O$], Copper acetate monohydrate [$Cu(CH_3COO_2)_2.H_2O$], and Ethylene glycol [$(CH_2OH)_2$] were purchased from Merck and were of high purity. The chemical structure of the Congo red dye is shown in Figure 4.1.

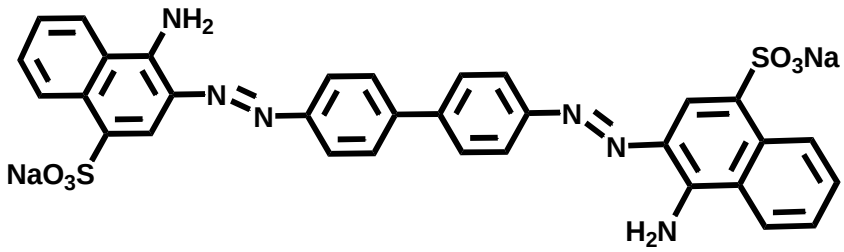

Figure 4.1 Structure of Congo red dye.

4.2.2 Preparation of EG modified Zn-Cu HDS

1.2 g of Zinc acetate and 0.42 g of copper acetate were dissolved in a mixture of distilled water and ethylene glycol (50:50 by volume). After that, the mixture was ultrasonicated for 30 minutes, and, then it was heated in the oven at a constant temperature of 120℃ till total volume was reduced to 10 mL. Following filtration and washing with distilled water and ethanol, the product was dried at 60°C in an oven.

4.2.3 Instrumentation

PXRD patterns of the samples were recorded using a high-resolution Bruker D8 advanced diffractometer, employing Cu Kα radiation (λ = 1.5418 Å) obtained through a gobel mirror with a scan rate of 1.0 second/step and step size 0.02° at 298 K over the range of 2θ = 5-70°. FTIR spectra were recorded using PerkinElmer (version 10.5.3) spectrometer using KBr disks. Thermogravimetric analysis was conducted using the PerkinElmer TGA in the range 50-900°C under flowing nitrogen at a uniform heating rate of 10°C min^{-1}. FE-SEM with EDX analysis of Zn/Cu HDS was performed using a Zeiss GeminiSEM. Brunauer-Emmett-Teller (BET) surface area was recorded at 77 K using Quanta chrome Nova-1000 instrument by N_2 adsorption-desorption isotherm. PHI 5000 VersaProbe III was used to record XPS measurements with Al Kα for photoelectron excitation.

4.2.4 Details of adsorption experiments

EG modified HDS was used as an adsorbent for the sequestration of CR dye where an adsorption experiment was performed in triplicates. Kinetic studies were conducted to determine how contact time affects removal of CR dye in a batch experiment. At 3000 rpm, the mixture was centrifuged for 10 minutes to separate the adsorbent from the residual solution. The residual concentration of CR dye solution at 497 nm (λ_{max}) was measured using a double beam UV-visible spectrophotometer (Cary 300 UV-Vis). sThe percentage removal of CR dye and amount of dye adsorbed (q_e in mg/g) was calculated by using the following equations:

$$\% \text{ Removal} = \frac{Co\text{-}Ce}{Co} \times 100 \quad (4.1)$$

$$\text{Adsorption capacity at equilibrium} = q_e = \frac{C_o\text{-}C_e}{W} \times V \quad (4.2)$$

Adsorption capacity at time t = $q_t = \frac{C_o - C_t}{W} \times V$ (4.3)

4.3 Results and Discussion

4.3.1 Structure, morphology, and thermal stability

The PXRD pattern of Ethylene Glycol (EG) modified Zn/Cu HDS exhibits strong intense reflection at a low value of 2θ (around 10.76°) followed by less intense reflections at a higher values of 2θ around 21°, 32°, 36°, 44° and 57° suggesting the presence of EG molecules in the interlayer region of Zinc/Copper HDS (Figure 4.2). The observed reflections could be indexed in rhombohedral symmetry with *a* = 3.15 and *c* = 25.77 Å. It is reported that the first intense peak at (003) reflection is attributed to the sum of interlamellar distance and thickness of the brucite-like sheet (4.8 Å). The observed gallery height of EG modified Zn/Cu HDS is 3.42 Å which is close to the thickness of the EG layer (4.2 Å) [22]. Therefore, ethylene glycol anions may be accommodated in the monolayer arrangement in the layered structure of Zn/Cu HDS.

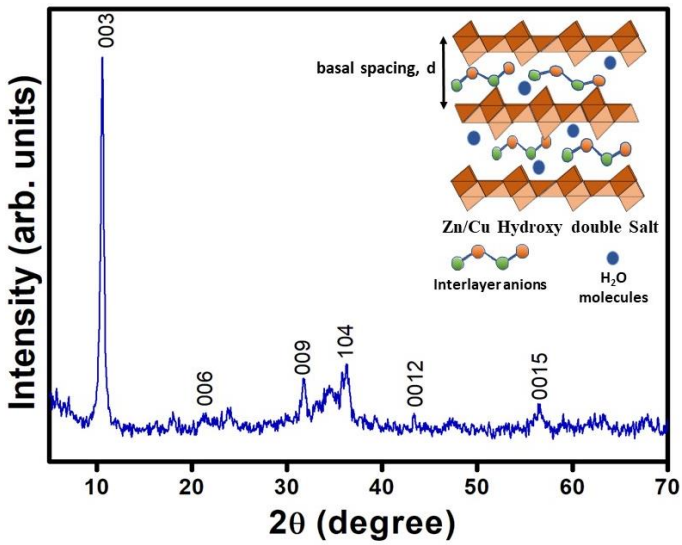

Figure 4.2 PXRD pattern of EG modified Zn/Cu HDS.

The FTIR spectrum of the layered HDS is depicted in Figure 4.3. The existence of a broad and intense band at 3434 and 1574 cm^{-1} signifies the stretching and bending vibrations of hydroxide ions and indicates the hydrogen bonding between them. The bands positioned at 2883 and 2834 cm^{-1} are due to the asymmetric and symmetric vibration of the $-CH_2$ group, respectively. The lower wavenumber values as well as broadening and weak nature of C-H stretching vibrations as compared to pure EG (2941, 2874 cm^{-1}) confirm the intercalation of EG in the interlamellar region. In addition, a series of low-intensity absorption bands observed at 1412, 1071, and 908 cm^{-1} may be ascribed to CH_2 wagging, C-O-H bending, and CH_2 rocking vibrations of modified ethylene glycol anions, respectively [22–24]. Although the original bands for CH_2 rocking vibration in EG molecules appear at at 882 and 864 cm^{-1} but in present case, it can be observed that it gets shifted to higher wavenumber side (908 cm^{-1}) with a single broad absorption which might be due to the increased bond order of C-C bond in modified HDS [25]. The bands in the range of 500-800 cm^{-1} arise from metal-oxygen linkages [26].

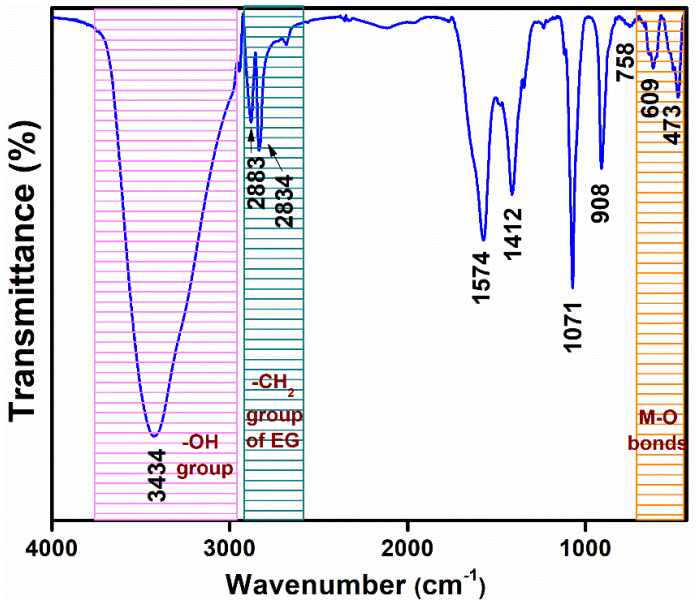

Figure 4.3 FTIR analysis of EG modified Zn/Cu HDS.

EG modified Zinc/Copper HDS showed sheet-like morphology in SEM micrograph as shown in Figure 4.4. This observation strengthened our assignment of layered structural arrangement for EG-modified Zn/Cu HDS. The EDX analysis revealed that the as-obtained EG modified Zn/Cu HDS contain Zn, Cu, and O elements. Element mapping images, as shown in Figure 4.4(c-f), clearly illustrates even distribution of the elements within a lattice.

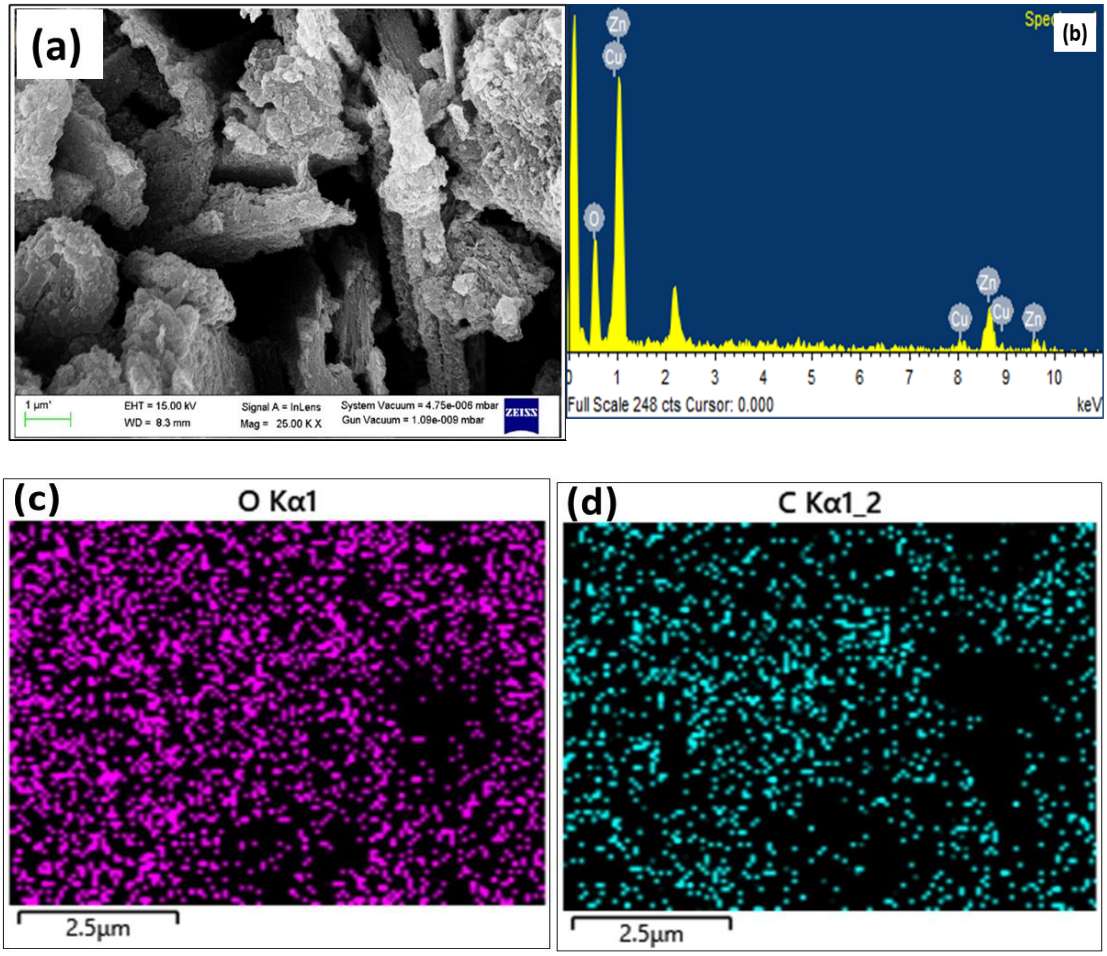

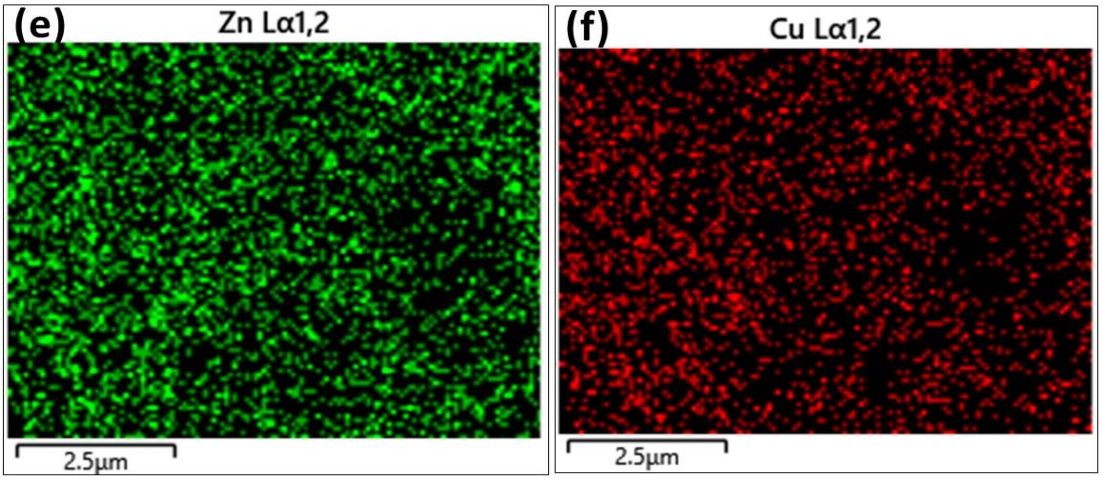

Figure 4.4 (a) SEM image, (b) EDX spectrum and (c−f) corresponding elemental mapping of O, C, Zn, and Cu respectively of EG intercalated Zn/Cu HDS.

The thermal analysis was carried out under a flowing nitrogen atmosphere and the obtained traces are reproduced in Figure 4.5. Though the lattice was losing weight gradually and constantly with increasing temperature, three distinct steps could be observed in the thermogravimetric (TG) trace of the sample. The mass loss below 174 °C could be attributed to the elimination of surface adsorbed molecular water. Whereas the weight loss between 174-260 °C could be accredited to departure of the water and physically adsorbed ethylene glycol molecules. Weight loss between 260-465°C suggested the combustion of EG, as well as the dehydroxylation of the lattice [27,28]. No weight loss after 560°C was observed thus conforming the formation of metal oxide.

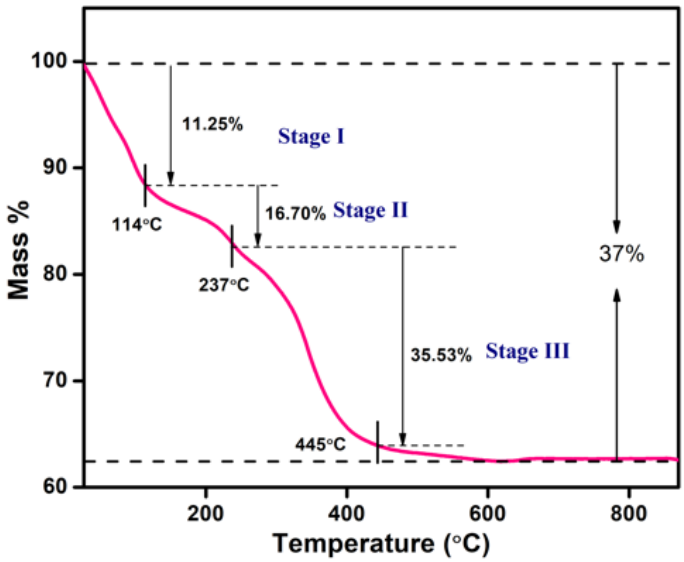

Figure 4.5 Thermogravimetric trace of EG modified Zn/Cu HDS.

The sample was analyzed using XPS for elemental distribution and oxidation state determination. Figure 4.6 presents the survey XPS spectrum and the core level spectra of Zn *2p*, Cu *2p*, O *1s*, and C *1s*. The full survey spectrum shown in Figure 4.6a suggested the presence of zinc, copper, oxygen, and carbon elements.

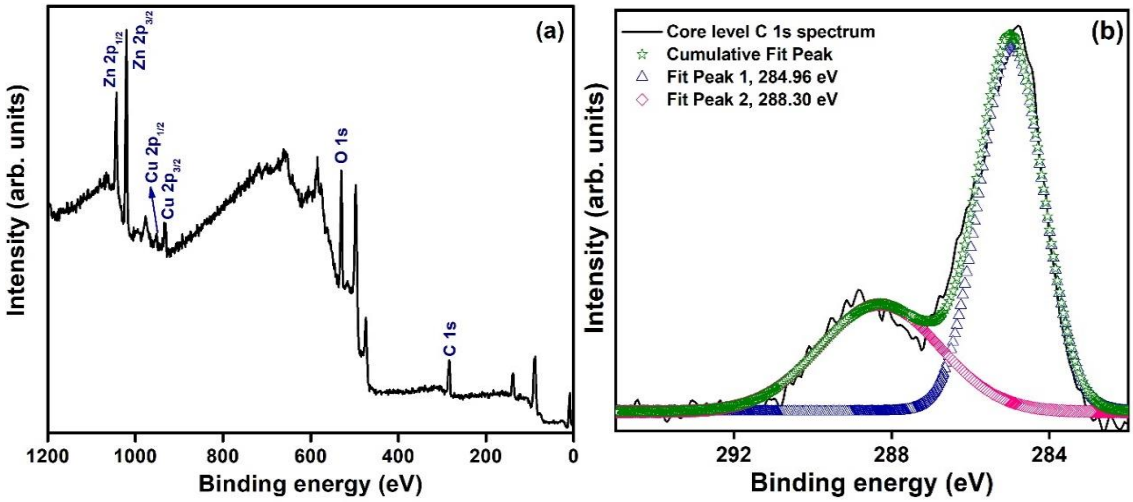

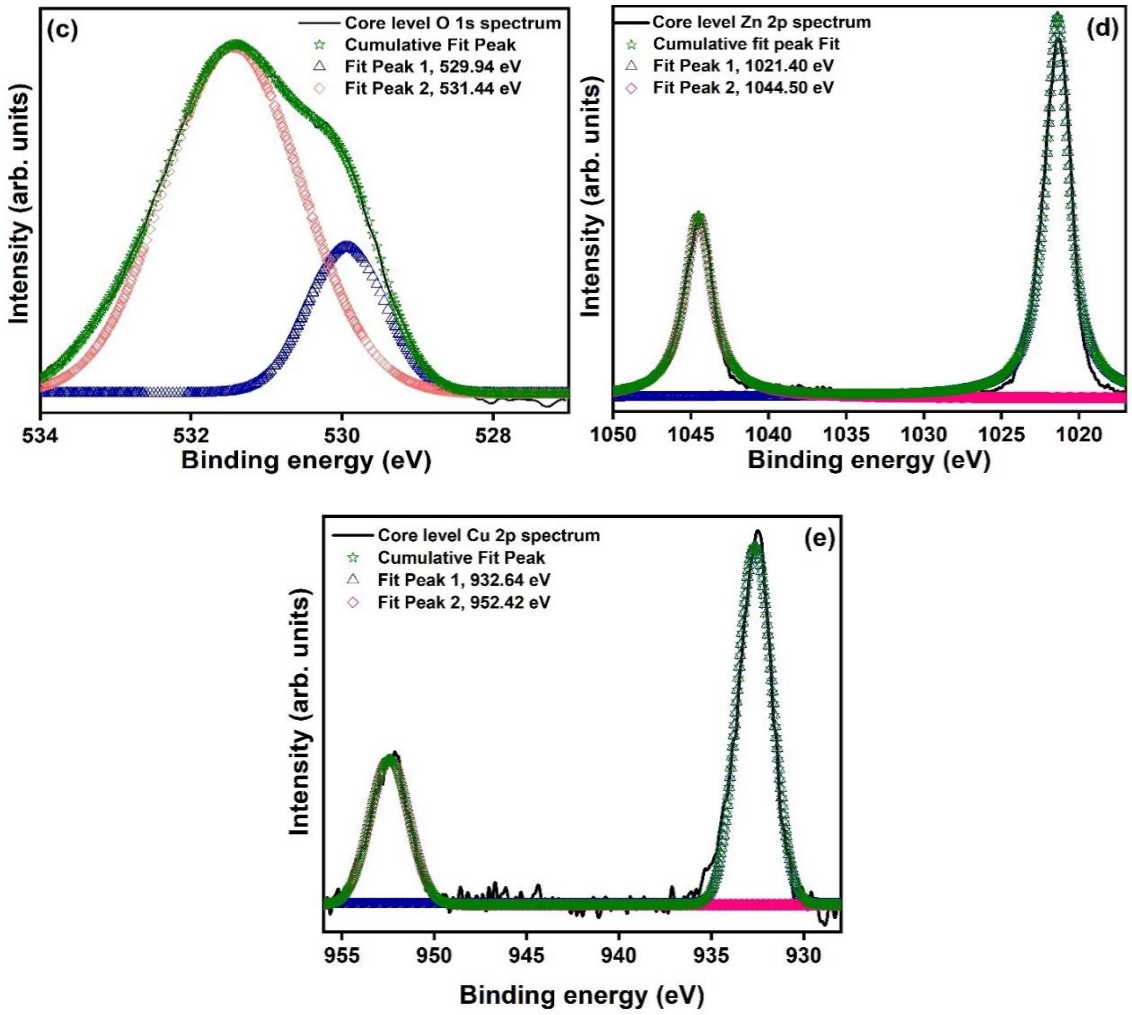

Figure 4.6 (a) Survey XPS spectrum of EG modified Zn/Cu HDS. (b), (c), (d), and (e) show the XPS spectrum of C *1s*, O *1s*, Zn *2p*, and Cu *2p*, respectively.

The deconvolution of C *1s* spectrum (Figure 4.6b) of EG modified Zn/Cu HDS was attempted and two peaks were detected at 284.96 and 288.30 eV which are assigned to the C-C and C-O bonds of ethylene glycol, respectively [29]. The deconvoluted O *1s* spectrum (Figure 4.6c) exhibits two peaks at 529.94 and 531.44 eV, corresponding to the C-OH group of ethylene glycol and metal-oxygen linkage (M-O), respectively. The observance of two prominent peaks in Figure 4.6d at 1021.40 and 1044.50 eV in core spectra of Zn *2p* confirmed the presence of Zn (II) ions [30]. The existence of copper in the sample in the

core level XPS spectrum of Cu *2p* has been confirmed from peaks at 932.64 and 952.42 eV (Figure 4.6e).

The porosity of EG-modified Zn/Cu HDS sample was examined using N_2 adsorption-desorption isotherm. According to BET calculations, the adsorbent has a specific surface area of 32.295 m^2/g, whereas the average pore size diameter and pore volume evaluated by BJH (Barrete-Joynere-Halenda) method are 2.218 nm and 0.070 cm^3g^{-1} respectively (Figure 4.7a). The isotherm depicts a type-IV isotherm with H_3 hysteresis loop, that is suggestive of the material's mesoporous nature [31]. The H_3 hysteresis is a feature of materials with slit-shaped pores [32].

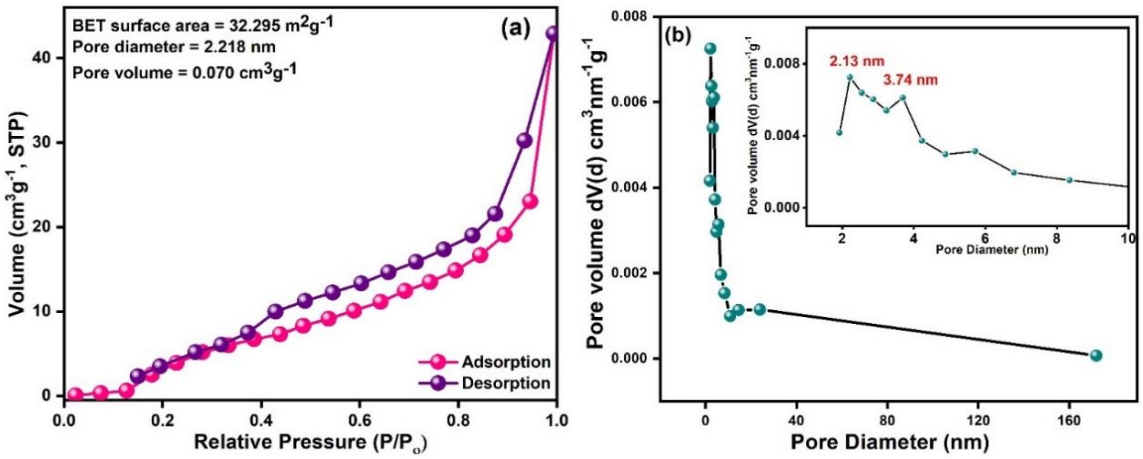

Figure 4.7 (a) N_2 Adsorption-desorption isotherm and (b) Plot of BJH pore size distribution of EG-modified Zn/Cu HDS.

BJH pore size distribution indicated that the lattice was composed of pores sizes ranging from 2.13 to 3.74 nm, as shown in Figure 4.7b. According to these findings, the porous nature of the synthesized material contributes greatly to its excellent sorption properties. With large surface areas and small pore sizes, mesoporous channels offer a sufficient

surface to adsorb molecules of large size such as organic dyes. As a result of the mesoporosity of the material, its potential as a sorbent for CR dye uptake from solution phase has been examined.

4.3.2 Adsorption study

4.3.2.1 Adsorption of various dye pollutants

In order to assess the efficacy of synthesized lattice for the uptake of various dyes adsorption experiment was performed. For this study, two cationic dyes (crystal violet (CV) and methylene blue (MB)) and three anionic dyes (congo red (CR), methyl orange (MO), and eriochrome black T (EBT)) were selected. The sequestration of dyes was performed with 20 mg/L concentration of dye with a fixed sorbent dose. Figure 4.8a illustrates the plot for uptake of different dyes and it can be observed that it follows the trend: CR (96 %) > EBT (77 %) > MO (70 %) > CV (13 %) > MB (2 %). From the order, it can be deduced that the synthesized material exhibit higher affinity for the anionic dyes which can be attributed to the fact that Zn/Cu HDS possess excess positive charge on the layers and there occurs an electrostatic interaction between the positively charged layers and anionic dye molecules.

In addition, selective adsorption of CR dye was also performed in presence of cationic dye, i.e., MB under similar reaction conditions. The synthesized adsorbent exhibits high selectivity towards the anionic dye with the removal efficiency of 96 %. The results obtained are illustrated in Figure 4.8b.

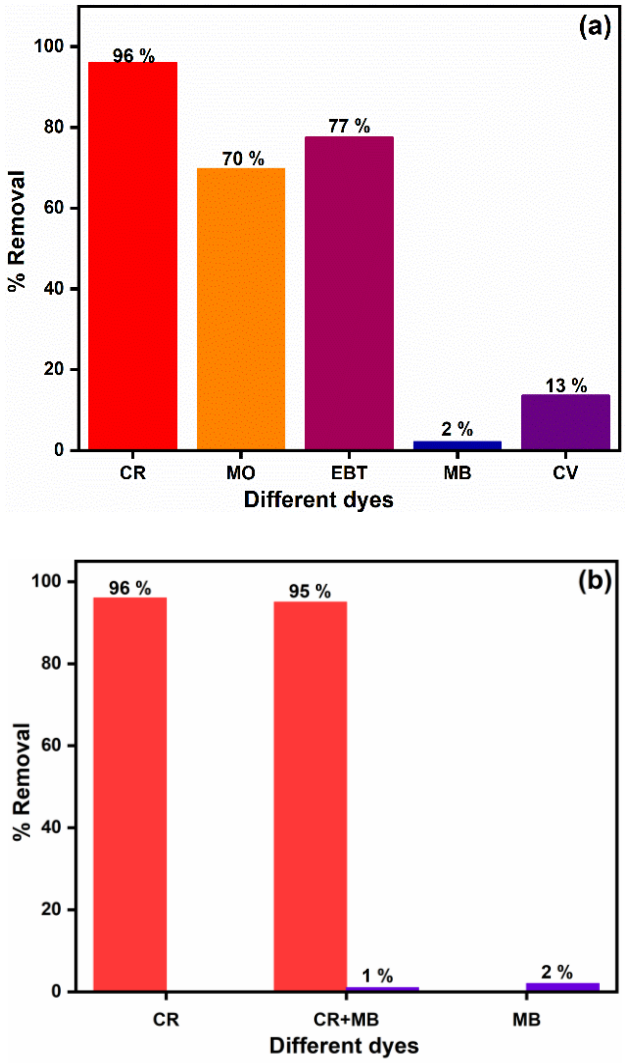

Figure 4.8 Plots of (a) % removal of different dyes and (b) selective removal of CR dye.

4.3.2.2 Effect of contact time

Treatment of wastewater by the adsorption route relies significantly on the contact time between adsorbents and pollutants. The plot of absorbance vs contact time is depicted in Figure 4.9a. CR dye uptake was shown to have greatly increased with time and subsequently reached equilibrium afterward. A significant increase in dye adsorption occurred during the first 5 minutes of reaction time as shown in Figure 4.9b, reaching >90%, following which equilibrium was achieved (after 10 minutes). More than 96% of

the CR was removed, and it remains almost constant as contact time increases, suggesting that equilibrium has been reached. This was mainly because of the large area of surface area available for adsorption during the initial five minutes of contact time. Subsequently, vacant sites decreases as the contact time increases because of repulsive interactions between solid and bulk phases.

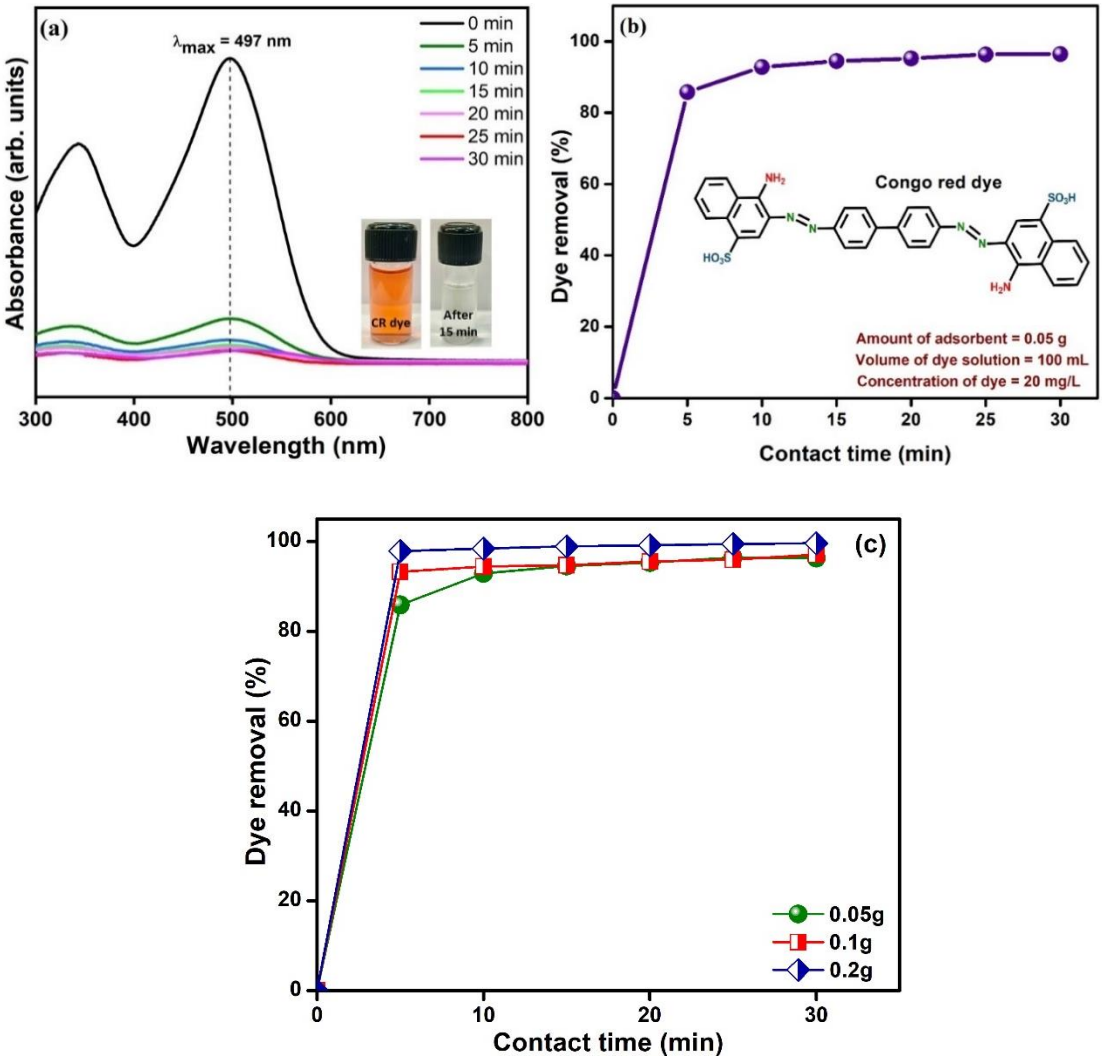

Figure 4.9 Plots of (a) absorbance vs wavelength, (b) effect of contact time and (c) effect of adsorbent dosage on percentage dye removal.

4.3.2.3 Effect of adsorbent dosage

The effect of the amount of adsorbent on the removal of dye was studied using three different doses of adsorbent (0.05g, 0.1g, and 0.2g) while maintaining the other parameters (initial dye concentration of 20 ppm and reaction time of 30 minutes) constant. Figure 4.9c shows that the percentage removal of dye increases with an increase in adsorbent dosage, which confirms the fact that the more adsorption sites, the greater the removal.

4.3.2.4 Effect of pH on dye removal

The pH of the dye solution plays a crucial role in determining the efficiency of adsorbents for water treatment applications. Experiments were performed at varying pH (pH 3–11) with 20 ppm concentrations of dye solutions and 0.05 g of adsorbent dosage for 30 mins. Figure 4.10a shows the removal of dye at different pH values. As pH varied from 3 to 11 removal percentage was decreased from 99.54% to 21.62% and pH = 3 & 7 showed maximum removal. In general, the adsorption of anionic dyes like Congo Red decreases with an increase in pH. The presence of excessive hydroxide ions at higher pH values causes dye molecules to compete for sorption sites, resulting in decreased adsorption capacity as the pH increases.

PZC (point of zero charge) of the sorbent can explain the decline in adsorption efficiency with increased pH. PZC is the pH at which a material's surface becomes neutral. When pH of the material is below pH_{PZC}, the material's surface exhibits a positive charge, while above pH_{PZC}, the material is negatively charged. In this study, the PZC was found to be 7.6 (Figure 4.10b) indicating that the synthesized HDS exhibits a positively charged surface at pH < 7.6, resulting in enhanced dye adsorption due to electrostatic interactions. As the pH

of solution rises above 7.6, HDS hydroxide ions contest with anionic dye molecules causing a decline in the dye removal efficacy.

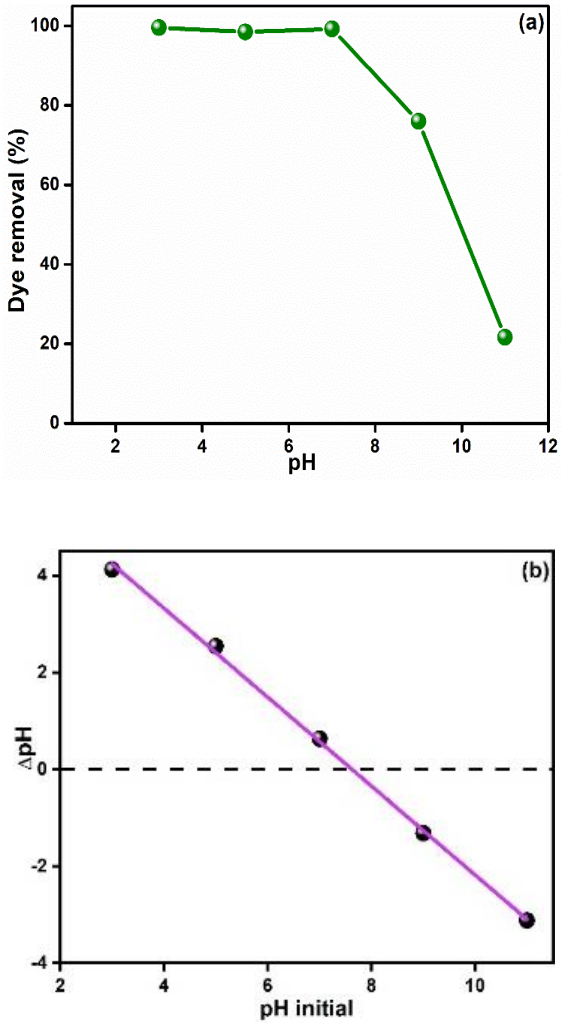

Figure 4.10 (a) pH effect on percentage dye removal and (b) plot of pH_{PZC}.

4.3.2.5 Effect of initial dye concentration

The impact of dye concentration was studied for aqueous solutions of 20-100 mg/L concentrations of dye with 0.05 g of EG modified Zn/Cu HDS (adsorbent) for 30 minutes. From Figure 4.11a. it can be observed that when the CR concentration increased from 20 to 100 mg/L (ppm), the adsorption capacity also increased from 39.18 to 195.25 mg/g. In

summary, the initial high concentration of dye presents a greater concentration slope or a stronger driving force between the liquid phase (dye solution) and adsorbent phase, leading to higher rate of adsorption.

4.3.2.6 Effect of interfering anions

Textile dyeing processes generate a large amount of toxic effluent, which generally contains various inorganic salts such as sodium chloride, sodium carbonate, etc. [33]. To estimate the dye removal efficacy of EG-modified Zn/Cu HDS as an adsorbent, the adsorption procedure needs to be analyzed to determine the impact of these anions. During this study, chloride (Cl^-), carbonate (CO_3^{2-}), nitrate (NO_3^-), and sulfate (SO_4^{2-}) anions were investigated and the adsorption experiment was carried out by taking 0.05 M concentration of each anion. A decrease in dye uptake was observed when Na_2SO_4 and Na_2CO_3 were added to the dye solution, as opposed to when NaCl, $NaNO_3$, or none of the electrolytes were added as given in Figure 4.11b. Cl^- and NO_3^- are monovalent ions and they did not influence the adsorption efficiency to great extent. Since carbonate ions are divalent ions and exhibit the strongest affinity for positively charged layers of anionic materials, the adsorption efficiency was decreased most in this case. Owing to the competitive uptake of dye molecules and inorganic salts on surface of adsorbent, dye solutions containing inorganic salts have a decreased adsorption efficiency. Consequently, it can also be stated that presence of divalent ions strongly influences the adsorptive removal of CR dye as compared to monovalent ions, which is in agreement with the fact that HDS has a high affinity for anions having high charge density [34].

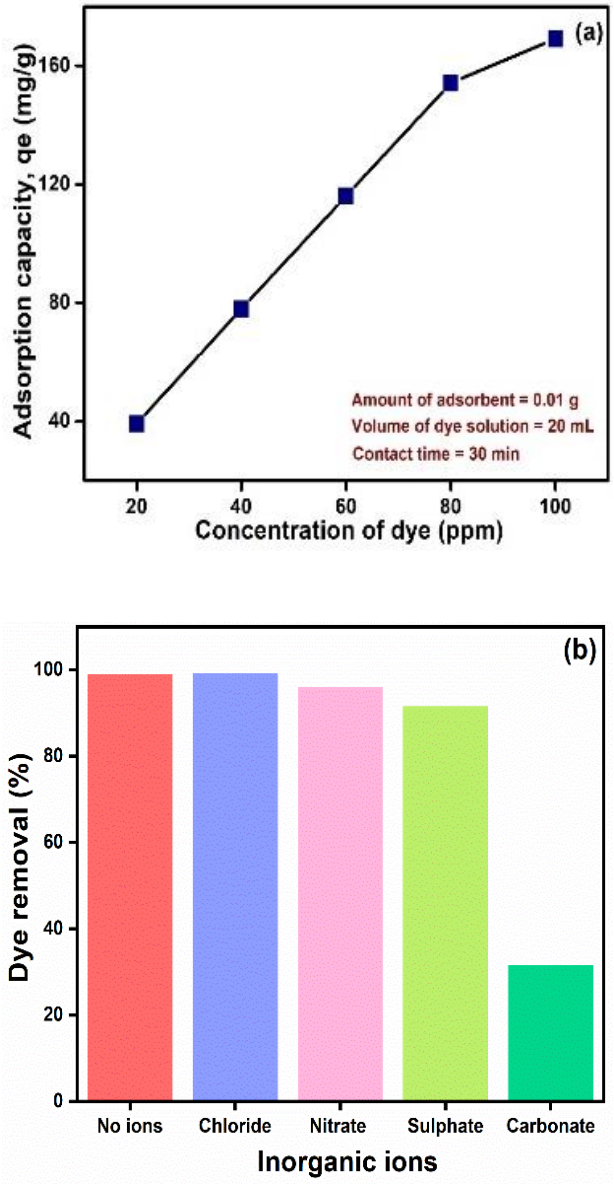

Figure 4.11 Influence of (a) concentration variation on adsorption capacity and (b) interfering anions on dye adsorption.

4.3.2.7 Adsorption isotherms

This study used Langmuir, Freundlich, and Temkin isotherm models to analyze the equilibrium adsorption experimental data for removing CR dye. LI implies that adsorptions take place on uniform, homogeneous surfaces with identical sites on an adsorbent and it is

often used to describe monolayer adsorptions [35]. The nonlinear and linearized form of LI is given in following equation:

$$\frac{C_e}{q_e} = \frac{1}{q_m k_L} + \frac{C_e}{q_m} \quad (4.4)$$

Where q_e is adsorption capacity (mg/g), C_e is equilibrium concentration (mg/L) of CR dye, q_m and K_L are Langmuir constants related to monolayer or maximum adsorption capacity (mg/g), and energy of adsorption (L/mg) respectively. In accordance with Eq. 4.4, when the Langmuir equation holds, the plot of C_e/q_e versus C_e should consist of a straight line with a slope of $1/q_m$ and an intercept of $1/q_mK_L$. A dimensionless factor, R_L, allows us to quantify this characteristic of the LI, which is given by:

$$R_L = \frac{1}{1+k_L C_0} \quad (4.5)$$

Where C_0 is initial concentration of dye (mg/L) and the R_L value indicates the nature of the adsorption: unfavourable ($R_L > 1$), linear ($R_L = 1$), favourable ($0 < R_L < 1$), or irreversible ($R_L = 0$).

In contrast to the monolayer LI model, the FI model can be linearly expressed as a function of interactions between adsorbed molecules and applies to all adsorption on heterogeneous surfaces:

$$\ln q_e = \ln k_F + \frac{1}{n} \ln C_e \quad (4.6)$$

where 1/n and K_F are Freundlich constant related to intensity and capacity of adsorption respectively. By plotting ln q_e against ln C_e, values of K_F and 1/n can be obtained from the slope and intercept of the plot. An adsorption process is characterized as favorable if the 1/n ratio is higher than 1, indicating favorable conditions for adsorption [36].

The indirect adsorbate-adsorbent interactions are taken into consideration in Temkin model. The increase in surface coverage is assumed to cause a linear decrease (rather than

logarithmic) in the heat of adsorption for all molecules in the layer as well [37,38]. The linear form of Temkin adsorption isotherm is given as follows:

$$q_e = B \ln A_T + B \ln C_e \quad (4.7)$$

B is constant related to the heat of sorption and A_T denotes the Temkin isotherm equilibrium binding constant.

The results for LI, FI, and TI fittings are depicted in Figure 4.12a-c, respectively. The relevant parameters of these isotherms are also given in Table 4.2. By examining the values of R^2, it is clear that the LI fits well with the experimental adsorption data, indicating the monolayer adsorption of CR dye onto EG-Zn/Cu HDS adsorbent.

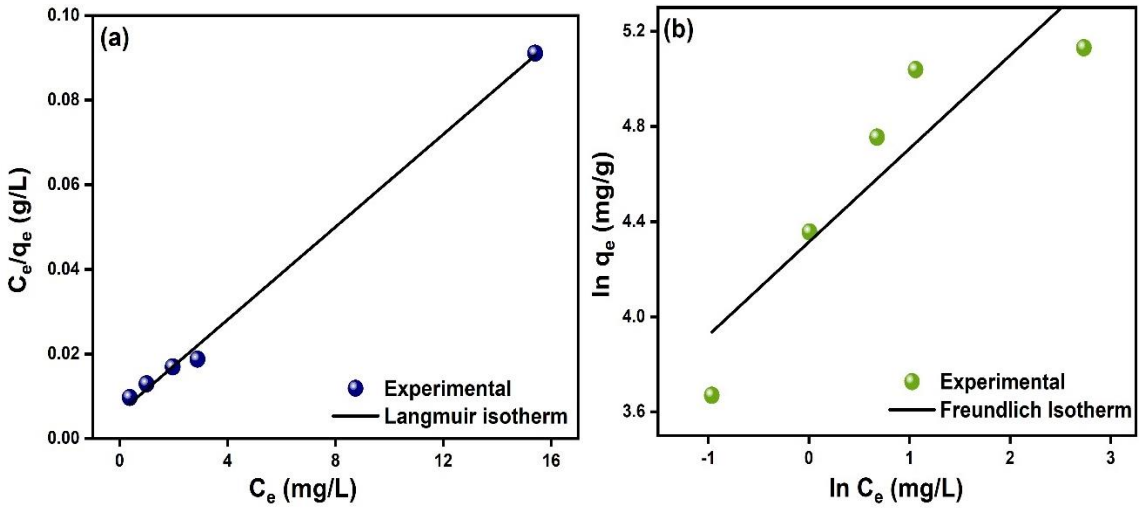

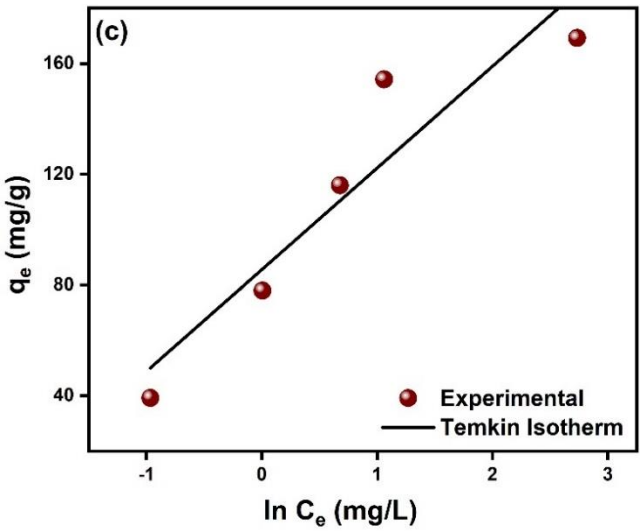

Figure 4.12 (a) Langmuir, (b) Freundlich, and (c) Temkin isotherm plots for removal of CR dye using EG-Zn/Cu HDS.

Table 4.2 Langmuir, Freundlich, and Temkin isotherm constants for the adsorption of CR dye onto EG modified HDS from aqueous solution.

Equilibrium isotherms	***Parameters***		
Langmuir	q_m (mg/g)	K_L (L/mg)	R^2
	181.81	0.90	0.9969
Freundlich	K_F (mg/g) $(L/mg)^{1/n}$	1/n	R^2
	74.73	0.39	0.8147
Temkin	B (J/mol)	A_T (L/g)	R^2
	36.71	10.26	0.8803

4.3.2.8 Kinetic studies

For design and modelling of adsorption processes, kinetic parameters can be used to predict adsorption rates. Based on the kinetic data, PFO, and PSO, and Intra-particle diffusion kinetic models were applied.

Adsorption rates can be expressed in terms of adsorption capacity based on Lagergren's first-order rate [39]. The linearized form of the PFO equation is as follows:

$$\ln(q_e - q_t) = \ln q_e - K_1 t \quad (4.8)$$

where, q_e = amount of dye adsorbed at equilibrium (mg/g), q_t = amount of dye adsorbed at time t, and K_1 = pseudo-first-order rate constant (min^{-1}).

Ho proposed that the adsorption kinetics may also be described by a PSO model [40]. The linearized equation for PSO kinetic is given as follows:

$$\frac{t}{q_t} = \frac{1}{K_2 q_e^2} + \frac{t}{q_e} \quad (4.9)$$

where, q_e = amount of dye adsorbed at equilibrium (mg/g), q_t = amount of dye adsorbed at time t, and K_2 = PSO rate constant (g mg^{-1} min^{-1}) which can be calculated from the linear plot of t/q_t vs t. The chemisorption step is assumed to be the rate-limiting step in the PSO kinetic model which is used to predict the behavior over the entire range of adsorption.

The linear form of the Intra-particle diffusion model is formulated in Eq. 4.10:

$$q_t = K_{id} t^{1/2} + C \quad (4.10)$$

where q_t = amount of dye adsorbed at time t, K_{id} is the intra-particle diffusion rate constant.

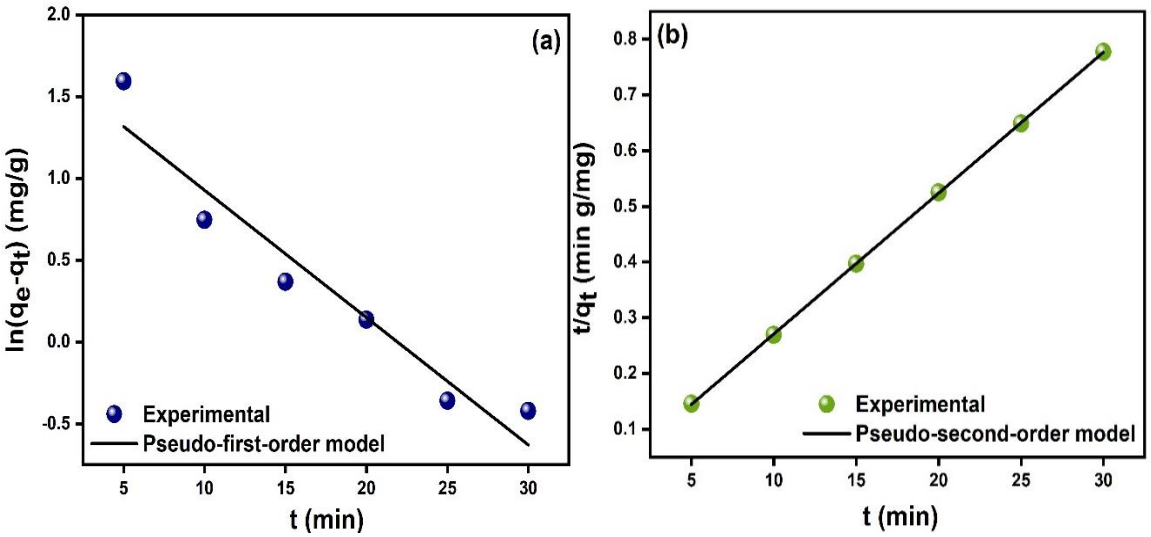

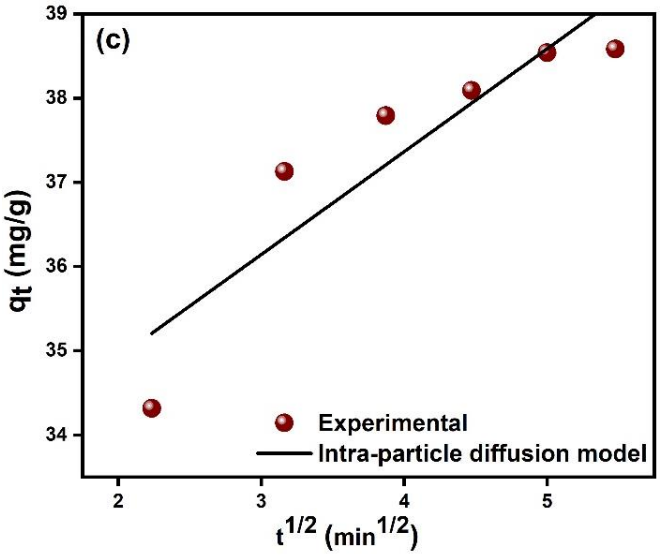

Figure 4.13 Linear plots of (a) PFO, (b) PSO, and (c) Intra-particle diffusion kinetic models.

The kinetic parameters for all the models are shown in Table 4.3 and linear plots are given in Figure 4.13a-c. It was evident that the PSO kinetic model, R^2 (0.9999) fits well over the entire range. Moreover, the value of adsorption capacity, q_e calculated (39.52 mg/g) from the PSO equation was highly consistent with the experimental value (39.23 mg/g). The results showed that adsorption of CR by synthesized HDS followed a PSO kinetic model.

Table 4.3 Kinetic parameters for CR dye adsorption onto EG modified Zn/Cu HDS.

Kinetic models	**Parameters**		
Pseudo-first order	K_1 (min^{-1})	q_e (mg/g)	R^2
	0.0660	5.50	0.9310
Pseudo-second order	K_2 (g mg^{-1} min^{-1})	q_e (mg/g)	R^2
	0.0331	39.52	0.9999
Intra-particle	K_{id} (g/mg $min^{-0.5}$)	C	R^2
diffusion	1.2215	32.47	0.7475

4.3.2.9 Proposed adsorption mechanism

Hydroxy double salts are porous materials having numerous adsorption sites. The mechanisms involved in the adsorption of pollutants using layered materials generally include physical adsorption, ion exchange reactions, electrostatic interactions, *pi-pi* interactions, and chemical bonding [41]. The mechanism of adsorption can be explained by the change in values of the zeta potential value of the adsorbent. The zeta potential value of Zn/Cu HDS was found to be 9.79 and 4.95 mV before and after adsorption, respectively. The positive value of zeta potential suggests that the surface of the adsorbent possesses a positive charge. However, CR has a high solubility in water and exists in anionic form under aqueous phase. Thus, a decrease in value of zeta potential upon adsorption of CR can be attributed to the electrostatic interactions occurring between the positive layers of adsorbent and negative dye molecules at neutral or low pH environments. Therefore, it can be stated that electrostatic interaction (between metal ions and dye molecules), as well as hydrogen bonding (between EG and dye molecules), are responsible for the high removal efficiency of synthesized adsorbent towards CR dye. The proposed mechanism of adsorption is depicted in Figure 4.14.

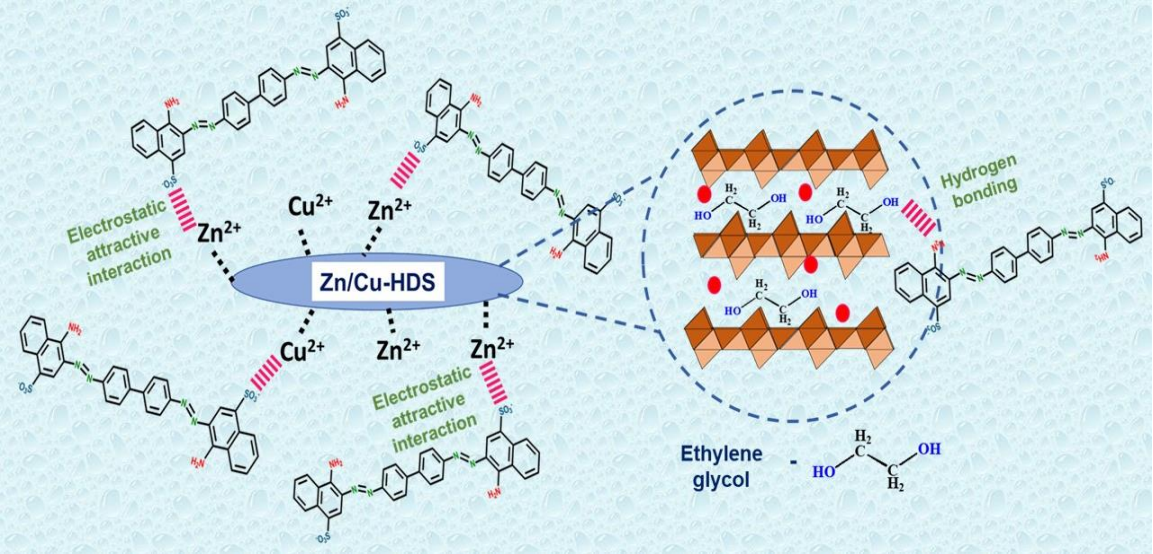

Figure 4.14 Plausible mechanism of adsorption of CR dye onto EG-Zn/Cu HDS.

4.3.2.10 Effect of temperature

During adsorption, entropy and energy are important factors to consider when determining the spontaneity of the process. A thermodynamic analysis of CR adsorbed at equilibrium at different temperatures, 303.15, 313.15, and 323.15 K, was conducted in order to determine the thermodynamic parameters of the adsorption system. The following equations were used to estimate changes in enthalpy, Gibbs free energy, and entropy of adsorption:

$$\ln K = -\frac{\Delta H^0}{RT} + \frac{\Delta S^0}{R} \quad (4.11)$$

$$K = \frac{q_e}{C_e} \quad (4.12)$$

$$\Delta G^0 = \Delta H^o - T\Delta S^0 \quad (4.13)$$

The adsorbates' distribution coefficient, gas constant, and absolute temperature are denoted by K, R (8.314 J/K/mol), and T, respectively. The values of ΔH° and ΔS° can be obtained

from the linear plot of ln K vs 1/T (Figure 4.15a). The parameters calculated are in given in Table 4.4. The positive value of change in enthalpy demonstrated that adsorption process is endothermic in nature and during adsorption, there is a higher degree of disorderness at the solid-solution interface. The adsorption capacity increased with increase in temperature. The collision rate of dye and Zn/Cu HDS increased at elevated temperatures because of the increase in kinetic energy of adsorbate molecules (Figure 4.15b). Generally, when enthalpy changes are high, chemisorption is more likely to occur (more than 20 KJ mol^{-1}) than physisorption (<20 KJ mol^{-1}) [42]. Since the ΔH° value obtained in the present case is 38.83 KJ mol^{-1}, it can be stated that the adsorption process is a chemisorption process. Furthermore, it can also be stated that physisorption and chemisorption take place in exothermic and endothermic processes, respectively [43]. In addition, the negative value of $\Delta G°$ confirms that process is spontaneous and increasing value of $\Delta G°$ with increasing temperature suggests that rate of adsorption is higher at high temperatures.

Table 4.4 Thermodynamic parametric values for CR dye uptake.

Temperature (K)	**qe (mg/g)**	**ΔG° (KJ/mol)**	**ΔH° (KJ/mol)**	**ΔS° (J/mol/K)**
303.15	39.68	-13.61	38.83	173.02
313.15	39.72	-15.35		
323.15	39.88	-17.07		

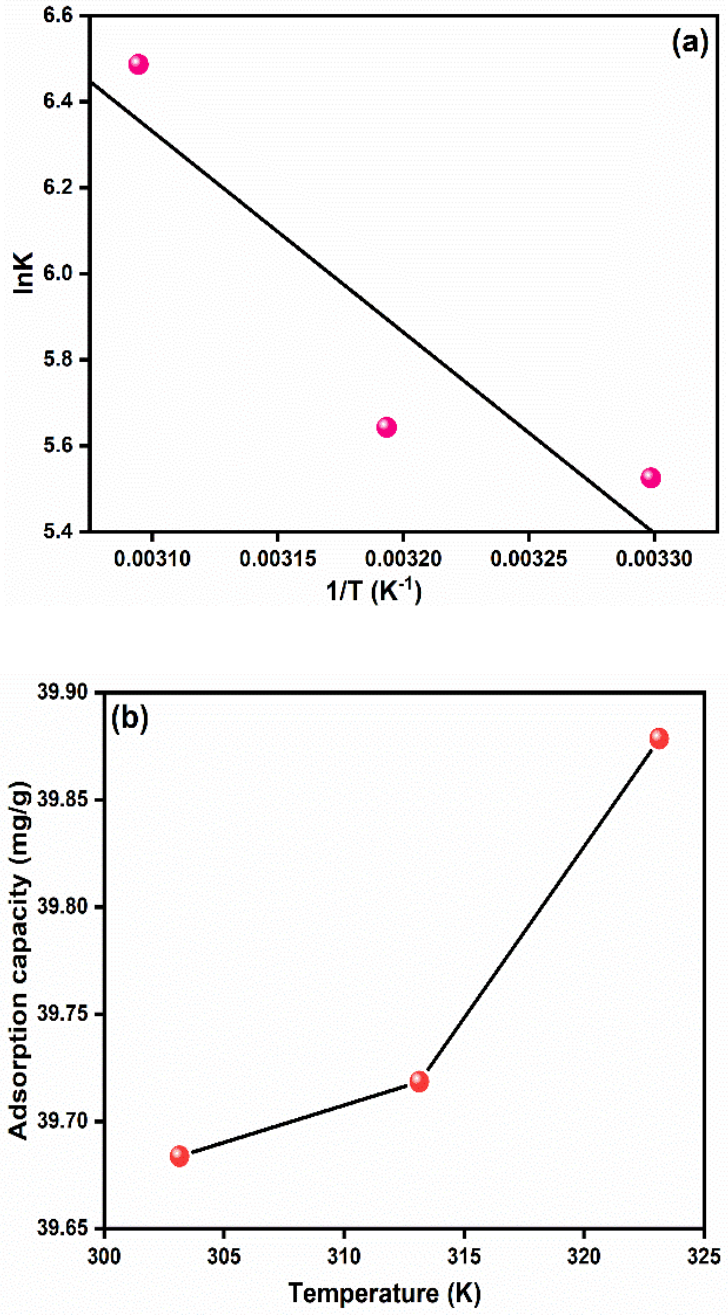

Figure 4.15 (a) Van't Hoff plot for ln K vs 1/T and (b) effect of temperature on adsorption capacity.

4.3.2.11 Regeneration study

In order to investigate synthesized adsorbent's stability, regeneration ability, and reusability for removing Congo red dye set of experiments were performed under same reaction

conditions for up to five cycles. Following adsorption, the EG-Zn/Cu HDS adsorbent was centrifuged, washed with ethanol, and dried, then reused for the subsequent cycles. The recovered adsorbent was found to be reusable up to five cycles without significant loss in its dye uptake efficiency. The plot for removal efficiency for consecutive five cycles is presented in Figure 4.16.

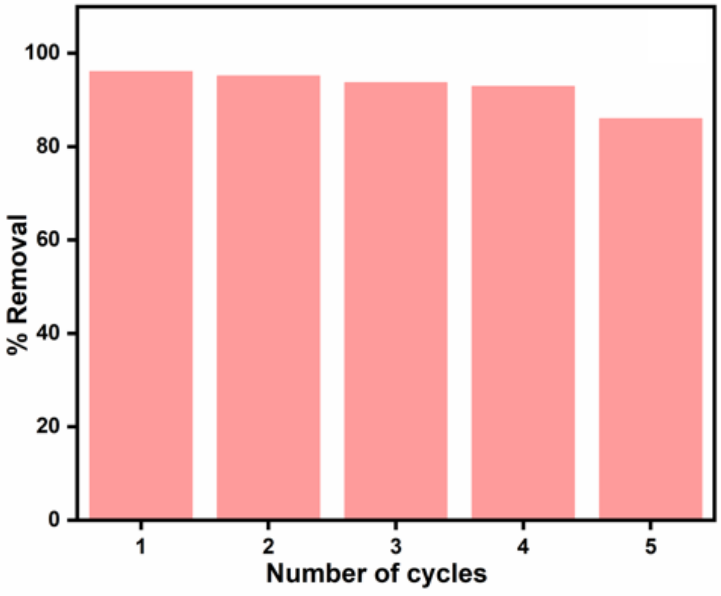

Figure 4.16 Reusability of EG-Zn/Cu HDS for Congo red removal.

Adsorption efficiency for CR dye uptake in the first cycle was 96.06%. and it decreased slightly in the subsequent cycles and reached 92.86% after 4 cycles. After 5 cycles of regeneration study, the percentage removal decreased further in the 5th cycle and it was found to be 85. 98%. In light of these results, EG-Zn/Cu HDS serves as a potential candidate for dye-loaded wastewater remediation due to its stability and reusability.

4.4 Conclusion

Ethylene glycol modified HDS containing zinc and copper metal ions have been synthesized via a one-pot synthesis route and characterized using PXRD, FTIR, TGA, SEM/EDX, and XPS analysis. The present study demonstrated that EG modified HDS acts as an efficient sorbent for CR dye uptake. To do so, batch experiments, adsorption isotherms, and kinetic studies for CR sorption on synthesized layered material have been examined. The maximum dye removal percentage was 96% with sorption capacity 39.23 mg/g (with only 0.05 g of adsorbent). It was found out that the kinetic data fit well with the PSO kinetic model and the adsorption isotherm followed the Langmuir model. In addition, results indicated that EG modified HDS showed a maximum monolayer adsorption capacity of 181.81 mg/g. Hence, EG modified HDS can be used as a cost-effective alternative material for removing CR dye from wastewater.

4.5 References

[1] Williams GR, Hare DO. Towards understanding , control and application of layered double hydroxide chemistry. J Mater Chem 2006;16:3065–74. https://doi.org/10.1039/b604895a.

[2] Centi G, Perathoner S. Catalysis by layered materials: A review. Microporous Mesoporous Mater 2008;107:3–15. https://doi.org/10.1016/j.micromeso.2007.03.011.

[3] Kumar P, Abuhimd H, Wahyudi W, Li M, Ming J, Li L-J. Review—Two-Dimensional Layered Materials for Energy Storage Applications. ECS J Solid State Sci Technol 2016;5:Q3021–5. https://doi.org/10.1149/2.0051611jss.

[4] Kuthati Y, Kankala RK, Lee CH. Layered double hydroxide nanoparticles for biomedical applications: Current status and recent prospects. Appl Clay Sci 2015;112–113:100–16. https://doi.org/10.1016/j.clay.2015.04.018.

[5] Morioka H, Tagaya H, Karasu M, Kadokawa J, Chiba K. Preparation of hydroxy double salts exchanged by organic compounds. J Mater Res 1998;13:848–51.

[6] Kandare E, Hossenlopp JM. Hydroxy Double Salt Anion Exchange Kinetics : Effects of Precursor Structure and Anion. J Phys Chem B 2005;109:8469–75.

[7] Kaassis AYA, Xu S, Guan S, Evans DG, Wei M, Williams GR. Hydroxy double salts loaded with bioactive ions : Synthesis , intercalation mechanisms , and functional performance. J Solid State Chem 2016;238:129–38. https://doi.org/10.1016/j.jssc.2016.03.019.

[8] Li A, Mu X, Li T, Wen H, Li W, Li Y, et al. Formation of porous Cu hydroxy double salt nanoflowers derived from metal–organic frameworks with efficient peroxidase-like activity for label-free detection of glucose. Nanoscale 2018;10:11948–54. https://doi.org/10.1039/C8NR02832J.

[9] Lu J, Xu C, Tian Z, Lu J, Lina Y, Shi Z. Green emission and Ag^{+} sensing of hydroxy double salt supported gold nanoclusters. Nanoscale 2016;8:5120–5. https://doi.org/10.1039/C5NR07029E.

[10] Crini G. Non-conventional low-cost adsorbents for dye removal: A review. Bioresour Technol 2006;97:1061–85. https://doi.org/10.1016/j.biortech.2005.05.001.

[11] Zhou Y, Ge L, Fan N, Xia M. Adsorption of Congo red from aqueous solution onto shrimp shell powder. Adsorpt Sci Technol 2018;36:1310–30. https://doi.org/10.1177/0263617418768945.

[12] Ahmed MB, Zhou JL, Ngo HH, Guo W, Thomaidis NS, Xu J. Progress in the biological and chemical treatment technologies for emerging contaminant removal from wastewater: A critical review. J Hazard Mater 2017;323:274–98. https://doi.org/10.1016/j.jhazmat.2016.04.045.

[13] Mohapatra DP, Kirpalani DM. Advancement in treatment of wastewater: Fate of emerging contaminants. Can J Chem Eng 2019;97:2621–31. https://doi.org/10.1002/cjce.23533.

[14] J.C. Mu˜noz-Senmache, S. Kim, R.R. Arrieta-P´erez, C.M. Park, Y. Yoon A, Hern´andez-Maldonado J. Activated carbon–metal organic framework composite for the adsorption of contaminants of emerging concern from water. ACS Appl Nano Mater 2020;3:2920–40. https://doi.org/10.1021/acsanm.0c00190.

[15] Erol K, Köse K, Köse DA, Sızır Ü, Satır İT. Adsorption of Victoria Blue R (VBR) dye on magnetic microparticles containing Fe (II)– Co (II) double salt. Desalin Water Treat 2016;57:9307–17. https://doi.org/10.1080/19443994.2015.1030708.

[16] Weeramonkhonlert V, Srikhaow A, Meejoo S. Formation of copper hydroxy double salts derived from metal oxides and their catalytic activity in degradation of methyl orange. Ceram Int 2019;45:993–1000. https://doi.org/10.1016/j.ceramint.2018.09.278.

[17] Lafi R, Charradi K, Amine M, Ben A, Amara H, Hafiane A. Adsorption study of

Congo red dye from aqueous solution to Mg – Al – layered double hydroxide. Adv Powder Technol 2015;27:232–7. https://doi.org/10.1016/j.apt.2015.12.004.

[18] Zheng X, Li X, Li J, Wang L, Jin W, Pei Y, et al. Efficient removal of anionic dye (Congo red) by dialdehyde microfibrillated cellulose / chitosan composite film with significantly improved stability in dye solution. Int J Biol Macromol 2017;107:283–9. https://doi.org/10.1016/j.ijbiomac.2017.08.169.

[19] Mandal S, Calderon J, Marpu SB, Omary MA, Shi SQ. Mesoporous activated carbon as a green adsorbent for the removal of heavy metals and Congo red: Characterization, adsorption kinetics, and isotherm studies. J Contam Hydrol 2021;243:103869. https://doi.org/10.1016/j.jconhyd.2021.103869.

[20] Han D, Zhao H, Gao L, Qin Z, Ma J, Han Y. Preparation of carboxymethyl chitosan / phytic acid composite hydrogels for rapid dye adsorption in wastewater treatment. Colloids Surfaces A Physicochem Eng Asp 2021;628:127355. https://doi.org/10.1016/j.colsurfa.2021.127355.

[21] Ghorai S, Kumar A, Panda AB, Pal S. Effective removal of Congo red dye from aqueous solution using modified xanthan gum / silica hybrid nanocomposite as adsorbent. Bioresour Technol 2013;144:485–91. https://doi.org/10.1016/j.biortech.2013.06.108.

[22] Nagarajan R, Gupta P, Singh P, Chakraborty P. An ethylene glycol intercalated monometallic layered double hydroxide based on iron as an efficient bifunctional catalyst. Dalt Trans 2016;45:17508–20. https://doi.org/10.1039/c6dt03129c.

[23] Tunney JJ, Detellier C. Preparation and characterization of two distinct ethylene

glycol derivatives of kaolinite. Clays Clay Miner 1994;42:552–60. https://doi.org/10.1346/CCMN.1994.0420506.

[24] Fukushima K, Matsuura H. Infrared spectroscopic study of solid films of poly(ethylene glycol) doped with cations. J Mol Struct 1995;350:215–9. https://doi.org/10.1016/0022-2860(94)08487-3.

[25] Kasai A, Fujihara S. Layered Single-Metal Hydroxide / Ethylene Glycol as a New Class of Hybrid Material. Inorg Chem 2006;45:415–8. https://doi.org/10.1021/ic051528d.

[26] Xi Y, Davis RJ. Intercalation of ethylene glycol into yttrium hydroxide layered materials. Inorg Chem 2010;49:3888–95. https://doi.org/10.1021/ic1000478.

[27] Wang C, Zhang X, Xu Z, Sun X, Ma Y. Ethylene Glycol-Intercalated Cobalt Nickel Layered Double Hydroxide Nanosheet Assemblies with Ultrahigh Specific Capacitance : Structural Design and Green Synthesis for Advanced Electrochemical Storage Ethylene Hydroxide Nanosheet Cobalt Nickel with Layer. Appl Mater Interfaces 2015;7:19601–10. https://doi.org/10.1021/acsami.5b03176.

[28] Wang H, Duan W, Wu Y, Tang Y, Li L. Synthesis of magnesium-aluminum layered double hydroxide intercalated with ethylene glycol by the aid of alkoxides. Inorganica Chim Acta 2014;148:163–70. https://doi.org/10.1016/j.ica.2014.04.031.

[29] Wang X, Zhou S, Xing W, Yu B, Feng X, Song L, et al. Self-assembly of Ni – Fe layered double hydroxide / graphene hybrids for reducing fi re hazard in epoxy. J Mater Chem A 2013;1:4383–90. https://doi.org/10.1039/c3ta00035d.

[30] Mallakpour S, Azimi F. Spectroscopic characterization techniques for layered double hydroxide polymer nanocomposites. Elsevier Ltd; 2020. https://doi.org/10.1016/b978-0-08-101903-0.00006-4.

[31] Stafford K, Sing W. Reporting Physisorption Data for Gas/Solid Systems with Special Reference to the Determination of Surface Area and Porosity. Pure Appl Chem 1982;54:2201–2018. https://doi.org/10.1351/pac198254112201.

[32] Alothman ZA. A Review: Fundamental Aspects of Silicate Mesoporous Materials. Materials (Basel) 2012;5:2874–902. https://doi.org/10.3390/ma5122874.

[33] Aouni A, Fersi C, Cuartas-Uribe B, Bes-Pía A, Alcaina-Miranda MI, Dhahbi M. Reactive dyes rejection and textile effluent treatment study using ultrafiltration and nanofiltration processes. Desalination 2012;297:87–96. https://doi.org/10.1016/j.desal.2012.04.022.

[34] Miyata S. Anion-exchange properties of hydrot alcite-like compounds. Clays Clay Miner 1983;31:305–11. https://doi.org/10.1346/CCMN.1983.0310409.

[35] Armbruster MH, Austin JB. The Adsorption of Gases on Plane Surfaces of Mica. J Am Chem Soc 1938;60:467–75. https://doi.org/10.1021/ja01269a066.

[36] Freundlich HMF. Over the adsorption in solution. J Phys Chem 1906;57:385–470.

[37] Olalekan AP, Olatunya A, Ekiti A, Dada AO. Langmuir , Freundlich , Temkin and Dubinin – Radushkevich Isotherms Studies of Equilibrium Sorption of Zn^{2+} Unto Phosphoric Acid Modified Rice Husk. J Appl Chem 2012;3:38–45. https://doi.org/10.9790/5736-0313845.

[38] Ayawei N, Ebelegi AN, Wankasi D. Modelling and Interpretation of Adsorption Isotherms. J Chem 2017;2017:1–11. https://doi.org/10.1155/2017/3039817.

[39] Lagergren S. Zur theorie der sogenannten adsorption geloÈster stoffe. Zeitschr f Chem Und Ind Der Kolloide 1907;2:15–15. https://doi.org/10.1007/BF01501332.

[40] Ho YS, Mckay G. Kinetic models for the sorption of dye from aqueous solution by wood. Process Saf Environ Prot 1998;76:183–91. https://doi.org/10.1205/095758298529326.

[41] Zubair M, Daud M, McKay G, Shehzad F, Al-Harthi MA. Recent progress in layered double hydroxides (LDH)-containing hybrids as adsorbents for water remediation. Appl Clay Sci 2017;143:279–92. https://doi.org/10.1016/j.clay.2017.04.002.

[42] Sheela T, Nayaka YA, Viswanatha R, Basavanna S, Venkatesha TG. Kinetics and thermodynamics studies on the adsorption of Zn(II), Cd(II) and Hg(II) from aqueous solution using zinc oxide nanoparticles. Powder Technol 2012;217:163–70. https://doi.org/10.1016/j.powtec.2011.10.023.

[43] Kim SH, Choi PP. Enhanced Congo red dye removal from aqueous solutions using iron nanoparticles: Adsorption, kinetics, and equilibrium studies. Dalt Trans 2017;46:15470–9. https://doi.org/10.1039/c7dt02076g.

Chapter 5 SYNTHESIS AND CHARACTERIZATION OF PMMA/Zn-Cu LDH COMPOSITES: MORPHOLOGICAL, THERMAL AND ADSORPTION PROPERTIES

5.1 Introduction

Over the past few years research and development concerning polymer composites have received considerable attention. In order to meet the increasing demands for unique materials, composites were developed with superior thermal, mechanical, and adsorption properties [1]. Composite materials are combinations of two or more distinct materials with the purpose of creating a new material that exhibits enhanced and tailored properties. Polymer/layered materials belong to new class of composite materials where the addition of inorganic fillers result in enhanced chemical, mechanical, thermal, and optical properties of the material in comparison to the neat polymer [2]. The incorporation of inorganic fillers in polymer matrices led to the application of polymer composites in various fields such as environmental remediation, packaging and automotive industries, etc.

Poly(methyl methacrylate) (PMMA) is an amorphous, colorless material that has excellent thermal properties and is extremely resistant to sunlight and has been extensively used in the fields of dentistry, construction buildings, automotive parts, home appliances, etc. [3]. Considering these factors, researchers selected PMMA as the host matrix for preparing enormous advanced polymer composite materials dispersed with appropriate amounts of inorganic and/or organic nanofillers. Most of the polymer composite studied till date are synthesized using cationic layered materials like silicates, montmorillonite, etc. whereas limited groups have studied the behavior of anionic layered materials like layered double

hydroxides (LDH) incorporated polymer composites [4]. A study by Sundaram and Dharmalingam reported that PMMA/clay nanocomposite act as a potential sorbent for the uptake of cationic dyes (amido black 10B and malachite green) [5]. Lin *et al.* synthesized PMMA/Na^+–montmorillonite (MMT) membranes acting as cation exchangers and carried out the adsorptive removal of methyl violet dye [6].

In preparing multifunctional polymer/layered composites, LDH is considered to be the most preferred layered material due to its tunable properties. Manzi-Nshuti *et al.* demonstrated that the addition of Al-based LDH enhanced the thermal, morphological, fire retardant, and mechanical properties of PMMA nanocomposite in comparison to neat polymer [7]. Barik *et al.* reported that PMMA reinforced with Mg/Al LDH resulted in improved thermal stability and reduced oxygen permeability enabling the nanocomposite to act as an efficient material for packaging application [8]. In literature mostly groups have studied the applications of PMMA/LDH composites in packaging industry, flame retardant materials, energy storage, etc., whereas their application in environmental remediation is yet to be explored [2],[9].

Water pollution is a significant problem associated with the food industry due to the large volumes of effluent discharged from the industry. In addition to being easily visible even in extremely diluted forms, dyes are non-biodegradable and are almost always toxic to microorganisms, humans, and aquatic life. Additionally, dye-containing effluents may increase biological, chemical, and oxygen needs in water sources [10]. Thus, it is crucial to eliminate dye contaminants before they are released into the environment. In the food industry, natural or synthetic dyes are often used to improve food's appearance and make it more appealing and appetizing by correcting or enhancing its natural color. Brilliant

black (BB) BN is a diazo anionic food dye which is prevalently used in food processing [11]. The presence of lone pairs of electrons in its chemical structure makes BB dye capable of bonding with and mobilizing toxic metals in the aquatic environment as well as triggering intolerance reactions and worsening illnesses such as asthma. In addition, there is very little literature concerning the removal of BB dye, while plenty of literature is available regarding the uptake of other dyes [12].

The sequestration of dyes from water resources can be accomplished through a number of processes, including biological, chemical, and physical ones. Adsorption is one of the most prevalent methods employed for environmental remediation and adsorbents such as activated carbon, metal hydroxide sludge, fly ash, etc. have been utilized by researchers for the treatment of industrial wastewater [13]. In the last few decades, it has been reported that polymer/composite materials can act as potential adsorbents for wastewater remediation.

The aim of the present study is four-fold. Firstly, PMMA has been synthesized via free radical polymerization using H_2O_2 solution as an oxidant instead of benzoyl peroxide which is traditionally used for PMMA preparation and is a more toxic precursor. Secondly, PMMA/Zn-Cu LDH composites (with 10% and 20% loading of LDH) have been prepared via solvent blending method where acetone has been used as the solvent. Thirdly, morphological, structural, and thermal properties of synthesized composites were investigated using FTIR, PXRD, SEM/EDX, and TGA analyses. Furthermore, i an attempt has been made to study the potential application of PMMA/LDH composite materials in wastewater treatment. Therefore, the composite was utilized for the sorptive removal of Brilliant black BN (food dye) from synthetic wastewater system.

5.2 Experimental Section

5.2.1 Materials and method

Methyl methacrylate (MMA) and Brilliant Black BN dye were obtained from CDH, whereas $Zn(CH_3COO)_2.2H_2O$, $Cu(CH_3COO)_2.H_2O$, and H_2O_2 were purchased from Merck.

5.2.2 Preparation of Poly(methyl methacrylate) (PMMA)

To 10 mL methyl methacrylate (MMA) solution, 3 mL 30% H_2O_2 was added and was stirred magnetically at 80°C in air atmosphere till polymerization process was complete. The obtained viscous solution was then cooled to room temperature and the dried product was later crushed into fine powder to get powdered poly(methyl methacrylate) (PMMA) polymer. The diagrammatic illustration of synthesis of PMMA is presented in Figure 5.1a.

5.2.3 Preparation of PMMA/LDH composites

Zn/Cu LDH was prepared by hydrolysis route [14]. PMMA/LDH composites were prepared by solvent blending approach with 10 wt % and 20 wt % of Zn/Cu LDH loading (relative to PMMA) using acetone as a solvent. 0.5g of synthesized PMMA was added to 15 mL acetone and stirred till it dissolved completely. After that, a desired amount of LDH was added to PMMA solution and ultrasonicated for one and a half hour to get a completely dispersed solution. The reaction mixture was again stirred for 2 hours and later dried at room temperature to obtain the desired product. The pure polymer and its composites with 10 and 20 wt % are referred as PMMA, PML10, and PML20, respectively. Figure 5.1b shows the procedure for synthesis of polymer/LDH composites.

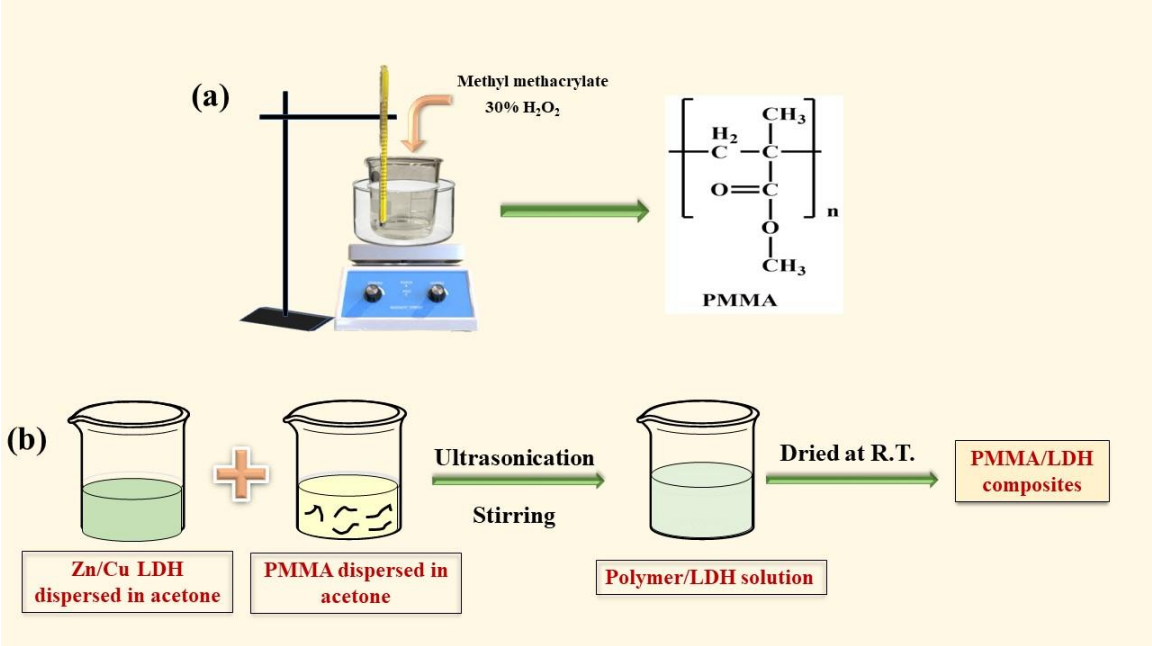

Figure 5.1 Schematic representation for synthesis of (a) pure PMMA and (b) PMMA/LDH composites.

5.2.4 Ultrasound-assisted adsorption experiment

Batch adsorption studies were performed using different starting concentrations of BB dye and all experiments were performed in a bath ultrasonicator. The impact of following parameters was studied on dye sequestration: pH of dye solution = 3 to 11, sonication time = 0 to 30 minutes, sorbent dose = 0.05 to 01 g, and dye concentration = 10 to 60 mg/L. The starting and equilibrium concentrations of BB dye were recorded using a spectrophotometer at 572 nm (λ_{max}) wavelength. The mixture was withdrawn at predetermined intervals and analyzed using UV–Vis absorption spectrophotometer. Following equations were utilized to compute the percent removal efficiency and adsorption capacities (q_e and q_t in mg/g) of the synthesized adsorbent:

$$\text{Removal efficiency (\%)} = \frac{\text{Co-Ce}}{\text{Co}} \times 100\ \% \qquad (5.1)$$

$$q_e = \frac{C_o - C_e}{W} \times V \quad (5.2)$$

$$q_t = \frac{C_o - C_t}{W} \times V \quad (5.3)$$

Where C_e and C_o, and C_t stand for dye concentration at equilibrium, initial stage and at time t, respectively. W denotes the amount of adsorbent and V is the volume of dye solution in mL.

5.2.2.1 Isotherm study

The outcomes of the sorption experiment were examined using Langmuir isotherm (LI) and Freundlich (FI) isotherm models and the appropriate model was selected on the basis of linear regression. Based on the LI hypothesis, there would be homogenous adsorption with single layer formation on the sorbent's surface and there would be no molecular interactions between the adsorbate and the active sites. The linear form of LI model is given as follows:

$$\frac{C_e}{q_e} = \frac{1}{q_m K_L} + \frac{C_e}{q_m} \quad (5.4)$$

where adsorption energy constant is denoted by K_L (L/g), and the maximum adsorption capacity is demoted by q_m (mg/g).

In accordance with FI model, a multi-layered adsorption occurs on the surface of adsorbent due to interactions between molecules that have been adsorbed. The FI expression is an exponential equation, so adsorbate concentration on the adsorbent surface increases as a function of adsorbate concentration. Eq. 5.5 represents the linearized form of FI model.

$$\ln q_e = \ln K_F + \frac{1}{n} \ln C_e \quad (5.5)$$

In the above equation, n represents the heterogeneity factor and K_F represents the Freundlich constant.

5.2.2.2 Kinetic study

Using kinetic models, the adsorption data were tailored to determine the pattern of adsorption kinetics. The linearized forms of PFO and PSO models are given in the following equations:

$$\ln(q_e - q_t) = \ln q_e - K_1 t \quad (5.6)$$

$$\frac{t}{q_t} = \frac{1}{K_2 q_e^2} + \frac{t}{q_e} \quad (5.7)$$

where K_1 (min^{-1}) (PFO rate constant), K_2 (g mg^{-1} min^{-1}) (PSO rate constant) and q_e (adsorption capacity, mg/g) were calculated based on the intercept and slope of the plots.

5.3 Results and Discussion

5.3.1 Structural and morphological properties

The PXRD patterns of pure PMMA, Zn/Cu LDH, and PMMA/LDH composites (PML10 and PML20) are presented in Figure 5.2a. The broad peaks at 2θ values of 14 and 30° correspond to the amorphous nature of pure PMMA. The synthesized PMMA/LDH composites showed the predominant peaks of both PMMA and LDH. However, with increase in the concentration of LDH the intensity of basal reflection of Zn/Cu LDH tends to increase. The observed trend can be accredited to the exfoliation of LDH layers during composite formation.

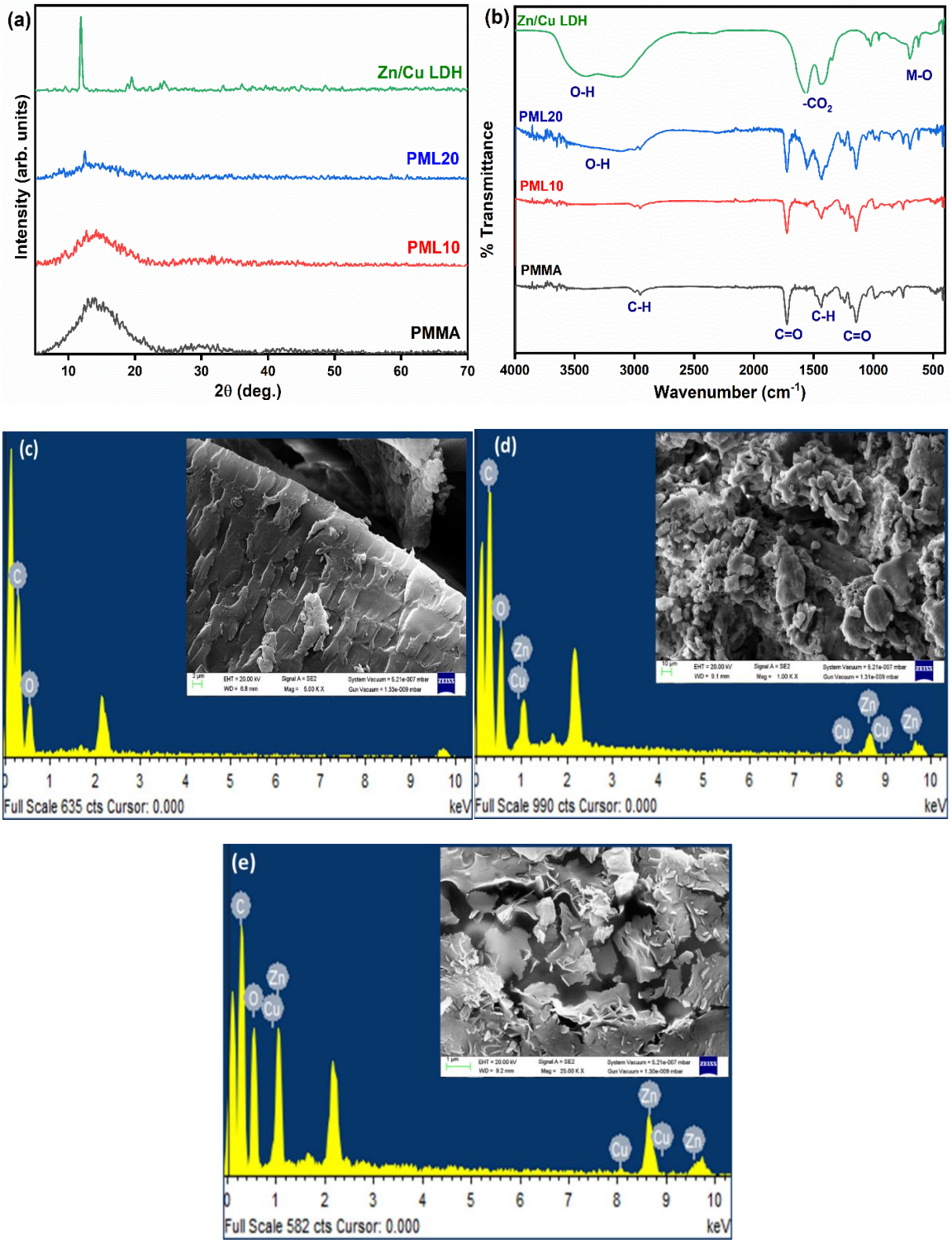

Figure 5.2 (a) PXRD pattern, (b) FTIR spectra, and (c)-(e) SEM/EDX analysis of pure PMMA, PML10, and PML20.

The FTIR spectra of PMMA, LDH, and PMMA/LDH composites are presented in Figure 5.2b. The occurrence of characteristic peaks of PMMA in the FTIR spectrum confirmed the successful synthesis of pure polymer. The weakly intense peaks centred at 3000 and 2953 cm^{-1} correspond to the C-H stretching vibrations of methyl and methylene groups whereas a strong band at 1725 cm^{-1} is attributed to the presence of carbonyl group in the polymer [4]. Other peaks at 1433 and 1145 cm^{-1} can be accredited to O-CH_3 deformation and O-CH_2 stretching vibrations, respectively. However, Zn/Cu LDH exhibit broad and sharp bands around 3500 and 1600-1400 cm^{-1} corresponding to the hydroxy groups present in LDH and acetate groups, respectively conforming the presence of acetate ions in inter gallery region. It can be observed that the synthesized composites exhibit the characteristic bands of both PMMA and Zn/Cu LDH. All composites synthesized shows signature bands due to both PMMA and LDH. Thus, it can be concluded that the PMMA/LDH composites were successfully prepared.

The surface morphology of neat PMMA, Zn/Cu LDH and PMMA/LDH composites was studied using SEM analysis and the micrographs are presented in Figure 5.2c-e. The surface of neat PMMA is relatively smooth and does not exhibit any microstructure [15]. SEM images of PMMA composites indicate that LDH particles are randomly distributed within the polymer matrix and as the LDH loading is increased the amount of dispersion of LDH into the polymer increases. EDX results confirmed the dispersion of zinc and copper metal ions in the synthesized PMMA composites.

5.3.2 Thermal stability

One of the commonly used techniques for assessing thermal stability of different materials and assessing a polymer's decomposition at various temperatures is thermogravimetric

analysis. TGA thermograms of pure PMMA, Zn/Cu LDH, and PMMA/LDH composites are given in Figure 5.3a. It is evident from the thermogravimetric (TG) trace that the sample was losing weight steadily in three distinct steps with increasing temperature. The first spanning from 100 to 190 °C was attributed to the elimination of water molecules from the surface and interlayer region. The second weight loss step from 190-220°C corresponds to dihydroxylation of hydroxide layers and the final stage corresponds to decomposition of interlayer anion. It can be observed that the major weight loss of pure PMMA occurred in the range of 304-436 °C and approximately 4% residue is left beyond 450 °C. The thermogram displayed that there occurred a two-step degradation of PMMA/LDH composites where in the first step, weight loss occurs due to the removal of surface absorbed and interlayer water molecules of the layered material in the temperature range of 150-250 °C. The second weight loss step ranging from 250-580 °C resulted in formation of char on decomposition of organic component of the composite. After complete degradation only inorganic residue is left resulting in flat curves above 600°C.

In Figure 5.3b, the derivative curves of pure PMMA and its composites are given, where the peaks denote the maximum degradation temperature, i.e., T_{max}. Compared to pure PMMA, the composites show increased value of T_{max} and the decomposition temperatures for PMMA, PML10 and PML20 was found to be to be 356.36, 362.95, and 369.12 °C respectively. The results indicate that PMMA composites are more thermally stable than pure PMMA and the stability increases with increase in LDH loading.

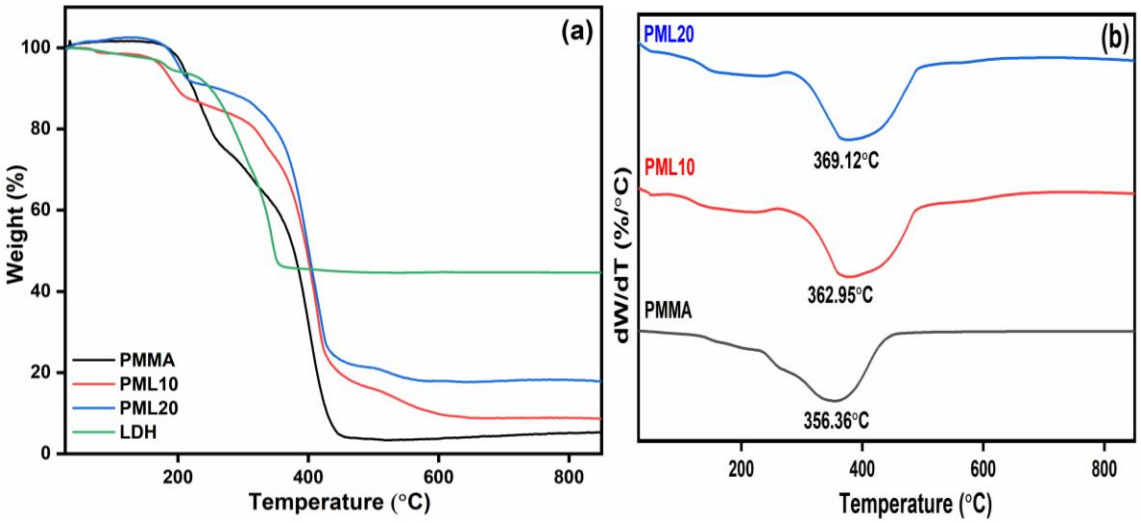

Figure 5.3 (a) TGA thermogram and (b) Derivative of TGA plot.

The TGA thermogram can also be utilized to govern the factors determining the thermal stability of materials, including char yield and IPDT. Doyle proposed an Eq. (5.8) for the determination of the integral procedure decomposition temperature (IPDT) from TGA thermograms which can be used to evaluate the inherent thermal stability of polymeric composite materials [16].

$$\text{IPDT } (℃) = A^{*}K^{*}\,(T_f\text{-}T_i) + T_i \qquad (5.8)$$

Where $A^{*} = \frac{S1+S2}{S1+S2+S3}$ and $K^{*} = \frac{S1+S2}{S1}$

*A** and *K** can be defined as the area ratio of experimental curve divided by total TGA thermogram and coefficient of *A**, respectively. The initial and final temperature of experiment are given by T_i and T_f, respectively. In Figure 5.3a, areas S1, S2, and S3 indicate the 3 regions into which the TGA plot was divided. The thermal analysis data is shown in Table 1 where it can be seen that with increasing LDH content in the PMMA composites the IPDT increases (Figure 5.4b). Therefore, it can be stated that with the

addition of inorganic content into the polymer matrix the thermal stability of composites increases.

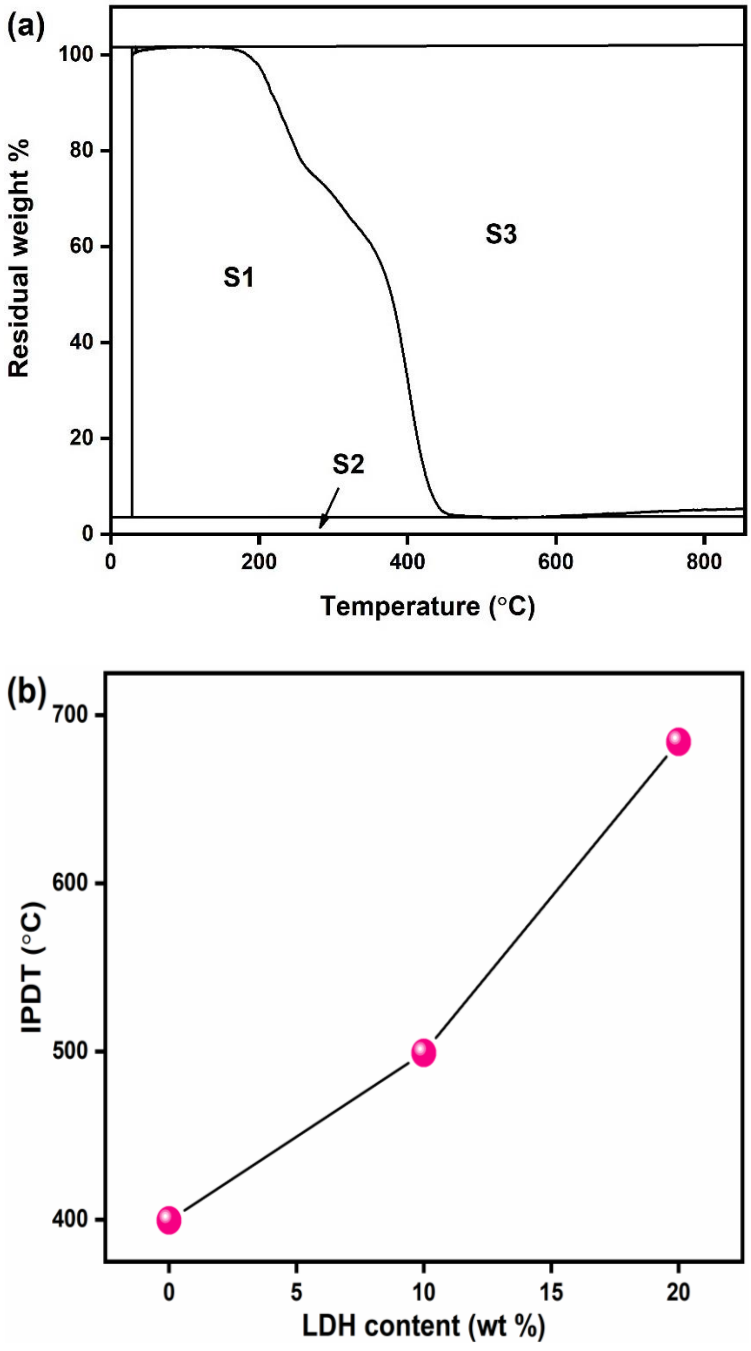

Figure 5.4 (a) Representation of S1, S2, and S3 for IPDT determination and (b) linear dependence of LDH content on thermal stability of PMMA composites.

Table 5.1 TGA data of PMMA and its composites.

Materials	T_{max} (°C)	IPDT (°C)	Char yield (weight%)
PMMA	356.36	399.55	3.76
PML10	362.95	499.24	17.89
PML20	369.12	684.17	24.89

5.3.3 Adsorption behavior

5.3.3.1 Factors affecting uptake of Brilliant Black dye

Influence of pH. Since pH affects the properties of both adsorbent and adsorbate, it acts as one of the crucial factors which influences the adsorption process. The pH variation associated with dye adsorption is therefore consistent with the nature of the solute-surface interaction, which can be either electrostatic or non-electrostatic. The impact of pH on BB dye removal was studied in the range of pH 3 to 11. Based on Figure 5.5a, it is evident that the maximum dye removal efficiency occurred at pH 9 (90 %). When the pH is increased from 2 to 9, removal efficiency increases and then declines sharply as it increases further. It is possible that OH^- ions could compete with anionic dye molecules at higher pH values due to an abundance of hydroxyl ions.

Influence of starting concentration of dye. In the removal process, the starting concentration of dye is crucial in predicting how it will affect equilibrium adsorption capacity (q_e). The effect of initial dye concentration was studied at pH 9 with 0.1 g of adsorbent. From Figure 5.5b it can be deduced that when the initial dye concentration is low there are sufficient number of available adsorption sites on the adsorbent material, allowing for effective dye removal. However, as the dye concentration increases, the number of available adsorption sites becomes limited, and the adsorbent becomes

saturated. This leads to reduced removal efficiency as the adsorption sites become occupied.

Influence of sonication time. The impact of sonication time on the removal efficiency and adsorption capacity of the sorbent is presented in Figure 5.5c. The dye uptake rapidly increases within first 2 minutes and slowly reached equilibrium in 30 minutes. The reason for this is that at the beginning, there is an abundance of adsorption sites and a high concentration of BB, but after 2 minutes, both BB concentration and number of adsorption sites decreased simultaneously.

Influence of amount of adsorbent. When analysing adsorption isotherms as well as in practical applications, absorbent mass is a crucial parameter to optimize. Following conditions were used to study the impact of adsorbent amount on removal efficiency: pH = 9, dye concentration = 10 mg/L, sonication time = 30 minutes and amount of sorbent = 0.05, 0.1 and 0.2 g. The experimental results suggested that there occurs a decrease in adsorption capacity (q_e) and increase in removal efficiency (% R) with increase in the adsorbent dosage (Figure 5.5d). Increasing the amount of sorbent results in enhanced removal efficiency due to the increased number of adsorption sites and functional groups.

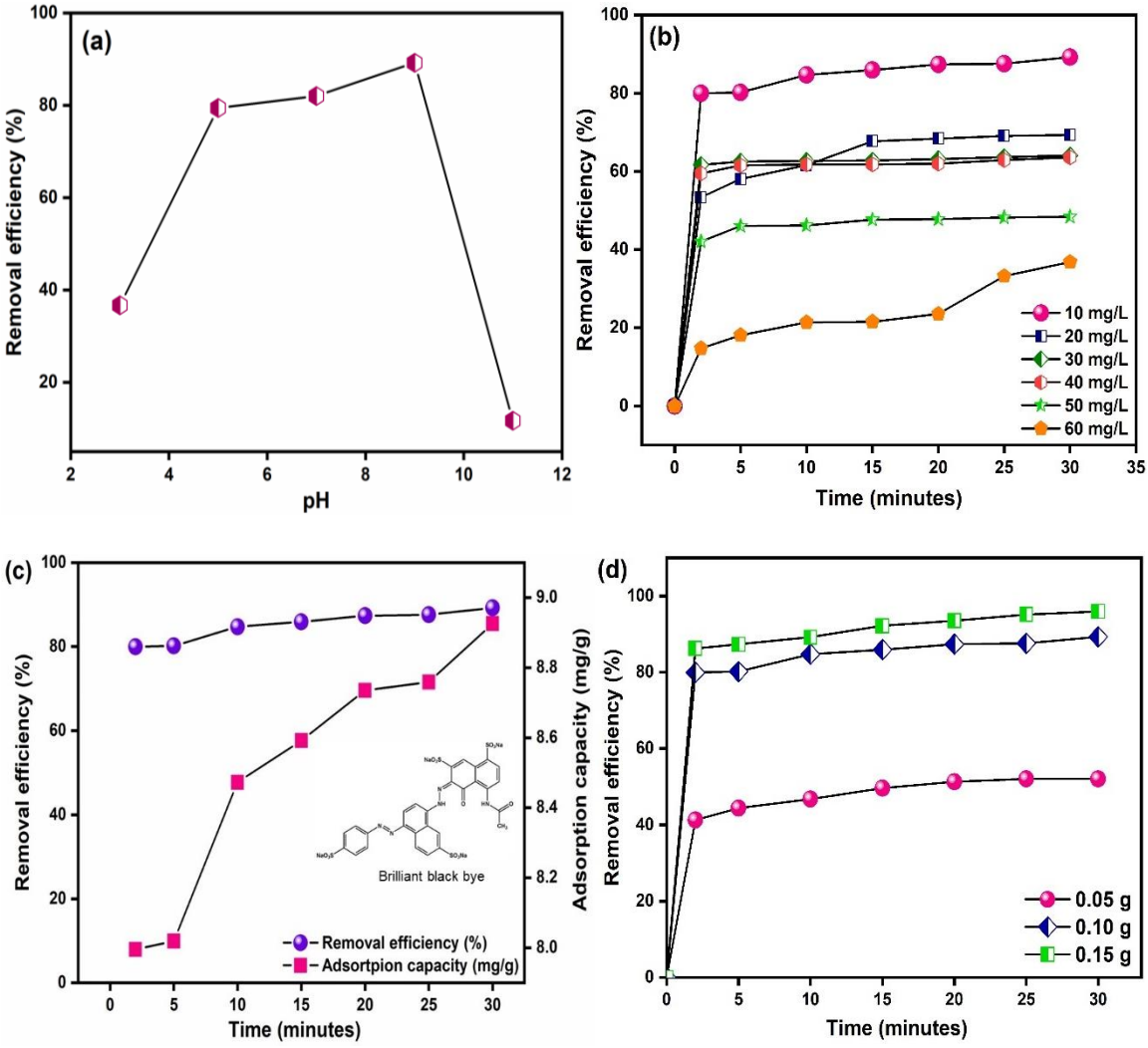

Figure 5.5 Influence of (a) pH, (b) dye concentration, (c) time, and (d) adsorbent dosage on removal efficiency of BB dye.

The BB dye uptake was also studied using pure PMMA and PML10 composite and the results were compared with that of PML20. The sorption experiment was performed at similar reaction conditions (dye concentration = 10 mg/L, pH = 9, sonication time = 30 min) where fixed amount of PMMA, PML10, and PML20 were added. The results obtained are depicted in Figure 5.6 where it can be seen that the incorporation of Zn/Cu LDH into the polymer matrix results in high removal efficiency towards BB dye. Pure PMMA

exhibits poor adsorption properties. With 10 wt % loading of LDH it was increased to 30 % whereas with further increase in LDH loading the removal efficiency was increased approximately up to 90 %.

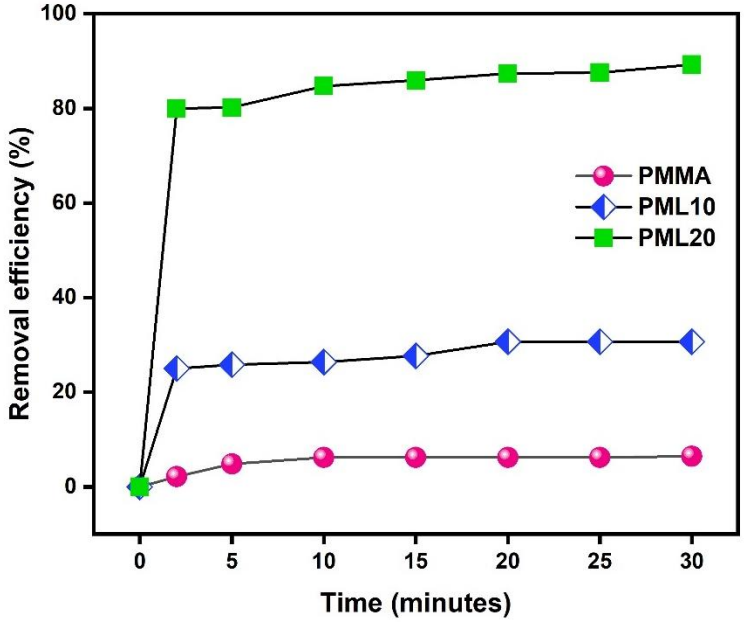

Figure 5.6 Comparison of removal efficiencies of PMMA, PML10, and PML20.

5.3.3.2 Isotherm behavior

The interaction between BB dye and PMMA/LDH adsorbent was examined utilizing Langmuir and Freundlich isotherms. Table 5.2 presents the results of BB dye adsorption on PML20. The linear LI model is accompanied by a high correlation coefficient (R^2 = 0.9806) and exhibits a maximum monolayer adsorption capacity (q_m) of 25 mg/g (Figure 5.7a). FI is another model used to assess the adsorption behavior of BB dye onto PML20's surface. According to the ln q_e vs ln C_e plot shown in Figure 5.6b the values of K_F and 1/n were calculated from the intercept and slope. In accordance with the results obtained it can be stated that the adsorbent's surface adsorb BB dye molecules in monolayer fashion.

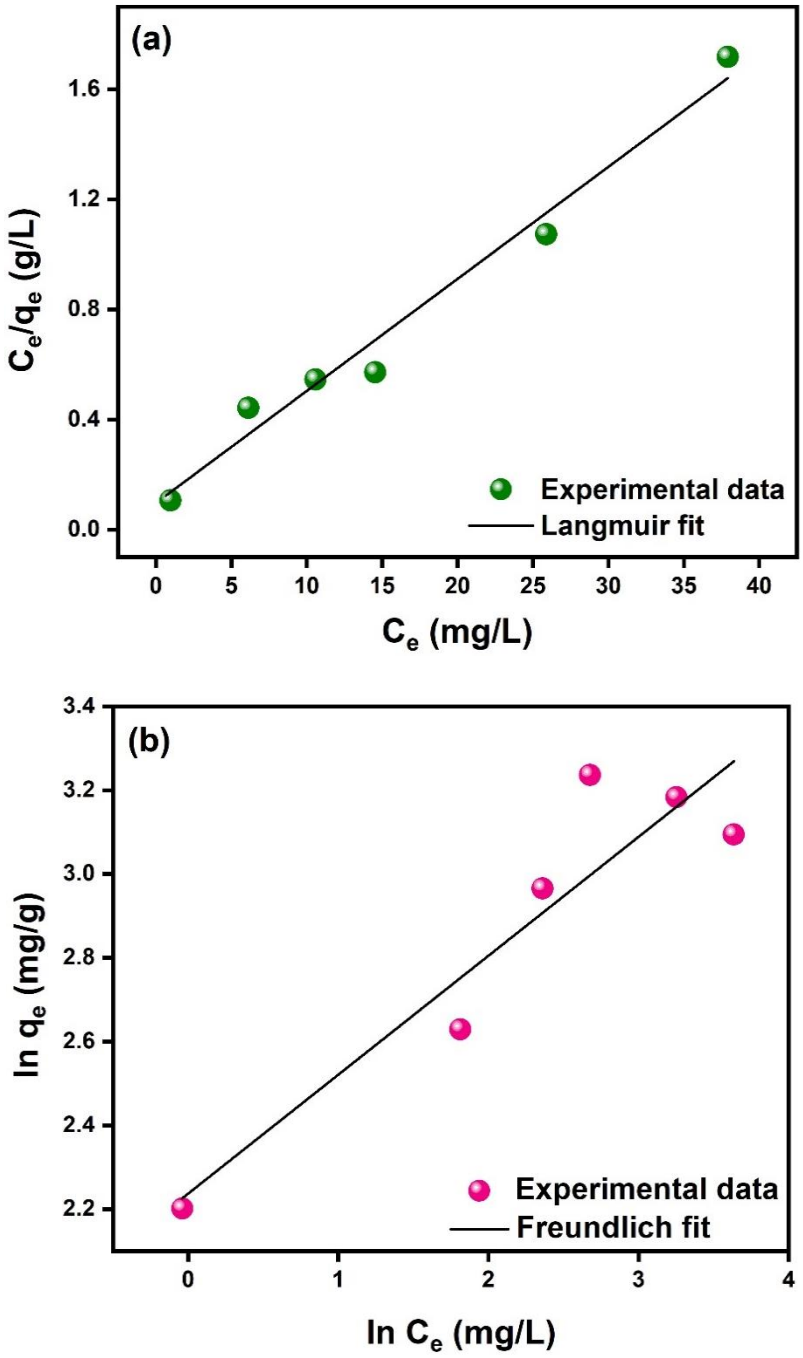

Figure 5.7 Linear plots of (a) Langmuir and (b) Freundlich isotherm for BB dye uptake.

Table 5.2 Equilibrium constants for CR dye removal.

Adsorption isotherms	Plot	Slope and intercept	Parameters

Langmuir	C_e/q_e vs C_e	Slope =	q_{max} (mg/g)	25
$\frac{C_e}{q_e} = \frac{1}{q_{max}K_L} + \frac{C_e}{q_{max}}$		$1/q_{max}$	K_L (L/mg)	0.44
		Intercept =	R^2	0.9806
		$1/(K_L q_{max})$		
Freundlich	ln q_e vs ln	Slope = 1/n	K_F (mg/g) $(L/mg)^{1/n}$	9.29
$\ln q_e = \ln K_F + \frac{1}{n} \ln C_e$	C_e	Intercept = ln	1/n	0.28
		K_F	R^2	0.8650

5.3.3.3 Kinetic behavior

PFO and PSO models have been employed to study the kinetic behavior of the adsorption process. The linear graph for PFO shown in Figure 5.8a illustrates that the rate constant, K_1, and q_e can be calculated from ln (q_e - q_t) vs time (t) plot. Figure 5.8b shows the slope and intercept of the t/qt vs t plot, which are used to calculate equilibrium adsorption capacity (q_e) and second order rate constant (K_2). The values obtained from PFO and PSO models for rate constants, adsorption capacities and related R^2 are presented in Table 5.3 where it can be seen that the PSO exhibits the highest R^2 values, concluding that it is the most suitable kinetic model. Moreover, the q_e value obtained from PSO model (9.00 mg/g) is in accordance with the experimentally obtained value (9.04 mg/g).

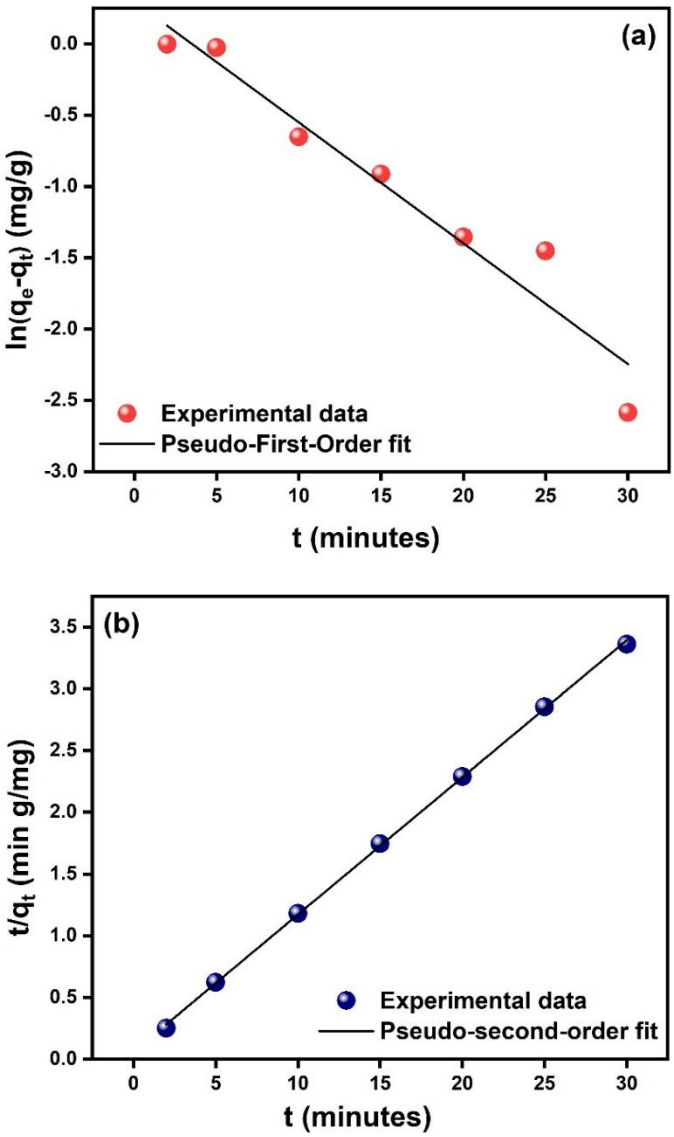

Figure 5.8 Plots of (a) PFO and (b) PSO kinetic models.

Table 5.3 Kinetic parametric values for BB dye uptake.

Kinetic model	**Plot**	**Slope and intercept**	**Parameters**	
Pseudo-first order	ln (q_e-	Slope = -K_1	K_1 (min^{-1})	0.07
$\ln(q_e\text{-}q_t) = \ln q_e\text{-}\ K_1 t$	q_t) vs t	Intercept =	q_e (mg/g)	1.33
		ln q_e	R^2	0.9417

Pseudo-second order $\frac{t}{q_t} = \frac{1}{K_2 q_e^2} + \frac{t}{q_e}$	t/q_t vs t	Slope = $1/q_e$	K_2 (g mg^{-1} min^{-1})	0.21
		Intercept = $1/(K_2 q_e^2)$	q_e (mg/g)	9.00
			R^2	0.9996

5.3.3.4 Comparison with reported sorbents for BB dye

The removal efficiency of synthesized material for BB dye sequestration was also compared with the adsorbents reported in literature which are presented in Table 5.4. The q_{max} obtained in the present study is almost the highest among the previously reported sorbents.

Table 5.4 Comparison of maximum sorption capacity of sorbents reported in literature for BB dye sequestration.

Material	**Maximum adsorption capacity (q_{max}) (mg/g)**	**Time**	**pH**	**References**
Chitosan-lignin-TiO_2	15.80	30 min	5.8	[17]
Iron-modified hydrochar	10.49	26.30 min	-	[11]
Activated pine wood	2.50	24 hours	2	[10]
Acid-activated-kaolinitic clay	1.05	24 hours	7	[18]
Chemically activated biochar	23.40	24 hours	2	[19]

PMMA/ZnCu LDH	**25**	**30 min**	**9**	**This work**

5.4 Conclusions

The current work summarizes the synthesis of PMMA via free radical polymerization using H_2O_2 solution as an oxidant. Afterwards, PMMA/Zn-Cu LDH composites (with 10% and 20% loading of LDH) were successfully synthesized using solvent blending method where acetone was used as the solvent. The structural, morphological, and thermal properties of synthesized composites were studied using PXRD, FTIR, SEM/EDX, and TGA analyses. Furthermore, the potential application of PMMA/LDH composite material in wastewater treatment was studied. The composite material was later utilized as an adsorbent for the removal of Brilliant black BN (BB) dye. The results obtained suggested that the incorporation of Zn/Cu LDH into the polymer matrix results in high removal efficiency towards BB dye. Pure PMMA exhibits poor adsorption properties whereas with 10 wt % loading of LDH it was increased to 30 % however, with further increase in LDH loading, i.e., 20 wt %, the removal efficiency was increased approximately up to 90 %. Therefore, the synthesized composite can be efficiently used for its real-time application in wastewater treatment.

5.5 References

[1] Zhao G, Huang X, Tang Z, Huang Q, Niu F, Wang X. Polymer-based nanocomposites for heavy metal ions removal from aqueous solution: A review. Polym Chem 2018;9:3562–82. https://doi.org/10.1039/c8py00484f.

[2] Leroux F, Besse J. Polymer interleaved layered double hydroxide: A new emerging

class of nanocomposites. Chem Mater 2001;13:3507–15. https://doi.org/10.1021/cm0110268.

[3] Rajabi M, Mahanpoor K, Moradi O. Thermodynamic and kinetic studies of crystal violet dye adsorption with poly(methyl methacrylate)–graphene oxide and poly(methyl methacrylate)–graphene oxide–zinc oxide nanocomposites. J Appl Polym Sci 2019;136:1–12. https://doi.org/10.1002/app.47495.

[4] Chakraborty S, Kumar M, Suresh K, Pugazhenthi G. Investigation of Structural , Rheological and Thermal Properties of PMMA/ONi-Al LDH Nanocomposites Synthesized via Solvent Blending Method : Effect of LDH Loading. Chinese J Polym Sci 2016;34:739–54. https://doi.org/10.1007/s10118-016-1786-4.

[5] Sundaram EJS, Dharmalingam P. Synthesis and characterization of PMMA polymer/clay nanocomposites for removal of dyes. Asian J Chem 2019;31:2589–95. https://doi.org/10.14233/ajchem.2019.22131.

[6] Lin RY, Chen BS, Chen GL, Wu JY, Chiu HC, Suen SY. Preparation of porous PMMA/Na+-montmorillonite cation-exchange membranes for cationic dye adsorption. J Memb Sci 2009;326:117–29. https://doi.org/10.1016/j.memsci.2008.09.038.

[7] Manzi-Nshuti C, Wang D, Hossenlopp JM, Wilkie CA. Aluminum-containing layered double hydroxides: The thermal, mechanical, and fire properties of (nano)composites of poly(methyl methacrylate). J Mater Chem 2008;18:3091–102. https://doi.org/10.1039/b802553c.

[8] Barik S, Badamali SK, Behera L, Kumar P. Mg – Al LDH reinforced PMMA

nanocomposites : a potential material for packaging industry. Compos Interfaces 2018;6440:1–12. https://doi.org/10.1080/09276440.2018.1439628.

[9] Barik S, Badamali SK, Behera L, Jena PK. Mg–Al LDH reinforced PMMA nanocomposites: a potential material for packaging industry. Compos Interfaces 2018;25:369–80. https://doi.org/10.1080/09276440.2018.1439628.

[10] Al-Ghouti MA, Issa AA, Al-Saqarat BS, Al-Reyahi AY, Al-Degs YS. Multivariate analysis of competitive adsorption of food dyes by activated pine wood. Desalin Water Treat 2016;57:27651–62. https://doi.org/10.1080/19443994.2016.1174742.

[11] Çatlıoğlu FN, Akay S, Gözmen B, Turunc E, Anastopoulos I, Kayan B, et al. Fe-modified hydrochar from orange peel as adsorbent of food colorant Brilliant Black: process optimization and kinetic studies. Int J Environ Sci Technol 2020;17:1975–90. https://doi.org/10.1007/s13762-019-02593-z.

[12] Pandey B, Singh P, Kumar V. Photocatalytic-sorption processes for the removal of pollutants from wastewater using polymer metal oxide nanocomposites and associated environmental risks. Environ Nanotechnology, Monit Manag 2021;16:100596. https://doi.org/10.1016/j.enmm.2021.100596.

[13] Kumar Reddy DH, Lee SM. Water Pollution and Treatment Technologies. J Environ Anal Toxicol 2012;02:2–4. https://doi.org/10.4172/2161-0525.1000e103.

[14] Pandey B, Singh P, Kumar V. Facile synthesis of Zn/Cu and PANI modified layered double hydroxides with insights into structural memory effect property. Bull Mater Sci 2022;45:169. https://doi.org/10.1007/s12034-022-02754-w.

[15] Tripathi SN, Saini P, Gupta D, Choudhary V. Electrical and mechanical properties of PMMA/reduced graphene oxide nanocomposites prepared via in situ polymerization. J Mater Sci 2013;48:6223–32. https://doi.org/10.1007/s10853-013-7420-8.

[16] Doyle CD. Estimating thermal stability of experimental polymers. Anal Chem 1961;33:77–9. https://doi.org/10.1021/ac60169a022.

[17] Masilompane TM, Chaukura N, Mishra SB, Mishra AK. Chitosan-lignin-titania nanocomposites for the removal of brilliant black dye from aqueous solution. Int J Biol Macromol 2018;120:1659–66. https://doi.org/10.1016/j.ijbiomac.2018.09.129.

[18] Issa AA, Abdel-Halim HM, Al-Degs YS, Al-Masri HA. Application of multivariate calibration for studying competitive adsorption of two problematic colorants on acid-activated-kaolinitic clay. Res Chem Intermed 2017;43:523–44. https://doi.org/10.1007/s11164-016-2638-0.

[19] Issa AA, Al-Degs YS, El-Sheikh AH, Al-Reyahi AY, Al Bakain RZ, Abdelghani JI, et al. Application of Partial Least Squares-Kernel Calibration in Competitive Adsorption Studies Using an Effective Chemically Activated Biochar. Clean - Soil, Air, Water 2017;45:1–13. https://doi.org/10.1002/clen.201600333.

Chapter 6 SYNTHESIS AND CHARACTERIZATION OF POLYSTYRENE AND Zn/Cu LDH COMPOSITE FILMS: MORPHOLOGICAL, THERMAL, AND OPTICAL PROPERTIES

6.1 Introduction

During the last few years, there have been enormous advances in the research and development of hybrid materials that combine natural and synthetic polymers with inorganic particles to create multifunctional materials. Polymer/layered inorganic hybrid materials have become the subject of extensive research due to their unique mechanical, thermal, optical, morphological, and physicochemical properties, which are not found in pure polymers or traditional composite materials [1]. Recent studies have demonstrated that the dispersion of layered compounds can alter the properties of polymers. Although most of the studies have investigated the effect of cationic materials like montmorillonite whereas anionic layered materials such as LDHs, have been less explored. Owing to the highly tunable properties of LDHs, they are considered to be among the most suitable filler materials for the synthesis of multifunctional polymer-layered composite systems [2],[3]. The versatility of composition is one of the most attractive features of LDHs since they can be tailored to possess a broad range of desirable properties [4]. Various applications have been explored for LDH-based composites, including energy storage, bioimaging, optoelectronics, hydrogen production, bioremediation, and catalysis. Additionally, LDH-based polymer composites exhibit excellent flame retardancy, excellent thermal stability, and outstanding mechanical properties [5]. A variety of polymers including poly (methyl

methacrylate) (PMMA), poly (vinyl chloride) (PVC), polystyrene (PS), polyethylene (PE), polypropylene (PP), polyamide 6 (PA 6), and polyethylene-vinyl acetate (PEVA) have been thoroughly studied over a range of applications. Manzi-Nshuti *et al.* modified polyethylene (PE) with oleate intercalated Zn/Al LDH to enhance its fire retardancy. It was observed that PE became more thermally stable and fire-resistant when 10 or 20% ZnAl LDH was loaded [6]. A study conducted by Suresh *et al.* studied the mechanical structural, and thermal properties of Co/Al LDH-incorporated PS nanocomposites and reported that the synthesized nanocomposites exhibit enhanced thermal and mechanical properties as compared to pure PS [7]. Synergistic effects between LDH and polymer result in the improvement of these properties of the synthesized composite materials.

A thermoplastic polymer, polystyrene (PS), is a valuable material for large-scale applications owing to its high thermal resistance, low density, and mechanical durability [8]. While there has been abundant research on polymer/LDH composites, few studies have examined PS/ LDH 's optical properties. The exceptional chemical and physical properties of PS have enabled it to be used for the development of optoelectronic devices such as LEDs, solar cells, etc. Researchers have found that the physicochemical properties of the polymer matrix can be enhanced by incorporating uniformly dispersed LDHs in it.

The materials interaction with light plays a significant role in optical applications, as a result of the wide application of optical properties, various researchers focused their studies on this aspect. Polymers can be made to exhibit optical and electrical properties by incorporating inorganic materials into the matrix [9]. In literature, there have only been a few studies so far that investigated the optical properties of PS/LDH composites.

Therefore, an attempt has been made to fabricate PS/LDH composite films to study their optical properties.

In the current work, the solvent casting method was employed to fabricate composite films of PS loaded with 5 and 10% of LDH. The objective of this work was to examine how the Zn/Cu LDH loading affects the structural, morphological, thermal, and optical properties of PS/LDH composites formulated via solvent blending method where xylene is used as a solvent. The synthesized composite films were characterized using different spectroscopic techniques, i.e., PXRD, SEM/EDX, FTIR, and TGA. The optical properties of PS/LDH films were also studied in detail using Photoluminescence spectroscopy.

6.2 Experimental Section

6.2.1 Preparation of Zn/Cu LDH and PS/LDH composite film

The preparation of the Zn/Cu LDH precursor was based on the previously described hydrolysis route [10]. The polystyrene and Zn/Cu LDH composite films were fabricated by solvent casting method where xylene is used as a solvent. Firstly, the desired quantity of Zn/Cu LDH (5 and 10 weight % relative to polystyrene) was added to 10 mL xylene solution and ultrasonicated for three hours. Afterwards, LDH solution was added to PS solution (1g PS in 20 mL Xylene), and stirred for 24 hours. PS/LDH composite films were formed at room temperature by spreading the mixture over a glass plate and leaving it undisturbed. The prepared films were named PS, PSL05, and PSL10 having 0%, 5%, and 10% LDH loading, respectively.

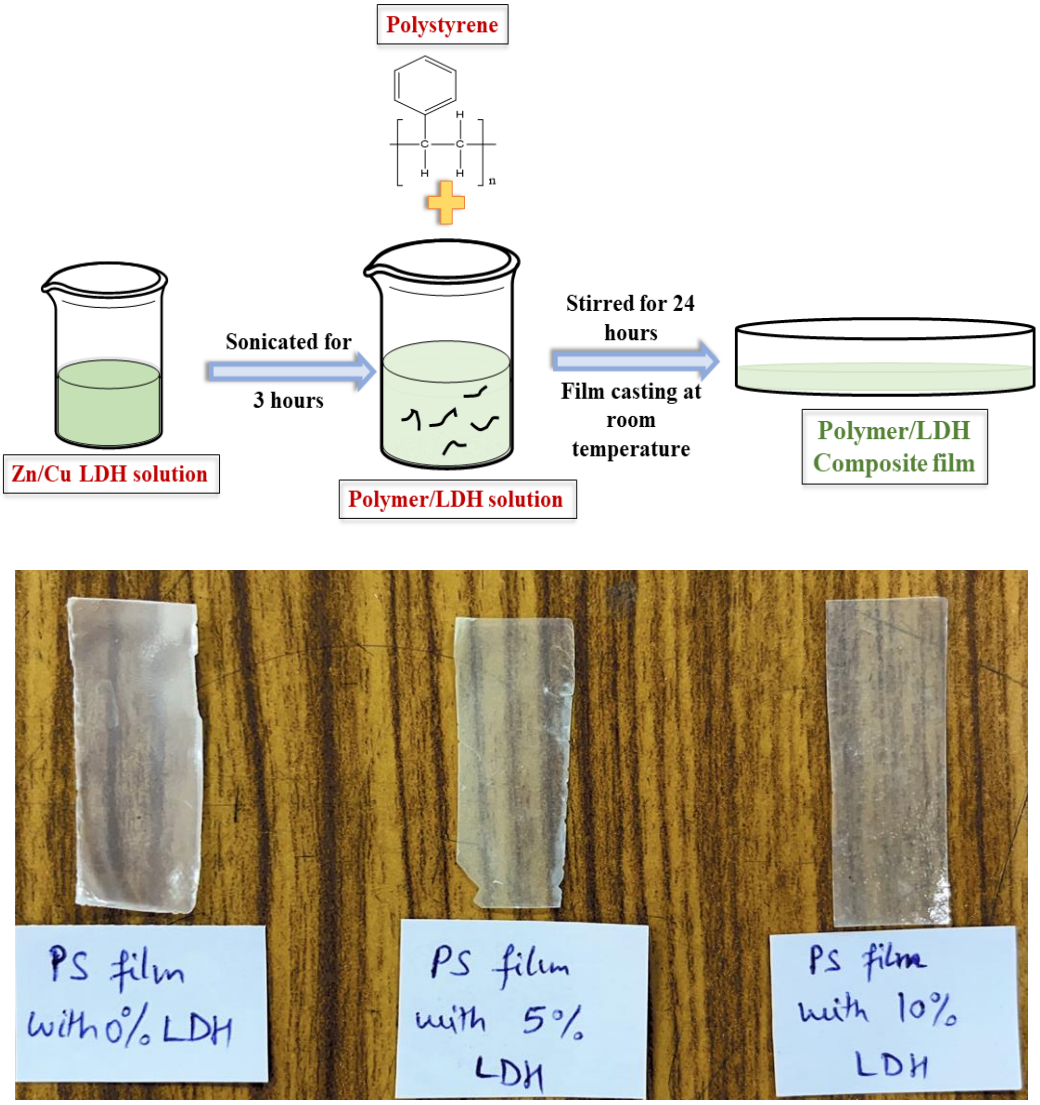

Figure 6.1 Preparation of Polystyrene/LDH composite files with 0%, 5%, and 10% loading of LDH.

6.2.2 Instrumentation

A High-resolution Bruker D8 advanced x-ray diffractometer was used to record PXRD patterns having Cu Kα radiation (λ = 1.5418 Å), with a scan rate and step size of 1.0 second/step and 0.02°, respectively. PerkinElmer (version 10.5.3) spectrometer was used to record FTIR spectra. A PerkinElmer TGA was used at a uniform temperature rate of

10°C per minute in the range 50-900°C under flowing nitrogen for thermal analysis. A Hitachi S-3700 M microscope was used for SEM micrographs and EDS analysis of the samples. An Agilent Technologies, Cary 60 UV–Vis spectrometer was used for optical absorption measurements.

6.3 Results and Discussion

6.3.1 Structural and morphological properties

The PXRD patterns of PS and PS/LDH composites loaded with 5 and 10 wt% of Zn/Cu LDH are depicted in Figure 6.2. In the PXRD pattern of pure polystyrene, a broad peak in the range of 2θ (15-20°) was observed, signifying the amorphous nature of pure PS. However, the appearance of additional reflections of Zn/Cu LDH with weak intensity at 2θ value of 12.5° in the PXRD pattern of PS/LDH composite indicated the formation of intercalated or exfoliated structures [11]. It can further be observed that with increase in the loading of LDH the intensity of peak conforming to LDH increases in the PXRD pattern of PS/LDH composites.

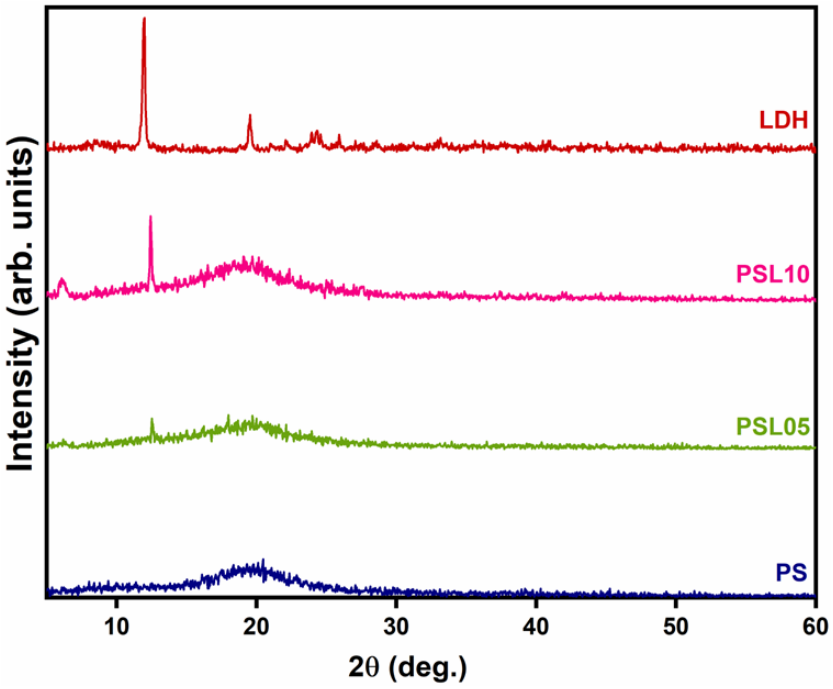

Figure 6.2 PXRD patterns of PS, PSL05 (5% LDH), PSL10 (10% LDH), and Zn/Cu LDH.

The FTIR spectra of pure polystyrene and PS/LDH composites are shown in Figure 6.3. In the FTIR spectrum of polystyrene peak at 3027 cm^{-1} can be observed which corresponds to the aromatic stretching vibration (=C-H) followed by two peaks at 2919 and 2854 cm^{-1} indicating antisymmetric and symmetric vibrations of $-CH_2$ group, respectively. Three peaks at 1600, 1492, and 1448 cm^{-1} can be ascribed to the stretching vibrations of the benzene ring. The out-of-plane bending vibrations of C-H group appeared at 752 and 695 cm^{-1} [12].

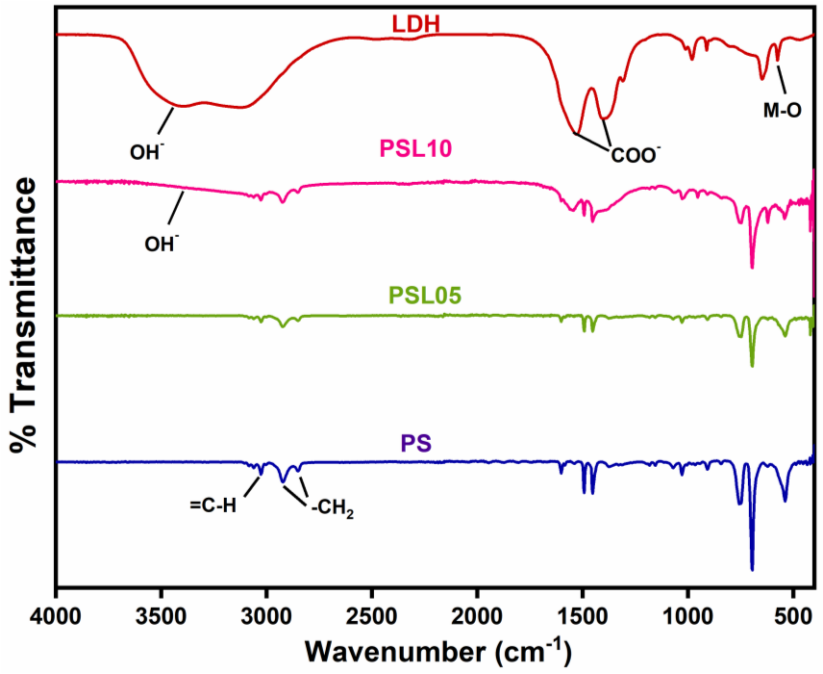

Figure 6.3 FTIR spectra of PS, PSL05 (5% LDH), PSL10 (10% LDH), and Zn/Cu LDH.

However, the typical peak at 3451 cm^{-1} is accredited to the O-H stretching vibrations while the characteristic peaks of carboxylate group (COO^-) can be observed at 1568 and 1472 cm^{-1} in LDH spectrum [13]. FTIR spectra of PS/LDH composites show peaks due to PS (around 3000 and 1500 cm^{-1}) and Zn/Cu LDH (around 3400, 1600, and 500 cm^{-1}). It can be seen that with increased LDH concentration, the intensity of characteristic peaks of PS i.e., vibrations associated with benzene ring decreases, whereas the intensity of peaks attributable to LDH including hydroxyl, acetate, and meta-oxygen bonds increases.

Figure 6.4 presents the SEM micrograph images and EDX analysis of PS, PSL05 (5% LDH), and PSL10 (10% LDH) composite films. The surface of composite films exhibits a dense and homogeneous appearance with better LDH dispersion in polymer matrix [14]. The EDX analysis also confirmed the distribution of metal ions in the composites.

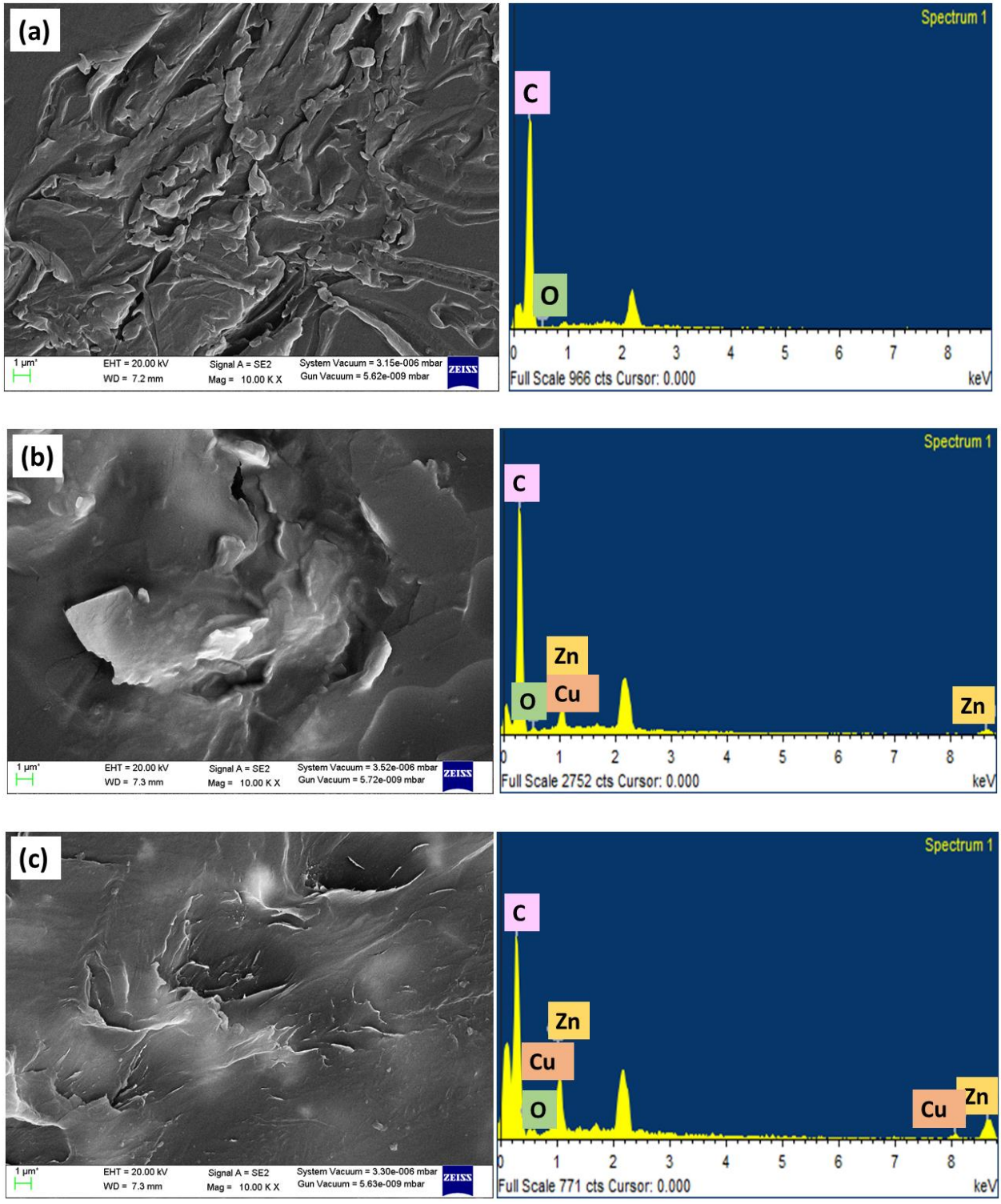

Figure 6.4 SEM micrographs and EDX analysis of (a) PS, (b) PSL05, and (b) PSL10.

6.3.2 Thermal properties

Polymer nanocomposites' thermal stability is considered one of the most important factors both in science and industry that determines their usability. The thermograms of pure PS and composites with varying amounts of LDH (5 and 10 %) are given in Figure 6.5a. Comparing PS composites with pure PS, the TGA curve shows delayed decomposition, i.e., the thermal stability is enhanced. It is also evident that with an increase LDH content the thermal stability of composites increases. This improvement in thermal stability can be attributed to the hindrance effect caused by LDH platelets on low molecular mass molecules during thermal degradation. Additionally, during the degradation of PS/LDH composites, LDH facilitates the formation of carbonaceous layered char [15].

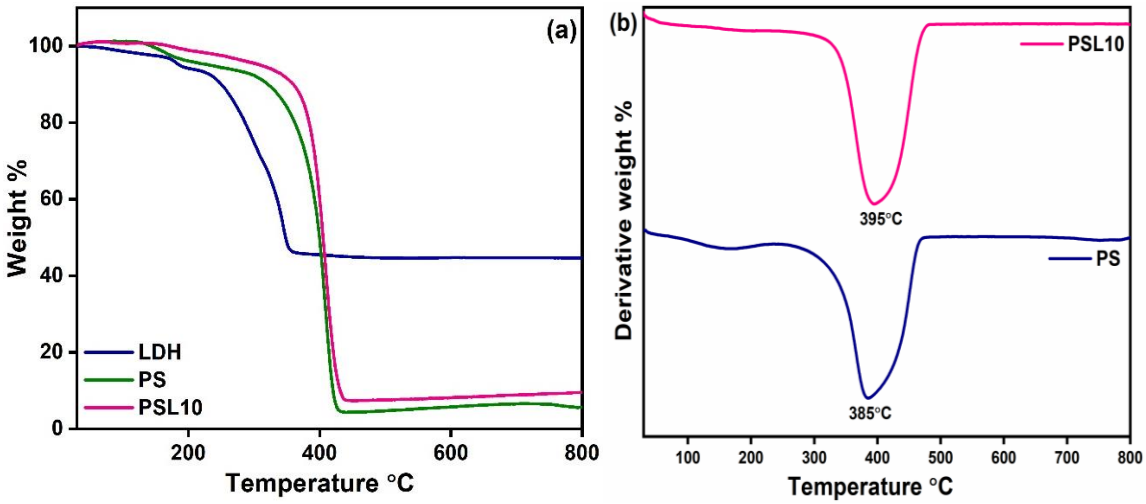

Figure 6.5 TGA plots of PS, PSL10 (10% LDH), and Zn/Cu LDH.

The DTG curves depicted in Figure 6.5b further demonstrate the improved thermal stability of PS composites. The broad and downward peaks indicate the temperature (T_{max}) at which maximum degradation occurs. Pure PS has a T_{max} value of 385°C, whereas PS

nanocomposite with 10 wt % Zn/Cu LDH has a T_{max} value of 395°C, indicating an improvement of 10°C over pure PS [16].

6.3.3 Optical properties

In the emission spectra of Zn/Cu LDH (Figure 6.6a) a broad emission peak can be observed in the range of 400-550 nm which can be deconvoluted into four distinct peaks at 410, 430, 457, and 512 nm. The bands in UV region are generally believed to occur due to surface defects. LDHs have high surface area which results in increased surface defects, which ultimately act as traps for the generation of luminescence. However, the presence of copper ions resulted in additional peaks in visible region due to d-d transitions.

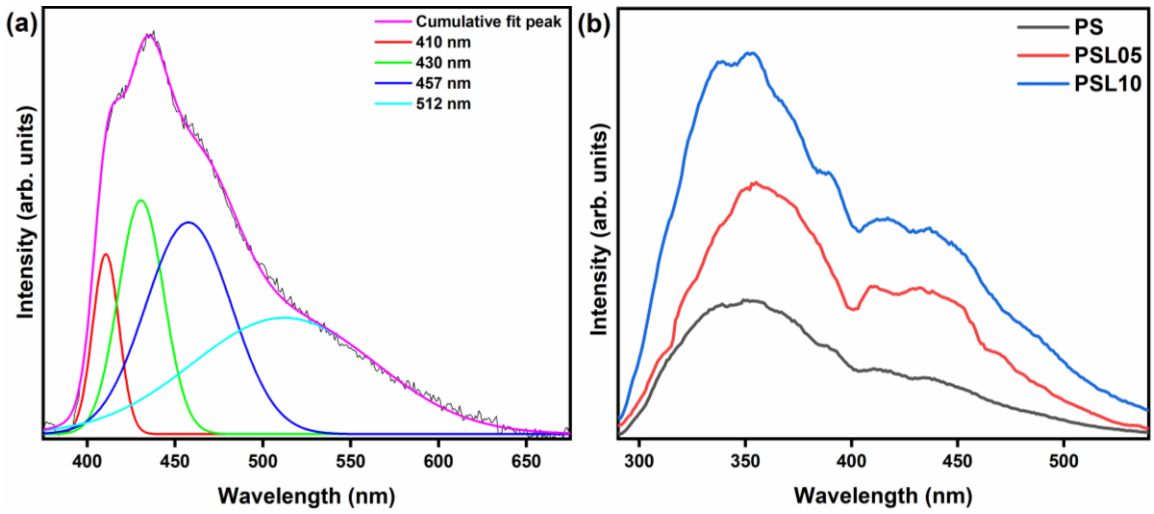

Figure 6.6 Photoluminescence emission spectra of (a) Zn/Cu LDH and (b) pure PS and PS/LDH composite films with 5% and 10% loading of Zn/Cu LDH.

The photoluminescence (PL) emission spectra of PS, PSL05, and PSL10 are presented in Figure 6.6b. The PL spectra of pure polymer and its composites were recorded at an excitation wavelength of 280 nm. Pure polystyrene is generally considered optically

inactive and shows a broad emission peak around 350 nm corresponding to the π-π* transition of the benzenoid unit of PS. An additional peak in visible region around 435 nm can be noticed in the PL spectra of composite films which can attributed to the loading of copper ions containing LDH. Further, with increase in LDH loading an increase in PL intensity and red shift can also be observed [17].

6.4 Conclusion

In the current study, LDH-based polystyrene composite film was prepared by solvent casting method with 5 and 10 weight % Zn/Cu LDH i.e., PSL05 and PSL10. The structural, thermal, and optical properties of composite films were studied. PXRD and FTIR analysis confirmed the incorporation of LDH into the polymer matrix. The thermal analysis data (TGA) depicted that the thermal stability of composite films increases with increased LDH loading. In addition, the optical properties of synthesized films were also studied which suggested that resulting films exhibit enhanced photoluminescence behavior as compared to the pure polymer. These obtained results suggested that the synthesized composite material may act as a potential candidate for optoelectronic applications in photodetectors, optoelectronic gadgets, solar cells, etc.

6.5 References

[1] Li X, Chen L, Li Q, Zhang J, Zhang X, Zheng K, et al. Structural characteristics and interfacial relaxation of nanocomposites based on polystyrene and modified layered double hydroxides. Colloid Polym Sci 2016;294:815–22. https://doi.org/10.1007/s00396-016-3834-6.

[2] Para ML, Versaci D, Amici J, Caballero MF, Cozzarin MV, Francia C, et al.

Synthesis and characterization of montmorillonite/polyaniline composites and its usage to modify a commercial separator. J Electroanal Chem 2021;880:114876. https://doi.org/10.1016/j.jelechem.2020.114876.

[3] Kartsonakis IA, Karaxi EK, Charitidis CA. Evaluation of polymer composites based on core/shell polystyrene/Mg-Al-NO_3 layered double hydroxides for chloride entrapment. Plast Rubber Compos 2016;45:50–7. https://doi.org/10.1080/14658011.2015.1133116.

[4] Pandey B, Singh P. Statistical Optimization of Process Parameters for Ultrafast Uptake of Anionic Azo Dyes by Efficient Sorbent: Zn/Cu Layered Double Hydroxide. Appl Organomet Chem 2023;37:1–18. https://doi.org/10.1002/aoc.7072.

[5] Matusinovic Z, Lu H, Wilkie CA. The role of dispersion of LDH in fire retardancy: The effect of dispersion on fire retardant properties of polystyrene/Ca-Al layered double hydroxide nanocomposites. Polym Degrad Stab 2012;97:1563–8. https://doi.org/10.1016/j.polymdegradstab.2012.07.020.

[6] Ghanbari N, Ghafuri H. Design and preparation of nanoarchitectonics of LDH/polymer composite with particular morphology as catalyst for green synthesis of imidazole derivatives. Sci Rep 2022;12:1–15. https://doi.org/10.1038/s41598-022-15582-z.

[7] Suresh K, Pugazhenthi G, Uppaluri R. Properties of polystyrene (PS)/Co-Al LDH nanocomposites prepared by melt intercalation. Mater Today Proc 2019;9:333–50. https://doi.org/10.1016/j.matpr.2019.02.163.

[8] Moulay S. Functionalized polystyrene and polystyrene-containing material platforms for various applications. Polym - Plast Technol Eng 2018;57:1045–92. https://doi.org/10.1080/03602559.2017.1370109.

[9] Stroe M, Cristea M, Matei E, Galatanu A, Cotet LC, Pop LC, et al. Optical properties of composites based on graphene oxide and polystyrene. Molecules 2020;25:1–11. https://doi.org/10.3390/molecules25102419.

[10] Pandey B, Singh P, Kumar V. Facile synthesis of Zn/Cu and PANI modified layered double hydroxides with insights into structural memory effect property. Bull Mater Sci 2022;45:169. https://doi.org/10.1007/s12034-022-02754-w.

[11] Barkoula NM, Alcock B, Cabrera NO, Peijs T. Flame-Retardancy Properties of Intumescent Ammonium Poly(Phosphate) and Mineral Filler Magnesium Hydroxide in Combination with Graphene. Polym Polym Compos 2008;16:101–13. https://doi.org/10.1002/pc.

[12] Botan R, Nogueira TR, Wypych F, Lona LMF. In Situ Synthesis, Morphology, and Thermal Properties of Polystyrene—MgAl Layered Double Hydroxide Nanocomposites. Polym Eng Sci 2012;52:1754–60. https://doi.org/10.1002/pen.

[13] Meenakshi P, Sitharaman U, Rajamani N. Facile synthesis and characterization of acetate intercalated Co-La layered double hydroxide. J Rare Earths 2017;35:474–9. https://doi.org/10.1016/S1002-0721(17)60936-0.

[14] De La Rosa-Guzmán MÁ, Guzmán-Vargas A, Cayetano-Castro N, Del Río JM, Corea M, Martínez-Ortiz MDJ. Thermal stability evaluation of polystyrene-Mg/Zn/Al LDH nanocomposites. Nanomaterials 2019;9:1528.

https://doi.org/10.3390/nano9111528.

[15] Krishna S V., Pugazhenthi G. Structural and thermal properties of polystyrene/CoAl-layered double hydroxide nanocomposites prepared via solvent blending: Effect of LDH loading. J Exp Nanosci 2013;8:19–31. https://doi.org/10.1080/17458080.2011.551894.

[16] Majoni S. Thermal and flammability study of polystyrene composites containing magnesium-aluminum layered double hydroxide (MgAl-$C1_6$ LDH), and an organophosphate. J Therm Anal Calorim 2015;120:1435–43. https://doi.org/10.1007/s10973-015-4427-1.

[17] Kumar S, Krishnakumar B, Sobral AJFN, Koh J. Bio-based (chitosan/PVA/ZnO) nanocomposites film: Thermally stable and photoluminescence material for removal of organic dye. Carbohydr Polym 2019;205:559–64. https://doi.org/10.1016/j.carbpol.2018.10.108.

Chapter 7 STRUCTURAL MEMORY EFFECT PROPERTY AND ANION EXCHANGE ABILITY OF Zn/Cu LAYERED DOUBLE HYDROXIDE

7.1 Introduction

Anionic clays or LDHs are highly adaptable materials and their properties can be modified/tuned easily by varying the nature of metal ions, anions or metal ions ratio [1]. The positively charged layered structure of LDHs contributes to anion mobility, surface basicity, and anion exchangeability [2]. LDHs can therefore be intercalated with a wide variety of organic/inorganic anions and polymers using anion exchange reactions [3]. The intercalation chemistry and anion exchange property of LDHs, as well as their superior thermal stability, have attracted enormous attention from researchers [4]. Zhao *et al.* demonstrated that carbonate and SDS intercalated Mg/Al LDH act as potential sorbents for removal of thiophene with removal efficacy of 73 and 78%, respectively [5]. Colombo *et al.* synthesized molybdate ions intercalated Ni/Zn LDH via anion exchange method and demonstrated that the lattice having molybdate as interlayer anion shows catalytic efficiency towards methyl transesterification of soyabean oil [6]. A study by Suresh *et al.* suggested that polystyrene intercalated Co/Al LDH demonstrated superior thermal properties. They reported that the introduction of LDH increased the maximum degradation temperature of pure polymer from 415.7 to 421.8℃ [7].

Another notable characteristic of LDHs is the "memory effect" property which is usually achieved by treating the mixed metal oxide with a solution containing the desired anion

after the LDH has been decomposed at a high temperature. Anions incorporated need not necessarily be the same as those present in the pristine LDH, and thus memory effect also acts as a valuable method for obtaining LDHs with various intercalated inorganic or organic anions. A substantial influence on the reconstruction process can be attributed to the calcination temperature of the LDH sheets as well as the chemical composition of the species involved [8]. It should be noted that when calcination temperature is sufficiently increased the memory effect property is lost due to the diffusion of divalent metal ions into tetrahedral sites, resulting in production of spinels. Anions can be introduced in the interlamellar region of layered hosts materials using this structure regeneration ability of layered materials [9,10] (Figure 7.1).

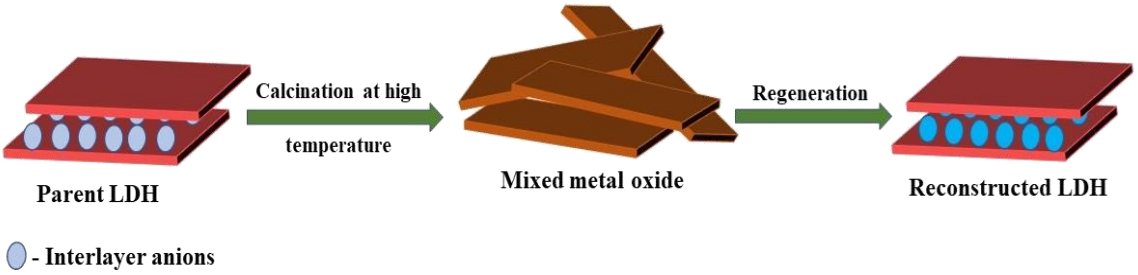

Figure 7.1 Illustration of structural memory effect of LDH.

Recently, researchers have focused a great deal of attention upon inorganic nanocomposites containing polymeric species within the LDH hosts [11]. Among all the widely studied polymeric species the good environmental and redox stability, high specific capacitance and electrical conductivity make polyaniline (PANI) the most widely explored conducting polymer [12]. The structure of different forms of PANI are presented in Figure 7.2. Its numerous advantages have made PANI an excellent material for electronic devices, supercapacitors, photocatalysis, humidity sensors, and environmental applications [13–

15]. PANI exhibit a strong affinity towards inorganic and organic molecules since it contains various imine and amine functional groups. Additionally, the nitrogen-containing functional groups of PANI interact with the hydroxyl or carboxyl groups of the LDH surface to incorporate PANI into the layered structure. As a result of synergistic interactions between PANI and LDH, a hybrid material with improved properties is also formed [16].

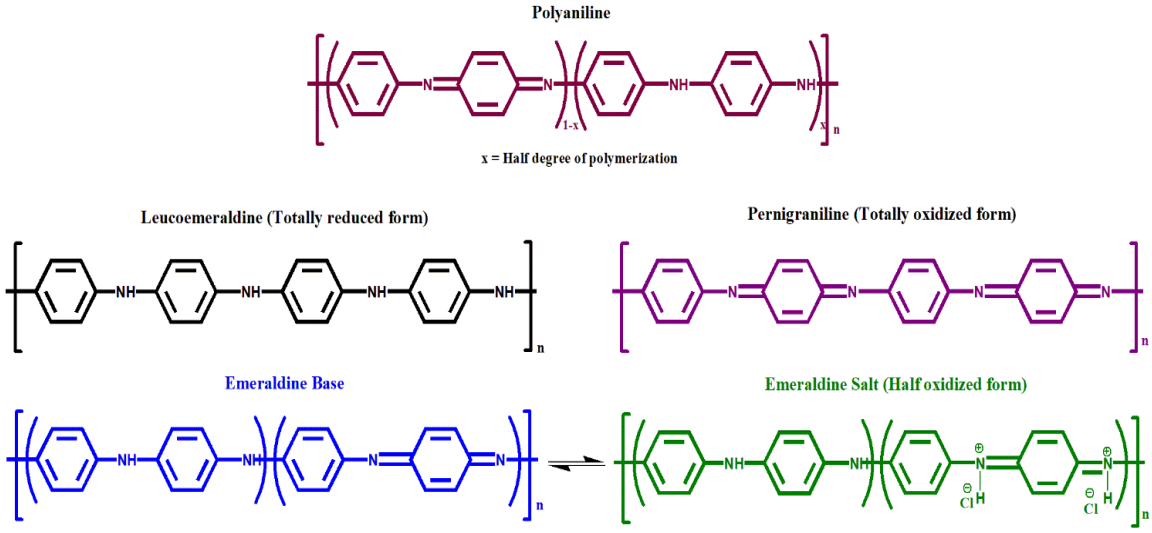

Figure 7.2 Structures of different forms of polyaniline.

Recently, studies have shown that PANI can improve active surface areas, electrochemical performance, and electronic conductivity of electrode materials by combining it with inorganic materials [17]. The PANI functionalized Cobalt/Aluminum LDH modified glassy carbon electrode prepared by Jiao *et al.* described efficacy of the synthesized material in detecting pesticides including carbaryl and isoprocarb [18]. In a study by Hu *et al.*, a PANI coated molybdate-intercalated nickel-cobalt LDH was synthesized and the electrochemical properties (overpotential = 307 mV) of the nanocomposite were reported to be enhanced as compared to the LDH alone [19]. In a paper by Dinari and Neamati, a

Ca/Fe LDH and PANI nanocomposite was synthesized and exhibited high sorption capacity of 109.71 mg/g towards lead ions [13]. Thus, the research work proposed a simple and efficient approach for exchange of intergallery acetate anion with PANI, leading to the production of a material exhibiting enhanced electrical, thermal, and optical properties that can be employed in different applications.

7.2 Experimental Section

7.2.1 Decomposition and regeneration of layered structure

For regeneration of layered structure, 0.1 g of MMO or LDO obtained on calcination of Zn-Cu LDH (0.25 g) at 350°C (for 6 hours) was first suspended in the 50 mL of acetic acid solution. The resultant solution was then kept for heating with simultaneous stirring till the total volume of the solution was reduced to 10 mL. After that 30 mL of deionized water and 2 mL H_2O_2 was added to the above solution and later stirred for 24 hours, then dried at 60°C in an oven.

7.2.2 PANI modified Zn/Cu LDH synthesis

First, the Zn/Cu LDH was prepared via hydrolysis route as reported in Chapter 2. Later oxidative in situ polymerization was utilized to synthesize PANI/LDH [20]. The synthesis was carried out by mixing 25 mL aniline, 0.25g of Zn-Cu LDH, and 2.5 mL of H_2O_2. Afterwards, reaction mixture was refluxed at at 60°C for 9 hours with continuous stirring at 400 rpm was followed by washing the obtained product with acetone, DMSO, and ethanol and drying at 60°C.

7.2.2 Instrumentation

The PXRD pattern of the synthesized lattice was recorded by an advanced Bruker D8 diffractometer over the range of 2θ = 5-70°, employing Copper Kα radiation with 1.5418 Å wavelength acquired via a gobel mirror with 1.0 second/step scan rate and 0.02° step size at 298 K. The sample was analyzed using a PerkinElmer FTIR (version 10.5.3). Thermogravimetric analysis was conducted using the PerkinElmer TGA in the 50-900°C range under flowing nitrogen and at a uniform heating rate of 10°C min^{-1}. PHI 5000 VersaProbe III was used to record XPS measurements with Al Kα for photoelectron excitation. FE-SEM with EDX analysis of Zn/Cu HDS was accomplished using a Zeiss GeminiSEM.

7.3 Results and discussion

7.3.1 Memory effect property of synthesized material

Following the successful synthesis of Zn/Cu LDH, the memory effect property of lattice was investigated by conducting calcination-regeneration experiments. The decomposition of Zn/Cu LDH at 350°C for 6 hours in a muffle furnace resulted in the formation of copper-doped zinc oxide. The PXRD pattern of the calcined oxide (Figure 7.3a) confirms the loss of acetate anions from the interlayer region in addition to disintegration of the layered arrangement and shows reflection due to amorphous wurtzite ZnO [21].

A regeneration experiment was carried out where the LDO was introduced to a similar environment as the parent LDH and its structure regaining capability (referred to as memory effect) was analyzed. The PXRD patterns of parent and regenerated product are depicted in Figure 7.3a, consisting of high intensity sharp peak at the low value of 2θ

(around 12°) accompanied by weak reflections at high values of 2θ. Moreover, the nonexistence of sharp intense reflection at d = 9.42 Å due to copper hydroxide acetate indicated the successful formation of a hydrotalcite structure in the pure phase [22,23]. The reconstructed LDH pattern also demonstrates good structural integrity, both in peak positions and relative intensities, compared to the parent LDH. Molecular regeneration of the LDH pattern resembles the pattern of the parent LDH sufficiently well, concluding that the structural memory effect has been successfully stimulated. The FTIR spectra of parent lattice and regenerated LDH were similar, indicating successful reconstruction of lattice after calcination and rehydration (Figure 7.3b).

Additionally, the thermally treated sample may exhibit large anion exchange capacities, which may result in selective adsorption of anionic species during the regeneration process [9]. Thus, the 'memory effect' can act as a rational and effective approach for the synthesis of LDH-based materials with potential biomedical and environmental applications.

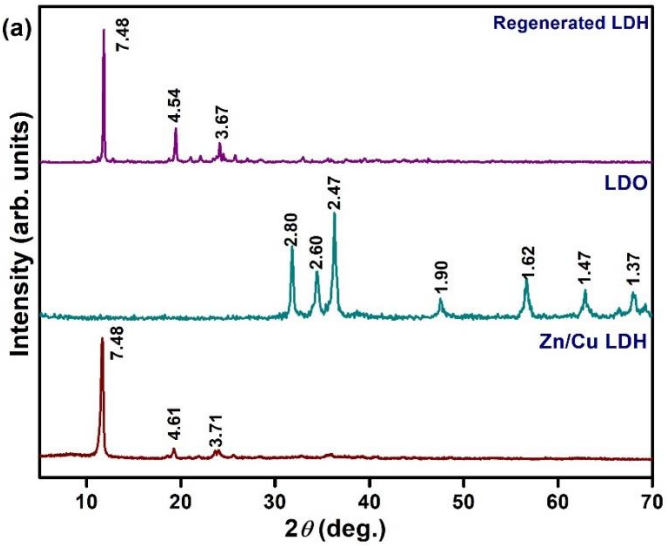

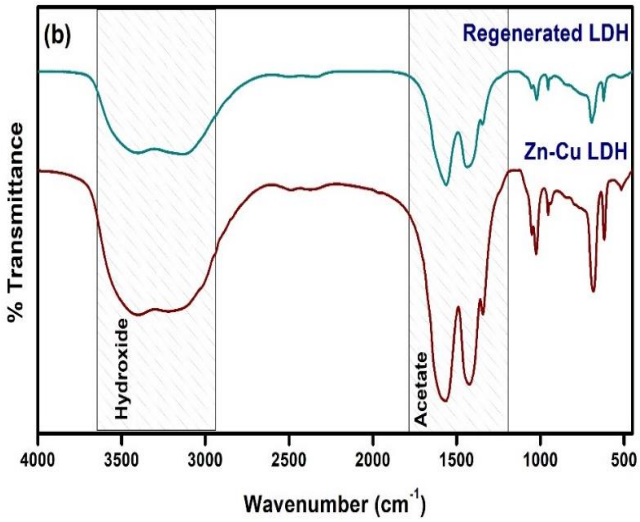

Figure 7.3 Comparative plots of (a) PXRD patterns and (b) FTIR spectra of pristine and regenerated Zn/Cu LDH.

7.3.2 PANI-modified Zn/Cu LDH

The PXRD patterns of parent lattice and polyaniline intercalated Zn-Cu LDH are presented in Figure 7.4a & b. From PXRD pattern it can be seen that the intercalation of polyaniline influences the intergallery distance of the layered structure and the expansion of the *c*-axis from 7.53 Å to 15.57 Å can observed thereby suggesting successful incorporation of PANI into the lattice [24].

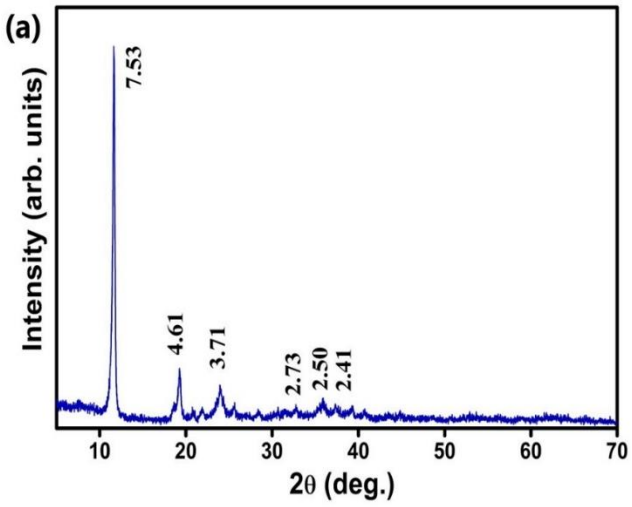

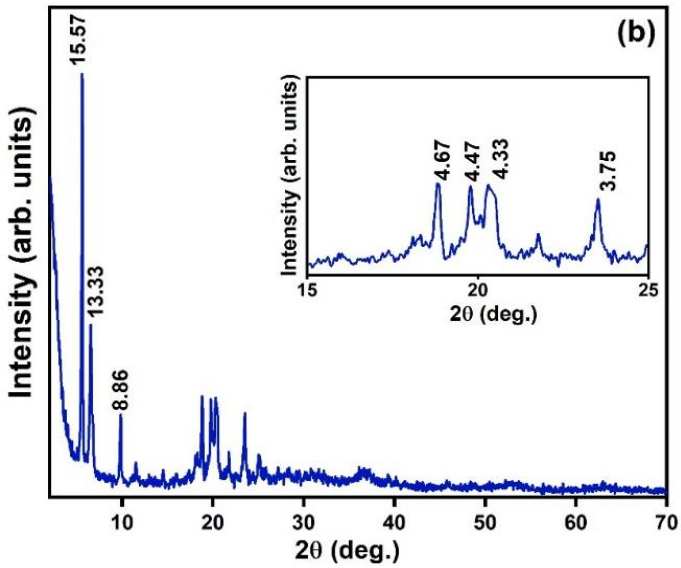

Figure 7.4 PXRD pattern of (a) Zn-Cu LDH having acetate as interlayer anion and (b) PANI intercalated Zn-Cu LDH.

The presence of acetate and PANI in the synthesized lattices was confirmed using FTIR analysis (Figure 7.5). FTIR spectrum of pristine LDH (Figure 7.5a) corroborated the existence of the interlayer acetate anion in the lattice. The -OH groups of the brucite layer and the interlayer H_2O molecules resulted in a strong and broad band centred at 3409 cm^{-1} [25]. The bands observed at 1570, 1421, 1025, 689, and 614 cm^{-1} established the presence of acetate ions in the interlayer region [26]. Further, a metal-oxygen band centred at 517 cm^{-1} suggested the presence of direct metal-oxygen linkage [27]. It can be noticed that FTIR spectrum of composite (Figure 4.5b) exhibits bands corresponding to both LDH and PANI. The band at 3257 cm^{-1} can be accredited to the binding N-H and O-H bonds, whereas the band near 3500 cm^{-1} can be credited to the stretching vibration of free hydroxyl and amine groups of LDH and PANI, respectively [27]. Incorporation of PANI into the lattice is strongly supported by the observed bands at 1575, 1499, 1293, 1171, 750, 697, 606 cm^{-1}. The bands at 1575 and 1499 cm^{-1} are ascribed to C=N and C=C stretching vibrations

(characteristic of the benzenoid units and quinoid units in PANI) [19], [28]. The band centered at 1293 cm^{-1} corresponds to the C–N stretching vibration of 2° aromatic amine. However, band observed near 1171 cm^{-1} corresponds to the vibrational mode of (B-NH^{+}-B) or (B-NH^{+}=Q) states. Bands below 800 cm^{-1} correspond to M-O, M-O-M, and O-M-O vibrational modes [29].

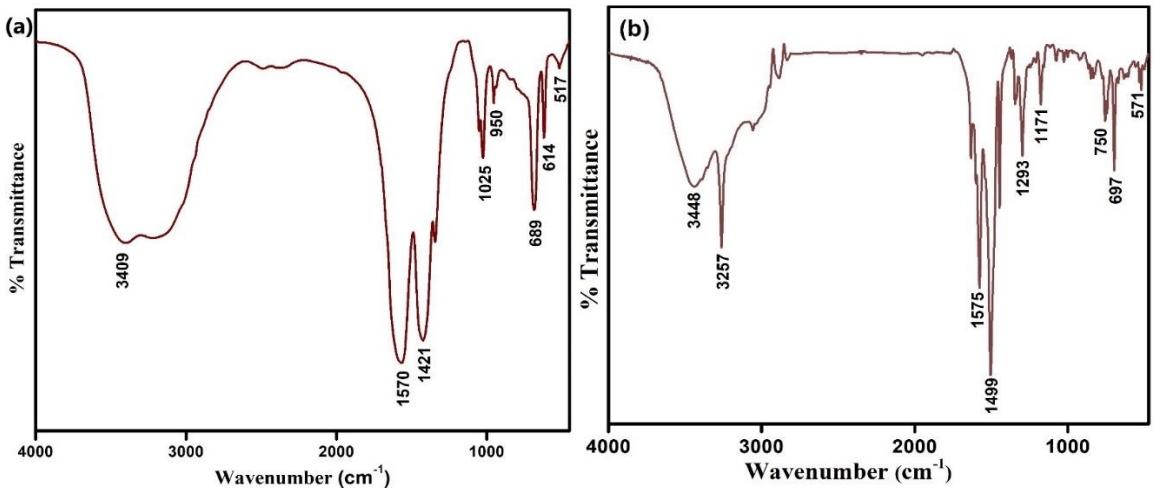

Figure 7.5 FTIR spectrum of (a) Zn-Cu LDH having acetate as interlayer anion and PANI intercalated Zn-Cu LDH.

Table 7.1 Functional group analysis of pristine and modified LDH using FTIR.

Wavenumber (cm^{-1})	**Functional group**	**Inference**
Zn/Cu LDH		
3409	O-H stretch.	Due to stretching vibration of -OH groups where broadness indicates the H-bonding between -OH groups and interlayer H_2O molecules
1570 & 1421	Anti symmetric and symmetric	Confirm the presence of acetate anions

	stretch. of COO^- group	
1025	C-H rocking	
960	C-C stretch.	
689	O-C-O bending	
614	CO_2^- rocking	
517	M-O stretch.	Presence of metal oxygen linkage
PANI-modified LDH		
3500	N-H & O-H stretch.	Presence of free hydroxyl and amine groups
3257		Binding N-H & O-H
1575	C=N stretch.	Confirm the presence of benzenoid and
1499	C=C stretch.	quinoid units of polyaniline
1293	C-N stretch.	Presence of secondary aromatic amines
1171	-	Presence of B-NH^+-B or B-NH^+=Q states (B = benzenoid & Q = Quinoid)
750 697 571	M-O, M-O-M, O-M-O	Metal oxygen linkages

The thermal stability of acetate and PANI intercalated Zn-Cu LDH was investigated using thermogravimetric (TG) analysis (Figure 7.6). The decomposition of pristine LDH eoccurred in three-step (Figure 7.6a) where the initial step observed within the temperature range of 50 to 190 °C can be ascribed to the elimination of H_2O molecules from surface

adsorbed and interlamellar region. However, second and third steps observed in the range of 190 to 370°C and above 370°C corresponds to the dehydroxylation of lattice and elimination of interlayer acetate ion [26],[30]. Thermal analysis further confirmed the fabrication of polyaniline modified Zn-Cu LDH, as depicted in Figure 7.6b. The weight loss below 260 °C can be accredited to the loss of physisorbed H_2O molecules. Nevertheless, above 260 °C dehydration and removal of the interlayer anion is the main cause of weight loss. Additionally, polyaniline-modified LDHs exhibit a steep downward trend in the TG curve, further confirming that PANI has been incorporated successfully into the lattice of LDHs [19].

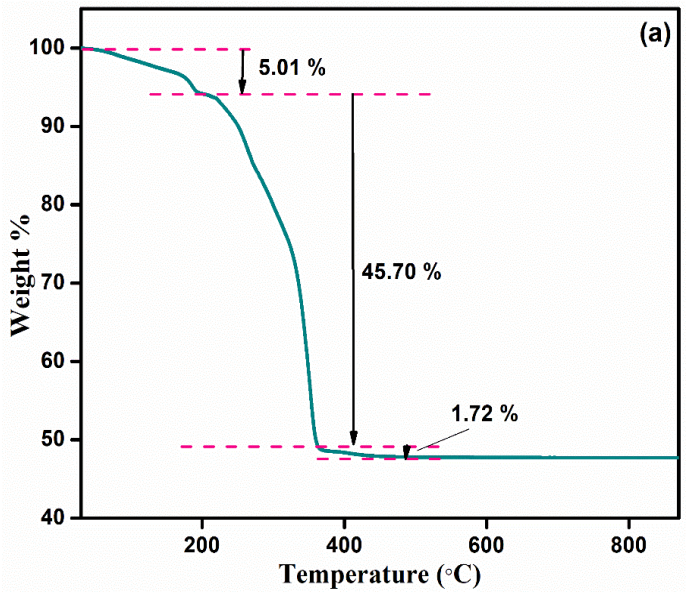

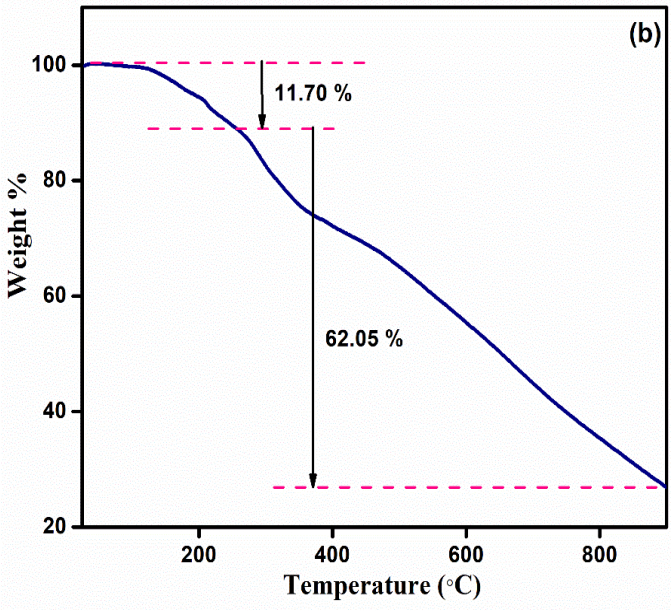

Figure 7.6 Thermogravimetric traces of (a) Zn-Cu LDH having acetate as interlayer anion and (b) PANI-modifies Zn/Cu LDH.

Table 7.2 TGA data for Zn/Cu LDH and PANI-modified LDH.

Sample	**Temperature range (°C)**	**Weight loss (%)**	**Total weight residue (%)**
LDH			
Stage I	32-190	5.01	
Stage II	190-370	45.70	52.27
Stage III	< 370	1.72	
PANI/LDH			
Stage I	27-260	11.70	73.50
Stage II	< 260	62.05	

The SEM micrographs of parent LDH and PANI modified LDH are presented in Figure 7.7. According to Figure 7.7b, PANI tubes grow alongside Zn/Cu LDH, with the structure

and plate-like morphology of parent LDH remaining intact after the addition of PANI. It appears that the carbon, nitrogen, zinc, and copper elements are uniformly dispersed in the PANI/LDH lattice based on the EDX (Figure 7.8b) and elemental mapping (Figure 7.9) results [32].

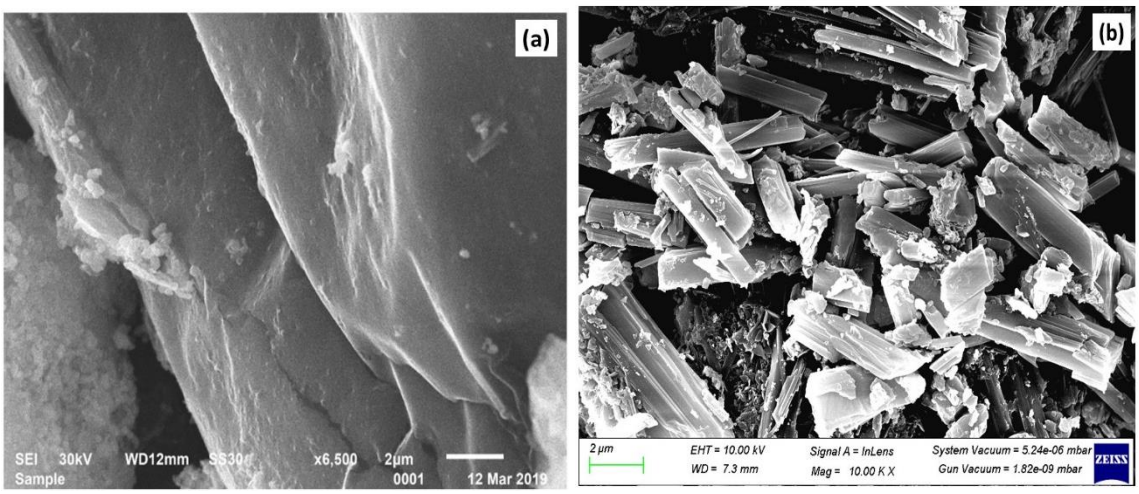

Figure 7.7 (a) SEM micrograph and (b) EDX of synthesized LDH.

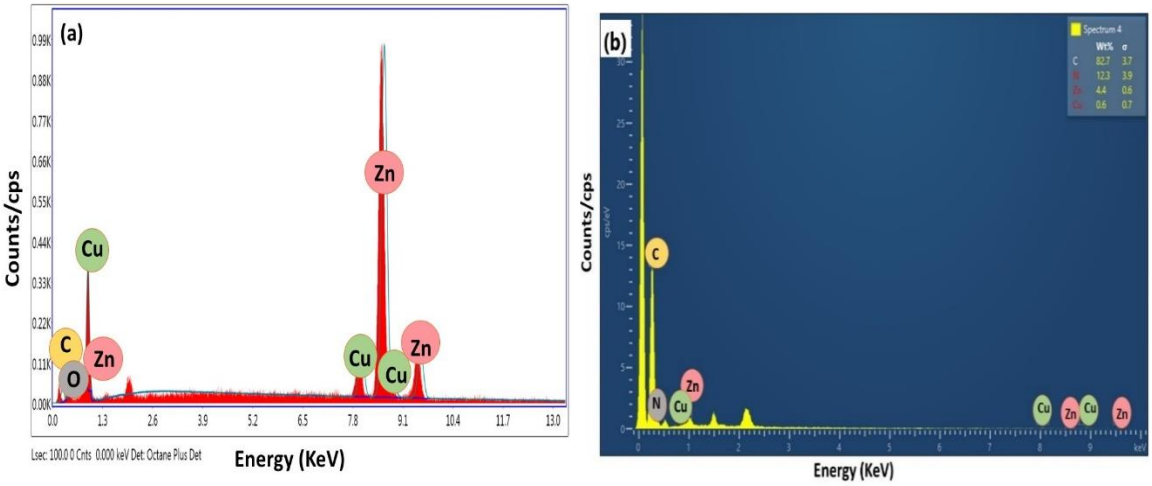

Figure 7.8 (a) SEM micrograph and (b) EDX of PANI intercalated LDH.

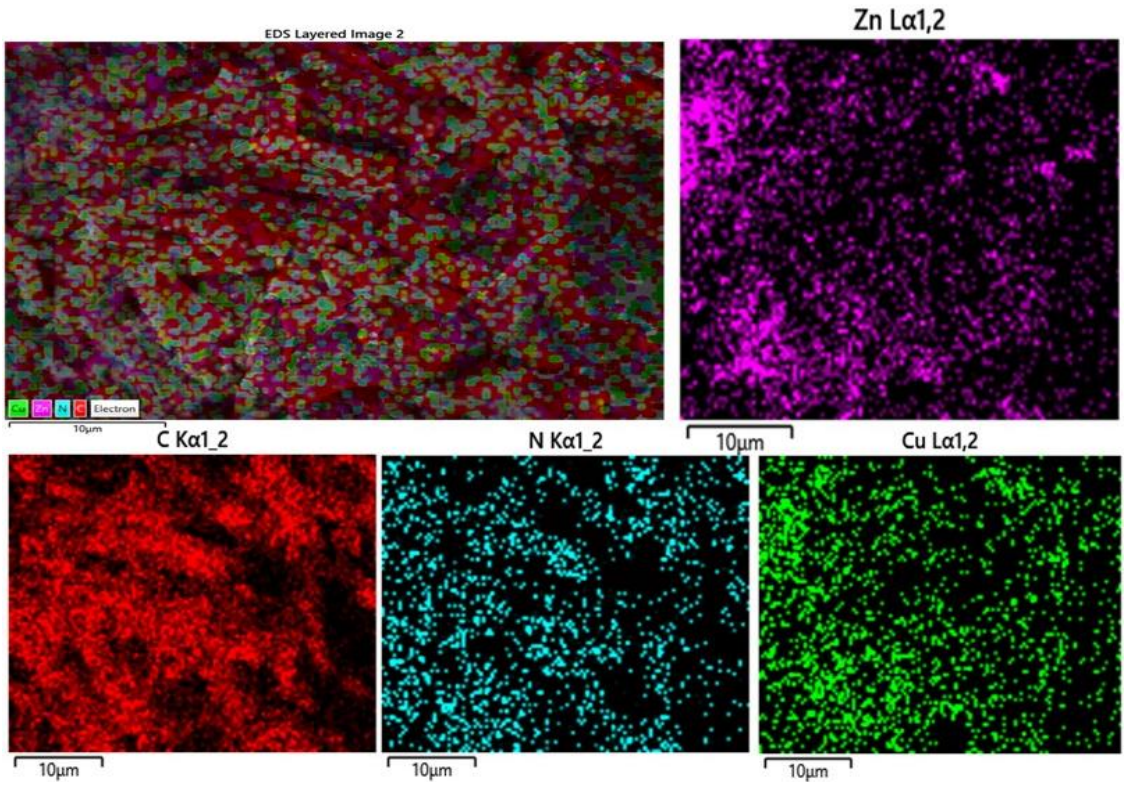

Figure 7.9 Elemental mapping of various elements of PANI intercalated LDH.

Chemical composition and electronic state of PANI intercalated LDH were determined using XPS. The presence of carbon *1s*, oxygen *1s*, nitrogen *1s*, zinc *2p*, and copper *2p* was revealed by the survey spectrum of PANI/LDH as depicted in Figure 7.10a.

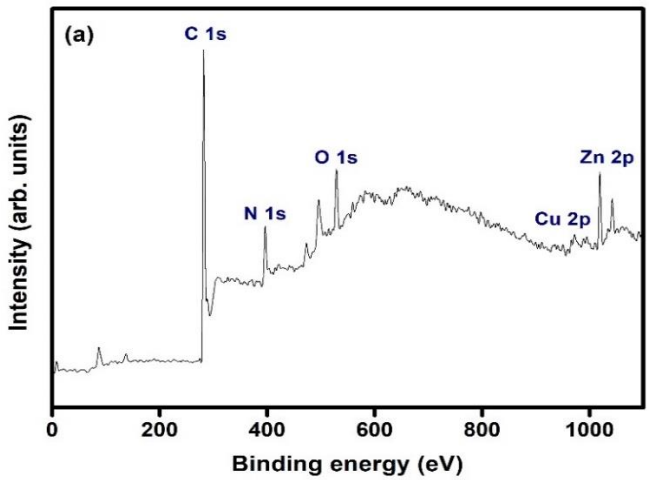

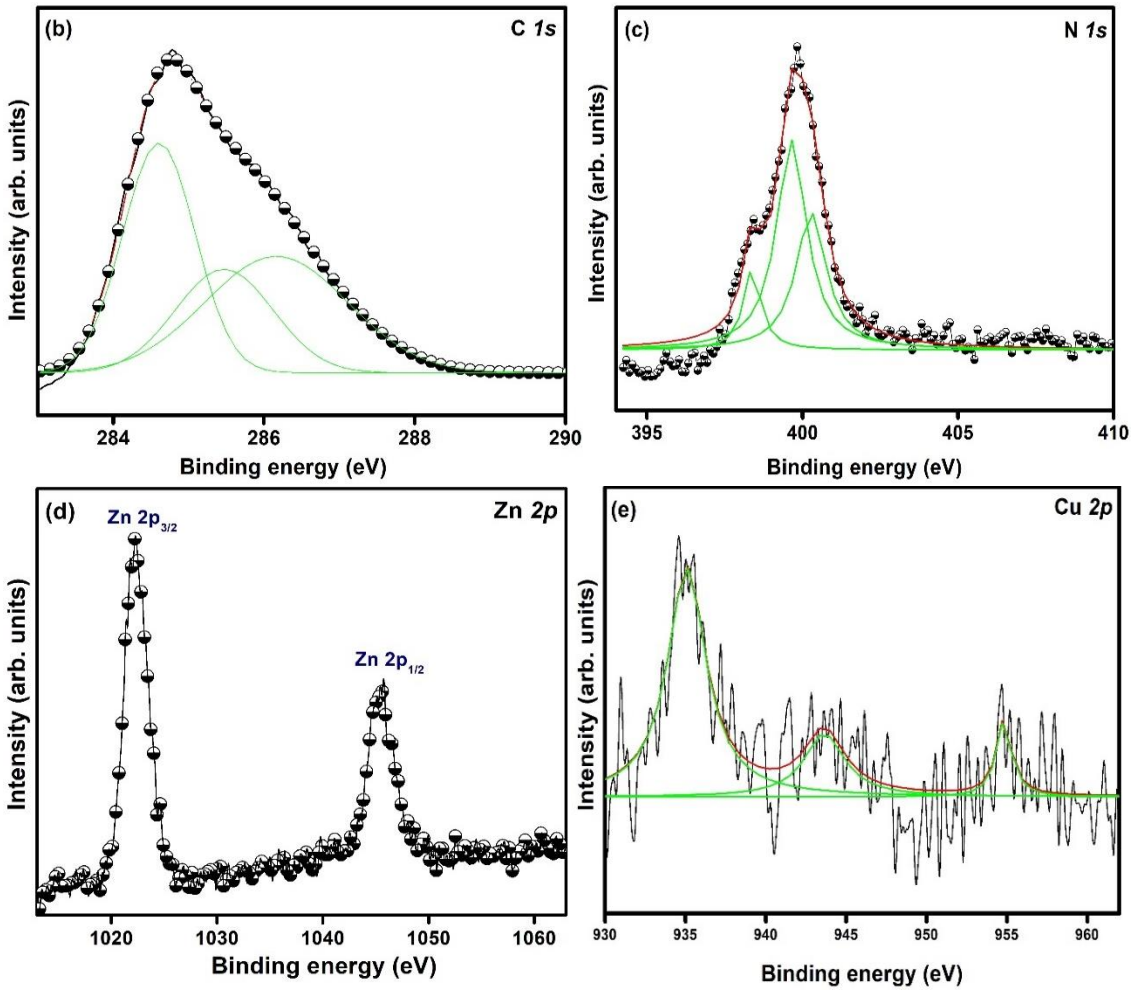

Figure 7.10 (a) XPS survey spectrum and core-level spectra of (b) C *1s*, (c) N *1s*, (d) Zn *2p*, and (e) Cu *2p* of PANI/Zn-Cu LDH.

C *1s* spectrum is presented in Figure 7.10b exhibits three peaks at binding energy values of 284.60, 285.47, and 286.16 eV that can be ascribed to C=C, C-H, C-N, and C=NH^+ groups. The N *1s* spectrum (Figure 7.10c) confirmed the presence of quinonoid imine (398.38 eV), benzenoid amine (399.64 eV), and positively charged nitrogen atoms of polyaniline (400.27 eV) in the lattice. In Figure 7.10d, two sharp peaks conforming to Zn $2p_{3/2}$ (1022 eV) and Zn $2p_{1/2}$ (1045 eV) can be seen [32,33]. Two peaks can be observed at 935.09 and 954.82 eV in the spectrum of Cu *2p* (Figure 7.10e), along with a satellite peak at 943.64 eV confirming that copper is in the +3-oxidation state [34]. Consequently, all

constituent elements of polyaniline and LDH can be detected in the composite according to the XPS survey spectrum.

7.4 Conclusion

Herein, the regeneration experiment verified that the synthesized Zn/Cu LDH exhibits structural memory effect property after calcination. The reconstitution of layered structure could be used as an intermediate step for the functionalization of LDHs by intercalating suitable anions in the interlayer region. Furthermore, PANI incorporated Zn/Cu LDH was prepared via oxidative in situ polymerization where interlayer acetate anion was employed to carry out anion exchange reaction. Adding conductive polymer resulted in an increase in interlayer spacing (to 15.57 Å from 7.53 Å) and the preservation of the host framework following intercalation of PANI. The incorporation of polyaniline was confirmed using FTIR and TGA studies. The composition and electronic states of the elements employed were confirmed using SEM/EDX and XPS analyses. Consequently, the study opens up the possibility of fabricating new inorganic–organic composite materials with unusual mechanical, chemical, and thermal properties by using such host lattices with adjustable interlayer spacing.

7.5 References

[1] Kuthati Y, Kankala RK, Lee CH. Layered double hydroxide nanoparticles for biomedical applications: Current status and recent prospects. Appl Clay Sci 2015;112–113:100–16. https://doi.org/10.1016/j.clay.2015.04.018.

[2] Shi H, He J. Orientated intercalation of tartrate as chiral ligand to impact asymmetric catalysis. J Catal 2011;279:155–62. https://doi.org/10.1016/j.jcat.2011.01.012.

[3] Khan AI, O'Hare D. Intercalation chemistry of layered double hydroxides: Recent developments and applications. J Mater Chem 2002;12:3191–8. https://doi.org/10.1039/b204076j.

[4] Singh P, Nagarajan R. Synthesis and characterization of hydrotalcite type structure containing Zn^{2+} and La^{3+}-ions. Mater Lett 2015;159:58–60. https://doi.org/10.1016/j.matlet.2015.06.071.

[5] Zhao Q, Chang Z, Lei X, Sun X. Adsorption behavior of thiophene from aqueous solution on carbonate- and dodecylsulfate-intercalated ZnAl layered double hydroxides. Ind Eng Chem Res 2011;50:10253–8. https://doi.org/10.1021/ie201021k.

[6] Colombo K, Maruyama SA, Yamamoto CI, Wypych F. Intercalation of molybdate ions into Ni/Zn layered double hydroxide salts: Synthesis, characterization, and preliminary catalytic activity in methyl transesterification of soybean oil. J Braz Chem Soc 2017;28:1315–22. https://doi.org/10.21577/0103-5053.20160298.

[7] Suresh K, Pugazhenthi G, Uppaluri R. Properties of polystyrene (PS)/Co-Al LDH nanocomposites prepared by melt intercalation. Mater Today Proc 2019;9:333–50. https://doi.org/10.1016/j.matpr.2019.02.163.

[8] Arrabito G, Bonasera A, Prestopino G, Orsini A, Mattoccia A, Martinelli E, et al. Layered double hydroxides: A toolbox for chemistry and biology. Crystals 2019;9:361. https://doi.org/10.3390/cryst9070361.

[9] Teixeira AC, Morais AF, Silva IGN, Breynaert E, Mustafa D. Luminescent layered double hydroxides intercalated with an anionic photosensitizer via the memory

effect. Crystals 2019;9:1–11. https://doi.org/10.3390/cryst9030153.

[10] Klemkaite K, Prosycevas I, Taraskevicius R, Khinsky A, Kareiva A. Synthesis and characterization of layered double hydroxides with different cations (Mg, Co, Ni, Al), decomposition and reformation of mixed metal oxides to layered structures. Cent Eur J Chem 2011;9:275–82. https://doi.org/10.2478/s11532-011-0007-9.

[11] Leroux F, Besse J. Polymer interleaved layered double hydroxide: A new emerging class of nanocomposites. Chem Mater 2001;13:3507–15. https://doi.org/10.1021/cm0110268.

[12] Bhadra S, Khastgir D, Singha NK, Lee JH. Progress in preparation, processing and applications of polyaniline. Prog Polym Sci 2009;34:783–810. https://doi.org/10.1016/j.progpolymsci.2009.04.003.

[13] Dinari M, Neamati S. Surface modified layered double hydroxide/polyaniline nanocomposites: Synthesis, characterization and Pb2+ removal. Colloids Surfaces A Physicochem Eng Asp 2020;589:124438. https://doi.org/10.1016/j.colsurfa.2020.124438.

[14] Li XZ, Liu SR, Guo Y. Polyaniline-intercalated layered double hydroxides: Synthesis and properties for humidity sensing. RSC Adv 2016;6:63099–106. https://doi.org/10.1039/c6ra10093g.

[15] Liu L, Hu X, Zeng HY, Yi MY, Shen SG, Xu S, et al. Preparation of NiCoFe-hydroxide/polyaniline composite for enhanced-performance supercapacitors. J Mater Sci Technol 2019;35:1691–9. https://doi.org/10.1016/j.jmst.2019.04.003.

[16] Sanchez C, Julián B, Belleville P, Popall M. Applications of hybrid organic-inorganic nanocomposites. J Mater Chem 2005;15:3559–92. https://doi.org/10.1039/b509097k.

[17] Harraz FA, Ismail AA, Al-Sayari SA, Al-Hajry A, Al-Assiri MS. Highly sensitive amperometric hydrazine sensor based on novel α-Fe_2O_3/crosslinked polyaniline nanocomposite modified glassy carbon electrode. Sensors Actuators, B Chem 2016;234:573–82. https://doi.org/10.1016/j.snb.2016.05.021.

[18] Jiao W, Ding G, Wang L, Liu Y, Zhan T. Polyaniline functionalized CoAl-layered double hydroxide nanosheets as a platform for the electrochemical detection of carbaryl and isoprocarb. Microchim Acta 2022;189:1–11. https://doi.org/10.1007/s00604-022-05183-y.

[19] Hu Q, Wang H, Feifei X, Zheng Q, Ma X, Huo Y, et al. Critical roles of molybdate anions in enhancing capacitive and oxygen evolution behaviors of LDH@PANI nanohybrids. Chinese J Catal 2021;42:980–93. https://doi.org/https://doi.org/10.1016/S1872-2067(20)63724-X.

[20] Zhu K, Gao Y, Tan X, Chen C. Polyaniline-Modified Mg/Al Layered Double Hydroxide Composites and Their Application in Efficient Removal of Cr(VI). ACS Sustain Chem Eng 2016;4:4361–9. https://doi.org/10.1021/acssuschemeng.6b00922.

[21] Bresser D, Mueller F, Fiedler M, Krueger S, Kloepsch R, Baither D, et al. Transition-metal-doped zinc oxide nanoparticles as a new lithium-ion anode material. Chem Mater 2013;25:4977–85. https://doi.org/10.1021/cm403443t.

[22] Pereira DC, De Faria DLA, Constantino VRL. CuII hydroxy salts: Characterization of layered compounds by vibrational spectroscopy. J Braz Chem Soc 2006;17:1651–7. https://doi.org/10.1590/S0103-50532006000800024.

[23] Zhitova ES, Krivovichev S V., Pekov I V., Yakovenchuk VN, Pakhomovsky YA. Correlation between the d-value and the M2 +:M3 + cation ratio in Mg–Al–CO3 layered double hydroxides. Appl Clay Sci 2016;130:2–11. https://doi.org/10.1016/j.clay.2016.01.031.

[24] Hu J, Gan M, Ma L, Li Z, Yan J, Zhang J. Synthesis and anticorrosive properties of polymer-clay nanocomposites via chemical grafting of polyaniline onto Zn-Al layered double hydroxides. Surf Coatings Technol 2014;240:55–62. https://doi.org/10.1016/j.surfcoat.2013.12.012.

[25] Cheng X, Huang X, Wang X, Sun D. Influence of calcination on the adsorptive removal of phosphate by Zn-Al layered double hydroxides from excess sludge liquor. J Hazard Mater 2010;177:516–23. https://doi.org/10.1016/j.jhazmat.2009.12.063.

[26] Manohara G V., Vishnu Kamath P, Milius W. Reversible hydration and aqueous exfoliation of the acetate-intercalated layered double hydroxide of Ni and Al: Observation of an ordered interstratified phase. J Solid State Chem 2012;196:356–61. https://doi.org/10.1016/j.jssc.2012.06.017.

[27] Poul L, Jouini N, Fievet F. Layered hydroxide metal acetates (metal = zinc, cobalt, and nickel): Elaboration via hydrolysis in polyol medium and comparative study. Chem Mater 2000;12:3123–32. https://doi.org/10.1021/cm991179j.

[28] Cao X, Zeng HY, Xu S, Yuan J, Han J, Xiao GF. Facile fabrication of the polyaniline/layered double hydroxide nanosheet composite for supercapacitors. Appl Clay Sci 2019;168:175–83. https://doi.org/10.1016/j.clay.2018.11.011.

[29] Challier T, Slade RCT. Nanocomposite materials: Polyaniline-intercalated layered double hydroxides. J Mater Chem 1994;4:367–71. https://doi.org/10.1039/jm9940400367.

[30] Yang G, Takei T, Yanagida S, Kumada N. Enhanced supercapacitor performance based on coal layered double hydroxide-polyaniline hybrid electrodes manufactured using hydrothermal-electrodeposition technology. Molecules 2019;24:976. https://doi.org/10.3390/molecules24050976.

[31] Kandare E, Hossenlopp JM. Thermal degradation of acetate-intercalated hydroxy double and layered hydroxy salts. Inorg Chem 2006;45:3766–73. https://doi.org/10.1021/ic060071k.

[32] Wani AA, Khan AM, Manea YK, Salem MAS, Shahadat M. Selective adsorption and ultrafast fluorescent detection of Cr(VI) in wastewater using neodymium doped polyaniline supported layered double hydroxide nanocomposite. J Hazard Mater 2021;416:125754. https://doi.org/10.1016/j.jhazmat.2021.125754.

[33] Sun X, Liu X, Liu R, Sun X, Li A, Li W. PANI@Co-FeLDHs as highly efficient electrocatalysts for oxygen evolution reaction. Catal Commun 2020;133:105826. https://doi.org/10.1016/j.catcom.2019.105826.

[34] Brown DG, Weser U. XPS Spectra of Copper and Nickel Biuret Complexes — Observations of Intense Satellite Structure in the 2P Spectrum of a Copper(III)

System. Zeitschrift Fur Naturforschung 1979;34:989–94. https://doi.org/10.1515/znb-1979-0721.

Chapter 8 CONCLUSION AND FUTURE PROSPECTS

8.1 Conclusion

The layered double hydroxide and their composites containing Zn and Cu metal ions have been successfully synthesized. The formation of pure phase lattices was established by PXRD, BET, TGA, FTIR, SEM/EDX, and XPS analyses. The adsorptive behavior of parent lattice i.e., Zn/Cu LDH was studied for the sequestration of anionic azo dyes and the optimization of process parameters was performed using CCD-RSM approach. The impact of four operational factors including pH of dye solution, adsorbate concentration, adsorbent amount and contact time were investigated for the efficient removal of CR dye using Zn/Cu LDH. The optimum conditions derived from CCD-RSM approach for CR dye uptake were found to be: pH =7, dye concentration = 50 mg/L, dose of adsorbent = 0.01 g and contact time = 4 minutes. However, the Zn/Cu LDO obtained on calcination of LDH acted as a useful sorbent for the uptake of cationic azo dye (malachite green). The study also revealed that a smartphone-based detection technique can be efficiently employed for the determination of dye concentration as compared to the conventionally used method, i.e., UV-Visible spectroscopy.

Moreover, the EG-modified Zn/Cu HDS demonstrated high efficiency towards anionic dyes in comparison to cationic dyes. The material also showed high reusability up to 5 adsorption-desorption cycles. The PMMA/LDH composites were synthesized with different weight % of Zn/Cu LDH and the composite with 20 wt % LDH displayed adsorption behavior towards the food dye i.e., Brilliant black (anionic dye).

In addition, formation of PS/LDH composite films suggested that the incorporation of LDH resulted in enhanced thermal, morphological, and optical properties of the polymeric materials.

Furthermore, the LDO obtained on calcination of parent lattice showed regeneration ability i.e., memory effect property. The anion exchange property of Zn/Cu LDH was also studied in which polyaniline was incorporated into lattice showing increase in the gallery height from 7.53 to 15.57 Å.

In conclusion, a series of Zn/Cu LDH based materials have been successfully synthesized that may act as potential sorbent for sequestration of anionic and cationic azo dyes. The materials exhibit potential to replace traditionally used adsorbents suggesting their real time applicability for wastewater treatment. Furthermore, LDH incorporation act as a means of enhancing the overall performance of polymeric materials.

8.2 Future prospects

Zn/Cu LDH based materials have shown promising potential for practical application in environmental contexts based on the current research work. Following key aspects can be explored in future research in this field:

- Investigation of photocatalytic efficiency of the synthesized lattices for the sequestration of other toxic pollutants including pharmaceutical wastes, toxic metal ions, fertilizers, pesticides, microplastics, etc.
- Further investigation of PANI/LDH composite for energy storage, catalysis, and sensing applications.

LIST OF PUBLICATIONS AND CONFERENCES

Journal articles:

1. **Bhamini Pandey** and Poonam Singh. Statistical Optimization of Process Parameters for Ultrafast Uptake of Anionic Azo Dyes by Efficient Sorbent: Zn/Cu Layered Double Hydroxide. Applied Organometallic Chemistry 2023;1–18. https://doi.org/10.1002/aoc.7072 (I.F. = 4.072) **(SCI/SCIE)**
2. **Bhamini Pandey**, Poonam Singh, Vinod Kumar. Facile synthesis of Zn/Cu and PANI modified layered double hydroxides with insights into structural memory effect property. Bulletin of Materials Science 2022;45(3):169. https://doi.org/10.1007/s12034-022-02754-w (I.F. = 1.878) **(SCIE)**
3. **Bhamini Pandey**, Poonam Singh, Vinod Kumar. Photocatalytic-sorption processes for the removal of pollutants from wastewater using polymer metal oxide nanocomposites and associated environmental risks. Environment Nanotechnology, Monitoring & Management 2021;16:100596. https://doi.org/10.1016/j.enmm.2021.100596 **(Scopus)**
4. **Bhamini Pandey**, Poonam Singh, Vinod Kumar. Adsorption of anionic dye from aqueous environment using surface-engineered Zn/Cu hydroxy double salt-based material: mechanistic, equilibrium, and kinetic studies. Journal of Environmental Science and Health Part A 2023. https://doi.org/10.1080/10934529.2023.2243193 (I.F. = 2.582) **(SCIE)**
5. **Bhamini Pandey**, Jigyasa Pathak, Poonam Singh, Ravinder Kumar, Amit Kumar, Sandeep Kaushik, Tarun Kumar Thakur. Microplastics in the

Ecosystem: An Overview on Detection, Removal, Toxicity Assessment, and Control Release. Water 2023;15;51. https://doi.org/10.3390/w15010051 (I.F. = 3.53) **(SCIE)**

6. Jigyasa Pathak, **Bhamini Pandey**, Poonam Singh, Ravinder Kumar, Sandeep Kaushik, Ishwar Prasad Sahu, Tarun Kumar Thakur. Exploring the Paradigm of Phyto-Nanofabricated Metal Oxide Nanoparticles: Recent Advancements, Applications, and Challenges. Molecular Biotechnology 2023. https://doi.org/10.1007/s12033-023-00799-8 (I.F. = 2.86) **(SCIE)**
7. **Bhamini Pandey**, Hema Tewatia, Dipendra Meel, Poonam Singh. Phyto-fabrication of zinc oxide nanoparticles using *Ficus religiosa* and its potential application in degradation of crystal violet dye. Applied Chemical Engineering 2023; 6:3. http://dx.doi.org/10.24294/ace.v6i3.2024 **(Scopus)**
8. **Bhamini Pandey** and Poonam Singh. Ultrasonic-assisted adsorptive uptake of Malachite green dye onto Zn/Cu layered double oxide: Spectrophotometric and smartphone-based detection. **(Communicated)**
9. **Bhamini Pandey** and Poonam Singh. Synthesis and characterization of PMMA/Zn-Cu LDH composites: Morphological, thermal, and adsorption properties. **(communicated)**

Publications in conference/workshop proceeding:

1. Presented paper in International Conference on "Chemical and Allied Science and their Applications" organized by Department of Applied Chemistry, DTU on 20th January, 2023. **(Oral Presentation)**

2. Presented paper in "2nd International Conference on Green and Sustainable Chemistry Conference-2022" organized by Department of Chemistry, Manav Rachna University, Faridabad, Haryana-121004 on 17th to 19th November, 2022. **(Oral Presentation)**
3. Presented paper in "International Conference on Advances in Chemical Sciences and Nanocomposites-ACSN 2022" jointly organized by Zakir Husain Delhi College & ISAS on 1st and 2nd April, 2022. **(Oral Presentation) (Received best oral presentation award)**
4. Presented paper in "International Conference on Innovation and Application in Science and Technology" organized by Department of Applied Sciences, Galgotias College of Engineering and Technology, Greater Noida, UP, India on 21-23rd December, 2021. **(Oral Presentation)**
5. Participated in Online Workshop on 'Accelerators/Incubation-Opportunities for Students & Faculties Early-Stage Entrepreneurs' organized by Department of Applied Chemistry, Delhi Technological University, Delhi on 19th June, 2021.
6. Participated in INUP-i2i 6th User Awareness Workshop on Fabrication & Characterization Facility for Nanotechnology, held at IIT Delhi during 4-5 March, 2023.
7. Attended workshop on "Field Emission Scanning Electron Microscopy Based Lithography" organized jointly by AIRF-JNU & Advance Scientific Equipment Pvt. Ltd. (TESCAN, BrnoCzech Republic) on 5th-6th September, 2019 at AIRF, JNU, New Delhi, India.
8. Participated in International Conference on "Atomic Molecular, Optical and Nano Physics with Applications" organized by Delhi Technological University, Delhi during 18-20th December, 2019.